AD-A249 728

‖‖‖‖‖‖‖‖‖‖

DCUMENTATION PAGE

Form Approved
OMB No 0704-0188

	2. REPORT DATE	3. REPORT TYPE AND DATES COVERED
	1991	XXXXXXXXDISSERTATION

4. TITLE AND SUBTITLE
An Investigation of Spinup Dynamics of Axial Gyrostats
Using Elliptic Integrals and the Method of Averaging

5. FUNDING NUMBERS

6. AUTHOR(S)

Christopher D. Hall, Captain

7. PERFORMING ORGANIZATION NAME(S) AND ADDRESS(ES)

AFIT Student Attending: Cornell University

8. PERFORMING ORGANIZATION REPORT NUMBER

AFIT/CI/CIA-91-026D

9. SPONSORING/MONITORING AGENCY NAME(S) AND ADDRESS(ES)

AFIT/CI
Wright-Patterson AFB OH 45433-6583

DTIC
ELECTE
MAY 6 1992
S c D

10. SPONSORING/MONITORING AGENCY REPORT NUMBER

11. SUPPLEMENTARY NOTES

12a. DISTRIBUTION/AVAILABILITY STATEMENT
Approved for Public Release IAW 190-1
Distributed Unlimited
ERNEST A. HAYGOOD, Captain, USAF
Executive Officer

12b. DISTRIBUTION CODE

13. ABSTRACT (Maximum 200 words)

14. SUBJECT TERMS

15. NUMBER OF PAGES
205

16. PRICE CODE

17. SECURITY CLASSIFICATION OF REPORT	18. SECURITY CLASSIFICATION OF THIS PAGE	19. SECURITY CLASSIFICATION OF ABSTRACT	20. LIMITATION OF ABSTRACT

AN INVESTIGATION OF SPINUP DYNAMICS OF AXIAL GYROSTATS
USING ELLIPTIC INTEGRALS AND THE METHOD OF AVERAGING

Christopher Dean Hall, Ph.D.

Cornell University 1992

A gyrostat is a rigid body containing an internal source of angular momentum which does not alter the geometry of the system. Because of their relative simplicity, gyrostats are frequently used to model dual-spin spacecraft. An axial gyrostat is composed of two rigid bodies: an asymmetric platform and an axisymmetric rotor aligned with a principal axis of the platform. Rotation of the rotor relative to the platform provides a source of internal angular momentum, and does not affect the moment of inertia tensor of the gyrostat. In this thesis, we consider the dynamics of axial gyrostats in the absence of energy dissipation and external torques. Spinup of the rotor is effected by a small constant internal axial torque, g_a. The dynamics are described by four first-order ordinary differential equations, which admit exact solutions in terms of elliptic functions for $g_a = 0$. Application of the method of averaging (valid for small g_a) reduces the problem to a single first-order differential equation, which is studied analytically and numerically. This single equation accurately describes most spinup trajectories. However, when spinup trajectories cross the instantaneous separatrices

of the $g_a = 0$ system, the $\mathcal{O}(1)$ frequency of the unaveraged system vanishes. The averaged equations are not valid near these separatrix crossings, and we develop an approximate equation valid in a neighborhood of the separatrix, which we use to connect the averaged solutions across the separatrix. When applied iteratively in a neighborhood of the separatrix, the approximate equation agrees qualitatively with the exact solution.

Bibliography

[1] Paul F. Byrd and Morris D. Friedman. *Handbook of Elliptic Integrals for Engineers and Physicists*. Springer-Verlag, Berlin, second edition, 1971.

[2] John E. Cochran, Ping-Huei Shu, and Stephen D. Rew. Attitude motion of asymmetric dual-spin spacecraft. *Journal of Guidance, Control and Dynamics*, 5(1):37–42, Jan–Feb 1982.

[3] Vincent T. Coppola and Richard H. Rand. Chaos in a system with a periodically disappearing separatrix. *Nonlinear Dynamics*, 1:401–420, 1990.

[4] J. R. Gebman and D. Lewis Mingori. Perturbation solution for the flat spin recovery of a dual spin spacecraft. *AIAA Journal*, 14(7):859–867, Jul 1976.

[5] Christopher D. Hall. Equivalence of two classes of dual-spin spacecraft spinup problems. *Journal of Guidance, Control and Dynamics*, 1992. (To appear).

[6] Carl Henry Hubert. *An Attitude Acquisition Technique for Dual-Spin Spacecraft*. PhD thesis, Cornell University, Ithaca, NY, 1980.

[7] Peter C. Hughes. *Spacecraft Attitude Dynamics*. John Wiley & Sons, New York, 1986.

[8] R. J. Kinsey, D. L. Mingori, and R. H. Rand. Spinup through resonance of rotating unbalanced systems with limited torque. In *Proceedings of the 1990 AIAA/AAS Astrodynamics Conference, Part 2*, pages 805–813, Aug 1990. AIAA Paper 90-2966.

[9] Jan A. Sanders and Ferdinand Verhulst. *Averaging Methods in Nonlinear Dynamical Systems*, volume 59 of *Applied Mathematical Sciences*. Springer-Verlag, New York, 1985.

AN INVESTIGATION OF SPINUP DYNAMICS OF AXIAL GYROSTATS USING ELLIPTIC INTEGRALS AND THE METHOD OF AVERAGING

Christopher Dean Hall, Ph.D.

Cornell University 1992

A gyrostat is a rigid body containing an internal source of angular momentum which does not alter the geometry of the system. Because of their relative simplicity, gyrostats are frequently used to model dual-spin spacecraft. An axial gyrostat is composed of two rigid bodies: an asymmetric platform and an axisymmetric rotor aligned with a principal axis of the platform. Rotation of the rotor relative to the platform provides a source of internal angular momentum, and does not affect the moment of inertia tensor of the gyrostat. In this thesis, we consider the dynamics of axial gyrostats in the absence of energy dissipation and external torques. Spinup of the rotor is effected by a small constant internal axial torque, g_a. The dynamics are described by four first-order ordinary differential equations, which admit exact solutions in terms of elliptic functions for $g_a = 0$. Application of the method of averaging (valid for small g_a) reduces the problem to a single first-order differential equation, which is studied analytically and numerically. This single equation accurately describes most spinup trajectories. However, when spinup trajectories cross the instantaneous separatrices

of the $g_a = 0$ system, the $\mathcal{O}(1)$ frequency of the unaveraged system vanishes. The averaged equations are not valid near these separatrix crossings, and we develop an approximate equation valid in a neighborhood of the separatrix, which we use to connect the averaged solutions across the separatrix. When applied iteratively in a neighborhood of the separatrix, the approximate equation agrees qualitatively with the exact solution.

Bibliography

[1] Paul F. Byrd and Morris D. Friedman. *Handbook of Elliptic Integrals for Engineers and Physicists*. Springer-Verlag, Berlin, second edition, 1971.

[2] John E. Cochran, Ping-Huei Shu, and Stephen D. Rew. Attitude motion of asymmetric dual-spin spacecraft. *Journal of Guidance, Control and Dynamics*, 5(1):37–42, Jan–Feb 1982.

[3] Vincent T. Coppola and Richard H. Rand. Chaos in a system with a periodically disappearing separatrix. *Nonlinear Dynamics*, 1:401–420, 1990.

[4] J. R. Gebman and D. Lewis Mingori. Perturbation solution for the flat spin recovery of a dual spin spacecraft. *AIAA Journal*, 14(7):859–867, Jul 1976.

[5] Christopher D. Hall. Equivalence of two classes of dual-spin spacecraft spinup problems. *Journal of Guidance, Control and Dynamics*, 1992. (To appear).

[6] Carl Henry Hubert. *An Attitude Acquisition Technique for Dual-Spin Spacecraft*. PhD thesis, Cornell University, Ithaca, NY, 1980.

[7] Peter C. Hughes. *Spacecraft Attitude Dynamics*. John Wiley & Sons, New York, 1986.

[8] R. J. Kinsey, D. L. Mingori, and R. H. Rand. Spinup through resonance of rotating unbalanced systems with limited torque. In *Proceedings of the 1990 AIAA/AAS Astrodynamics Conference, Part 2*, pages 805–813, Aug 1990. AIAA Paper 90-2966.

[9] Jan A. Sanders and Ferdinand Verhulst. *Averaging Methods in Nonlinear Dynamical Systems*, volume 59 of *Applied Mathematical Sciences*. Springer-Verlag, New York, 1985.

AN INVESTIGATION OF SPINUP DYNAMICS OF

AXIAL GYROSTATS USING ELLIPTIC INTEGRALS

AND THE METHOD OF AVERAGING

A Dissertation

Presented to the Faculty of the Graduate School

of Cornell University

in Partial Fulfillment of the Requirements for the Degree of

Doctor of Philosophy

by

Christopher Dean Hall

January 1992

AN INVESTIGATION OF SPINUP DYNAMICS OF AXIAL GYROSTATS USING ELLIPTIC INTEGRALS AND THE METHOD OF AVERAGING

Christopher Dean Hall, Ph.D.

Cornell University 1992

A gyrostat is a rigid body containing an internal source of angular momentum which does not alter the geometry of the system. Because of their relative simplicity, gyrostats are frequently used to model dual-spin spacecraft. An axial gyrostat is composed of two rigid bodies: an asymmetric platform and an axisymmetric rotor aligned with a principal axis of the platform. Rotation of the rotor relative to the platform provides a source of internal angular momentum, and does not affect the moment of inertia tensor of the gyrostat. In this thesis, we consider the dynamics of axial gyrostats in the absence of energy dissipation and external torques. Spinup of the rotor is effected by a small constant internal axial torque, g_a. The dynamics are described by four first-order ordinary differential equations, which admit exact solutions in terms of elliptic functions for $g_a = 0$. Application of the method of averaging (valid for small g_a) reduces the problem to a single first-order differential equation, which is studied analytically and numerically. This single equation accurately describes most spinup trajectories. However, when spinup trajectories cross the instantaneous separatrices

of the $g_a = 0$ system, the $\mathcal{O}(1)$ frequency of the unaveraged system vanishes. The averaged equations are not valid near these separatrix crossings, and we develop an approximate equation valid in a neighborhood of the separatrix, which we use to connect the averaged solutions across the separatrix. When applied iteratively in a neighborhood of the separatrix, the approximate equation agrees qualitatively with the exact solution.

Biographical Sketch

Christopher Dean Hall was born on November 10, 1957 in Rockingham, North Carolina, and graduated from Richmond Senior High School in 1975. After a brief study of architecture at the University of North Carolina at Charlotte, he abandoned academia and went on the road (in the sense of Kerouac), where for two years he wandered around North America, before enlisting in the United States Air Force in 1978. His first duty station was RAF Mildenhall, United Kingdom, where he took classes in physics and calculus, met his future wife, developed a liking for Real Ale, and was awarded an Air Force scholarship to attend Auburn University, where he received a Bachelor's degree in Aerospace Engineering with High Honor in March 1984. He then attended Officer Training School at Lackland AFB, Texas, and was commissioned a Second Lieutenant in June 1984. For the next three years he worked as an astronautical engineer at Onizuka AFB in Sunnyvale, California. In June 1987 he entered the Air Force Institute of Technology (AFIT) at Wright-Patterson AFB in Fairborn, Ohio, and in December 1988 was awarded a Master's degree in Systems Engineering. He was subsequently selected to join the faculty in AFIT's Department of Aeronautics and Astronautics. He entered the Graduate School at Cornell University in the field of Theoretical and Applied Mechanics in January 1989.

to my wife

Rhoda

and our sons

Duncan and Casey

Acknowledgements

I am especially grateful to my major advisor, Professor Richard Rand, for his guidance and support throughout this research. Although he taught me a great deal about dynamics and mathematics, perhaps his most important lessons were on pedagogy, especially on writing and talking about dynamics and mathematics. I hope those lessons stay with me.

I am also grateful to Professor Philip Holmes, who also served on my committee. His course on nonlinear vibrations inspired me to apply modern nonlinear analysis to spacecraft dynamics. His close reading of my thesis resulted in invaluable comments. Thanks also to my minor advisor, Professor Hsiao-Dong Chiang, who taught me a lot about stability theory.

I would also like to thank Professor Tim Healey for his encouragement for my initial investigation of the rotational dynamics of coupled rigid bodies, Dr. Carl Hubert of General Electric Astro Space for giving me a tour of the GE satellite facility in Princeton, and Professor Peter Torvik of the Department of Aeronautics and Astronautics at the Air Force Institute of Technology (AFIT) for encouraging me to apply for a position in the AFIT faculty.

The graduate students in Theoretical and Applied Mechanics have also contributed enormously to the richness of my experience here. I especially want to

Table of Contents

List of Tables

List of Figures

Chapter 1

Introduction

A dual-spin spacecraft consists of two bodies constrained to relative rotation about a shaft connecting the bodies, but otherwise free to rotate in space (see Fig. 1.1). The bodies are in general flexible and dissipative, as is the connection between them, and all spacecraft are subject to environmental torques such as the gravity gradient torque; however, as a first approximation it is useful to model dual-spin spacecraft as two rigid bodies connected by a rigid shaft, free of external torques, and without energy dissipation. Such a model is made more tractable by further assuming one of the bodies is axisymmetric about the axis of relative rotation. The principle benefit of this assumption is that the moment of inertia tensor is constant for the model spacecraft. The axisymmetric body is called the *rotor*, or *wheel*, while the other body is called the *platform* or *core*. This model is called a *gyrostat*, and the differential equations describing its motion are completely integrable in two important cases: when there is no axial torque between the bodies, and when the relative angular velocity is held constant by an appropriate torque. In fact, these two cases are equivalent under a suitable change of variables, as was first shown by Kane and Fowler [45] for the special class of *axial* gyrostats, where the rotor axis is aligned with, or parallel to, a principal axis of the platform. For axial gyrostats, a closed form solution for

the angular momentum or angular velocity variables in terms of Jacobi's elliptic functions has been given by several authors (see Section 1.2.1).

Dual-spinners are usually placed into orbit with zero relative angular velocity, *i.e.*, the spacecraft spins as a single body. Then a spinup motor provides an equal and opposite torque to both bodies along the shaft. The desired effect of the axial torque is to spin up the rotor and despin the platform, thereby transferring all or most of the angular momentum to the rotor. Usually this torque is constant for simplicity of control system design, and small to prevent counter-rotation of the platform. For some gyrostat configurations, a large torque is preferable to a small torque, as demonstrated in Chapter 3.

The success of this maneuver, known as the *dual-spin turn*, *platform despin*, or simply *spinup*, depends on the energy dissipation inherent in all real spacecraft. The dual-spin condition is asymptotically stable provided the energy dissipation rates of the platform and rotor satisfy certain conditions. These conditions depend on the particular configuration being analyzed, but roughly speaking, platform energy dissipation is stabilizing, and rotor energy dissipation is destabilizing. These stability criteria hold even if the rotor is designed to spin about its minor moment of inertia axis; thus the dual-spin spacecraft defies the so-called major axis rule [38, ch. 7].

Actual implementations of dual-spinners vary significantly: for example, the first prolate dual-spin satellite, TACSAT I (Fig. 1.1), was mostly rotor, while a typical geostationary communications satellite consists of a large platform with a relatively small, fast momentum wheel [38, ch. 11]. The latter are usually called *bias momentum* satellites. Although these two extremes bear little resemblance to one another, they may both be successfully modeled by the *simple gyrostat*. A gyrostat is a body with moving parts but constant moment of inertia tensor. A simple gyrostat is a rigid body with an attached rigid wheel spinning about an axis of symmetry fixed in the body.
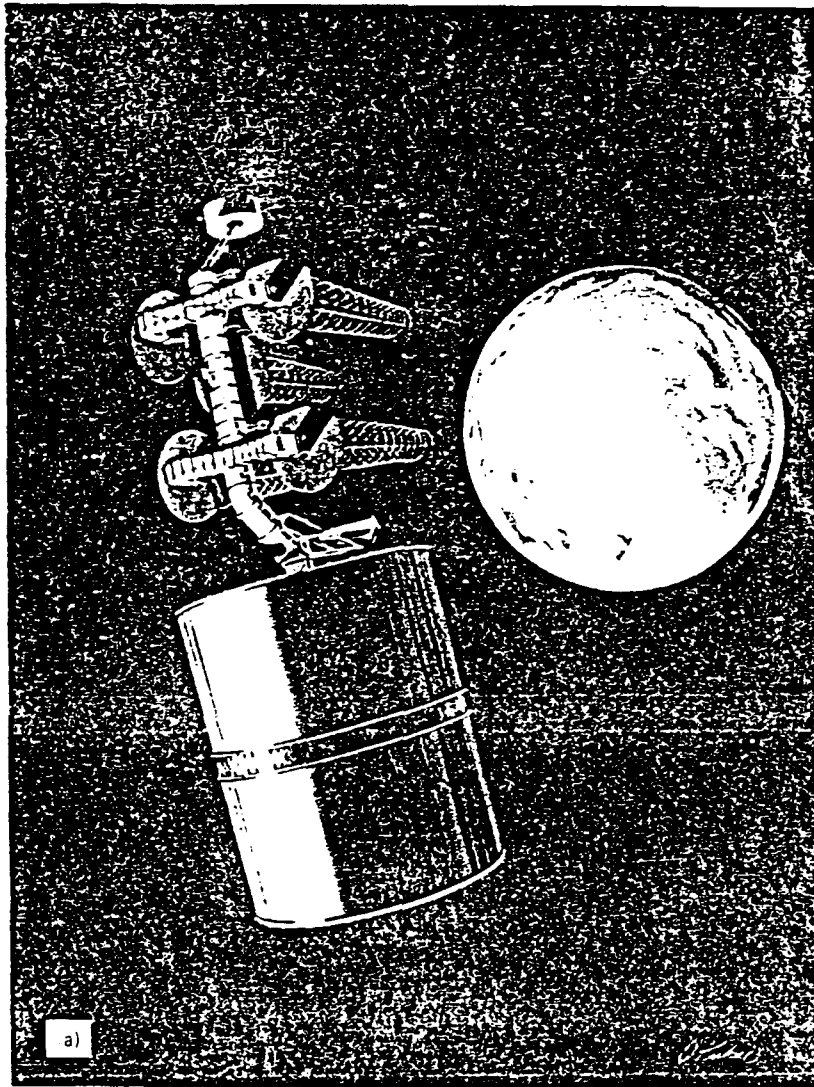
Figure 1.1. The TACSAT I Dual-Spin Satellite. TACSAT I, launched in 1968, was the first satellite to successfully spin about its minor axis [38, pp. 448-449]. The antenna is the *platform*, and is intended to point continuously at the Earth. The cylindrical component is the *rotor*, providing gyroscopic stability through its spin of about 60 rpm [42].

Over the years, many researchers have investigated the gyrostat and other dual-spin models in many settings, including such variations as spring-mass-dampers, rotor flexibility, flexible appendages, time-dependent inertia properties, and external torques. A good general reference is the textbook by Hughes [38]. An introduction to the literature is given in the next chapter.

As noted above, the simple gyrostat leads to a completely integrable system of equations in two important cases: zero internal axial torque, and constant rotor angular momentum relative to the platform. The dynamics are fairly well understood in these cases, in both the torque-free and inverse-square central force environments. Unfortunately, these cases only represent quasi-static views of the system dynamics. In particular, the dynamics during rotor spinup offer further challenges to researchers, especially in the presence of rotor asymmetry and/or unbalance.

Since a closed form solution exists for the angular momentum of an axial gyrostat with zero axial torque, the introduction of a small constant torque invites the use of perturbation methods to study the equations of motion. A special case where the unperturbed solution takes the form of trigonometric functions has been investigated by Gebman and Mingori [23]. No one, however, has used the full elliptic function solution in a perturbation analysis of spinup dynamics. This leads us to the following problem statement.

1.1 Problem Statement

The goal of this thesis is to study the spinup dynamics of dual-spin spacecraft using the axial gyrostat as an approximate model. Specifically, the elliptic function solution of the non-dimensionalized equations of motion for zero axial torque is to be used as the starting point for a perturbation analysis based on the method of averaging, valid for small spinup torques.

1.2 Related Work

Before describing our approach and results, we give a brief discussion of published work related to what we have done. The first topic is the elliptic function solution for the zero torque case, *i.e.*, the unperturbed problem. Then we discuss other investigations of spinup dynamics, *i.e.*, the perturbed problem. A more in-depth introduction to the literature of dual-spin spacecraft is given in Chapter 2.

There is also a large body of literature on the subjects of averaging and elliptic functions. Rather than discuss references here, we refer the reader to the appropriate chapters of the thesis.

1.2.1 Closed Form Solutions for the Unperturbed Problem

As we have stated above, the equations of motion for the simple gyrostat are integrable in two cases: zero axial torque, and constant relative angular velocity. This fact has been rediscovered several times over the past century.

In 1898, Volterra [98] proposed a gyrostat model in an effort to explain the Earth's wobble about its spin axis. This is apparently the only treatment of a *natural*, *i.e.*, non-technological, gyrostat. He gave a quite thorough treatment of the zero axial torque case, obtaining solutions for the angular velocities as functions of time using the Weierstrassian elliptic functions. The principal disadvantage of his solution is the absence of any physical interpretation of the results.

More recently, in 1961, Masaitis [70] suggested that the axial gyrostat might provide useful stabilization properties for artificial satellites. Considering the zero axial torque case, he derived solutions for the angular velocities using Jacobi's elliptic functions. He also obtained rigorous stability results, and he suggested that the elliptic function solution offered "possibilities for a perturbation treatment."

The zero axial torque case was also investigated by Leipholz [57] in 1963, motivated by flight of aerospace vehicles containing rotating parts. He also obtained the solution for the angular velocities in terms of Jacobi's elliptic functions.

In 1965 Leimanis [56] gave an extensive treatment of the axial gyrostat with zero axial torque, complete with solutions for the angular velocities in terms of Jacobi's elliptic functions, apparently following the work of Masaitis [70] and Leipholz [57]. However, there are two errors in Leimanis' work, one of which also appears in Leipholz's work. First, Leimanis states that the assumption of a prolate gyrostat may be made without loss of generality. This is not true. There is a symmetry relationship between prolate and oblate gyrostats, as we show here in Section 3.5. However, there is a distinct difference between prolate and intermediate gyrostats, discussed here in Section 4.7. This error does not appear in the earlier references. Second, he omitted a factor in the quartic which occurs in the elliptic integral, a mistake which also appears in Leipholz's paper. We give the details in Appendix C.

In 1975 Wittenburg devoted his *habilitationschrift* [103] to the study of the dynamics of gyrostats in the integrable cases, giving solutions for the angular momentum variables for several combinations of asymmetry and rotor alignment. He developed his solutions for the constant relative rotor speed case, using Jacobi's elliptic functions. For the cases where the rotor is not aligned with a principal axis of the asymmetric platform, he showed how to reduce the equations to a quadrature, but did not evaluate the quadrature. He also discussed this development in his book [104].

The next, and most recent, appearance of the solution was published in 1982, when Cochran *et al* [16] extended the previous results by obtaining a complete analytical solution for the Euler angles and angle of relative rotation in terms of elliptic functions and elliptic integrals. They used the nature of these solutions to discuss a particular resonance problem which will be discussed here in Section 2.6.2.

1.2.2   Investigations of Spinup Dynamics

The elliptic function solutions discussed in the previous section are relevant for the motion of gyrostats with free or constant-speed rotor. Of course, during spinup, the rotor satisfies neither of these conditions. The interesting and very important problem of the variable-speed rotor has been studied by several authors. Kane [43] showed that, for axisymmetric gyrostats, the precession speed and nutation angle are *constant* during spinup, which means that an axisymmetric gyrostat in a state of "flat spin" cannot recover its *nominal* spin about its axis of symmetry. Sen and Bainum [93] also studied spinup of axisymmetric gyrostats. They obtained a closed form solution for the case where the rotor axis of symmetry lies on the body's symmetry axis, and used a perturbation analysis to handle slight misalignment.

The work of Gebman and Mingori [23] has some similarities to the present work. They used a perturbation analysis to obtain an approximate solution for a flat spin recovery problem. The principal difference between the two approaches is that they investigated a very specific spinup problem for a subset of axial gyrostats, with the motion starting exactly at an equilibrium of the unperturbed system, whereas our investigation covers all possible spinup problems for all axial gyrostats. Mathematically, their perturbation scheme involved perturbing off of solutions using trigonometric functions, whereas our more general approach involves starting with elliptic functions. Their work is discussed in more detail in Appendix A.

Kane [44] investigated the spin-up dynamics of a *zero-momentum* gyrostat, that is, a gyrostat with zero total angular momentum. This problem is also addressed in Kane *et al* [47]. Chen and Kane [12] considered the inverse problem: given a desired platform rotation axis and angle, determine the necessary rotor rotation axis and angle. Hughes [38] has shown, however, that this configuration has the same qualitative behavior as a single non-spinning rigid body. We do not

treat zero-momentum gyrostats in this thesis.

Hubert [34,35,36,37] investigated spinup of a rigid gyrostat with two rotors: one a constant-speed rotor, the other subject only to a viscous damping torque. He proved that the dual-spin condition is asymptotically stable for *all* initial conditions provided the relative angular velocity of the constant-speed rotor is fast enough. This result corrected a previous misconception about possible instabilities (cf. Kaplan [49, p. 378]). An interesting improvement to Hubert's dual-spin maneuver has been proposed by Weissberg and Ninomiya [99]: instead of depending on passive energy dissipation, rotor torque control can be used to decrease the core energy, leading to asymptotic stability for the dual-spin condition.

Li and Longman [59] conducted a detailed analysis using a feedback system to control the internal axial torque of a rigid gyrostat in a circular orbit. They determined stability and instability criteria for a number of important cases. Among their results is an interesting extension of the free rotor – constant-speed rotor equivalence discussed earlier.

The problem of optimally recovering from intermediate motions (*i.e.*, not flat spin) has been examined by Guelman [28]. He focused on prolate simple gyrostats, and developed a control law to bring the state to one of the unperturbed equilibrium points. Slotine and Di Benedetto [94] have developed an adaptive control law for rigid three-rotor gyrostats that is applicable even if the mass properties of the system are unknown.

In all these spinup studies, the rotor was taken to be axisymmetric and spinning about its symmetry axis. Real rotors are of course slightly asymmetric and slightly unbalanced. The effects of these imperfections can have dramatic effects on spinup dynamics. These effects are discussed further in Chapter 2.

1.3 Approach and Results

In this thesis, we give a comprehensive treatment of spinup of all axial gyrostats where the axisymmetric rotor is aligned with a principal axis of the asymmetric platform, and spinup is effected by a small constant axial torque. The dynamics are described by *four* first-order ordinary differential equations. We work with a dimensionless form of the equations, equating the axial torque to a small parameter ε. When $\varepsilon = 0$ the system has a closed form solution in terms of Jacobi's elliptic functions as noted above. We use conservation of angular momentum to reduce the order of the equations by one. Then by averaging over the *fast* dynamics, we obtain a *single* first-order non-autonomous differential equation for the slow evolution of kinetic energy. This equation involves complete and incomplete elliptic integrals of the first and second kinds; numerical integration shows that this single equation captures the salient features of spinup dynamics. For small ε, numerical integration of this equation is more efficient than integrating the full system of equations, since the averaged equation is independent of ε.

There are difficulties with averaging over the fast dynamics, however. For some types of spinup trajectories, the flow passes through one or more *resonances*, associated with the flow of the perturbed system *crossing* a separatrix of the unperturbed system. In the vicinity of these resonances, the averaging assumptions are invalid, and it becomes necessary to deal with the fast equation and develop a solution in a neighborhood of the resonance. We obtain an accurate approximation for the "thickness" of the last cycle before the separatrix crossing, and we use a simple Euler integration technique to connect the averaged solutions across the separatrix.

The reduction from four differential equations to one has a geometric counterpart which we have found simplifies the framework in which to view spinup dynamics. In contrast to the momentum sphere approach, which requires picturing the gradual evolution of a set of integral curves drawn on a sphere (see,

e.g., Ref. [37]), our approach permits the spinup dynamics to be described by an abbreviated but equivalent flow on a plane.

One result of the geometric study of spinup is the discovery of a new symmetry of the system, which is used to reduce the number of cases studied. The transformation is discussed in Section 3.5, and a paper describing it has been accepted for publication [30].

An important contribution is the development of the averaged equations. Although the $\varepsilon = 0$ solution in terms of elliptic functions has been known for some time, apparently the solution has not previously been used to investigate the perturbed dynamics of gyrostats. The averaged equations allow the easy identification of the *resonant zones* for the system. Although *resonance capture* in the usual sense is not possible here, the resonances have a *dispersive* effect that makes the flow sensitive to small changes in the initial conditions. In fact, one class of resonance capture problems can be studied using our approach, and we discuss this fact in Section 4.6.

The averaged equations also have several exact solutions. We use a further perturbation analysis based on these exact solutions to obtain approximate solutions to the averaged equations for some regions of phase space.

1.4   Outline of the Thesis

In Chapter 2 we give a review of the literature on dual-spin spacecraft and gyrostats. While many of these references cover topics outside the scope of this thesis, they are included as a source for those who are interested in pursuing some of the many open problems in this field.

The model and the basic equations of motion are developed in Chapter 3. Also in this chapter we discuss the various symmetries of the equations, which are used to reduce the number of cases which must be considered. Then we use conservation of angular momentum to reduce the order of the equations from

four to three, and we further reduce the equations to a single elliptic integral for the case of zero spinup torque. The dimensionless inertia parameters used here are discussed in some detail in Appendix B. In Chapter 4 we discuss the geometric aspects of spinup dynamics. In Appendix E, we apply the equivalent analysis to a simple nonlinear second-order differential equation with a slowly varying parameter.

As we have mentioned above, when there is no axial torque between the bodies, there is a closed form solution for the angular momenta in terms of Jacobi's elliptic functions. In Chapter 5 we give the solution for all possible cases of axial gyrostats. As a supplement to this chapter, Appendix C details the use of Byrd and Friedman's [10] tables to evaluate the elliptic integrals.

In Chapter 6 we apply the method of averaging to the equations of motion in order to derive approximate equations governing the slow evolution of the system. In the process we identify resonances associated with *instantaneous separatrix crossings*. These resonances are the subject of Chapter 7, where we investigate more closely the flow near the separatrix.

In Chapter 8 we obtain approximate solutions to the slow flow equation based on perturbing off of special exact solutions to the averaged equations developed in Chapter 6. The resulting approximations are valid for trajectories that remain near equilibrium points of the unperturbed system. The series expansion of complete elliptic integrals of the third kind is required for these approximate solutions. These expansions are developed in Appendix D.

Finally, in Chapter 9 we summarize this work and discuss future directions for related research.

Chapter 2

Dual-Spin Spacecraft and Gyrostats: A Guide to the Literature

The dynamics of gyrostats, and of dual-spin spacecraft in general, has been actively studied since the beginning of the space age. Researchers have examined many modifications of the basic problem, using a wide range of techniques from applied mathematics. There is an extensive body of literature on the subject. In this review, we try to discuss most of the important results concerning these systems. We make no claim to completeness; however, we have tried to obtain all of the published works which are relevant to this thesis: namely, the elliptic function solutions, spinup dynamics, and internal resonances due to asymmetry and unbalance.

2.1 Textbook Treatments

The simple gyrostat and some of its simpler variations have been studied for long enough to find their way into textbooks. An excellent general reference is the text book by Hughes [38]. He gives an extensive treatment of several basic problems in attitude dynamics. In particular, he treats the simple gyrostat with and without damping mechanisms, in and out of orbit, and addresses the

stability of the equilibrium motions. However, even though he gives the elliptic function solution to the torque-free rigid body equations of motion, he doesn't even mention that the rigid gyrostat is integrable in some cases.

Leimanis [56] and Wittenburg [104] both treat the simple gyrostat and provide at least partial solutions to the equations of motion. Kane *et al* [47] cover the rigid gyrostat in the torque-free and circular orbit environments; they also examine a simple spinup maneuver for an initially motionless gyrostat. Rimrott [86] devotes two chapters to the attitude dynamics of rigid gyrostats and the special case of torque-free axisymmetric gyrostats with energy dissipation. He also gives a brief discussion of the effects of friction in the rotor bearing. Kaplan [49] discusses the spinup problem for the simple gyrostat, but draws erroneous conclusions about the possibilities of dual-spin stabilization. Elementary treatments of dual-spin spacecraft are also given by Agrawal [3] and Wiesel [102]. Finally, the volume edited by Wertz [101] addresses some of the practical details of dual-spin satellites and the use of passive damping mechanisms in spacecraft, and gives some details of specific dual-spin spacecraft implementations.

Remark 1 *Other than the simple spin-up maneuver solved in Kane et al [47], none of these books addresses spinup dynamics, or the resonance problems associated with rotor asymmetry and unbalance.*

2.2 Classical Origins

Like most other rigid body problems, the gyrostat is not a new idea; a detailed study of its classical roots would probably turn up several interesting results. Roberson appears to have done some research in this direction; in [89], he stated that the equations of motion for the simple gyrostat were given as early as 1862 by Résal. In another paper, Roberson [87] cited Volterra's 1898 treatise [98] as a "beautiful and definitive treatment of torque-free gyrostatic motion." In this treatise, Volterra introduced the gyrostat as a model for the earth in order to

explain the earth's wobble about its axis. He obtained a solution to the equations of motion in terms of elliptic functions. Leimanis [56] and Wittenburg [104] also cited Volterra's work, though their solutions differ markedly from Volterra's.

2.3   Initial Stability Investigations

The modern dual-spin concept has its origins in the independent discovery of its stabilization properties by both Landon [54] and Iorillo [41] in the early 1960's[1]. Landon's work was restricted to the case where damping exists on only one of the two bodies; using an *energy sink* argument analogous to the major axis rule for spinning spacecraft, he concluded that damping on the despun platform is stabilizing, while damping on the rotor is destabilizing. Iorillo's work extended the energy sink analysis to account for damping on both bodies. In both cases the physical model consisted of two axisymmetric bodies constrained to relative rotation about their mutual axis of symmetry.

Remark 2 *In the energy sink argument, one supposes that the relative angular velocity of the two bodies is fixed, and that the kinetic energy is approximately described by the expression obtained if both bodies are rigid. Then in the presence of "slow" energy dissipation, the kinetic energy will seek its minimum. As we discuss below, one difficulty with this assumption is that the constant relative angular velocity condition requires a non-zero motor torque, which constitutes an energy source, complicating the energy sink argument. Note also that the mechanism by which energy is dissipated is not specified.*

Remark 3 *Although the two papers [54,41] just mentioned are usually cited as the first dual-spin papers, there were actually two earlier papers in the English language literature. In 1961, Masaitis [70] published a very thorough analysis (discussed above in Section 1.2.1), and in 1963, Huston [39] published an interesting*

---

[1]The survey paper by Likins [60] provides an excellent account of this early history.

"note" on the gyrostat's stabilization possibilities. Also, Leimanis' book [56] appeared in 1965, at about the same time as the two papers, and Leipholz's paper [57] was published (in German) in 1963.

Since the benefits of dual-spin stabilization were readily apparent, but the costs of on-orbit failure were high, it was necessary to verify the idea's feasibility analytically. In Likins [61], a linearized stability analysis was shown to provide results identical to the energy sink argument for a specific system consisting of an asymmetric body with a spring-mass-damper and a symmetric rotor. Again, both bodies were statically and dynamically balanced, and the results agreed with the earlier work of Landon and Iorillo.

A frequently seen model in many early papers is the one introduced by Mingori [73]. This model consists of two rigid, axisymmetric bodies connected by a rigid shaft along the axis of symmetry; each body has a spring-mass-damper to provide energy dissipation. In [73] a Floquet analysis was used to construct stability charts in terms of a variety of dimensionless parameters. Again the results were in agreement with previous studies.

The success of these analyses resulted in the 1969 launch of the first minor axis dual-spinner, TACSAT I (see [38, pp. 448–449]). A slight wobble about the spacecraft's nominal spin axis inspired Likins, Mingori, and Tseng to search for an explanation. Their interesting results were reported in [62] and [74]. In [62], the introduction of nonlinear damping in Mingori's model led to the possibility of stable limit cycles, while in [74], the addition of nonlinear springs was shown to lead to variable amplitude limit cycles.

It is important to note that in all these studies, the researchers were examining local behavior near the dual-spin condition. Global analysis of the simple gyrostat provides more concrete results for dual-spin dynamics, particularly in regards to the existence and stability of equilibrium rotations, usually called *permanent rotations.*

2.4 Global Analysis of the Gyrostat

Strictly speaking, the dual-spin models discussed above are not gyrostats, since the motion of spring-mass-dampers results in time-varying inertia properties. The gyrostat, as already noted, has the nice property of being integrable in two important cases. An important method for analyzing nonintegrable systems is to model them as perturbations of an integrable system. Thus it makes sense to understand the gyrostat before investigating its nonintegrable variations. However, the historical development did not follow this route. In this section, we discuss some of the interesting and useful properties of the simple gyrostat, most of which were published after the energy sink and linearized analyses discussed above.

2.4.1 An interesting parallelism

In most of the early dual-spin stability analyses, *the internal torque parallel to the axis of relative rotation is taken to be zero*. For the dual-spin equilibrium position those researchers were interested in, this would indeed be the case. However, for the general problem, internal torques due to friction or a driving motor would certainly be present. It turns out that the case of zero internal axial torque is exactly equivalent to the case for constant angular velocity of the rotor relative to the platform, and that these two cases are completely integrable. The first evidence of this parallelism is found in Kane and Fowler [45], where the authors showed the equivalence of the two problems in the case where the rotor axis is parallel to a platform principal axis. In particular they showed how a simple reinterpretation of parameters transforms the equations for the free rotor case to those of the driven rotor case, and they exploited this equivalence in a discussion of the stability of the dual-spin equilibrium condition. More complete investigations of this equivalence were given by Roberson [89] and Crespo da Silva [20]. In addition, Krishnaprasad [52] has shown that this remarkable relationship is a

consequence of the identical Lie-Poisson structure of the two sets of equations of motion. The book by Olver [79] contains an introduction to Lie-Poisson structures, as well as an extensive list of references.

2.4.2 Core energy: An integral of the motion

The energy sink analyses used by Landon [54], Iorillo [41], Likins [61] and others were based on the idea of decreasing kinetic energy due to internal dissipation. For a single spinning body, this idea leads to the major axis rule. As Landon [54] pointed out, however, for driven rotor dual-spinners, the kinetic energy does not necessarily decrease, since in addition to the energy *sink*, the motor torque acts as an energy *source*. In fact, Spencer [95] has shown that Likins' analysis [61] was incorrect for gyrostats with asymmetric platforms; he also provided a refined stability condition for this more general case. Later, Kane and Levinson [46] gave a counterexample to "show that the energy-sink method can lead to both quantitatively and qualitatively incorrect descriptions of attitude motions." These efforts made it clear that energy sink analysis for dual-spinners requires more care than for single spinners.

Remark 4 *Although the energy sink argument has intuitive appeal, it is possible to find counter-examples even in the case of a single spinning body. Levi [58] has shown that it is possible for the angular velocity vector of an axisymmetric body with an internal spring-mass-damper to asymptotically approach a precessing motion, rather than approaching a constant pure spin.*

In the case of the gyrostat, exploitation of an energy integral for the rigid case has led to more rigorous justification and guidelines for use of the energy sink method. Hubert [37] coined the term "core energy" to describe the component of the kinetic energy of a gyrostat due to body rotation. In the case of constant angular velocity of the rotor relative to the platform, this is an integral of the motion, a fact recognized earlier by Leimanis [56], Wittenburg [104],

and Roberson [87], but not exploited by them in any stability analyses. Hubert showed that, for certain kinds of internal platform energy dissipation, the core energy is a strong Lyapunov function for the system. This result was given a solid theoretical basis in later work by Cochran and Shu [15], Krishnaprasad [52], and Guelman [27].

2.4.3 Relative equilibria

As already noted, most dual-spin studies have been concerned with the motion near the dual-spin condition. Gyrostat investigators, however, have identified the global structure of relative equilibria, or permanent rotations, with very interesting results. Masaitis [70] identified all relative equilibria for the balanced gyrostat with asymmetric platform and zero internal axial torque. He also determined the stability of the equilibria in each case, and provided a closed form solution for the angular velocities. Remarkably, this work appeared before any of the dual-spin studies appeared in the spacecraft engineering literature. Roberson [87] gave an elegant formulation for the gyrostat equilibria, interpreting the resulting fixed points as points of tangency between the core energy and angular momentum ellipsoids. He showed that there are two, four, or six relative equilibria depending on the values of certain parameters. Wittenburg [104] extended Roberson's results, showing how the changing number of relative equilibria may be interpreted on a certain bifurcation diagram. Krishnaprasad and Berenstein [53] determined conditions for the existence of only two equilibria on the momentum sphere. Most of these results are given a thorough treatment in the textbook by Hughes [38].

2.5 Gyrostats in Orbit

Just as the torque-free gyrostat offers greater potential for attitude stabilization, so does the gyrostat in a gravity field. The problem of a gyrostat in a circular orbit has been addressed by several authors. The problem was first examined

by Kane and Mingori [48], before all but the earliest of the dual-spin studies were published. They dealt with the specific case where the mass centers of the asymmetric body and symmetric rotor coincide, and the rotor symmetry axis is a principal axis of the platform. Longman and Roberson [67] considered the simple gyrostat under more general assumptions and identified analytically all of the relative equilibria. Roberson [88] then determined the stability of a subset of these equilibria, and Longman [64] determined the stability of all the equilibria. In [65], Longman considered the special case where the bifurcation changing the number of equilibria results in an infinity of relative equilibria. In [66], Longman *et al* generalized the stability regions (in a certain parameter space) of a rigid body in a circular orbit to include the rigid gyrostat. An interesting example of the type of nonlinear resonance that regularly occurs in spacecraft attitude dynamics was analyzed by Crespo da Silva [19]. In this work, he made explicit use of the equivalence property discussed here in Section 2.4.1.

Note that in all these studies the orbit was assumed to be circular. To date, very little has been done with dual-spin spacecraft in elliptic orbits. However, an interesting paper by Pascal [81] addressed the restricted three-body problem where the third body is a gyrostat near one of the five libration points. She identified the equilibria and determined their stability regions. Also, Mavraganis [71] has identified 9 first integrals for the n-body problem where all n bodies are gyrostats.

2.6 Rotor Asymmetry and Unbalance

One of the more interesting variations on the gyrostat model is that of asymmetry of the rotor and/or rotor imbalance. In general, the immediate effect of such changes is to destroy the constant inertia property of the gyrostat. A consequence of this is that the new system is no longer completely integrable, and most of the nice results discussed in Section 2.4 no longer hold. However, it is possible to

reverse the roles of rotor and platform; hence the axisymmetric, balanced platform with asymmetric and/or unbalanced rotor can be studied without giving up the gyrostat's constant inertia tensor.

As with the early dual-spin stability investigations, the approach taken by researchers has involved various approximation techniques such as linearization, perturbation analysis and averaging, with varying degrees of success. We group these studies into three categories: small-angle dynamics, large-angle dynamics, and evidence for chaos.

2.6.1 Small-angle dynamics

Scher [91] examined the effects of bearing assembly flexibility on the stability of the dual-spin condition. McIntyre and Gianelli [72] considered the wobble caused by slight static and dynamic unbalance and obtained analytical expressions for the resulting motion. They also gave a nice review of the state of the art of dynamic balancing. Bainum *et al* [5] considered damping and flexibility in the rotor, for an axisymmetric gyrostat with a planar pendulum damper. They reduced the stability criterion to a single first order ordinary differential equation. Small-angle dynamics in the presence of rotor asymmetry or imbalance has also been considered by Agrawal [2].

Similar studies have been conducted with an additional degree of freedom added to the joint. These are discussed here in Section 2.7.

2.6.2 Large-angle dynamics

The earliest treatment of large-angle dynamics in the presence of rotor asymmetry appears to be that of Scher and Farrenkopf [92] in 1974. The system investigated incorporated both dynamic imbalance of the platform and asymmetry of the rotor. Based primarily on numerical results, the authors identified two *trap states*: a minimum energy state corresponding to the eventual decay of the relative mo-

tion when bearing friction torques exceed the motor torque, and a resonance trap state when the motor has insufficient torque to achieve the dual-spin condition. Their primary recommendation was to use a "sufficiently powerful motor," but they also described a motor pulsing procedure that can result in escape from either of the two traps.

The resonance trap was investigated further by Cochran [13] and Cochran and Beaty [14], where the method of averaging was applied to the equations and first integrals were obtained for the averaged equations. These authors showed that asymmetry of the rotor and platform dynamic unbalance are necessary for the resonance trap to occur. They also provided a relation for estimating the required motor torque for a given system. Cochran *et al* [16] derived a closed form solution for the balanced gyrostat and used this to explain how the loss of symmetry leads to resonance.

Tsuchiya [96] also applied averaging to the equations for a spacecraft with asymmetric rotor and platform, but no imbalance. He investigated the attitude motion as the spacecraft passes through the "unstable region." Further, he obtained criteria for the onset of resonance while passing through this region. Because there is no platform unbalance, this is a different type of phenomenon than that treated by Scher and Farrenkopf [92]; thus it appears there are at least three trap states associated with rotor asymmetry.

Adams [1] examined the dynamics of a dual-spinner in which motor failure combined with bearing friction causes the platform to spin up. Besides the obvious minimum energy trap state, he also identified a resonance trap he called *precession phase lock*, or PPL. He conducted numerical investigations for several sets of inertia parameters, and compared his results to on-orbit experience with DSCS-II and TACSAT. He also showed that this type of PPL only occurs in oblate dual-spin spacecraft.

Hollars [32] started with a general dual-spin model with both bodies asym-

metric and unbalanced, then assumed the unbalance and one asymmetry were "small." Essentially, he determined estimates for the bearing torques required to avoid the resonance trap state, with specific application to the Jupiter orbiter Galileo.

Lukich and Mingori [68] carried out a parametric analysis of the model used by Tsuchiya [96]. They applied Hill's infinite determinant method and Floquet analysis to obtain stability diagrams in certain parameter planes. In the process they showed that Tsuchiya's assumptions were severely restrictive.

Kinsey *et al* [50] investigated spinup with small constant torque of a dual-spinner with axisymmetric bodies and dynamic imbalance of the rotor. Their work focused on the precession phase lock problem, and the principal result was a method for determining estimates for the cone angle caused by the rotor imbalance. Numerical results were obtained to corroborate their estimates. A similar model, with rotor asymmetry rather than imbalance, was investigated by Yang [106]. Exploiting the three first integrals available in the zero axial torque case, he obtained three first order differential equations for the Euler angles, averaged them and determined stability criteria for motion near the dual-spin condition. His results agreed with those of Tsuchiya [96].

Remark 5 *The systems studied by Kinsey et al [50], and Yang [106] are, in fact, gyrostats. Hence, some of the previous gyrostat results may be applicable. Kinsey's constant torque assumption removes that problem from the two known integrable cases, but a perturbation approach may result in an approximate closed form solution to the equations of motion. However, since Yang used zero axial torque, that system is completely integrable.*

2.6.3 Rotor asymmetry as a route to chaos

The effects of rotor asymmetry have also been analyzed from another point of view. Holmes and Marsden [33] have shown, using a simplified set of equations

based on the gyrostat, that a slight asymmetry of the rotor induces Smale horse-shoes in the flow, implying both nonintegrability and the presence of chaotic motion. Koiller [51] has produced similar results using a full gyrostat model. In both cases, a Melnikov function analysis was used to obtain the results (see Guckenheimer and Holmes [26, pp. 184–204]).

2.7 Other Two-Coupled-Body Problems

In concluding this literature review, we point out some other, non-dual-spin, two-coupled-body systems that have been studied.

Paquette [80] investigated controlling the motion of hinge-jointed attachments to effect a decrease in the kinetic energy and stabilize a tumbling spacecraft. He tested linear and nonlinear control laws derived using Lyapunov functions. (This concept recalls the controlled spinup idea of Weissberg and Ninomiya [99].)

Cretcher and Mingori [21] added a degree of freedom and studied the motion of an asymmetric platform connected by a gimbal-spring-dashpot to a slightly statically unbalanced rotor. They showed how the extra dimension can diminish the effects of the imbalance, while at the same time reducing the time constant of the nutation damping. At about the same time, Wenglarz [100] considered a similar system and arrived at the same conclusions. Cronin and Kane [22] studied a similar model in a circular orbit. They obtained the linearized equations of motion and determined stability criteria for certain equilibrium motions.

Grossman *et al* [25] and Patrick [82] added yet another rotational degree of freedom to the second body by considering a spherical, or ball-and-socket, joint instead of a bearing joint. In [25], the equations of motion were derived in a Hamiltonian form, with special attention paid to the Poisson structure of the equations, while in [82], the bodies were assumed to be identical cylinders, and the relative equilibria were then explicitly determined. In addition, a modified Energy-Casimir method was used to determine stability criteria for the equilibria.

Chapter 3

Equations of Motion

Our analysis of gyrostat dynamics begins with a description of the model, including derivation of the differential equations of motion. These equations turn out to be similar to Euler's equations for the angular velocities or angular momenta of a single rigid body, with one additional equation for the axial angular momentum of the rotor, for a total of four first-order ordinary differential equations. The equations are greatly simplified by changing to dimensionless variables, in which the axial torque is represented by the parameter ϵ. Three finite symmetry transformations are then used to reduce the number of cases to be studied. The existence of first integrals permits reduction of the number of equations in both the unperturbed ($\epsilon = 0$) and the perturbed ($\epsilon \neq 0$) systems. For the unperturbed system, the reduction leads to a single elliptic integral. The perturbed system is reduced from four differential equations to three equations which have the advantage of being "almost" in the correct form for applying the method of averaging.

3.1 The Model and Euler's Equations

The gyrostat model we consider in this thesis is shown in Fig. 3.1. The gyrostat consists of two rigid bodies: a *platform* $\mathcal{P}$, and a *rotor* $\mathcal{R}$, connected by a rigid

shaft with frictionless bearings. A spinup motor is available to provide a torque to both bodies along the shaft. The mass of this motor may be part of either or both of the two bodies. The entire gyrostat is free to rotate in space, but the relative motion of the two bodies is constrained to rotation about the axis of the shaft. The platform may be asymmetric; however, we require an axisymmetric rotor, with the axis of symmetry coinciding with the axis of relative rotation. We also assume the total gyrostat is asymmetric, or triaxial, that is to say, the three principal moments of inertia of the gyrostat are distinct. Furthermore, we assume the rotor's spin axis is aligned with or parallel to a principal axis of the platform. It is clear that this axis is then also a principal axis of the gyrostat. In Fig. 3.1, the spin axis is shown aligned with the principal axis $\mathbf{e}_1$; however, the equations of motion are not affected by moving the rotor axis away from $\mathbf{e}_1$, as long as the rotor axis and $\mathbf{e}_1$ are parallel.

Our derivation of the equations of motion for the axial gyrostat begins with defining the angular velocities and angular momenta of the system. The body-fixed principal axis frame $\mathcal{F}_p$ rotates relative to an inertial frame $\mathcal{F}_i$ with angular velocity $\boldsymbol{\omega}$, which may be written in body-fixed coordinates as $\boldsymbol{\omega} = (\omega_1, \omega_2, \omega_3)$. In addition, we need the angular velocity of $\mathcal{R}$ relative to $\mathcal{P}$, denoted ω_s. Thus the absolute angular velocity of $\mathcal{R}$ relative to $\mathcal{F}_i$ about its axis of symmetry is $\omega_1 + \omega_s$.

Similarly, the gyrostat's angular momentum vector is $\mathbf{h}$ which may be projected onto the principal axes as $\mathbf{h} = (h_1, h_2, h_3)$. Since there are no external torques, the time derivative of this vector in an inertial frame is

$$\left. \frac{d\mathbf{h}}{d\tilde{t}} \right|_{\mathcal{F}_i} = \mathbf{0} \tag{3.1}$$

while in the body-fixed frame

$$\left. \frac{d\mathbf{h}}{d\tilde{t}} \right|_{\mathcal{F}_p} = -\boldsymbol{\omega} \times \mathbf{h} \tag{3.2}$$

In order to evaluate this equation, we need to express the angular momenta in
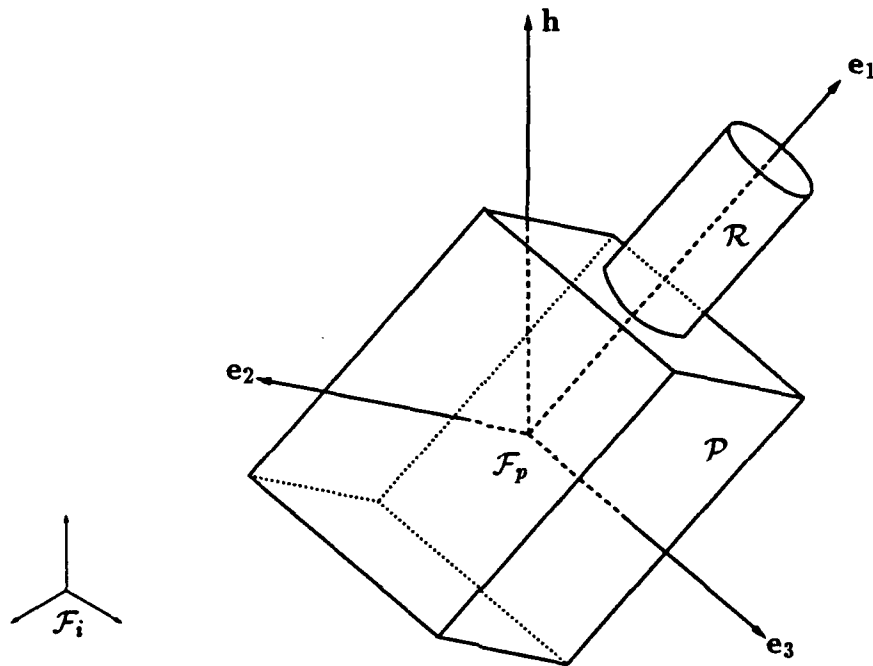
Figure 3.1. Axial Gyrostat $\mathcal{P} + \mathcal{R}$: $\mathcal{P}$ is rigid platform; $\mathcal{R}$ is rigid axisymmetric rotor; e_i, $i = 1, 2, 3$ are principal axes of $\mathcal{P} + \mathcal{R}$. The total angular momentum vector h is constant in direction and magnitude. The angle between h and e_1 is the *cone angle*, η. The reference frame $\mathcal{F}_i$ is an inertial frame, and $\mathcal{F}_p$ is a body-fixed reference frame aligned with the principal axes of the gyrostat, rotating relative to $\mathcal{F}_i$.

terms of the angular velocities and the moments of inertia. Thus

$$h_1 = I_1\omega_1 + I_s\omega_s \tag{3.3}$$

$$h_2 = I_2\omega_2 \tag{3.4}$$

$$h_3 = I_3\omega_3 \tag{3.5}$$

where I_1, I_2, and I_3 are the principal moments of inertia of $\mathcal{P} + \mathcal{R}$ and I_s is the *axial* principal moment of inertia of $\mathcal{R}$. Note that I_1 "includes" I_s, and I_2 and I_3 include the transverse moments of inertia of $\mathcal{R}$. The total axial angular momentum, h_1, differs from the transverse momenta, h_2 and h_3, due to the additional angular momentum of the rotor relative to the platform, $h_s = I_s\omega_s$. In addition to the principal momentum variables, we also use the total axial angular momentum of $\mathcal{R}$:

$$h_a = I_s(\omega_1 + \omega_s) \tag{3.6}$$

In addition to the motor torque, there are torques between the two bodies that are transverse to the rotor axis. These are not needed, however, to form the equations of motion. The axial torque provided by the motor from the platform to the rotor is denoted g_a. Hence the time derivative of h_a is given by

$$\frac{dh_a}{dt} = g_a \tag{3.7}$$

Equations (3.3)–(3.6) can be solved for the angular velocities in terms of the momenta, giving

$$\omega_1 = \frac{h_1 - h_a}{I_p} \tag{3.8}$$

$$\omega_2 = \frac{h_2}{I_2} \tag{3.9}$$

$$\omega_3 = \frac{h_3}{I_3} \tag{3.10}$$

$$\omega_s = \frac{1}{I_p}\left(\frac{I_1}{I_s}h_a - h_1\right) \tag{3.11}$$

which may then be used in Eq. (3.2) to obtain three differential equations for h_1, h_2, and h_3. Combined with Eq. (3.7), we have the following equations for the

angular momenta:

$$\frac{dh_1}{d\tilde{t}} = \frac{I_2 - I_3}{I_2 I_3} h_2 h_3 \tag{3.12}$$

$$\frac{dh_2}{d\tilde{t}} = \left(\frac{I_3 - I_p}{I_3 I_p} h_1 - \frac{h_a}{I_p} \right) h_3 \tag{3.13}$$

$$\frac{dh_3}{d\tilde{t}} = \left(\frac{I_p - I_2}{I_2 I_p} h_1 + \frac{h_a}{I_p} \right) h_2 \tag{3.14}$$

$$\frac{dh_a}{d\tilde{t}} = g_a \tag{3.15}$$

where

$$h_1 = I_1 \omega_1 + I_s \omega_s = \text{angular momentum of } \mathcal{P} + \mathcal{R} \text{ about } \mathbf{e}_1$$

$$h_i = I_i \omega_i = \text{angular momentum of } \mathcal{P} + \mathcal{R} \text{ about } \mathbf{e}_i, \ i = 2, 3$$

$$h_a = I_s(\omega_s + \omega_1) = \text{angular momentum of } \mathcal{R} \text{ about } \mathbf{e}_1$$

$$I_i = \text{moment of inertia of } \mathcal{P} + \mathcal{R} \text{ about } \mathbf{e}_i, \ i = 1, 2, 3$$

$$I_s = \text{moment of inertia of } \mathcal{R} \text{ about } \mathbf{e}_1$$

$$I_p = I_1 - I_s = \text{moment of inertia of } \mathcal{P} \text{ about } \mathbf{e}_1$$

$$\omega_i = \text{angular velocity of } \mathcal{P} \text{ about } \mathbf{e}_i, \ i = 1, 2, 3$$

$$\omega_s = \text{angular velocity of } \mathcal{R} \text{ about } \mathbf{e}_1 \text{ relative to } \mathcal{P}$$

$$\eta = \cos^{-1}\left(\frac{\mathbf{h} \cdot \mathbf{e}_1}{h} \right) = \text{nutation or cone angle}$$

$$g_a = \text{torque applied by } \mathcal{P} \text{ on } \mathcal{R} \text{ about } \mathbf{e}_1$$

$$\mathbf{e}_i = \text{principal axes of } \mathcal{P} + \mathcal{R}, \ i = 1, 2, 3$$

$$\tilde{t} = \text{time}$$

Note that for $h_a = 0$, Eqs. (3.12)–(3.14) are identical to Euler's equations for a torque-free rigid body with moments of inertia I_p, I_2, and I_3, while for $h_a = I_s \omega_1$ the equations correspond to a torque-free rigid body with moments of inertia I_1, I_2, and I_3. Of these two conditions, the former has practical application only in the case of flat spin, while the latter applies to any axial gyrostat in the *all-spun* condition (zero relative angular velocity, *i.e.*, $\omega_s = 0$).

A more complete study of the dynamics of rigid body systems includes the kinematic equations, usually given in terms of Euler angles. For our purposes, the only Euler angle of interest is the nutation angle, $\eta = \cos^{-1}(\mathbf{h} \cdot \mathbf{e}_1 / h)$, which may be written more simply as

$$\eta = \cos^{-1}(h_1/h) \tag{3.16}$$

The nutation angle is also known as the cone angle. Note that the well-known Euler angle singularity occurs at $\eta = 0$, which is precisely the desired operating condition for a dual-spin spacecraft. Thus a formal analysis of the kinematics would necessitate a different choice of kinematical variables. However, for our purposes, η is a useful measure of the deviation of a given motion from the desired or *nominal* state.

Since there are no external moments, angular momentum is conserved and the square of the magnitude of the angular momentum vector is a first integral of the motion:

$$h^2 = h_1^2 + h_2^2 + h_3^2 = \text{CONST} \tag{3.17}$$

This integral can be used to reduce the number of equations by one. Furthermore, if $g_a = 0$, there are two additional first integrals: the rotor axial angular momentum

$$h_a = \text{CONST} \tag{3.18}$$

and the rotational kinetic energy

$$\mathcal{T} = T + \frac{h_a^2}{2I_s} = \text{CONST} \tag{3.19}$$

where

$$T = \frac{1}{2}\left(\frac{(h_1 - h_a)^2}{I_p} + \frac{h_2^2}{I_2} + \frac{h_3^2}{I_3}\right) \tag{3.20}$$

Note that T is also constant since h_a is constant. Since T is equivalent to, but slightly simpler than $\mathcal{T}$, it is usually used in applications. Using the three first

integrals h^2, h_a, and T, Eqs. (3.12)–(3.15) may be reduced to a single elliptic integral of the first kind, as shown, for example, in Ref. [16].

Since we are interested in the case where g_a is a small constant, a natural question is: *What is the effect of $g_a \neq 0$ on the constants of the motion?* Using Eqs. (3.12)–(3.15), it is easy to show that

$$\frac{dh_a}{d\tilde{t}} = g_a \tag{3.21}$$

$$\frac{dT}{d\tilde{t}} = \frac{g_a}{I_p}(h_a(0) - h_1) + \frac{g_a^2}{I_p}\tilde{t} \tag{3.22}$$

and, since we have assumed zero external torque, $h^2 = \text{CONST}$ still holds. The fact that the two "constants" have rates of change of $\mathcal{O}(g_a)$ was the original motivation for our approach. Our perturbation analysis, based on the method of averaging, will be valid to $\mathcal{O}(g_a)$. Before proceeding, however, we simplify the notation by changing to dimensionless variables.

3.2 The Dimensionless Equations

Our dimensionless equations are equivalent to those given by Guelman [28]; the transformation is obtained by scaling the four momenta, time, and the axial torque as follows:

$$\begin{aligned}
x_1 &= h_1/h & \mu &= h_a/h \\
x_2 &= h_2/h & t &= h\tilde{t}/I_p \\
x_3 &= h_3/h & \epsilon &= g_a I_p/h^2
\end{aligned} \tag{3.23}$$

Derivatives with respect to t are denoted by an overdot: $\dot{()} = d()/dt$. Furthermore, we define three dimensionless inertia parameters by

$$i_j = 1 - I_p/I_j, \qquad j = 1, 2, 3 \tag{3.24}$$

Carrying out this change of variables leads to a new set of dimensionless equations:

$$\dot{x}_1 = (i_2 - i_3)x_2 x_3 \tag{3.25}$$

$$\dot{x}_2 = (i_3 x_1 - \mu) x_3 \tag{3.26}$$

$$\dot{x}_3 \quad = - (i_2 x_1 - \mu) \, x_2 \tag{3.27}$$

$$\dot{\mu} \quad = \quad \varepsilon \tag{3.28}$$

These equations are equivalent to Eqs. (3.12)–(3.15), but are simpler; in particular, there are only two inertia parameters rather than the original three. We note that the angular momentum integral, Eq. (3.17), becomes

$$x_1^2 + x_2^2 + x_3^2 = 1 \tag{3.29}$$

which defines a unit sphere in $\mathbf{R}^3$, normally called the *momentum sphere*; the dynamics on this sphere are discussed in detail in Section 4.2. Also, the cone angle becomes

$$\eta = \cos^{-1} x_1 \tag{3.30}$$

For future reference, we also note that the dimensionless version of Eq. (3.20) is

$$\hat{T} = \frac{I_p T}{h^2} = \frac{1}{2} \left((x_1 - \mu)^2 + (1 - i_2) x_2^2 + (1 - i_3) x_3^2 \right) \tag{3.31}$$

In Appendix B, we show that $i_2 < 1$ and $i_3 < 1$, hence $\hat{T}$ defines a two-parameter family of ellipsoids in $\mathbf{R}^3$, centered at $(\mu, 0, 0)$. The intersections of this *energy ellipsoid* with the momentum sphere defined by Eq. (3.29) are the integral curves of the $\varepsilon = 0$ system. These are discussed further in Chapter 4.

Like the first integrals and other quantities, the equilibrium points are also easier to express in terms of the dimensionless variables, as discussed in the next section.

Remark 6 *In the nondimensionalization used here, we assume $h \neq 0$. The $h = 0$ case is called the zero momentum gyrostat, which we discussed in Chapter 1. This configuration has the same qualitative behavior as a single non-spinning rigid body. Thus, since this case lacks the gyroscopic stabilization properties of the spinning gyrostat, we do not discuss it further. However, with the exception of Eq. (3.29), Eqs. (3.25)–(3.20) may be used to study the zero momentum gyrostat, since in Eq. (3.23). we can take $h = 1$. Equation (3.29) becomes $x_1^2 + x_2^2 + x_3^2 = 0$, which implies $x_1 = x_2 = x_3 = 0$, for all values of ε and μ.*

3.3 Equilibrium Points

The nature and number of equilibria of Eqs. (3.25)–(3.28) have been well documented. Here we obtain the values of the equilibria, and in Chapter 4 we discuss stability and bifurcations of the equilibrium points. For a more detailed discussion and a rigorous stability analysis, we refer the reader to the paper by Masaitis [70].

First, we note that when $\varepsilon \neq 0$, there are no equilibrium points of all four of Eqs. (3.25)–(3.28), since $\dot{\mu} = \varepsilon$ is only zero when $\varepsilon = 0$. However, if we consider Eqs. (3.25)–(3.27) as a non-autonomous system with $\mu = \mu_0 + \varepsilon t$, then there are two equilibrium points:

$$(x_1, x_2, x_3) = (\pm 1, 0, 0) \tag{3.32}$$

where we have made use of conservation of angular momentum, Eq. (3.29). These two equilibria are also present in the $\varepsilon = 0$ case, but there are additional possibilities.

From Eq. (3.25), it is evident that for equilibrium in the $\varepsilon = 0$ case, either $x_2 = 0$ or $x_3 = 0$. If $x_2 = 0$, then $\dot{x}_3 = 0$ is automatic, and $\dot{x}_2 = 0$ requires

$$x_1 = \frac{\mu}{i_3} \tag{3.33}$$

from which Eq. (3.29) gives

$$x_3 = \pm\sqrt{1 - (\mu/i_3)^2} \tag{3.34}$$

so that there are two "$x_2 = 0$" equilibrium points.

Similarly, if $x_3 = 0$, $\dot{x}_2 = 0$ automatically, and $\dot{x}_3 = 0$ implies

$$x_1 = \frac{\mu}{i_2} \tag{3.35}$$

$$x_2 = \pm\sqrt{1 - (\mu/i_2)^2} \tag{3.36}$$

giving two "$x_3 = 0$" equilibria.

Thus there are six possible equilibrium points:

$$(x_1, x_2, x_3) \;=\; (\pm 1, 0, 0) \qquad\qquad \forall \varepsilon \qquad\qquad (3.37)$$

$$(x_1, x_2, x_3) \;=\; \left(\mu/i_3, 0, \pm\sqrt{1 - (\mu/i_3)^2}\right) \qquad \varepsilon = 0 \qquad\qquad (3.38)$$

$$(x_1, x_2, x_3) \;=\; \left(\mu/i_2, \pm\sqrt{1 - (\mu/i_2)^2}, 0\right) \qquad \varepsilon = 0 \qquad\qquad (3.39)$$

Since the x_i are constrained to the unit momentum sphere by Eq. (3.29), it is evident that the "$x_2 = 0$" equilibrium points do not exist when $|\mu| > |i_3|$, and the "$x_3 = 0$" equilibria do not exist when $|\mu| > |i_2|$. These bifurcation values of μ depend on the inertia parameters i_2 and i_3, which are the subject of the next section. The bifurcations are examined in more detail in Chapter 4.

3.4 The Dimensionless Inertia Parameters

The three dimensionless inertia parameters defined by Eq. (3.24) retain the relative value relationships of the original moments of inertia, *i.e.*,

$$I_j > I_k \iff i_j > i_k, \; j, k = 1, 2, 3 \qquad\qquad (3.40)$$

In addition, the value of I_p relative to I_2 and I_3 determines the sign of i_2 and i_3, respectively, *i.e.*,

$$I_p > I_k \iff i_k < 0, \; k = 2, 3 \qquad\qquad (3.41)$$

$$I_p < I_k \iff i_k > 0, \; k = 2, 3 \qquad\qquad (3.42)$$

We will use these facts throughout this section.

Now, of the three dimensionless inertia parameters, only i_2 and i_3 appear in Eqs. (3.25)–(3.28). These parameters define the *dynamical* shape of the gyrostat, and we adopt the following nomenclature to describe the possibilities:

$$\text{A gyrostat is} \begin{cases} \textbf{oblate if } i_3 < i_2 < 0. \\[4pt] \textbf{prolate if } i_2 > i_3 > 0. \\[4pt] \textbf{intermediate if } i_2 > 0 > i_3. \end{cases}$$

in which we have made the tacit assumption $i_2 > i_3$, which we justify below.

The other inertia parameter, i_1, simplifies to $i_1 = I_s/I_1$, the ratio of the axial inertia of $\mathcal{R}$ to the axial inertia of $\mathcal{P} + \mathcal{R}$. Thus $0 < i_1 < 1$, with the limiting cases $i_1 = 0$ and $i_1 = 1$ corresponding to gyrostats with rod-shaped rotor and rod-shaped platform, respectively.

Since the definitions for oblate, prolate, and intermediate gyrostats do not involve i_1, and the equations of motion are independent of i_1, one might reasonably ask: *How does $i_1 = I_s/I_1$ affect the gyrostat's dynamics?* The answer to this question lies in defining the initial conditions for a particular spinup maneuver. We discuss spinup maneuvers in detail in Section 4.5, but we give a brief discussion here.

Typically, spinup begins with rotor and platform spinning as a single rigid body with zero relative angular velocity ($\omega_s = 0$). This condition may also be described by $\mu = i_1 x_1$. This initial spin is usually about either the major or minor axis of the total gyrostat, including the rotor. Applying the definitions for the major, minor, and intermediate axes of a rigid body to the rotor axis of a gyrostat results in the following definitions:

$$\text{The rotor axis is the} \begin{cases} \textbf{major axis} & \text{if } i_1 > i_2 > i_3. \\ \textbf{minor axis} & \text{if } i_2 > i_3 > i_1. \\ \textbf{intermediate axis} & \text{if } i_2 > i_1 > i_3. \end{cases}$$

Thus a gyrostat with major axis $\mathbf{e}_1$, *i.e.*, $i_1 > i_2 > i_3$, may be either oblate, prolate, or intermediate. All the possibilities are summarized in Table 3.1.

Another role for i_1 is in limiting physically possible values of i_2 and i_3 using the triangle inequalities for moments of inertia (see Appendix B). We have already noted that $0 < i_1 < 1$, and applying the inequalities to i_2 and i_3 leads to the conclusion that physically possible values of these parameters are restricted to a specific region of the $i_2 i_3$ plane depending on the value of i_1 as shown in Fig. 3.2.

Table 3.1. Gyrostat Types

Basic Type		Major Axis	
	Defined by	$i_1 > i_2$	$i_1 < i_2$
Oblate	$i_3 < i_2 < 0$	$\mathbf{e}_1$	—
Prolate	$0 < i_3 < i_2$	$\mathbf{e}_1$	$\mathbf{e}_2$
Intermediate	$i_3 < 0 < i_2$	$\mathbf{e}_1$	$\mathbf{e}_2$
We assume $i_2 > i_3$.			

The boundary curves in Fig. 3.2 are given by:

$$i_3 = \begin{cases} (1 - 2i_1 + i_1 i_2)/(i_2 - i_1) & \text{(I)} \\ (2i_2 - i_1 i_2 - 1)/(i_2 - i_1) & \text{(II)} \\ (1 - i_1 i_2)/(2 - i_1 - i_2) & \text{(III)} \end{cases} \qquad (3.43)$$

where the Roman numerals correspond to the labels in the figure. Note that i_2 and i_3 are both less than 1 for prolate gyrostats, while they are unbounded for intermediate gyrostats. The boundary curve (I) limits i_2 and i_3 for oblate gyrostats, and one may show that for $i_1 = 1/2$, this curve passes through the origin. Thus for $i_1 > 1/2$, a gyrostat is necessarily either prolate or intermediate. The $i_1 i_2 i_3$ parameter space is discussed further in Appendix B.

3.5 Symmetries

One often encounters in the literature statements such as: "Without loss of generality we may assume $A > B$." Such claims usually refer to some underlying symmetry of the system, and are often given without proof. We have, in fact, made such an assumption ($i_2 > i_3$) in the preceding section, and we make two more symmetry assumptions throughout this work. In this section, we give three finite symmetry transformations under which Eqs. (3.25)–(3.28) remain invariant, and we identify the corresponding assumptions. These assumptions are then
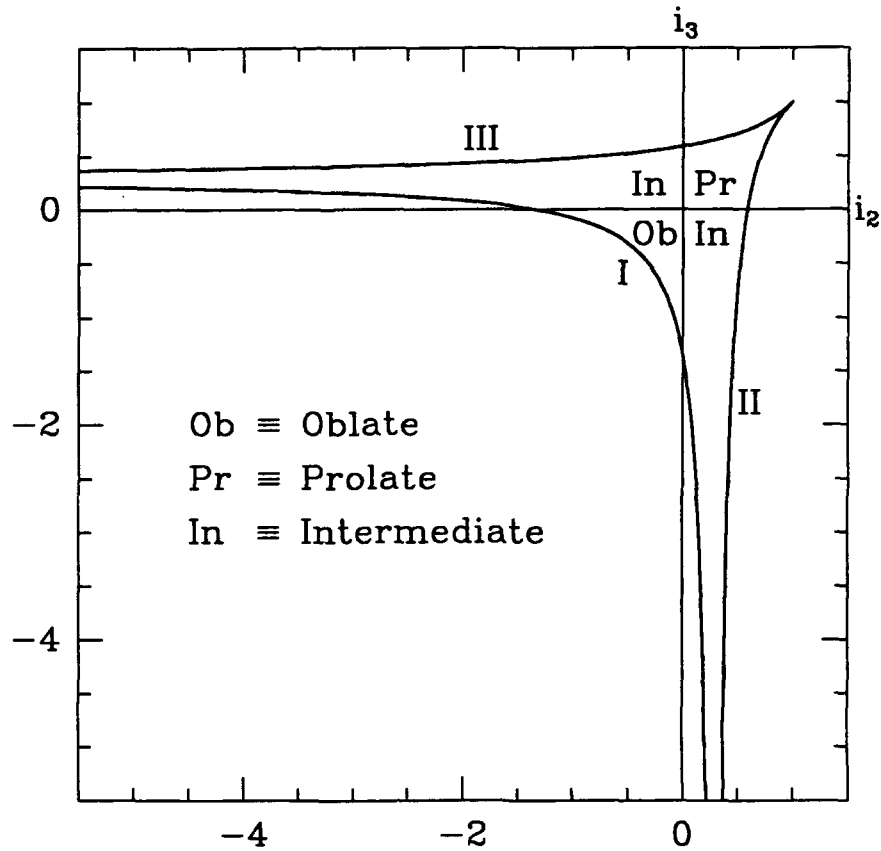
Figure 3.2. Admissible Regions in the $i_2 i_3$ Plane for $i_1 = 0.3$. Valid values of i_2 and i_3 lie inside the three curves. The region extends to $-\infty$ in the i_2 and i_3 directions. These limiting regions correspond to the vanishing of one or the other of the transverse inertias I_2 and I_3. The Roman numerals correspond to those in Eq. (3.43).

used to reduce the number of cases which must be considered in the remainder of the thesis. We also point out an apparently erroneous assumption previously appearing in the literature on axial gyrostats.

Symmetry 1 *Rotating the body-fixed principal axes through* 90° *about* $\mathbf{e}_1$ *leaves the equations of motion unchanged. Mathematically the transformation is*

$$(x_2, x_3, i_2, i_3) \mapsto (-x_3, x_2, i_3, i_2) \tag{3.44}$$

This symmetry transformation is shown schematically in Fig. 3.3. The transformation allows us to assume $i_2 > i_3$ with no loss of generality.
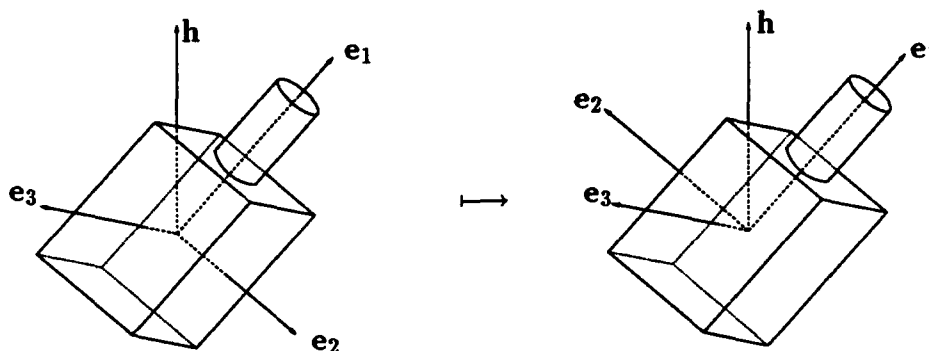
Figure 3.3. Transformation of Symmetry 1

Symmetry 2 *Reflection across the* e_2e_3 *plane, followed by a* $90°$ *rotation about* e_1 *and a simple change of inertia parameters leaves the equations of motion unchanged.*

$$(x_1, x_2, x_3, i_2, i_3) \mapsto (-x_1, x_3, -x_2, -i_3, -i_2) \tag{3.45}$$

This transformation is shown schematically in Fig. 3.4. The transformation allows us to map all prolate gyrostats ($i_2 > i_3 > 0$) into equivalent oblate gyrostats ($i_3 < i_2 < 0$), so we only consider the oblate and intermediate cases in this thesis. Thus, when we use the term prolate, we will be referring to the *equivalent* prolate gyrostat. Note that the cone angle is transformed by $\eta \mapsto \pi - \eta$. This means that the normal dual-spin condition is $\eta = \pi$ for prolate gyrostats transformed by Symmetry 2.

In Chapter 4 we interpret this transformation in terms of the momentum sphere. This symmetry appears to be a new result, and a paper describing it in terms of the original variables has been accepted for publication (see Hall [30]).
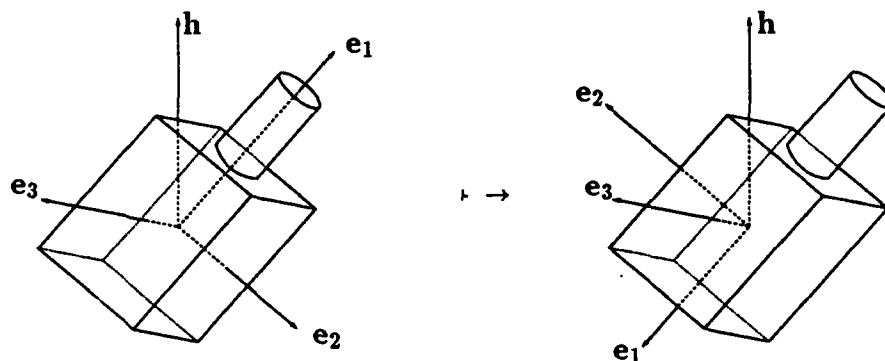
Figure 3.4. Transformation of Symmetry 2

Symmetry 3 *The equations of motion are invariant under a reversal of the variables* (x, μ, t).

$$(x, \mu, t) \mapsto (-x, -\mu, -t) \tag{3.46}$$

This transformation means we only need to consider $\mu \geq 0$. We postpone a graphical interpretation of this symmetry until Chapter 4, where its usefulness will be clear.

Finally, we point out that in Leimanis's treatment of axial gyrostats [56, p. 224], he assumes "without any loss of generality," that only prolate gyrostats must be considered. As we have noted above, the distinction between prolate and oblate gyrostats may be removed via Symmetry 2. It is possible this symmetry was known to Leimanis, although he did not state it explicitly. However, there is a significant difference between these gyrostats and the intermediate gyrostats, as is made clear in Section 4.7.

3.6 Reduction of Order

In case there is no axial torque ($\varepsilon = 0$), the system is completely integrable and admits a closed form solution which we give in detail in Chapter 5. Even when $\varepsilon \neq 0$, conservation of angular momentum means we can reduce the number

of equations from four to three. In this section we carry out these reductions, beginning with the reduction to quadrature for $\varepsilon = 0$. In Appendix E, we give for comparison an example using a class of conservative, nonlinear second-order oscillators, with a slowly varying parameter.

3.6.1 The $\varepsilon = 0$ Quadrature

As discussed in the introduction to this chapter, for $\varepsilon = 0$ there are three integrals of the motion, namely, total angular momentum, axial angular momentum of the rotor, and rotational kinetic energy. The kinetic energy integral is not, however, the most convenient quantity to use, so we choose an equivalent constant which is a functional combination of the three "standard" integrals. Rather than write down the desired integral, we proceed formally, integrating Eqs. (3.25)–(3.?8) directly.

First, $\varepsilon = 0$ implies $\mu = \text{CONST}$, giving the first integral:

$$c_1 = \mu = \text{CONST} \tag{3.47}$$

Next, dividing $\dot{x}_2$ by $\dot{x}_1$ and integrating yields another first integral:

$$c_2 = x_1^2 - \frac{i_2 - i_3}{i_3} x_2^2 - \frac{2}{i_3} \mu x_1 = \text{CONST} \tag{3.48}$$

Similarly, dividing $\dot{x}_3$ by $\dot{x}_1$ and integrating gives:

$$c_3 = x_1^2 + \frac{i_2 - i_3}{i_2} x_3^2 - \frac{2}{i_2} \mu x_1 = \text{CONST} \tag{3.49}$$

These three first integrals are sufficient to reduce the system to a single quadrature; however, we are ultimately interested in spinup and all three of these "constants" depend on time when $\varepsilon \neq 0$. In particular, $\dot{c}_1 = \dot{\mu} = \varepsilon$, and

$$\dot{c}_2 = -\frac{2\varepsilon x_1}{i_3} \tag{3.50}$$

$$\dot{c}_3 = -\frac{2\varepsilon x_1}{i_2} \tag{3.51}$$

Of course, any functional combination of the three first integrals, Eqs. (3.47)–(3.49), is also a first integral, and we use two simple linear combinations of c_2 and

c_3, denoted $\tilde{c}_2$ and y. We choose the form of $\tilde{c}_2$ and y by insisting that $\dot{\tilde{c}}_2 = 0$, and that $\dot{y}$ be "simple." From Eqs. (3.50) and (3.51) we find, for any ε:

$$i_3\dot{c}_2 - i_2\dot{c}_3 = 0 \tag{3.52}$$

and Eqs. (3.48) and (3.49) imply that

$$i_3 c_2 - i_2 c_3 = (i_3 - i_2)(x_1^2 + x_2^2 + x_3^2) \tag{3.53}$$

Thus we may obtain the angular momentum integral, Eq. (3.29) as the following combination of c_2 and c_3:

$$\begin{aligned}
\tilde{c}_2 &\triangleq \frac{i_3 c_2 - i_2 c_3}{i_3 - i_2} \\
&= x_1^2 + x_2^2 + x_3^2 = 1
\end{aligned} \tag{3.54}$$

Now to choose y, we note that

$$i_3\dot{c}_2 + i_2\dot{c}_3 = -4\varepsilon x_1 \tag{3.55}$$

To this combination of c_2 and c_3, we add a constant and a multiplying factor of 1/2, which simplifies Eqs. (3.58)–(3.61). Thus our energy-*like* constant, y, is defined by

$$\begin{aligned}
y &\triangleq \frac{1}{2}\left(i_3 c_2 + i_2 c_3 - i_2 - i_3\right) \\
&= \frac{1}{2}\left\{(i_2 + i_3)x_1^2 - (i_2 - i_3)(x_2^2 - x_3^2) - 4\mu x_1 - (i_2 + i_3)\right\}
\end{aligned} \tag{3.56}$$

and for $\varepsilon \neq 0$ y satisfies

$$\dot{y} = -2\varepsilon x_1 \tag{3.57}$$

Throughout this thesis we refer to y simply as the energy.

Using the constants μ, y, and $\tilde{c}_2 = 1$, we express x_2 and x_3 in terms of x_1, μ, and y, then eliminate x_2 and x_3 from Eq. (3.25). Thus,

$$x_2^2(x_1; \mu, y) = \frac{y_2(x_1; \mu) - y}{i_2 - i_3} \tag{3.58}$$

$$x_3^2(x_1; \mu, y) = \frac{y - y_3(x_1; \mu)}{i_2 - i_3} \tag{3.59}$$

where

$$y_2(x_1; \mu) = i_3 x_1^2 - 2\mu x_1 - i_3 \tag{3.60}$$

$$y_3(x_1; \mu) = i_2 x_1^2 - 2\mu x_1 - i_2 \tag{3.61}$$

are quadratic functions of x_1. Note that since $i_2 > i_3$, and since x_2 and x_3 are real, Eqs. (3.58) and (3.59) imply that

$$y_3(x; \mu) \leq y \leq y_2(x; \mu) \tag{3.62}$$

hence admissible values of the energy y are bounded by these parabolas in the $x_1 y$ plane. This observation is explored further in Chapter 4.

Then, substituting Eqs. (3.58) and (3.59) into (3.25) gives

$$\dot{x}_1 = \pm\sqrt{y_2(x_1; \mu) - y}\sqrt{y - y_3(x_1; \mu)} \tag{3.63}$$

This equation is separable and may be written as

$$\pm \int_{x_1(0)}^{x_1(t)} \frac{d\xi}{\sqrt{y_2(\xi; \mu) - y}\sqrt{y - y_3(\xi; \mu)}} = \int_0^t dt = t \tag{3.64}$$

where ξ is a dummy variable of integration, and $t_0 = 0$ has been chosen without loss of generality. The integral on the left hand side of Eq. (3.64) is an elliptic integral of the first kind. In Chapter 5 we carry out the evaluation of this integral, and its inversion in terms of Jacobi's elliptic functions. The $\pm$ in Eqs. (3.63) and (3.64) indicates that x_1 oscillates as its derivative changes sign.

3.6.2 The $\varepsilon \neq 0$ Reduced Equations

In case $\varepsilon \neq 0$, neither μ nor y is constant and the system is evidently non-integrable. Angular momentum is still conserved however, and we use this to reduce the number of equations from four to three. We already have $\dot{\mu} = \varepsilon$ from Eq. (3.28), and $\dot{y} = -2\varepsilon x_1$ from Eq. (3.57). Equation (3.63) for $\dot{x}_1$ is still valid, with the additional caveat that y and μ depend on time, so that the equation is no longer separable. These three equations for $\dot{x}_1$, $\dot{y}$, and $\dot{\mu}$ are free of x_2 and x_3. Having thus eliminated x_2 and x_3, from now on we drop the subscript

on x_1, except where needed for clarity. So we have reduced the four differential equations (3.25)–(3.28) to three:

$$\dot{x} = \pm\sqrt{y_2(x,\mu) - y}\sqrt{y - y_3(x,\mu)} \qquad (3.65)$$

$$\dot{y} = -2\varepsilon x \qquad (3.66)$$

$$\dot{\mu} = \varepsilon \qquad (3.67)$$

where $y_2(x,\mu)$ and $y_3(x,\mu)$ are defined by Eqs. (3.60) and (3.61).

We call Eqs. (3.65)–(3.67) the *reduced* equations. They are equivalent to Eqs. (3.25)–(3.28), and are not restricted to small ε or to $\varepsilon = \text{CONST}$. Throughout this work however, we will assume ε to be a small positive constant, except where otherwise noted.

The significance of Eqs. (3.65)–(3.67) is that they separate the motion into the "fast" oscillations of x and the "slow" evolution of y and μ, since $\dot{y}$ and $\dot{\mu}$ are both $\mathcal{O}(\varepsilon)$. Note that integration of Eq. (3.67) gives $\mu = \varepsilon t$ plus a constant of integration. Thus μ may be regarded as the "slow" time. In Chapter 6 we show that the slow flow of y *vs.* μ captures *most* of the dynamics of the system.

3.7 Summary

In this chapter, we derived the differential equations for the angular momenta of the axial gyrostat, and then non-dimensionalized these equations. We identified three symmetry transformations that allow us to reduce the number of cases to be studied. For the $\varepsilon = 0$ case, three first integrals were obtained and used to reduce the equations of motion to a single elliptic integral. When $\varepsilon \neq 0$, we showed that two of these first integrals are slowly varying quantities, and their derivatives with respect to time are useful differential equations for the system. In this way we reduced the number of equations from four to three. In addition, we identified the equilibrium points of the equations, for both the $\varepsilon = 0$ and $\varepsilon \neq 0$ cases. These will be discussed further in the following chapter.

Chapter 4

Graphical Representations of Spinup Dynamics

There are several ways to graphically depict the dynamics of gyrostats. In this chapter we present several graphical tools for representing the dynamics for both the unperturbed and perturbed systems. The purpose of this chapter is two-fold: (1) we introduce several illustrative examples which are referred to later in the thesis, and (2) we develop several conventions for depicting spinup dynamics. In particular, we show how spinup, described by four first-order differential equations, can be represented approximately by flow in the μy plane, where μ and y are the slow state variables. This representation also makes clear the effect of the size of the torque on the resulting motion of the gyrostat. We exploit this observation to discuss a *resonance capture* problem similar to one which has been previously discussed in the literature. Our approach identifies the location of the resonance in phase space and the qualitative effects of the resonance.

In this chapter, we also characterize the four different types of spinup trajectories which are of practical interest. Throughout this chapter, we use "exact" solutions to the original equations, (3.25)–(3.28), as represented by numerical integration. In subsequent chapters, we compare the observations made here with

the averaging results.

We begin by discussing oblate gyrostat dynamics in detail, then summarize the equivalent results for intermediate gyrostats.

4.1 Simple Representations

Given solutions to Eqs. (3.25)–(3.28), an obvious possibility would be to plot the x_i and μ as functions of time, as shown in Fig. 4.1. It is clear from this figure that the angular momenta are periodic when $\varepsilon = 0$, and that something interesting happens when $\varepsilon \neq 0$. However, for $\varepsilon \neq 0$, it is difficult to draw conclusions about solutions in general using such plots.
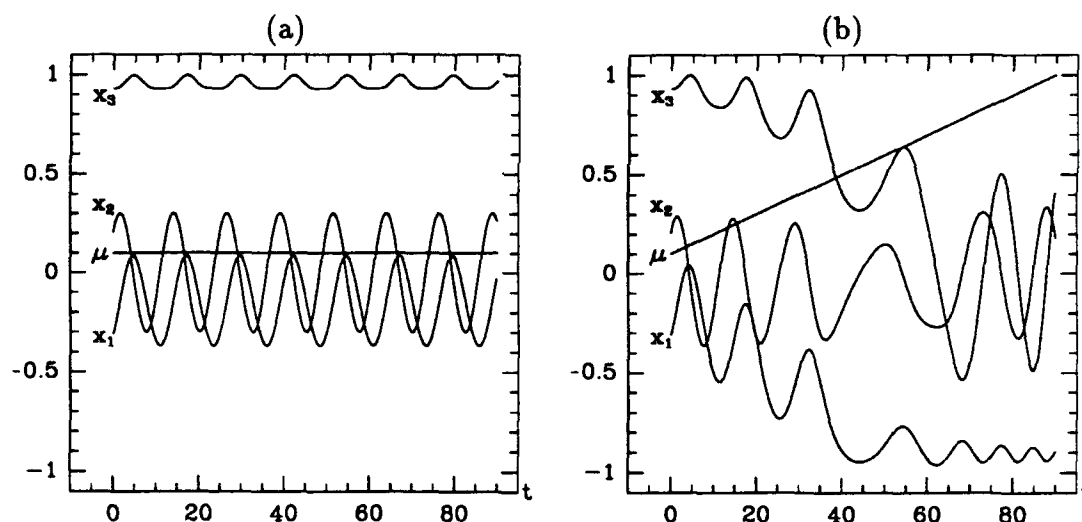
Figure 4.1. Angular Momenta *vs.* Time. (a) $\varepsilon = 0$. (b) $\varepsilon = 0.01$. In both plots, $(i_2, i_3) = (-0.3, -0.7)$.

Note that the μ *vs.* t curve is trivial in both plots in Fig. 4.1, as expected, since $\dot{\mu} = \varepsilon$. This suggests the possibility of ignoring μ and looking at the flow in the $x_1 x_2$ and $x_3 x_2$ planes. Of course, other combinations are equivalent. The trajectories of Fig. 4.1 are shown in these phase planes in Fig. 4.2.
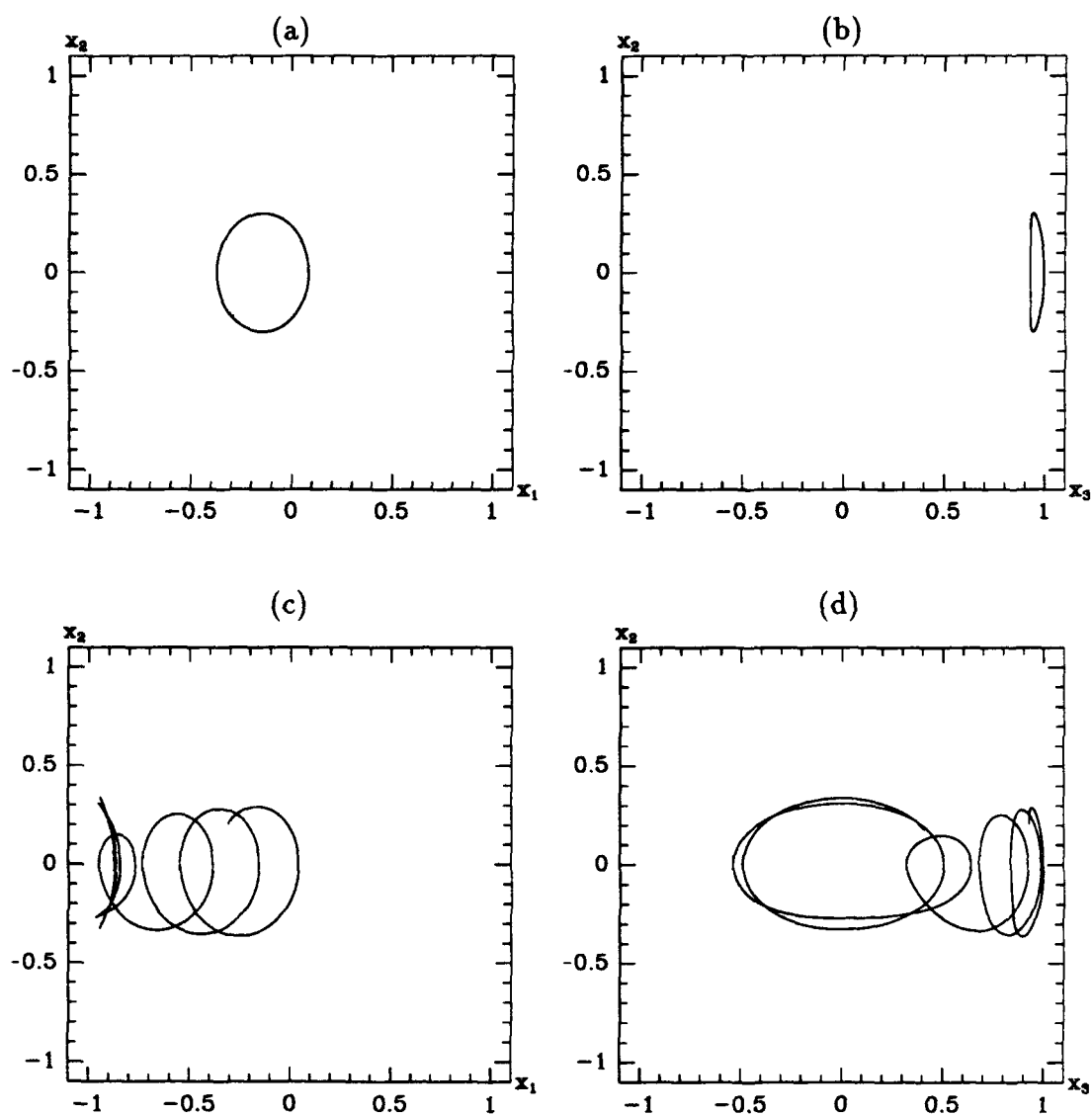
Figure 4.2. Angular Momentum Phase Planes. The flow of Fig. 4.1 is projected onto the x_1x_2 and x_3x_2 phase planes. (a) x_2 vs. x_1 with $\varepsilon = 0$. (b) x_2 vs. x_3 with $\varepsilon = 0$. (c) x_2 vs. x_1 with $\varepsilon = 0.01$. (d) x_2 vs. x_3 with $\varepsilon = 0.01$.

4.2 The Momentum Sphere

An elegant approach that works well for the $\varepsilon = 0$ system is to exploit the first integrals of energy and angular momentum. This allows one to consider the flow as constant energy curves on the angular momentum sphere. As we noted in Section 3.2, these curves may be interpreted as the intersections of the momentum sphere with the energy ellipsoids.

As was shown in the previous chapter, when $\varepsilon = 0$ the motion is essentially one-dimensional, with $x(t) = x_1(t)$ being the variable of choice. Since the motion is confined to the surface of the momentum sphere, trajectories are simply one-dimensional curves on the sphere, which are called *polhodes* in analogy with simple rigid body dynamics. The topology of the phase space on the sphere depends on the constant value of μ. In particular, there are either two, four, or six equilibrium points on the sphere, as given by Eqs. (3.37)–(3.39) in Section 3.3. The three possibilities are shown in the three spheres in Fig. 4.3. For fixed μ, there is a range of possible y values, limited by Eq. (3.62), with each polhode corresponding to a particular value of y. As shown in Fig. 4.3, some values of y correspond to fixed points on the sphere; these are the equilibrium points of Eqs. (3.25)–(3.28) with $\varepsilon = 0$, and correspond to particular steady state motions. Specifically, the point at the north pole of the sphere, $(x_1, x_2, x_3) = (1, 0, 0)$, is the point at which an oblate dual-spinner typically operates. The notation $\mathbf{O}_\mu$ denotes this equilibrium point, with the $\mathbf{O}$ suggesting *oblate*, and the subscript μ indicating that the dynamics depend on the value of μ. For example, $\mathbf{O}_1$ denotes the equilibrium point at the north pole of the momentum sphere for $\mu = 1$. Similarly the equilibrium at the south pole is associated with the operating condition of a *prolate* gyrostat, hence the notation $\mathbf{P}_\mu$. Note that $\mathbf{O}_\mu$ and $\mathbf{P}_\mu$ are equilibrium solutions for any ε, as we showed in Section 3.3.

The saddle points correspond roughly to unstable flat spin motions, and the notation $\mathbf{U}_\mu$ is used to indicate these unstable equilibria. Note that these equi-

Figure 4.3. Momentum Spheres for Oblate Gyrostats $(i_2, i_3) = (-0.3, -0.7)$, $\mu \in \{0.1, 0.4, 0.8\}$. Each sphere corresponds to a fixed value of μ. Constant energy curves on the sphere correspond to $y =$ CONST. The "cartoons" in the right half of the figure are topologically equivalent to the spheres "minus" the point at the north pole.

libria do not exist in the lower two spheres in Fig. 4.3. At $\mu = -i_2$, the two saddles $\mathbf{U}_\mu$ coalesce with the center $\mathbf{P}_\mu$ at the south pole, creating a saddle at the south pole. This bifurcation value of μ is denoted μ_2. This is an example of a pitchfork bifurcation [26, pp. 149–150], and is part of the reason that prolate gyrostats have more interesting dynamics than oblate gyrostats.

The equilibria in the "eyes" of the saddle connections correspond to stable flat spin. The notation $\mathbf{F}_\mu$ is used for these equilibrium points. At $\mu = -i_3$, these centers coalesce with the saddle at the south pole in another pitchfork bifurcation, creating a center there. We denote this bifurcation value of μ by μ_3.

In summary, fixing the rotor angular momentum μ determines the topology of the polhodes on the momentum sphere, and fixing the energy y determines which polhode a particular motion is on. For $0 \leq \mu < \mu_2$ all six equilibrium points exist; for $\mu_2 < \mu < \mu_3$ there are four equilibria; and for $\mu > \mu_3$ there are only two equilibria, both centers. Pitchfork bifurcations occur at the south pole for $\mu = \mu_2$ and $\mu = \mu_3$. The two pitchfork bifurcations are represented schematically in Fig. 4.4. The bifurcation values of μ are given in Table 4.1, and the equilibria are given in Table 4.2.

Table 4.1. Bifurcation Values of μ for Oblate Gyrostats

μ	Bifurcation
$\mu_2 \overset{\triangle}{=} -i_2 > 0$	Pitchfork bifurcation: the flat spin saddles $\mathbf{U}_\mu$ coalesce with the center at the south pole $\mathbf{P}_\mu$ creating a saddle at the south pole.
$\mu_3 \overset{\triangle}{=} -i_3 > 0$	Pitchfork bifurcation: the flat spin centers $\mathbf{F}_\mu$ coalesce with the saddle at the south pole $\mathbf{P}_\mu$ creating a center at the south pole.

Remark 7 *We have stated the stability types (center or saddle) for the equilibrium points without giving any proof of these properties. The stability of these equilibrium points is well-known, and is proved for example in Refs. [38] and [70].*
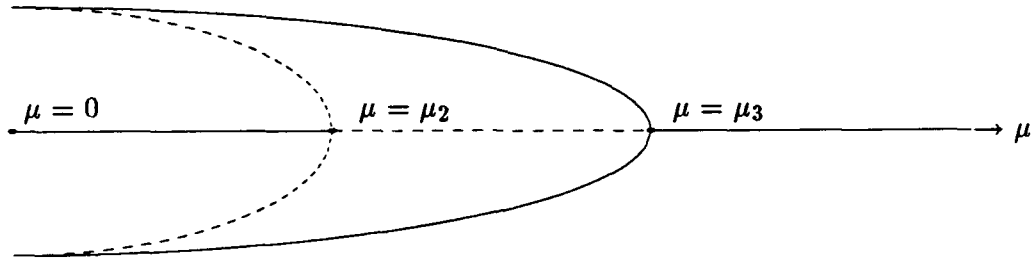
Figure 4.4. Schematic of the Two Pitchfork Bifurcations. The horizontal axis illustrates the changing nature of the equilibrium point at the south pole of the momentum sphere (P_μ) as μ increases. Where the horizontal line is dashed, P_μ is a saddle, and where it is solid, P_μ is a center. The first bifurcation occurs at $\mu = \mu_2$ when the two saddles on the sphere (U_μ) collide with the center P_μ, changing P_μ to a saddle. When $\mu = \mu_3$, the two centers F_μ collide with the saddle P_μ, changing P_μ back to a center.

Table 4.2. Equilibrium Points for Oblate Gyrostats

Equilibrium	x	Range of μ for center	for saddle	Energy (y)
O_μ	$+1$	$[0, \infty)$	—	-2μ
P_μ	-1	$[0, \mu_2)$ (μ_3, ∞)	(μ_2, μ_3)	$+2\mu$
F_μ	μ/i_3	$[0, \mu_3)$	—	$\mu^2/\mu_3 + \mu_3$
U_μ	μ/i_2	—	$[0, \mu_2)$	$\mu^2/\mu_2 + \mu_2$

The values of x_2 and x_3 are given at Eqs. (3.37)–(3.39).

4.3   The xy Plane

Recalling our convention that $x = x(t) = x_1(t)$, we now introduce the xy plane which is equivalent to the momentum sphere. Using Eqs. (3.60) and (3.61) we have plotted $y_2 = y_2(x; \mu)$ and $y_3 = y_3(x; \mu)$ in the left half of Fig. 4.5 using the same values of μ, i_2, and i_3 as for the spheres in Fig. 4.3. In the right half of the figure we have reproduced the topological cartoons of the momentum spheres. Recall that $y_3 \leq y \leq y_2$, so the motion is confined to the closed region between the two parabolas. It is easy to verify that the parabolas intersect at $x = \pm 1$, with $y_2(+1; \mu) = y_3(+1; \mu) = -2\mu$, and $y_2(-1; \mu) = y_3(-1; \mu) = +2\mu$. This is expected since $x = \pm 1$ are equilibrium points ($\mathbf{O}_\mu$ and $\mathbf{P}_\mu$) for all μ, and these intersections correspond to those equilibria. This also implies that the energy at $\mathbf{O}_\mu$ is -2μ, while the energy at $\mathbf{P}_\mu$ is $+2\mu$. That is, the energy at the poles varies linearly with the rotor angular momentum.

One can also readily see that the extrema of the two parabolas are:

$$y_2(\mu/i_3; \mu) \;=\; -\left(\mu^2/i_3 + i_3\right) = \mu^2/\mu_3 + \mu_3 \qquad (4.1)$$

$$y_3(\mu/i_2; \mu) \;=\; -\left(\mu^2/i_2 + i_2\right) = \mu^2/\mu_2 + \mu_2 \qquad (4.2)$$

The maximum of y_2 corresponds to the two centers $\mathbf{F}_\mu$, while the maximum of y_3 corresponds to the two saddles $\mathbf{U}_\mu$. These facts are easily verified by substituting the equilibrium values of x from Table 4.2 into Eqs. (3.60) and (3.61). The dashed line passing through the maximum of y_3 for $\mu < \mu_2$ in Fig. 4.5(a) represents the separatrices of the two saddles $\mathbf{U}_\mu$. The dashed line $y = 2\mu$ for $\mu_2 < \mu < \mu_3$ in Fig. 4.5(b) represents the separatrices of the saddle $\mathbf{P}_\mu$. Note from Eqs. (4.1) and (4.2) that the energy at the centers, $\mathbf{F}_\mu$ and the saddles, $\mathbf{U}_\mu$ varies quadratically with the rotor angular momentum.

In analogy with the momentum spheres, fixing μ determines the bounding curves y_2 and y_3, giving a specific admissible region in the xy plane, and fixing y gives a particular one-dimensional path which $x(t)$ must follow, $i.e.$, the straight
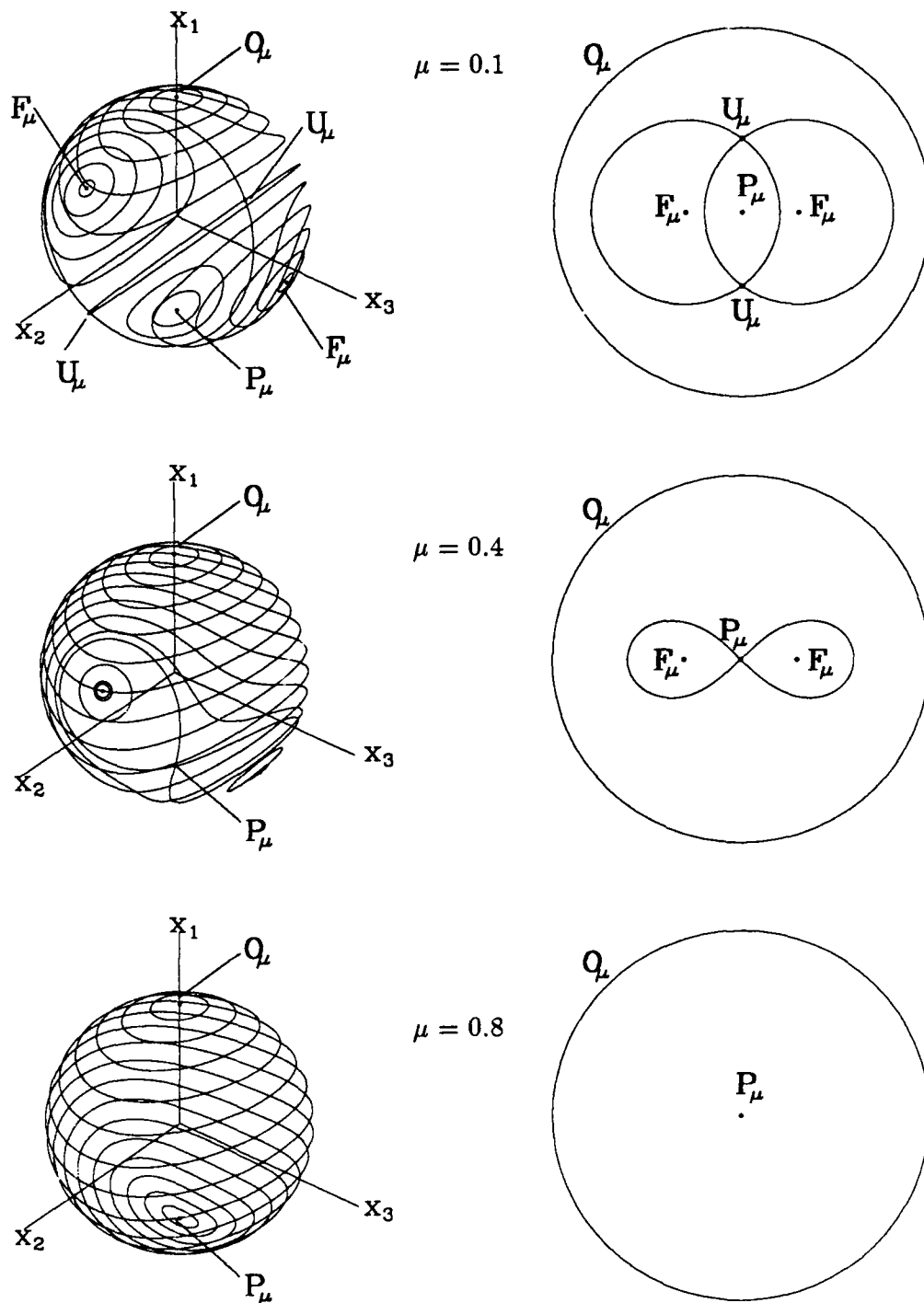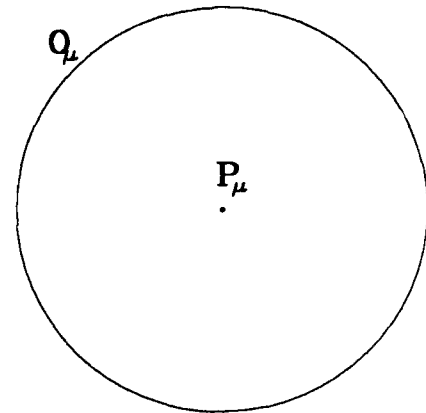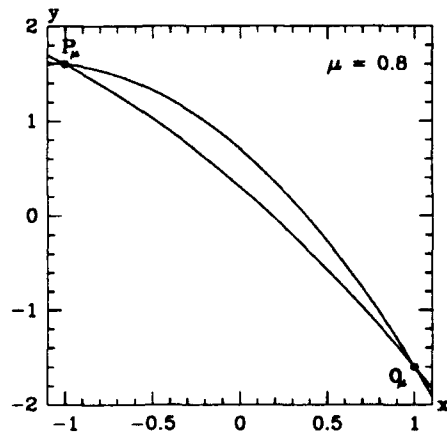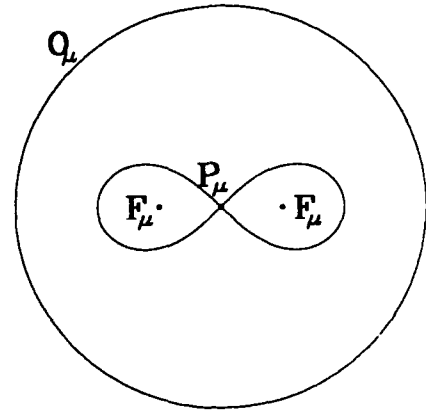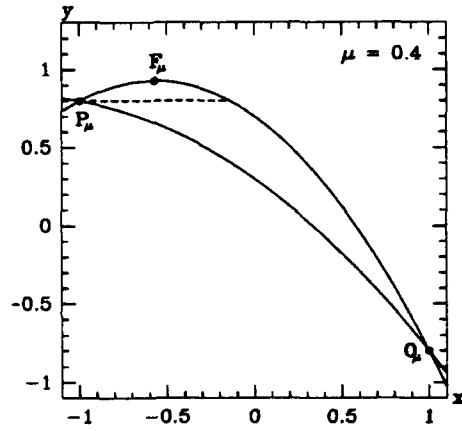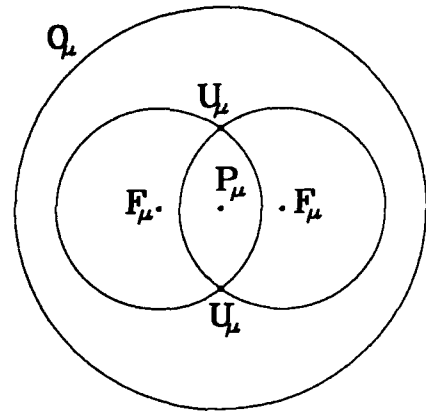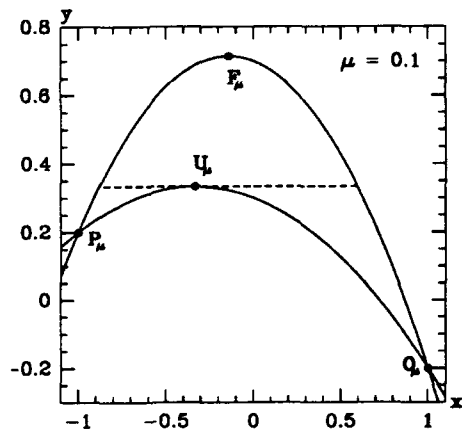
Figure 4.5. The xy Planes for Oblate Gyrostats $(i_2, i_3) = (-0.3, -0.7)$, $\mu \in \{0.1, 0.4, 0.8\}$. Each plane corresponds to a fixed value of μ. The "cartoons" relate these figures to the momentum spheres in Fig. 4.3. Constant energy curves on the sphere correspond to $y = \text{CONST}$.

line $y = \text{CONST}$, with $x(t)$ oscillating between the bounding curves.

4.4 The μy Plane

When $\varepsilon \neq 0$ the dynamics on the momentum sphere become more complicated. In this section we present the alternative of viewing spinup dynamics in the μy plane. First we discuss the differences between the unpertubed and perturbed systems.

To begin, when $\varepsilon \neq 0$, the flat spin ($\mathbf{F}_\mu$) and saddle ($\mathbf{U}_\mu$) equilibria are no longer fixed points of the governing equations. As discussed in Section 3.3, there are only two equilibria when $\varepsilon \neq 0$, namely $\mathbf{O}_\mu$ and $\mathbf{P}_\mu$. There are also no longer any polhodes, and even when $\mathbf{P}_\mu$ is a saddle point, it no longer has a separatrix. In fact $\mathbf{P}_\mu$ does not even possess stable and unstable manifolds since $\mathbf{P}_\mu$ changes to a center after a finite time (forward or backward). However, trajectories may pass arbitrarily close to the saddle point. As there is no standard term for such trajectories, we will use *pseudo-stable manifold* to refer to the set of trajectories which pass close to the saddle point. See Fig. 7.6 for an example of such a trajectory.

Now, having announced that all of the nice features of the $\varepsilon = 0$ system are destroyed by the spinup perturbation which changes the axial angular momentum of the rotor, μ, we reclaim these features by adding the adjective "instantaneous" to each term, and associating the "frozen" features with a corresponding value of μ. This view, which is fundamental to the perturbation approach which we take, is expected to be useful if the rotor momentum varies slowly, *i.e.*, if $\varepsilon \ll 1$. Thus, the flat spin centers become instantaneous flat spin centers, the $\varepsilon = 0$ polhodes become instantaneous polhodes, and so forth. These solutions to the unperturbed system are not solutions for $\varepsilon \neq 0$. However, they define non-invariant surfaces in the $\varepsilon \neq 0$ flow that are important to the perturbation method we use.

Of particular interest are the instantaneous separatrices of the saddle points.

In the unperturbed system, the separatrices truly separate different kinds of motion, since they cannot be crossed by trajectories. In the perturbed system, however, the instantaneous separatrices can be crossed, and it is precisely the *separatrix crossings* that introduce errors in our averaging results.

In order to view spinup dynamics, one could easily generate a sequence of instantaneous momentum spheres valid for fixed values of μ, and thereby possibly deduce the qualitative nature of the flow. However, as we have shown, the xy plane is equivalent to the momentum sphere, and has the advantage of being a two-dimensional object rather than a three-dimensional one. Thus, we create a sequence of xy planes for fixed values of μ, thereby obtaining a three-dimensional phase space for the flow. Furthermore, since x is a *fast* variable and y and μ are *slow* variables, the projection of the flow onto the μy plane can be justified by the method of averaging, yielding a two-dimensional state space, valid in the limit as $\varepsilon \to 0$.

Our approach, then, is to construct a sequence of xy planes for increasing μ, then project the *critical points* of the instantaneous y_2 and y_3 curves onto the μy plane. This is done in Fig. 4.6. Another view of the μy plane is given in Fig. 4.7. The solid curves in the μy plane represent the instantaneous centers on the momentum sphere, while the dashed curves represent the instantaneous saddles and their separatrices. Note that the μy plane is symmetric about $\mu = 0$, because of the symmetry $(x, \mu, t) \mapsto (-x, -\mu, -t)$, so we only need to consider $\mu \geq 0$. Also, for $\mu > \mu_3$, there are no additional bifurcations: the momentum spheres, the xy planes, and the μy plane remain qualitatively the same.

We can now make a general assertion about the flow in the μy plane when $\varepsilon = \text{CONST} > 0$: *Trajectories are confined to a "wedge" originating at the initial condition $\mu(0) = \mu_0$, $y(0) = y_0$, with edges parallel to $\mathbf{O}_\mu$ and $\mathbf{P}_\mu$*, as depicted in Fig. 4.8. The proof is easy. We have $\dot{y} = -2\varepsilon x$, and $\dot{\mu} = \varepsilon$, from which

$$\frac{dy}{d\mu} = -2x \tag{4.3}$$
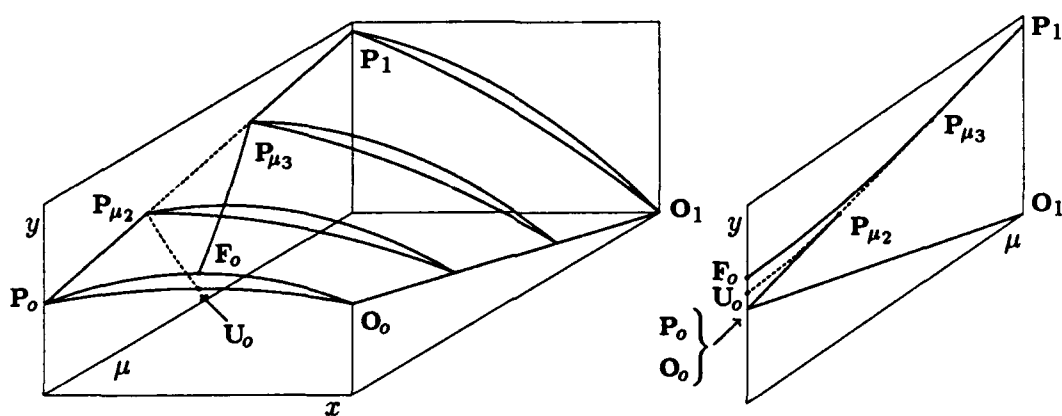
Figure 4.6. The $x\mu y$ Phase Space and the μy Plane for Oblate Gyrostats. The $x\mu y$ plot shows the phase space for all spinup problems for these values of i_2 and i_3. By projecting the critical points of the parabolas onto the μy plane, we represent the changing structure of the momentum sphere's phase portrait during spinup. The solid line $O_0 O_1$ represents the centers O_μ in Fig. 4.3. The line $P_0 P_1$ represents the equilibrium point at the south pole of the momentum sphere (cf. P_μ in Fig. 4.3); the solid segments $P_0 P_{\mu_2}$ and $P_{\mu_3} P_1$ denote the region where the equilibrium is a center, while the dashed segment $P_{\mu_2} P_{\mu_3}$ shows where the equilibrium is a saddle. The dashed curve $U_0 P_{\mu_2}$ represents the locus of saddle pairs (cf. U_μ in Fig. 4.3), while the solid curve $F_0 P_{\mu_3}$ represents the locus of center pairs (cf. F_μ in Fig. 4.3).

Figure 4.7. The μy Plane for Oblate Gyrostats. The solid line $\mathbf{O}_\mu$ represents the centers at the north pole in Fig. 4.3. The line $\mathbf{P}_\mu$ represents the equilibrium point at the south pole of the momentum sphere (cf. $\mathbf{P}_\mu$ in Fig. 4.3); the solid segments denote the region where the equilibrium is a center, while the dashed segment $\mathbf{P}_{\mu_2}\mathbf{P}_{\mu_3}$ shows where the equilibrium is a saddle. The dashed curve $\mathbf{U}_\mu$ represents the locus of saddle pairs (cf. $\mathbf{U}_\mu$ in Fig. 4.3), while the solid curve $\mathbf{F}_\mu$ represents the locus of center pairs (cf. $\mathbf{F}_\mu$ in Fig. 4.3). Note that this figure also applies to prolate gyrostats, by the equivalence transformation of Eq. (3.45). The μy plane for intermediate gyrostats is different however (cf. Fig. 4.20).

Now, since $|x| \leq 1$, we have

$$\left| \frac{dy}{d\mu} \right| \leq 2 \tag{4.4}$$

which completes the proof. While this is a very conservative bound for most trajectories, it allows us to state with certainty that for all initial conditions with $y < 2\mu$, $\mu \geq 0$, the spinup trajectory does not cross any instantaneous separatrix.
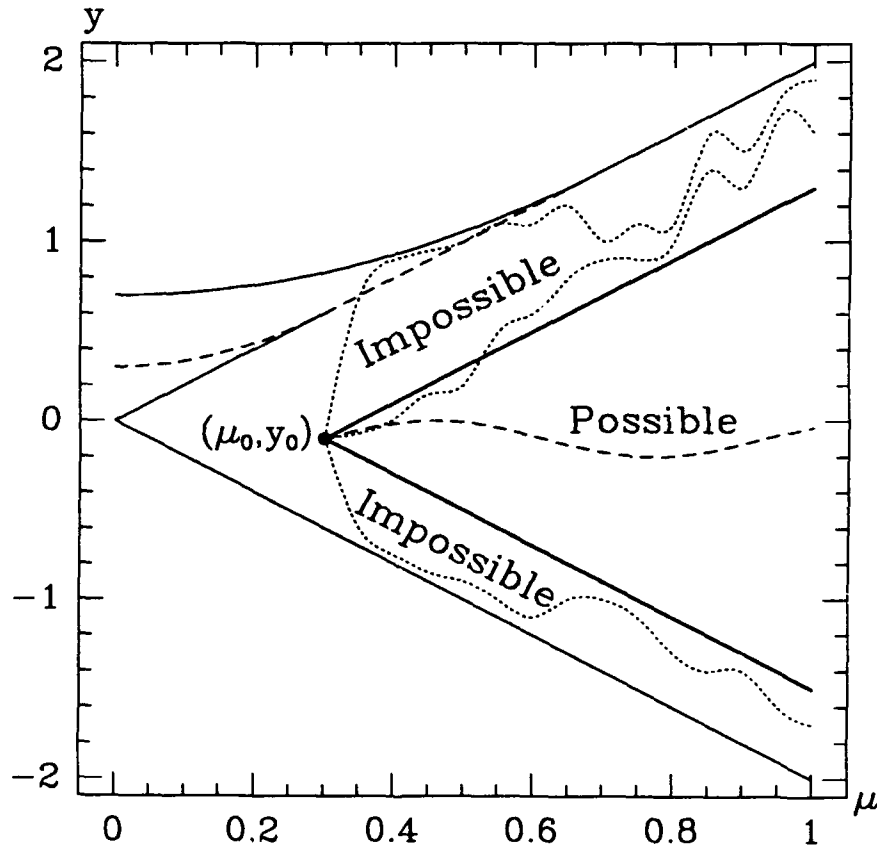
Figure 4.8. Bounds on Spinup Trajectories.

Incidentally, the μy plane is useful not only as the slow state space, but also as a bifurcation diagram for investigating all possible $\varepsilon = 0$ dynamics. For $\varepsilon = 0$, a given point in the μy plane corresponds to a specific polhode ($y = $ CONST) on a specific momentum sphere ($\mu = $ CONST). The missing information is the phase, or location of a point on the polhode, which is determined by $x = x_1$.

By way of contrast, we have included the $\mu\hat{T}$ plane as Fig. 4.9, obtained by using the dimensionless rotational kinetic energy, given at Eq. (3.31). Note that the straight lines of the μy plane become parabolas in the $\mu\hat{T}$ plane. This is another reason why we chose y as a phase variable instead of $\hat{T}$ (cf. discussion on pp. 39–40).
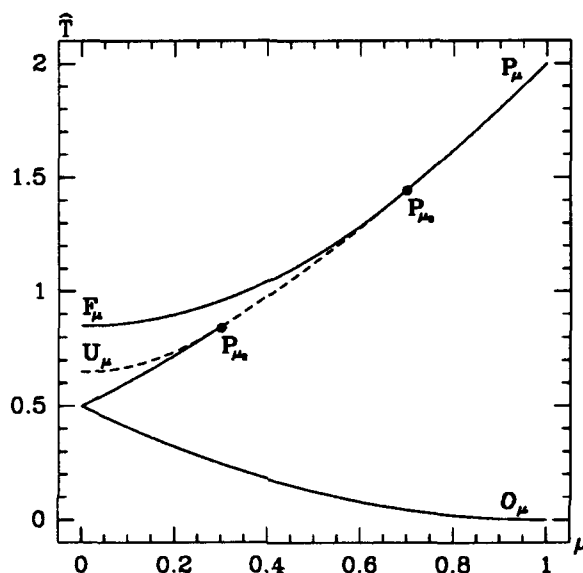
Figure 4.9. The $\mu\hat{T}$ Plane. Compare with Fig. 4.7.

4.5 Spinup Problems

In this section we define several classes of spinup trajectories which may occur for real spacecraft.

A spinup maneuver for a dual-spinner typically begins with the spacecraft operating near a "stable" equilibrium point, *i.e.*, near O_μ, P_μ, or F_μ, depending on the type of spacecraft. Thus there are three basic spinup problems for oblate spacecraft. The initial condition also usually corresponds to an "all-spun" condition, with rotor and platform spinning as a single rigid body with no relative rotation ($\omega_s = 0$). The small constant torque ε is then used to change the rotor angular momentum μ to the desired operating value, typically near

$\mu = 1$, after which the motor is turned off. An energy dissipation mechanism is then employed to reduce the final cone angle to zero by damping the transverse momentum ($x_2 = x_3 = 0$).

Before proceeding, a brief discussion of the all-spun condition is needed. As noted above, all-spun means $\omega_s = 0$. This is a special case of $\omega_s = \text{CONST}$, so let us treat the more general condition. Recalling Eq. (3.11), we have $\omega_s = (I_1 h_a / I_s - h_1)/I_p$; hence $\dot{\omega}_s = 0$ implies $\dot{h}_a = I_s \dot{h}_1 / I_1$, or, in dimensionless variables,

$$\dot{\mu} = i_1(i_2 - i_3)x_2 x_3 \stackrel{\triangle}{=} \varepsilon_{as} \tag{4.5}$$

Thus, the $\omega_s = \text{CONST}$ condition requires a specific axial torque, ε_{as}, which in general is neither zero nor constant. For the special case of $\omega_s = 0$, we obtain from Eq. (3.11), $h_a = I_s h_1 / I_1$, or, in dimensionless form,

$$\mu = i_1 x_1 \tag{4.6}$$

The point of this discussion is that, since $\varepsilon_{as} \neq 0$, the all-spun initial state does not correspond to a single point in the μy plane. In fact, the all-spun state defines a family of periodic orbits, depending on how close the all-spun motion is to an equilibrium point of the equations of motion for a single rigid body.

To see this, recall that the all-spun condition is equivalent to the torque-free motion of a rigid body with the same inertia properties as the gyrostat. This well-known problem also has a solution for the angular momentum variables in terms of elliptic functions (cf. Hughes [38]), hence x_1 is a periodic function of t, with the amplitude determined by the value of the rotational kinetic energy. Now, since $dy/d\mu = -2x_1$, we can use Eq. (4.6) to write

$$\frac{dy}{d\mu} = -\frac{2\mu}{i_1} \tag{4.7}$$

which we can integrate easily to obtain

$$y(\mu) = y(\mu_0) - \frac{1}{i_1}\left(\mu^2 - \mu_0^2\right) \tag{4.8}$$

Therefore, the all-spun trajectories in the μy plane are *segments* of parabolas, with μ oscillating between limits defined by the limits of the oscillation of x_1, and by Eq. (4.6).

Another important detail is the motor "cutoff" time, which we have stated usually occurs near $\mu = 1$. Two examples will serve to illustrate the nature of the cutoff condition, and to justify our choice of $\mu = 1$. Typically, a mission has a specific target value for the angular velocity of the platform about the rotor axis, determined by the relationship between the mission orbit and the object the platform is supposed to track. As a limiting case, one might wish to point the platform at the fixed stars, which requires $\omega_1 \equiv 0$. With zero transverse angular momentum, Eq. (3.8) then implies that $h \equiv h_a$, or $\mu \equiv 1$. Another, more common case is an earth-pointing platform. For a geostationary communications satellite, this implies $\omega_1 = 2\pi$ rad/day, or $\omega_1 \approx 7.3 \times 10^{-5}$ rad/s. Hence the cutoff value of μ is

$$\mu = 1 - (7.3 \times 10^{-5})\frac{I_p}{h} \tag{4.9}$$

Thus, assuming a reasonably high rate of spin ($h > I_p$, say), $\mu \approx 1$ still defines a good cutoff time for theoretical investigations.

Motor cutoff time has also been discussed by other authors, but apparently none have noted the simple relationship given here. For example, Hubert [37] defined the cutoff time as the time after which there are only two equilibria on the sphere, *i.e.*, $\mu = \mu_3$. While this is an important bifurcation point, it is not directly relevant to achieving a desired attitude of the platform. Gebman and Mingori [23] defined the cutoff time for flat spin recovery as the time at which ω_1 *passes through* zero. From Eqs. (3.8), (3.23), and (3.45), we find that their criterion is equivalent to $x_1 = -\mu$. Looking ahead to Fig. 4.13(b), we see that $x_1 = -\mu$ intersects the flat spin recovery trajectories several times before $\mu = 1$. However, they were investigating spinup for initial conditions exactly at flat spin, and in this case, with very small torques, their criterion is adequate.

We now proceed to the definition of the three kinds of spinup problems for oblate gyrostats, keeping in mind that prolate gyrostats are included by virtue of Symmetry 2. We call the three spinup problems Oblate Spinup (OSU), Prolate Spinup (PSU), and Flat Spin Recovery (FSR). In Figs. 4.10–4.13, the flow for all three problems is shown projected onto the μx and μy planes, obtained by numerically integrating Eqs. (3.25)–(3.28). We also show the cone angle as η *vs.* μ. The three spinup problems are discussed separately below.

4.5.1 Oblate spinup

From Table 3.1, we know that for all oblate spacecraft, the spin axis is also the major axis. Thus, prior to the spinup maneuver, an oblate spacecraft would typically be spinning about the rotor axis, near the equilibrium at the north pole (O_μ). We call the ensuing motion *oblate spinup* (OSU). If in the all-spun state, then $x \approx 1$, $\mu \approx i_1$, and $y \approx -2i_1$. As may be seen in Fig. 4.10, the oblate spinup trajectories in the μy plane are very nearly straight lines, and they *do not cross* either of the dashed lines representing the instantaneous separatrix energy levels. (Recall that in Fig. 4.8 we showed that they cannot cross the separatrices.) In the μx plane, the motion is an oscillation with slowly decreasing amplitude and slowly increasing frequency, while the cone angle, shown in the $\mu \eta$ plane, oscillates about a nearly constant value.

It is also possible that the initial condition could be near a flat spin state about the minor axis, *i.e.*, near F_μ with $\mu = 0$. This case is treated as flat spin recovery below.

4.5.2 Prolate spinup

Spinup of prolate gyrostats presents three possibilities depending on the inertia properties and the initial conditions. First, the rotor axis of a prolate gyrostat may be either the major, minor, or intermediate axis of the gyrostat. Also, the
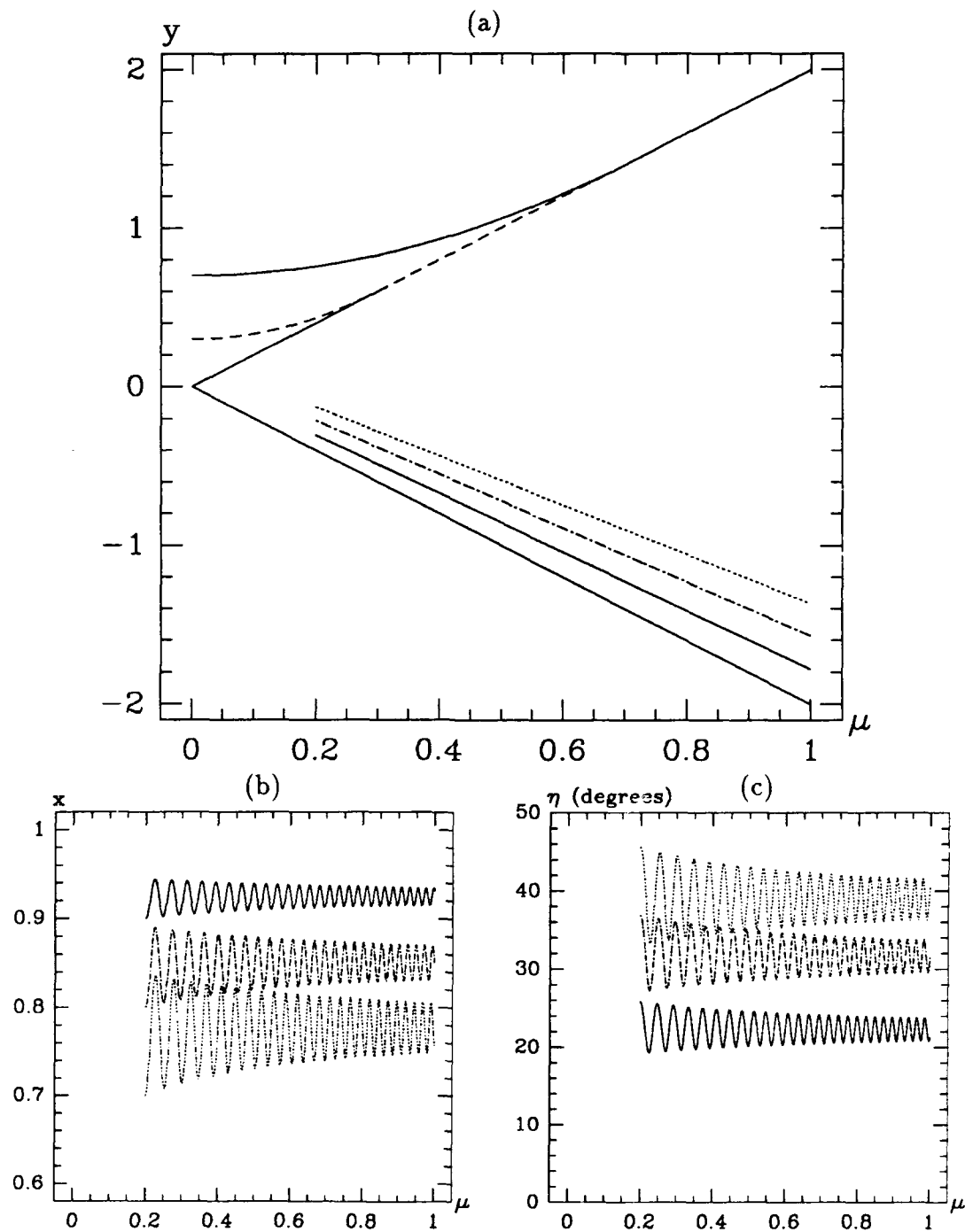
Figure 4.10. Oblate Spinup $(i_2, i_3) = (-0.3, -0.7)$. Three different initial conditions are shown in each plot. (a) Projection onto the μy plane. (b) Projection onto the μx plane. (c) The cone angle, η, in degrees.

gyrostat may initially be spinning about either its major axis or its minor axis.
The three possibilities are:

1. The gyrostat is spinning about the rotor axis, and the rotor axis is the gyrostat's minor axis ($i_1 < -i_2$).

2. The gyrostat is spinning about the rotor axis, and the rotor axis is the gyrostat's major axis ($i_1 > -i_2$).

3. The gyrostat is spinning about a transverse axis, which may be either the major or minor axis.

These three possibilities are shown in Fig. 4.11. The second case is similar to oblate spinup, and we do not discuss it any further. The third case is known as flat spin recovery and is treated below. For the rest of this subsection, we focus on the first possibility.
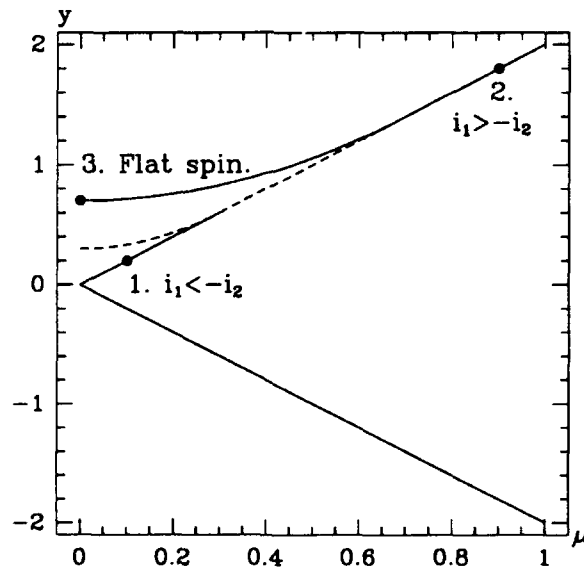
Figure 4.11. Three Possible Initial Conditions for Prolate Gyrostats $(i_2, i_3) = (-0.3, -0.7)$. These are ideal initial conditions, starting exactly at the equilibrium points of the all-spun system. Actual initial conditions would be on a polhode near one of the equilibrium points. Cf. discussion on page 58.

Prolate spinup (PSU) starts near the south pole, or $\mathbf{P}_\mu$, with $x \approx -1$, $\mu \approx i_1$, and $y \approx 2i_1$. Referring to Figs. 4.11 and Fig. 4.5, the initial condition is *near* the point $\mathbf{P}_\mu$, with $0 < \mu < \mu_2$. This means that actual trajectories will begin slightly above the line $\mathbf{P}_\mu$ in Fig. 4.11.

Unlike the oblate case, however, the y *vs.* μ trajectories are *not* nearly straight lines. Near $\mu = \mu_2$, the trajectories encounter the first instantaneous separatrix crossing, then almost immediately cross another separatrix. These crossings account for the sharp bend in the paths shown in Fig. 4.12.

4.5.3 Flat spin recovery

The final spinup possibility of practical interest is the flat spin recovery (FSR), which begins with the vehicle in a flat spin about a transverse axis, with $x \approx 0$, $x_3 \approx \pm 1$, $\mu \approx 0$, and $y \approx -i_3$. Note that this is the problem that was investigated in Ref. [23], for the *specific* initial condition $x_3 = 1$, $\mu = 0$. As shown in Fig. 4.13, the trajectory "follows" the locus of $\mathbf{F}_\mu$ equilibria, then crosses the dashed line which represents the locus of saddles at the south pole and their instantaneous separatrices.

It is also possible to have trajectories starting near one of the unstable equilibria. These trajectories are of limited practical interest and are not considered here.

4.5.4 The Effects of Torque Magnitude

In this section we investigate the effects of the order of magnitude of ε on the nutation or cone angle at the conclusion of spinup. The final values of y and μ for a particular trajectory may be used directly to compute an average residual nutation angle as is shown in Chapter 6. The closer the final point is to $\mathbf{P}_\mu$ (for prolate gyrostats) or $\mathbf{O}_\mu$ (for oblate gyrostats), the smaller the cone angle. Note that in Fig. 4.12, the final cone angle for prolate spinup is greater than for flat spin

(a)

(b)

(c)
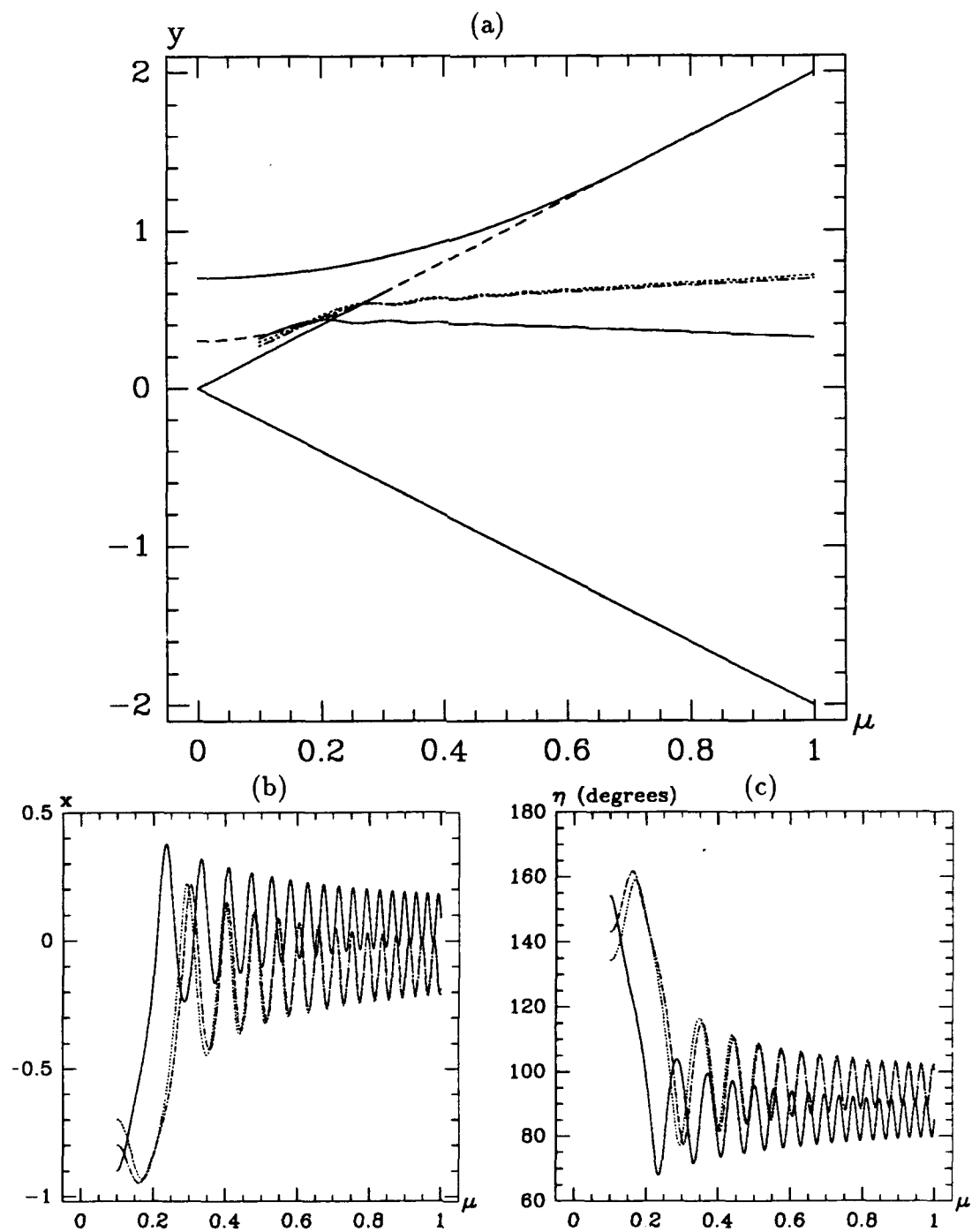
Figure 4.12. Prolate Spinup $(i_2, i_3) = (-0.3, -0.7)$. (a) Projection onto the μy plane. (b) Projection onto the μx plane. (c) The cone angle. Recall that for prolate gyrostats transformed by Symmetry 2, the nominal cone angle is $\eta = \pi$.
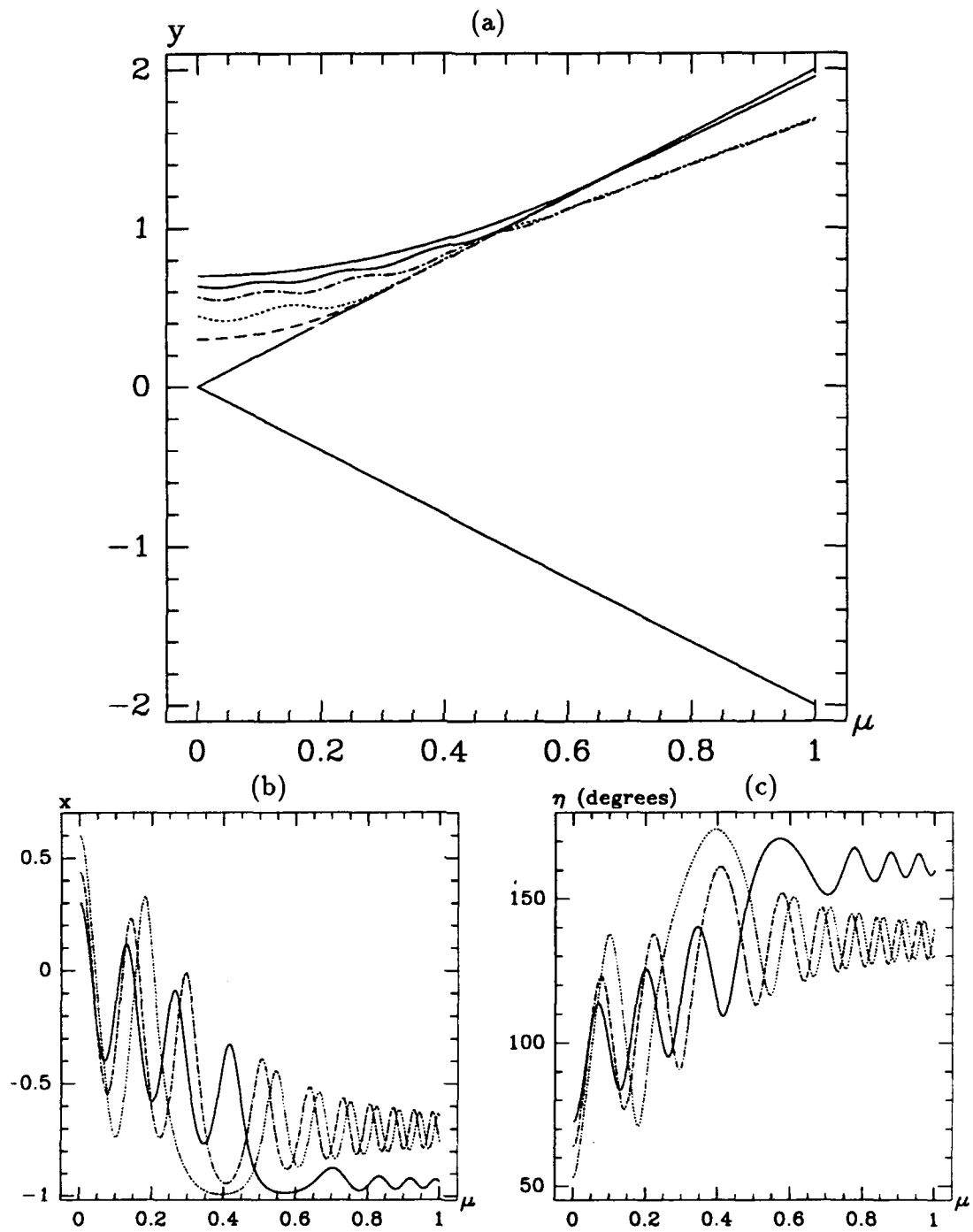
Figure 4.13. Flat Spin Recovery $(i_2, i_3) = (-0.3, -0.7)$. (a) Projection onto the μy plane. (b) Projection onto the μx plane. (c) The cone angle.

recovery in Fig. 4.13. This brings up an important difference between these two types of trajectories. *For flat spin recovery, making the torque smaller decreases the residual cone angle, whereas for prolate spinup smaller torque increases the cone angle.* Therefore, for flat spin recovery, our small torque assumption is relevant in a practical sense. For prolate spinup, however, one would expect a large torque to be used to obtain a smaller final cone angle. The differences are shown in Fig. 4.14

With this in mind, we focus on flat spin recovery for most of this work. However, we do develop and compare the averaged equations for prolate and oblate spinup as well.

4.5.5 The Effects of Initial Phase

Ultimately, we will average over the fast dynamics and focus entirely on the flow in the μy plane. The degree of success of this strategy will be determined by the importance of the effects being ignored, and in this section we examine those effects.

Recall that a point in the μy plane corresponds to a specific polhode on a specific momentum sphere, but does not identify any particular point on the polhode. If every point on a given *initial* polhode maps to the same *final* polhode, then we may ignore the phase with no error, since the quantity of interest, the final average cone angle, depends only on the final polhode and not on the final phase. More realistically, if an initial polhode maps to a bounded set of final polhodes, then we may ignore the phase with the error dependent on the size of the bounded set of final polhodes.

The phase is found to be less important for trajectories which do not cross an instantaneous separatrix. Those trajectories that do cross a separatrix experience a *dispersion*, so that an initial polhode maps to a large set of final polhodes. Thus oblate spinup is essentially independent of the initial phase, while both
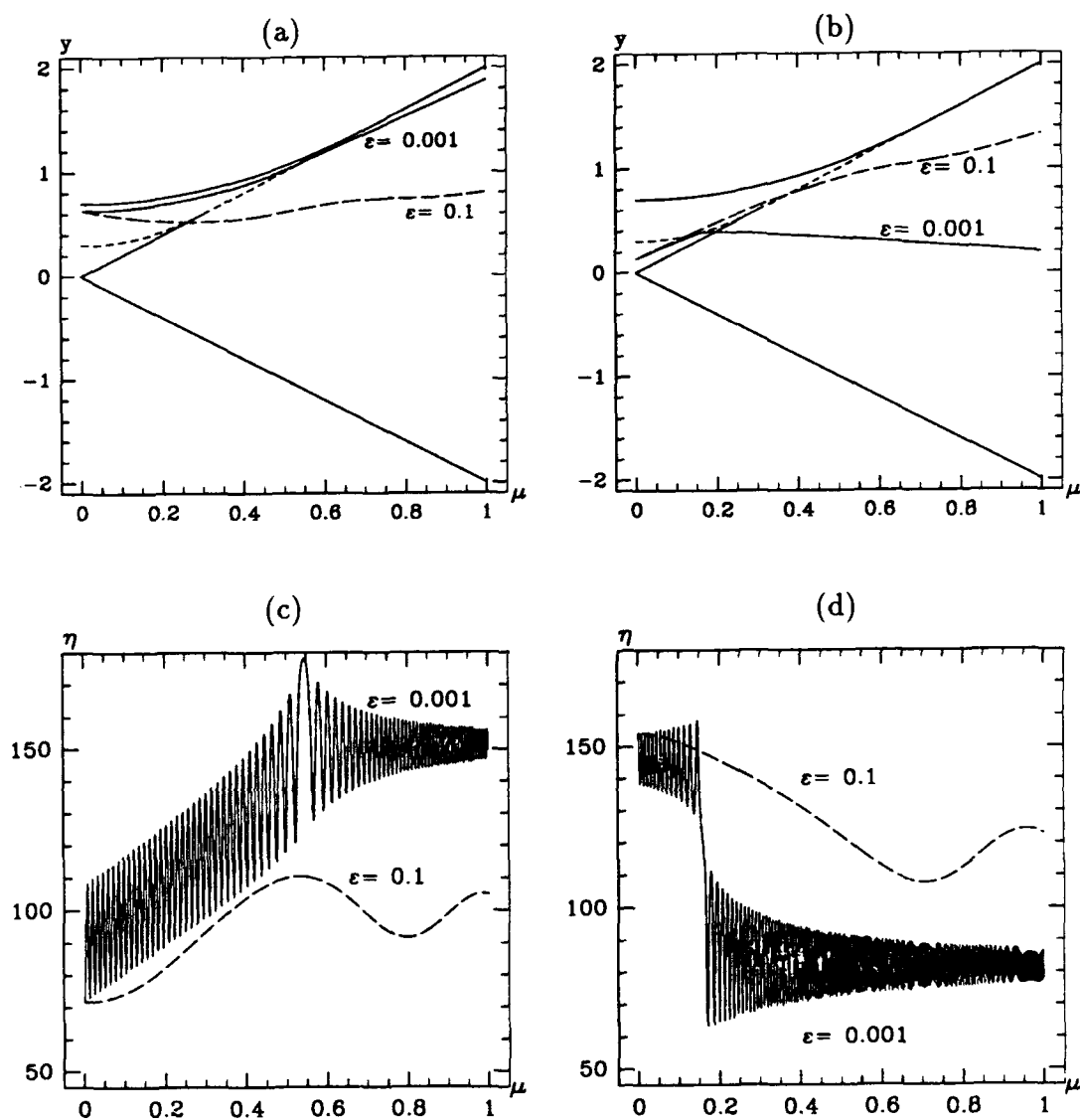
Figure 4.14. Effect of Torque Magnitude on Cone Angle $(i_2, i_3) = (-0.3, -0.7)$. (a) Flat spin recovery in the μy plane. Initial conditions are (x_1, x_2, x_3, μ) = $(0.31, 0, 0.95, 0)$. (b) Prolate spinup in the μy plane. Initial conditions are $(x_1, x_2, x_3, \mu) = (-0.90, 0, 0.436, 0)$. (c) Cone angle for flat spin recovery. (d) Cone angle for prolate spinup.

prolate spinup and flat spin recovery experience phase-dependent dispersion when crossing the separatrix. This is shown for flat spin recovery in Fig. 4.15. For prolate spinup the effect is similar.

We note also that a small change in ε has a similar effect to changes in initial phase, since it effects the time (hence the phase) at which the trajectory crosses the separatrix.

4.6   Application to Resonance Capture

As discussed in Section 2.6, asymmetry and unbalance of the rotor may induce resonances that interfere with the spinup process. One particular instance of such a resonance is *precession phase lock*, which was investigated by Kinsey *et al* [50]. In this section we use the μy plane to investigate resonance capture for a similar spinup problem. We also take this opportunity to demonstrate the use of the prolate-to-oblate symmetry transformation.

The model investigated by Kinsey *et al* [50] consists of a **slightly unbalanced rotor connected to an axisymmetric, balanced platform**. Since the platform is balanced and axisymmetric, this model is also a gyrostat, although it does not possess the same symmetries as the axial gyrostats considered in this thesis. A similar system, exhibiting the same capture phenomenon as precession phase lock, is an axial gyrostat with a **slightly asymmetric but balanced rotor and an axisymmetric, balanced platform**. That is, we replace the unbalance of the rotor with an asymmetry. To explain this difference, we compare the moment of inertia matrices for the two models, expressed in a body-fixed frame with the 1-axis aligned with the rotor.

$$
\text{Kinsey gyrostat} \qquad \text{Axial gyrostat}
$$

$$
\mathbf{I} = \begin{bmatrix} I_1 & I_{12} & 0 \\ I_{12} & I_1 & 0 \\ 0 & 0 & I_3 \end{bmatrix} \qquad \mathbf{I} = \begin{bmatrix} I_1 & 0 & 0 \\ 0 & I_2 & 0 \\ 0 & 0 & I_3 \end{bmatrix}
$$
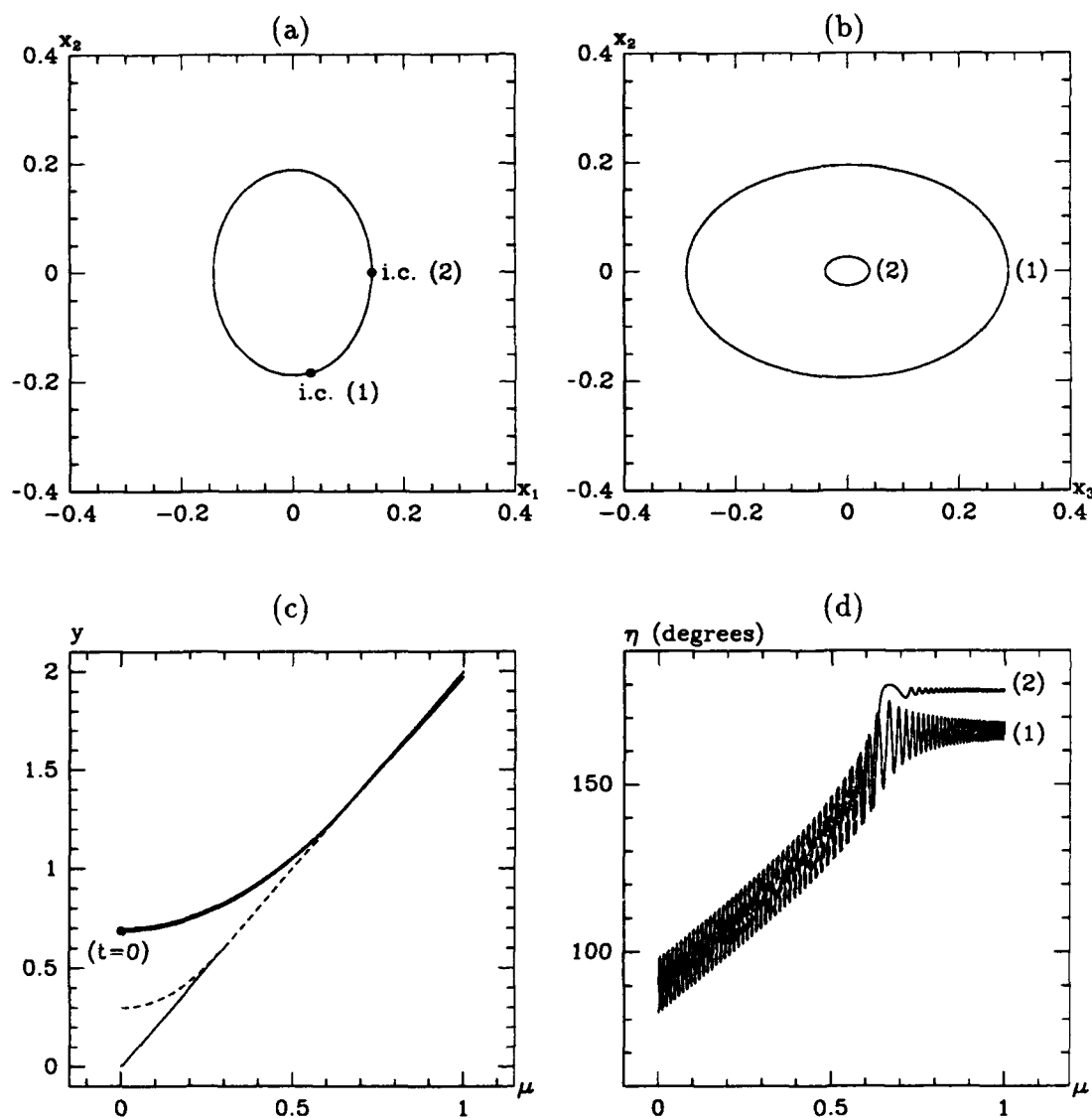
Figure 4.15. Effect of Initial Phase Difference for Flat Spin Recovery, with $(i_2, i_3) = (-0.3, -0.7), \varepsilon = 0.001$. (a) The initial polhode projected onto $x_1 x_2$ plane. (b) The final polhodes projected onto $x_3 x_2$ plane. (c) The flow in the μy plane. Note that the two trajectories are difficult to distinguish in the μy plane, because trajectory (2) is very close to the straight line $y = 2\mu$ ($\mathbf{P}_\mu$). (d) The cone angle.

Note that diagonalizing the Kinsey model inertia matrix will not result in an axial gyrostat, since the new 1-axis will not coincide with the axis of the rotor.

Now, the difference between the proposed model and the axial gyrostats we have been discussing is simply one of nomenclature: our gyrostats consist of balanced, asymmetric platforms with balanced, axisymmetric rotors. Switch the terms *rotor* and *platform*, and the two types of gyrostats are identical. However, since the goal in the proposed model is to despin the axisymmetric platform, this translates into despinning the rotor in our system.

In this case, we may use the equations and graphical tools developed here. We simply take the axial torque to be a small *negative* constant, and despin the *rotor* instead of the platform.

For a slightly asymmetric platform, $i_2 = i_3 + \varepsilon_1$, where ε_1 is the small positive asymmetry parameter. For definiteness, we consider a system with $(i_1, i_2, i_3) = (0.7, 0.6, 0.5)$. The μy plane for this system is shown in Fig. 4.16(a).

The gyrostat under consideration is a prolate gyrostat with the rotor axis as the major axis. Using Symmetry 2, we can transform this to an equivalent oblate gyrostat with $(i_1, i_2, i_3) = (0.7, -0.5, -0.6)$, and consider the equilibrium at the south pole of the momentum sphere. Since the south pole corresponds to the $\mathbf{P}_\mu$ line in the μy plane, we only need to look closely at the upper half of the μy plane, which is shown in Fig. 4.16(b).

Now, the initial condition for the equivalent oblate gyrostat in the all-spun condition is close to the equilibrium point $(x_1, x_2, x_3) = (-1, 0, 0)$, with $\mu = -i_1 x_1$, which is indicated in Fig. 4.16(b). Note that since $i_1 > |i_3|$, this equilibrium point corresponds to a point in the μy plane where there are only *two* equilibrium points on the momentum sphere; however, since the all-spun system rotates as a single rigid body, there are in fact *six* equilibria on the sphere. This apparent discrepancy is explained in Section 4.5 (cf. discussion following Eq. (4.5)).
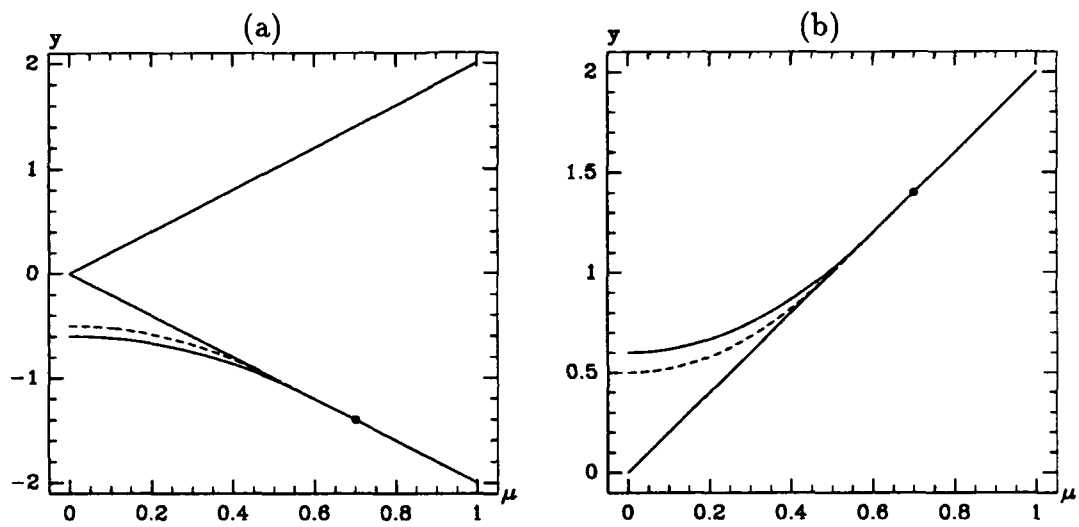
Figure 4.16. The μy Plane for a Prolate Gyrostat and the Equivalent Oblate Gyrostat $(i_1, i_2, i_3) = (0.7, 0.6, 0.5) \mapsto (0.7, -0.5, -0.6)$. The ideal initial condition is indicated with a dot in each graph. Note that in (a), the μy plane is "upside-down" from the usual plots we have shown. This figure graphically demonstrates the effect of the equivalence transformation of Eq. (3.45). In (b) we only show the upper half of the plane, since this is the only region of interest.

Having determined the exact initial condition for equilibrium, we assume the motion begins on a polhode near the equilibrium. That is, we choose a specific initial condition and investigate the despin dynamics in the μy plane for various values of ϵ. Sample trajectories are shown in Fig. 4.17.

The plots in Fig. 4.17 clearly illustrate the resonance capture phenomenon, and the fact that the *captured* trajectory ends up between $\mathbf{F}_\mu$ and $\mathbf{U}_\mu$ indicates the nature of the capture: *the captured trajectory ends up in one eye of the two heteroclinic orbits on the sphere.* To make this clear, in Fig. 4.18, we show the instantaneous polhodes for both trajectories at several points during the "despin" maneuver.

4.7 Intermediate Gyrostats

The intermediate gyrostats differ considerably from the oblate and prolate cases, principally in the topology of the momentum sphere when there are six equilibrium points. The two saddles are at opposite poles of the sphere, and the two pitchfork bifurcations occur at opposite poles, rather than at the same pole as in the oblate and prolate cases. In terms of the xy plane, this difference is seen in the fact that $y_3(x; \mu)$ is concave upwards rather than downwards as in the oblate case. There are still two bifurcations however, allowing for three different possibilities for the xy plane, as shown in Fig. 4.19.

The μy plane is shown in Fig. 4.20. As with the previous cases, the solid curves correspond to centers of the unperturbed system, and the dashed curves correspond to saddles (and their separatrices) of the unperturbed system.

There are two spinup problems of interest for intermediate gyrostats, but as they are qualitatively equivalent, we call them both intermediate spinup (ISU). These are shown as dotted lines in Fig. 4.21. Note that intermediate spinup trajectories are quite similar to flat spin recovery trajectories (compare Fig. 4.13).
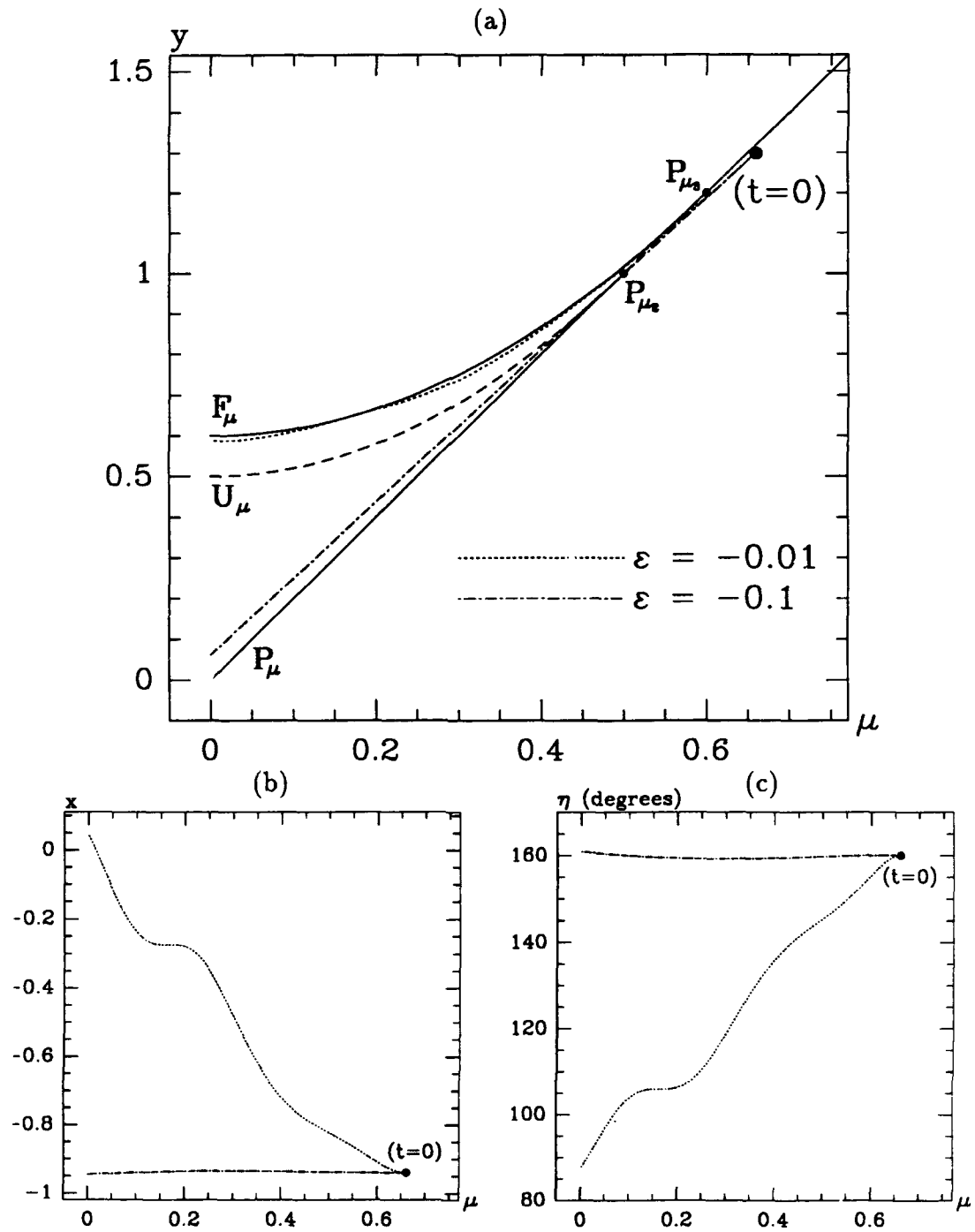
Figure 4.17. Resonance Capture. Inertia parameters are $(i_2, i_3) = (-0.5, -0.6)$. Initial conditions are $(x_1, x_2, x_3, \mu) = (-0.94, 0.34, 0.00, 0.66)$. Rotor despin torques are $\varepsilon \in \{-0.10, -0.01\}$. The dotted trajectory is *captured* near the flat spin equilibrium point, while the dashed trajectory *escapes* to oscillate near the south pole equilibrium point (see Fig. 4.18). *Note that the flow is from right to left in this figure.* (a) The μy plane. (b) The μx plane. (c) The cone angle.
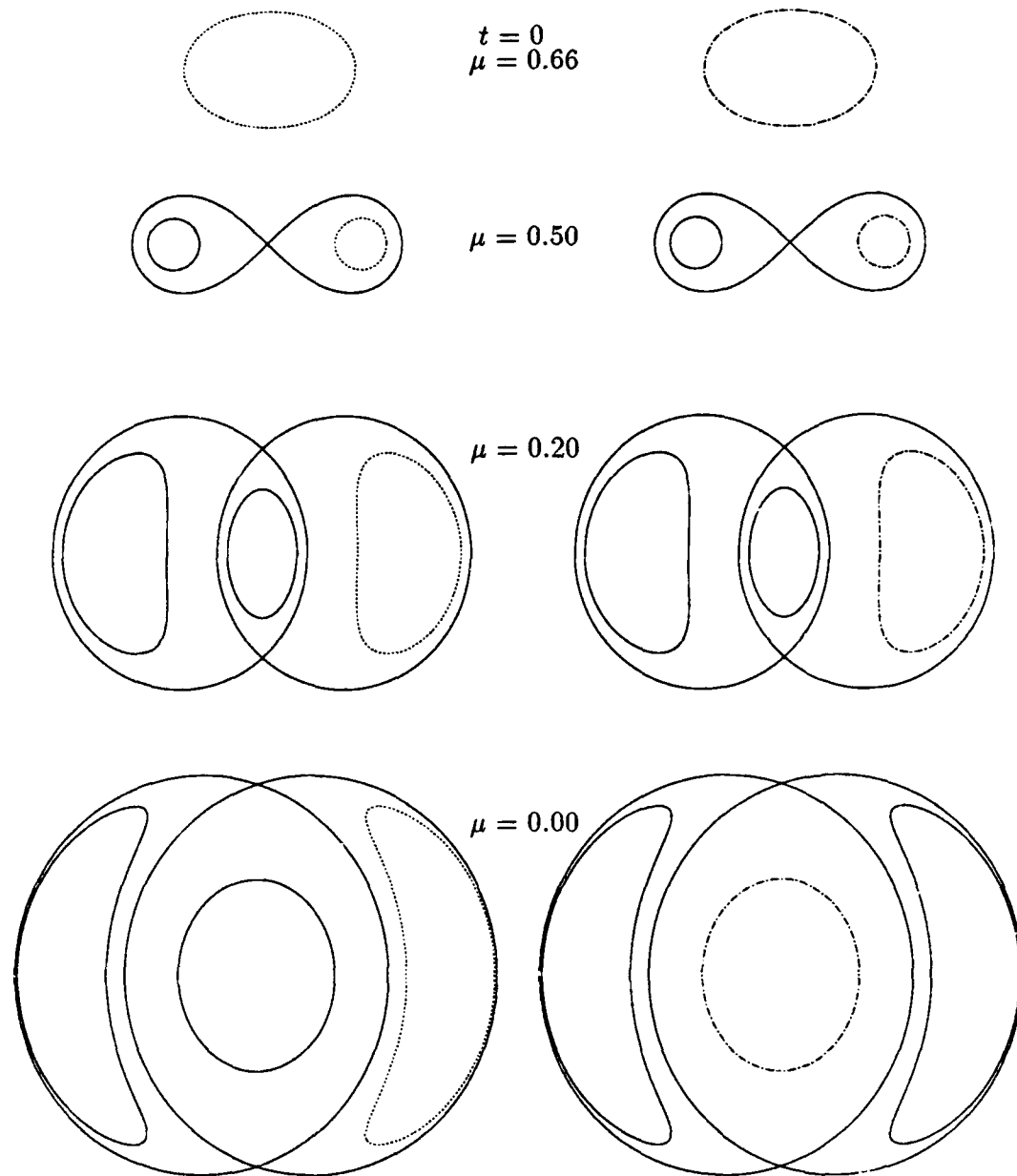
Figure 4.18. Schematic of Resonance Capture on the Momentum Sphere. Several instantaneous polhodes are shown for the flow in Fig. 4.17. The dotted and dashed polhodes represent the instantaneous polhodes for the trajectories in Fig. 4.17. The polhodes on the left side of the figure correspond to the *captured* trajectory, while those on the right correspond to *passage through resonance.*
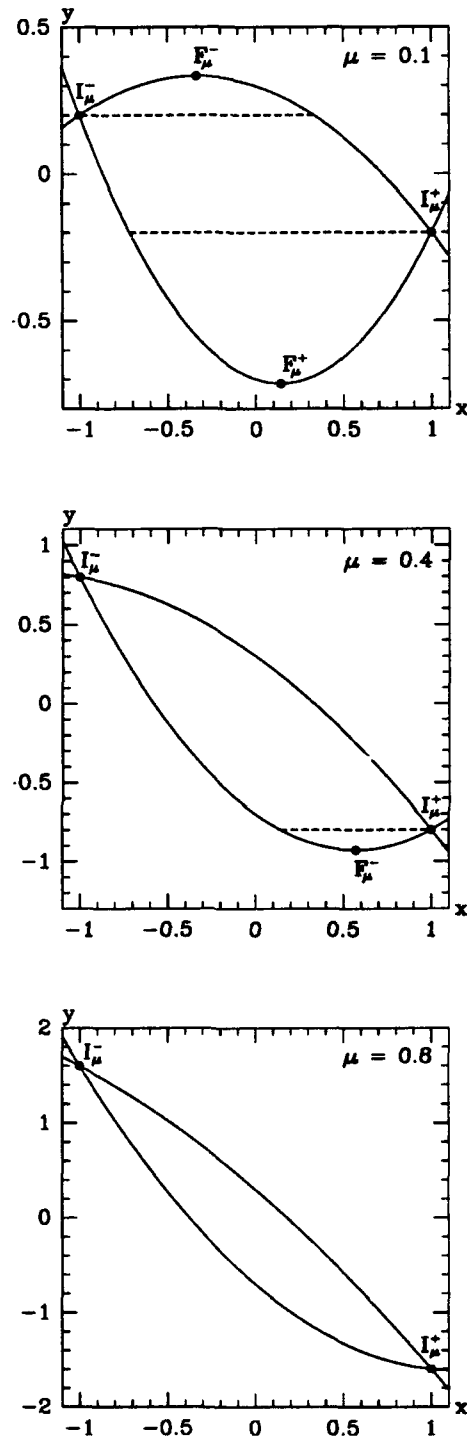
Figure 4.19. The xy Planes for Intermediate Gyrostats $(i_2, i_3) = (-0.3, -0.7)$, $\mu \in \{0.1, 0.4, 0.8\}$. Each plot corresponds to a fixed value of μ. Constant energy curves on the sphere correspond to $y = \text{CONST}$. Compare with Fig. 4.5.
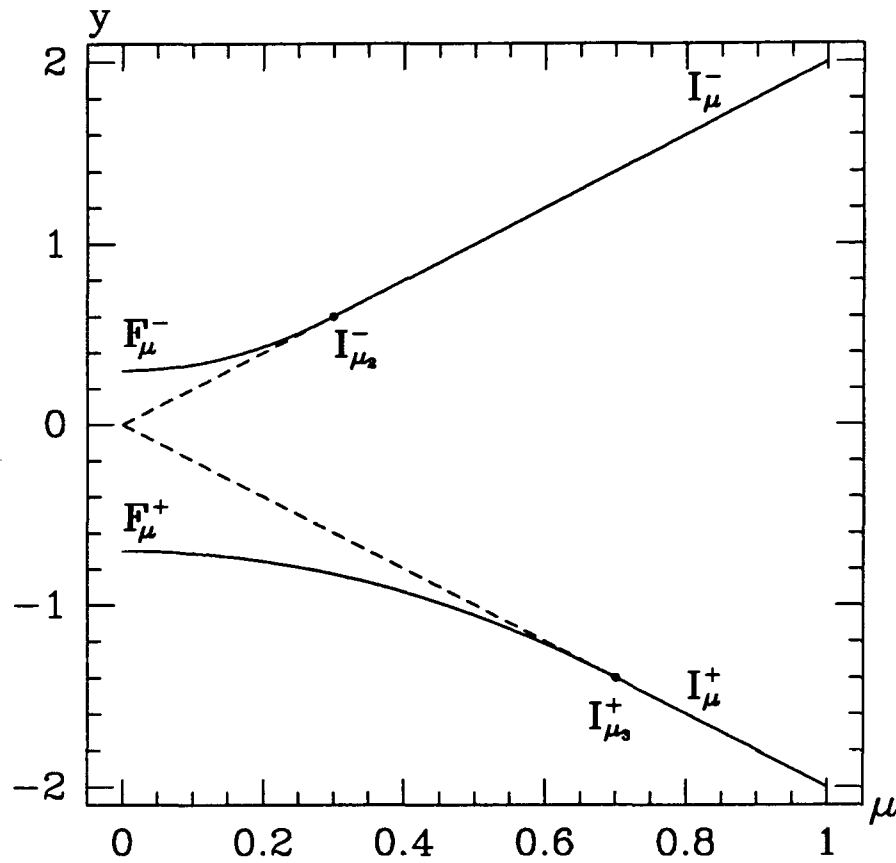
Figure 4.20. The μy Plane for Intermediate Gyrostats $(i_2, i_3) = (0.7, -0.3)$. Compare with Fig. 4.7.

Table 4.3. Bifurcation Values of μ for Intermediate Gyrostats

μ	Bifurcation
$\mu_2 \overset{\triangle}{=} i_2 > 0$	Pitchfork bifurcation: a pair of flat spin centers $\mathbf{F}_\mu^+$ coalesce with the saddle at the north pole $\mathbf{I}_\mu^+$ creating a center at the north pole.
$\mu_3 \overset{\triangle}{=} -i_3 > 0$	Pitchfork bifurcation: a pair of flat spin centers $\mathbf{F}_\mu^-$ coalesce with the saddle at the south pole $\mathbf{I}_\mu^-$ creating a center at the south pole.
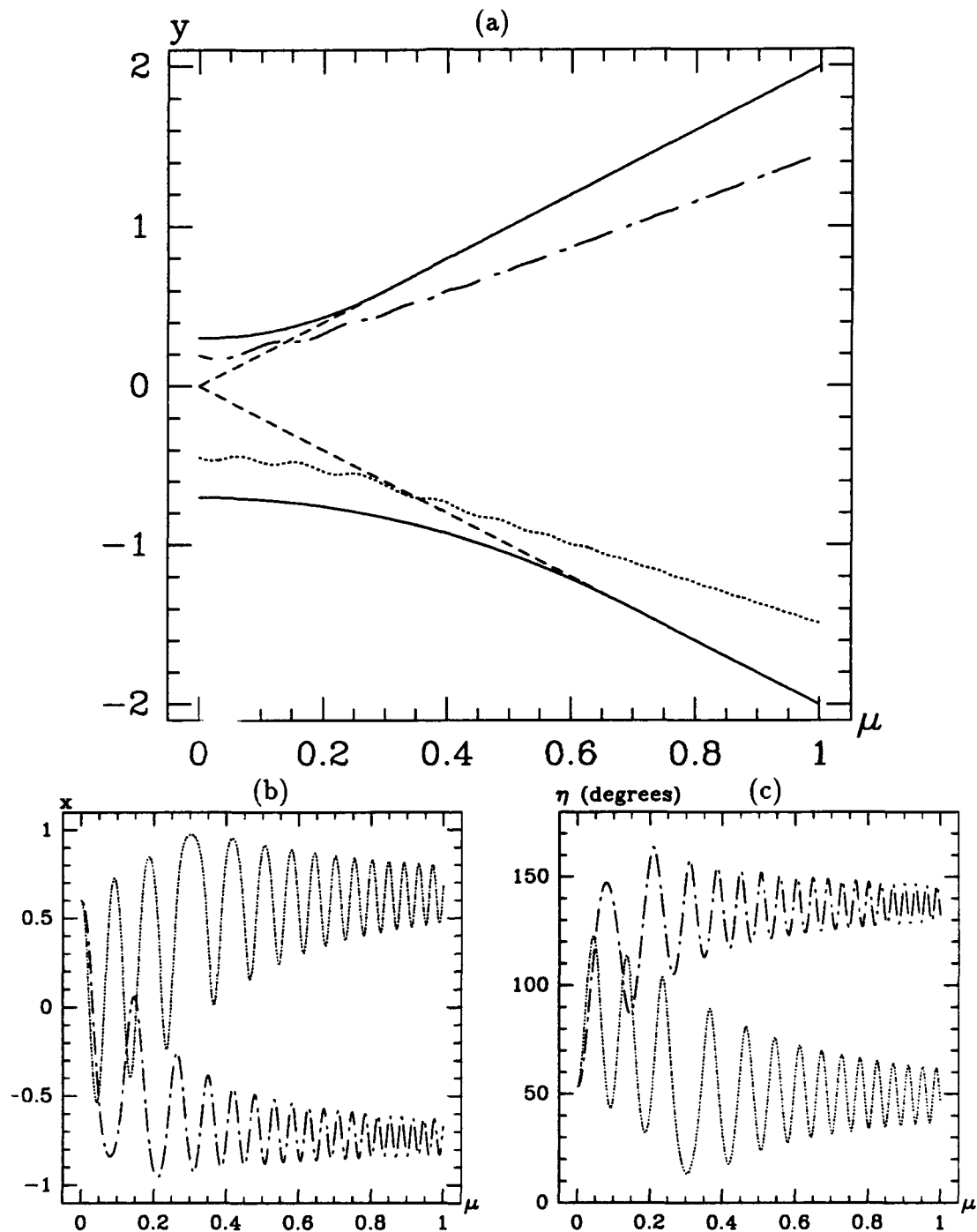
Figure 4.21. Intermediate Spinup $(i_2, i_3) = (0.7, -0.3)$. For both trajectories, the initial values of (x_1, μ) are $(0.6, 0.0)$. The initial values of (x_2, x_3) are $(0.8, 0.0)$ and $(0.0, 0.8)$, with the former corresponding to the trajectory where $y < 0$, and the latter corresponding to the trajectory with $y > 0$. The initial values are near the points $\mathbf{F}_\mu^-$ and $\mathbf{F}_\mu^+$, for $\mu = 0$ (see Fig. 4.20). (a) Projection onto the μy plane. (b) Projection onto the μx plane. (c) The cone angle.

Table 4.4. Equilibrium Points for Intermediate Gyrostats

Equilibrium	x	Range of μ		Energy (y)
		for center	for saddle	
I_μ^+	+1	(μ_2, ∞)	$[0, \mu_2)$	-2μ
I_μ^-	-1	(μ_3, ∞)	$[0, \mu_3)$	$+2\mu$
F_μ^-	μ/i_3	$[0, \mu_3)$	—	$\mu^2/\mu_3 + \mu_3$
F_μ^+	μ/i_2	$[0, \mu_2)$	—	$-(\mu^2/\mu_2 + \mu_2)$

The values of x_2 and x_3 are given at Eqs. (3.37)–(3.39).

4.8 Summary

In this chapter we have related classical approaches to viewing spinup dynamics to our approach, which represents spinup as a trajectory in the μy plane. We then applied the μy plane to a resonance capture problem similar to one which has previously been discussed in the literature. Although we have shown that trajectories in the μy plane approximately represent the full dynamics, we must keep in mind that these trajectories are obtained by integrating the full system of four differential equations. We would like to obtain a single differential equation describing the flow in the μy plane. In the next two chapters, we obtain such an equation. First we develop the periodic $\epsilon = 0$ solution for $x(t)$ in Chapter 5. Then in Chapter 6 we apply the method of averaging using this periodic solution.

Chapter 5

The $\varepsilon = 0$ Solution

In Chapter 3 we showed that the equations of motion reduce to a single elliptic integral when $\varepsilon = 0$. In this chapter, we give the solutions to this integral in terms of Jacobi's elliptic functions. Although the existence of such solutions is known and they have been given by several authors (see Section 1.2.1), the present work is apparently the first development in dimensionless form. We give the $\varepsilon = 0$ solution for all axial gyrostats, and furthermore, we use the μy plane as a bifurcation diagram to show where the various forms of the solution apply. We also identify two cases with elementary solutions that have not previously been reported.

In developing the elliptic function solution, we found the volume of tables by Byrd and Friedman [10] quite useful. Also the more recent text by Lawden [55] helped to clarify some points regarding elliptic functions and integrals. We begin this chapter with a brief introduction to elliptic functions, followed by the solution for the angular momentum x as a function of time. At the end of the chapter, we discuss several issues regarding the frequency and phase of the solution. The details of inverting the elliptic integrals are relegated to Appendix C.

5.1 Elliptic Functions

In what follows, we make use of the elliptic functions $sn(u; k)$ and $cn(u; k)$, which are similar to the familiar trigonometric functions $\sin u$ and $\cos u$. An obvious difference, of course, is the appearance of the parameter k, known as the *modulus*, which effects a change in the period of oscillation. In practice the modulus takes on real values on the interval $[0, 1]$. When $k = 0$, the elliptic functions reduce to their trigonometric counterparts, and when $k = 1$, they become infinite period hyperbolic functions. The limits are shown in Table 5.1, along with those for $dn(u; k)$. The elliptic function $dn(u; k)$ does not appear in the $\varepsilon = 0$ solution given here; however, it does arise in the averaging process in Chapter 6. In Fig. 5.1, we show the elliptic functions along with their elementary function counterparts.

Table 5.1. Limiting Values of Elliptic Functions

$k^2 = 0$	$k^2 = 1$
$sn(u; 0) = \sin u$	$sn(u; 1) = \tanh u$
$cn(u; 0) = \cos u$	$cn(u; 1) = \operatorname{sech} u$
$dn(u; 0) = 1$	$dn(u; 1) = \operatorname{sech} u$

The period of the elliptic functions $sn(u; k)$ and $cn(u; k)$ is $4K(k)$, where $K(k)$ is the complete elliptic integral of the first kind, defined by

$$K(k) = \int_0^{\pi/2} \frac{d\vartheta}{\sqrt{1 - k^2 \sin^2 \vartheta}} \tag{5.1}$$

It is easy to verify that $K(0) = \pi/2$, and $K(1) = \infty$. A plot of $K(k)$ is included in Fig. 5.1(d), as well as a plot of $E = E(k)$, which is the complete elliptic integral of the second kind. We also note that the period of $dn(u; k)$ is $2K(k)$, as may be seen in Fig. 5.1(c).
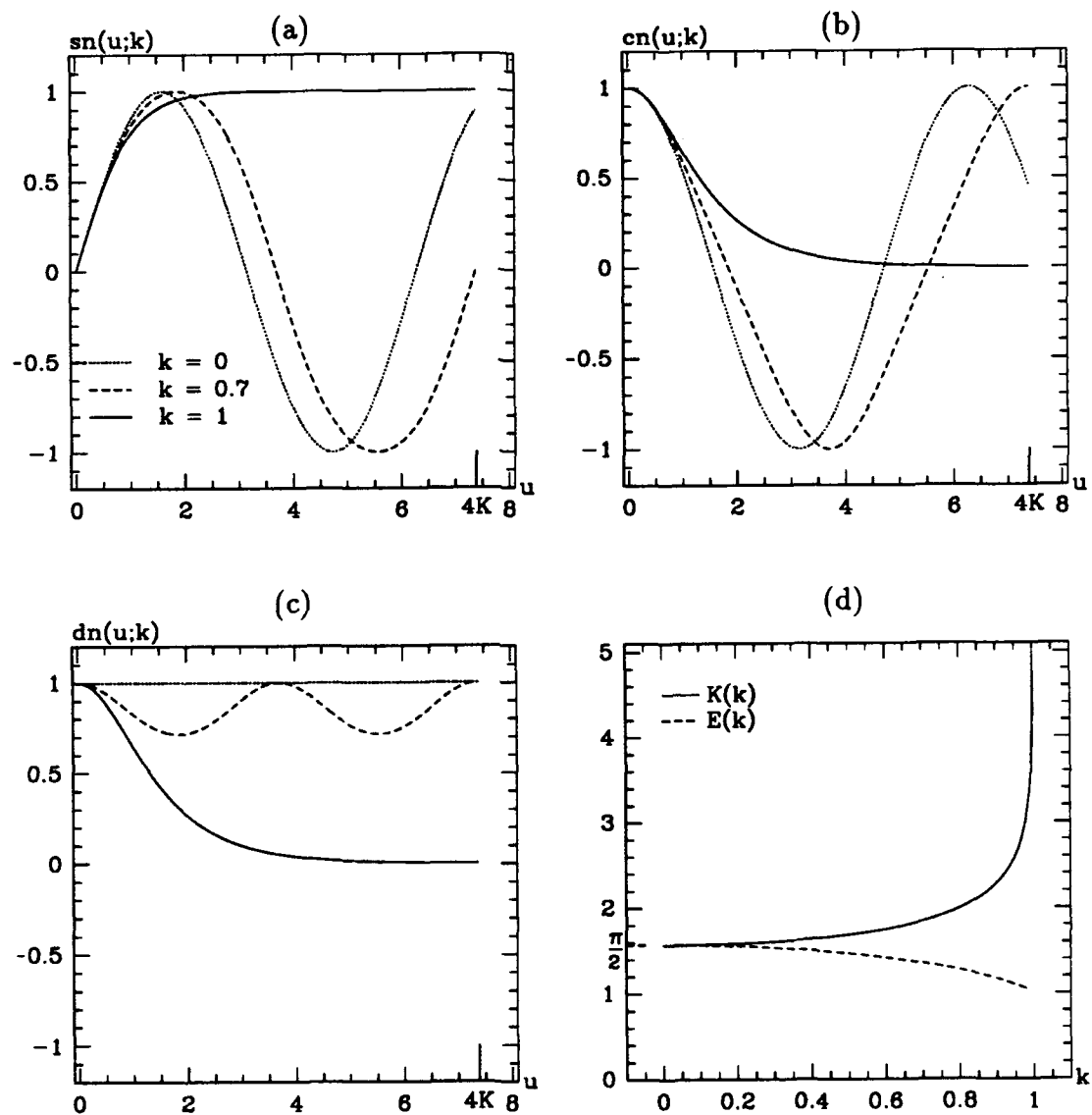
Figure 5.1. Elliptic Functions. (a) $\mathrm{sn}(u;k)$. (b) $\mathrm{cn}(u;k)$. (c) $\mathrm{dn}(u;k)$. (d) $K(k)$ and $E(k)$. In (a)–(c), the value of u indicated as $4K(k)$ is $u = 4K(0.7)$. Note that $K(0) = \pi/2$, while $K(1) = \infty$, as shown in (d).

5.2 The Gyroscopic Function and Its Roots

The elliptic integral we are interested in is given at Eq. (3.64), rewritten here as

$$t = \pm \int_{x(0)}^{x(t)} \frac{d\xi}{\sqrt{-W(\xi)}} \tag{5.2}$$

where $W(x)$ is the quartic polynomial in $x = x_1$ given by

$$W(x) = -\left(y_2(x; \mu) - y\right)\left(y - y_3(x; \mu)\right) \tag{5.3}$$

Recall that $y_2(x; \mu)$ and $y_3(x; \mu)$ are the quadratics given at Eqs. (3.60) and (3.61). Written out in full, this quartic is

$$W(x) = \left(i_3 x^2 - 2\mu x - i_3 - y\right)\left(i_2 x^2 - 2\mu x - i_2 - y\right) \tag{5.4}$$

Leimanis [56] calls $W(x)$ the *gyroscopic function*, apparently a translation of Leipholz's *kreiselfunktion* [57]. Since $W(x)$ is already conveniently factored, we choose to view it as the product of two quadratics, as discussed in Section 4.3. This approach has the additional advantage of requiring only one figure for a given value of μ, valid for all admissible values of y. The gyroscopic function, however, must be graphed for each value of μ and each value of y. Thus, to obtain the equivalent information contained in a single xy plane (see Fig. 4.5), one would require several $W(x)$ graphs. For reference, in Fig. 5.2 we show two $W(x)$ curves corresponding to the xy plane in Fig. 4.5(a). Further discussion of $W(x)$, including numerous figures, is available in §16 of Leimanis [56], and in Leipholz [57].

The solution to Eq. (5.2) depends on the roots of $W(x)$. The roots in turn depend on the constant values of μ and y, as well as on the parameters i_2 and i_3. We denote the roots of $y_2(x; \mu) - y = 0$ by $r_2^{\pm}$ and those of $y - y_3(x; \mu) = 0$ by $r_3^{\pm}$. The values of these roots are given by

$$r_2^{\pm} = \frac{\mu \pm \sqrt{\mu^2 + i_3(i_3 + y)}}{i_3} \tag{5.5}$$

$$r_3^{\pm} = \frac{\mu \pm \sqrt{\mu^2 + i_2(i_2 + y)}}{i_2} \tag{5.6}$$
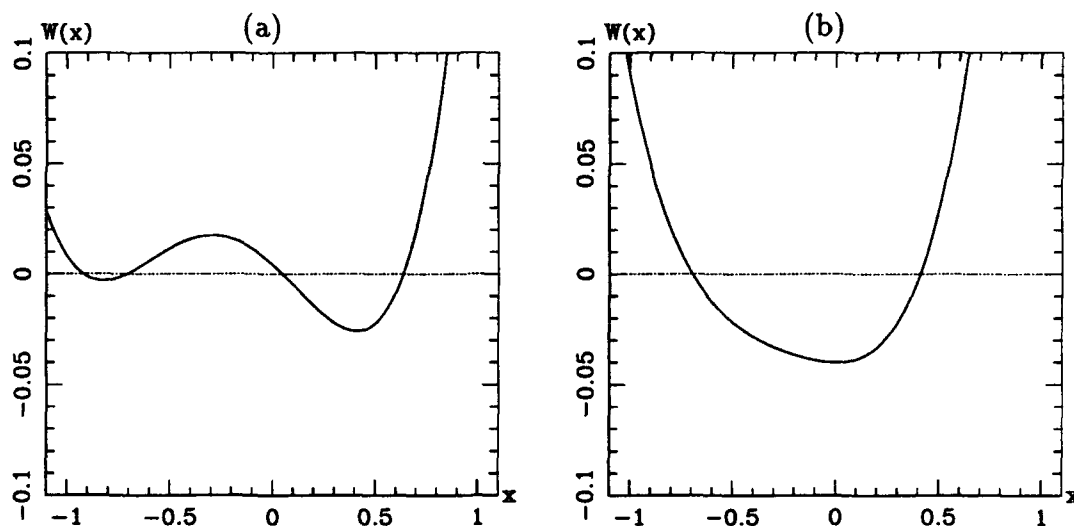
Figure 5.2. The Gyroscopic Function $W(x)$. The inertia parameters are $(i_2, i_3) = (-0.3, -0.7)$. The rotor momentum is $\mu = 0.1$. (a) $W(x)$ has four real, distinct roots for $y = 0.29$. (b) $W(x)$ has two real, distinct roots and two complex roots for $y = 0.5$.

There are a number of different possibilities depending on whether these roots are real or complex. Referring to the xy plane in Fig. 5.3, the four roots are the values of x at the intersections of a given straight line $y = \text{CONST}$ and the two parabolas $y_2(x; \mu)$ and $y_3(x; \mu)$. Since $y < y_2(x; \mu)$, the roots $r_2^{\pm}$ are always real; however, $r_3^{\pm}$ may be real or complex. For the elliptic function solutions, we adopt the notation used by Byrd and Friedman [10]; in particular, when all four roots, $r_2^{\pm}$, $r_3^{\pm}$, are real and distinct, they are renamed as a, b, c, and d so that $a > b > c > d$. When only $r_2^{\pm}$ are real and distinct, they are renamed a and b, with $a > b$, and the two complex roots are $c = r_3^-$, $\bar{c} = r_3^+$. Real repeated roots correspond to solutions in terms of elementary functions, and we list the possibilities later.

The rest of this chapter is devoted to a detailed exposition of the different forms of the solution to Eq. (5.2). As usual, we begin with the oblate case, then follow with the results for intermediate gyrostats.
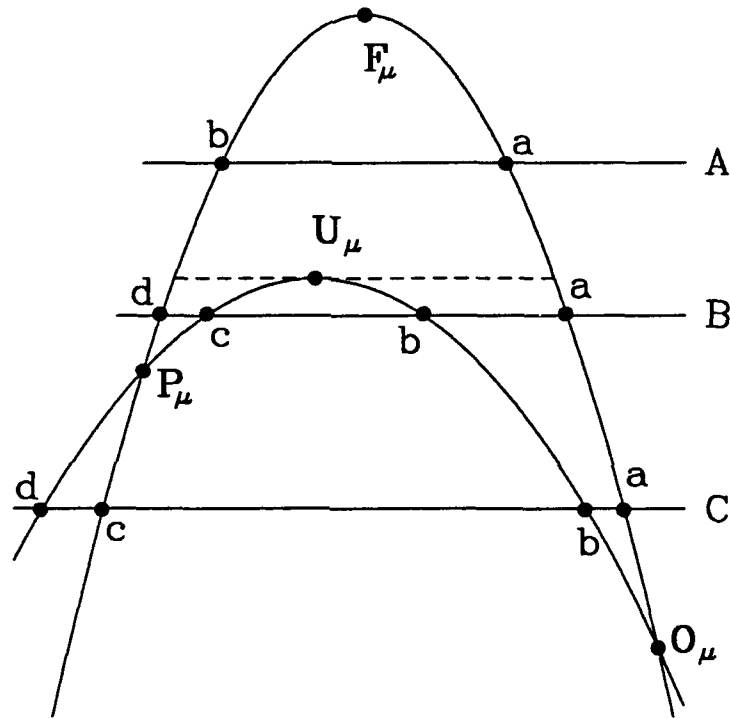
Figure 5.3. The xy Plane with Roots of the Gyroscopic Function Identified. The three straight lines correspond to different numbers and ordering of the real roots of $W(x)$: (A) two real roots, $a = r_2^-$, $b = r_2^+$, and two complex roots, $c = r_3^-$, $d = r_3^+$; (B) four real roots, $a = r_2^-$, $b = r_3^-$, $c = r_3^+$, $d = r_2^+$; (C) four real roots, $a = r_2^-$, $b = r_3^-$, $c = r_2^+$, $d = r_3^+$. Note that (A) corresponds to the gyroscopic function shown in Fig. 5.2(b), and (B) corresponds to Fig. 5.2(a). See also Fig. 4.5.

5.3 Oblate Gyrostats

As noted above, there are two basic cases: (1) there are four real roots, or (2) there are two real roots and two complex roots. The first of the two cases has two subcases depending on the range of x, and one of these two subcases also has three additional subcases. This gives a total of five different solution types, corresponding to the regions of the μy plane shown in Fig. 5.4. Note that an additional curve has been added to Fig. 4.6 to give Fig. 5.4: the thin solid line separating Region 2 from Region 1aiii is an extension of the locus of maxima of $y_3(x;\mu)$ given by Eq. (4.2). These points are not equilibrium points; however, they do correspond to special (trigonometric) solutions to Eqs. (3.25)–(3.28).

Because $i_3 < 0$ and $\mu \geq 0$, it is evident that $r_2^- \geq r_2^+$. Likewise, $r_3^- \geq r_3^+$ follows from $i_2 < 0$, and it is easy to verify that $r_2^- \geq \max\{r_2^+, r_3^\pm\}$. Hence throughout the μy plane, the largest root is $a = r_2^-$. The ordering of the other three roots to satisfy $b > c > d$ is determined by the constant values of μ and y.

Table 5.2. Regions of the μy Plane (Fig. 5.4) for Oblate Gyrostats ($i_3 < i_2 < 0$)

Region	Range of μ	Range of y	a	b	c	d
1ai	$[0, \infty)$	$[-2\mu, 2\mu]$	r_2^-	r_3^-	r_2^+	r_3^+
1aii	$[0, \mu_2)$	$[2\mu, \mu^2/\mu_2 + \mu_2]$	r_2^-	r_3^-	r_3^+	r_2^+
1aiii	(μ_2, μ_3)	$[2\mu, \min\{\mu^2/\mu_2 + \mu_2, \mu^2/\mu_3 + \mu_3\}]$	r_2^-	r_2^+	r_3^-	r_3^+
1b	$[0, \mu_2)$	$[2\mu, \mu^2/\mu_2 + \mu_2]$	r_2^-	r_3^-	r_3^+	r_2^+
2	$[0, \mu_3)$	$[\mu^2/\mu_2 + \mu_2, \mu^2/\mu_3 + \mu_3]$	r_2^-	r_2^+	r_3^-	r_3^+

In Region 1, the roots are ordered $a > b > c > d$, and all are real.

In Region 2, $a > b$ are real, but as $r_3^\pm$ are complex conjugates, $c > d$ is meaningless.

The roots $r_2^\pm$ and $r_3^\pm$ are given at Eqs. (5.5) and (5.6).
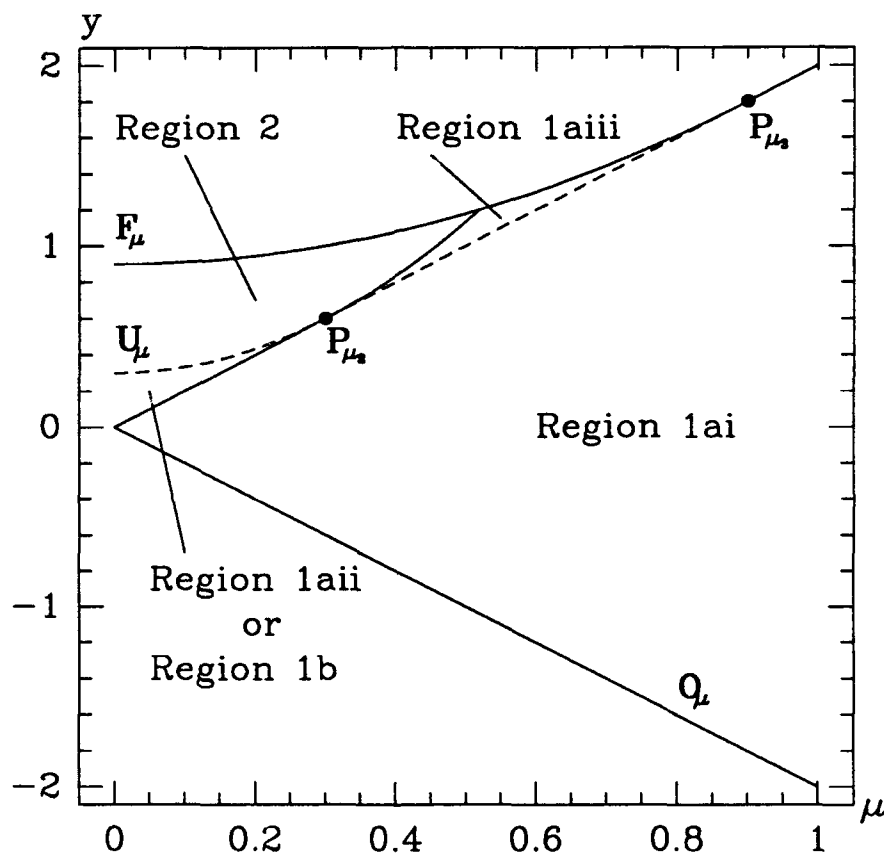
Figure 5.4. Regions in the μy Plane for $(i_2, i_3) = (-0.3, -0.9)$. The numbered regions correspond to those in Table 5.2. Regions 1aii and 1b occupy the same area of the plane because, in this region there are two polhodes corresponding to each y: one about O_μ and one about P_μ. See Fig. 4.5, $\mu = 0.1$.

5.3.1 Region 1

The $\epsilon = 0$ solution has the same form throughout Region 1 and its subregions. Of course, the ordering of the roots depends on the subregion as shown in Table 5.2. A more significant difference exists between Regions 1a and 1b. In Region 1a, $b \le x \le a$, and Eq. 256.00 in Ref. [10] applies, whereas in Region 1b, $d \le x \le c$, and Eq. 253.00 in Ref. [10] applies. The resulting difference between the two solutions involves simple parameter definitions as shown below. Thus the $\epsilon = 0$ solution for oblate gyrostats in Region 1 is:

$$x(u; k) = \beta \left\{ \frac{1 - \alpha_1^2 \text{sn}^2(u; k)}{1 - \alpha^2 \text{sn}^2(u; k)} \right\} \tag{5.7}$$

where β, α^2, and α_1^2 depend on whether the point (y, μ) is in Region 1a or Region 1b:

Region 1a   Region 1b

$$\beta = b \qquad \beta = c \tag{5.8}$$

$$\alpha^2 = \frac{a-b}{a-c} \qquad \alpha^2 = \frac{c-d}{b-d} \tag{5.9}$$

$$\alpha_1^2 = \frac{c}{b}\alpha^2 \qquad \alpha_1^2 = \frac{b}{c}\alpha^2 \tag{5.10}$$

and the rest of the parameters are

$$k^2 = \frac{(a-b)(c-d)}{(a-c)(b-d)} \tag{5.11}$$

$$u = \lambda t + u_0 \tag{5.12}$$

$$\lambda = \frac{1}{2}\sqrt{i_2 i_3(a-c)(b-d)} \tag{5.13}$$

Note from Eqs. (5.9) and (5.11) that $0 < k^2 < \alpha^2 < 1$ in both cases.

There is also an alternative solution for which $\alpha^2 < 0$, obtained via Eq. 252.00 or 257.00 of Ref. [10]. It has the same form as Eq. (5.7), but β, α^2, and α_1^2 are defined differently:

Region 1a   Region 1b

$$\beta = a \qquad \beta = d \tag{5.14}$$

$$\alpha^2 = \frac{b-a}{b-d} \qquad \alpha^2 = \frac{d-c}{a-c} \tag{5.15}$$

$$\alpha_1^2 = \frac{d}{a}\alpha^2 \qquad \alpha_1^2 = \frac{a}{d}\alpha^2 \tag{5.16}$$

and the rest of the parameters are given by Eqs. (5.11)–(5.13). The usefulness of this alternative is made clear in Chapter 6.

5.3.2 Region 2

In Region 2, where $a \geq x \geq b$, the roots $r_3^\pm$ are complex conjugates, while $r_2^\pm$ are real. The real roots are ordered so that $a = r_2^- > b = r_2^+$. The complex root c is:

$$c = \frac{\mu + \sqrt{\mu^2 + i_2(i_2 + y)}}{i_2} = b_1 + ia_1 \tag{5.17}$$

from which $b_1 = \mu/i_2$, and $a_1 = \sqrt{-(\mu^2 + i_2(i_2 + y))}/i_2$. Following Ref. [10], we define $A^2 = (a - b_1)^2 + a_1^2$, and $B^2 = (b - b_1)^2 + a_1^2$. Now, using Eq. 259.00 in Ref. [10], we obtain the $\varepsilon = 0$ solution for oblate gyrostats in Region 2:

$$x(u;k) = \beta \left\{ \frac{1 + \alpha_1 \mathrm{cn}(u;k)}{1 + \alpha \mathrm{cn}(u;k)} \right\} \tag{5.18}$$

where

$$\beta = \frac{aB + bA}{A + B} \tag{5.19}$$

$$\alpha = \frac{A - B}{A + B} \tag{5.20}$$

$$\alpha_1 = \frac{bA - aB}{aB + bA} \tag{5.21}$$

$$k^2 = \frac{(a - b)^2 - (A - B)^2}{4AB} \tag{5.22}$$

$$u = 2\lambda t + u_0 \tag{5.23}$$

$$\lambda = \frac{1}{2}\sqrt{i_2 i_3 AB} \tag{5.24}$$

The use of 2λ in Eq. (5.23) and the factor of 1/2 in Eq. (5.24) above simplifies later notation, as explained in Section 5.6 below. Note that since $a > b$, it is also true that $A > B$, which implies $0 < \alpha < 1$. This fact is useful in the application of the method of averaging in the next chapter.

5.4 Elementary Solutions

Recall that the solid ($\mathbf{F}_\mu$, $\mathbf{O}_\mu$, $\mathbf{P}_\mu$) and dashed ($\mathbf{U}_\mu$ and $\mathbf{P}_\mu$) curves in the μy plane correspond to branches of equilibrium points of the unperturbed system (cf. Fig. 4.7). It is easy to verify that the points on these curves correspond to constant values of $x(u; k)$. In terms of the elliptic function solutions given above, these special points in the μy plane correspond to a real repeated root of the gyroscopic function. In Table 5.3, we list all of the possible repeated roots for oblate gyrostats, including cases that do not correspond to equilibrium points of the unperturbed system.

Table 5.3. Repeated Roots for Oblate Gyrostats

Locus	Region	Repeated Root	Implication
$\mathbf{O}_\mu$	1ai	$a = b = 1$	$\alpha^2 = \alpha_1^2 = k^2 = 0, x \equiv 1$
$\mathbf{P}_\mu$	1ai	$a = b = -1$	$\alpha^2 = \alpha_1^2 = k^2 = 0, x \equiv -1$
$\mathbf{P}_\mu$	1ai ∩ 1aii	$c = d = -1$	$k^2 = 0, \mathrm{sn}(u; k) \to \sin u$
$\mathbf{P}_\mu$	1ai ∩ 1aiii	$b = c = -1$	$\alpha^2 = \alpha_1^2 = k^2 = 1, x \equiv -1$
$\mathbf{P}_\mu{}^*$	1ai ∩ 1aiii	$b = c = -1$	$k^2 = 1, \mathrm{sn}(u; k) \to \tanh u$
$\mathbf{U}_\mu$	1aii ∩ 2	$b = c = \mu/i_2$	$\alpha^2 = \alpha_1^2 = k^2 = 1, x = \mu/i_2$
$\mathbf{U}_\mu{}^*$	1aii ∩ 2	$b = c = \mu/i_2$	$k^2 = 1, \mathrm{sn}(u; k) \to \tanh u$
$\mathbf{U}_\mu{}^*$	1b ∩ 2	$b = c = \mu/i_2$	$k^2 = 1, \mathrm{sn}(u; k) \to \tanh u$
$\mathbf{F}_\mu$	2	$a = b = \mu/i_3$	$\alpha = \alpha_1 = k^2 = 0, x = \mu/i_3$
$\mathbf{F}_\mu$	1aiii	$a = b = \mu/i_3$	$\alpha^2 = \alpha_1^2 = k^2 = 0, x = \mu/i_3$
$\mu^2/\mu_2 + \mu_2$	2 ∩ 1aiii	$c = d = \mu/i_2$	$k^2 = 0, \mathrm{sn}(u; k) \to \sin u$

* Using the alternate solution.

Recall that we stated that the solid curve separating Region 2 from Region 1aiii corresponds to a trigonometric solution. The line separating Region 1aii

90

from Region 1ai also corresponds to a trigonometric solution. To the author's knowledge, these special solutions have not been identified previously. In this section, we detail how these elementary solutions are obtained from the elliptic function solutions. There are also hyperbolic cases corresponding to the separatrices of the saddle points. These are shown in Table 5.3, but we do not derive them here.

5.4.1 Region 1aii-to-Region 1ai

First, it is important to note that the segment of $\mathbf{P}_\mu$ ($y = 2\mu$) on the interval $\mu \in [0, \mu_2)$ is identified with two types of trajectories in the xy plane. Referring to Fig. 5.3, a point on this segment of $\mathbf{P}_\mu$ may be seen to correspond to the equilibrium point at the south pole, as well as to the trajectory with $b \leq x \leq a$. The latter of these corresponds to a trigonometric solution for $x(t)$. The repeated root in this case is $c = d = -1$. From Eqs. (5.8)–(5.13) we find that the only significant effect is that $k^2 = 0$ on this segment of $\mathbf{P}_\mu$. Thus the $\epsilon = 0$ solution along this segment of $\mathbf{P}_\mu$ in Region 1a has the same form as Eq. (5.7), but with $\mathrm{sn}(u; k) \to \sin u$. That is,

$$x(u) = \beta \left\{ \frac{1 - \alpha_1^2 \sin^2 u}{1 - \alpha^2 \sin^2 u} \right\} \tag{5.25}$$

where $\beta = b$, $\alpha^2 = (a - b)/(a + 1)$, $\alpha_1^2 = -\alpha^2/b$, and $u = \frac{1}{2}\sqrt{i_2 i_3(a + 1)(b + 1)}\, t + u_0$. The roots a and b are defined as in Table 5.2.

5.4.2 Region 2-to-Region 1aiii

This transition curve is defined by $y = \mu^2/\mu_2 + \mu_2$, with $\mu \in (\mu_2, \mu_3)$. The repeated root is $c = d = \mu/i_2$. Using the Region 1aiii solution at Eq. (5.7), we find a solution of the same form as Eq. (5.25) above, with the parameters given by $\beta = b$, $\alpha^2 = (a - b)/(a - \mu/i_2)$, $\alpha_1^2 = \mu\alpha^2/(i_2 b)$, and $u_0 = \frac{1}{2}\sqrt{i_2 i_3(a - \mu/i_2)(b - \mu/i_2)}\, t + u_0$. The roots a and b are defined as in Table 5.2.

5.5 Intermediate Gyrostats

For intermediate gyrostats, $i_2 > 0 > i_3$, and the symmetry transformation Eq. (3.45) allows us to further assume $i_2 > |i_3|$ with no loss of generality. All four roots $r_2^{\pm}$ and $r_3^{\pm}$ are always real in this case, and x is in the range $a > b \geq x \geq c > d$. The μy plane is divided into three regions as shown in Fig. 5.5, and the four roots are ordered differently in each region, as listed in Table 5.4.

Using Eq. 254.00 of Ref. [10], the elliptic function solution for $\epsilon = 0$ is

$$x(u; k) = \beta \left\{ \frac{1 - \alpha_1^2 \mathrm{sn}^2(u; k)}{1 - \alpha^2 \mathrm{sn}^2(u; k)} \right\} \tag{5.26}$$

where

$$\beta = c \tag{5.27}$$

$$\alpha^2 = \frac{b - c}{b - d} \tag{5.28}$$

$$\alpha_1^2 = \frac{d}{c} \alpha^2 \tag{5.29}$$

$$k^2 = \frac{(b - c)(a - d)}{(a - c)(b - d)} \tag{5.30}$$

$$u = \lambda t + u_0 \tag{5.31}$$

$$\lambda = \frac{1}{2} \sqrt{-i_2 i_3 (a - c)(b - d)} \tag{5.32}$$

Note that Eq. (5.26) has the same form as Eq. (5.7) for Region 1 of oblate gyrostats. However, *all* of the parameters are different. Most importantly, the parameter α^2 has a different range. Whereas for oblate gyrostats in Region 1, $0 < k^2 < \alpha^2 < 1$, with Eqs. (5.28) and (5.30), one may show that $0 < \alpha^2 < k^2 < 1$ for intermediate gyrostats. This fact affects the averaging result obtained in the next chapter.

As with Region 1 for the oblate gyrostat, there is an alternative solution for the intermediate gyrostat, having the same form as Eq. (5.26), but with different definitions for β, α^2, and α_1^2. Using Eq. 255 of Ref. [10], these parameters are

defined as

$$\beta = b \tag{5.33}$$

$$\alpha^2 = \frac{b-c}{a-c} \tag{5.34}$$

$$\alpha_1^2 = \frac{a}{b}\alpha^2 \tag{5.35}$$

Note that $0 < \alpha^2 < k^2 < 1$ still holds for this form of the solution.
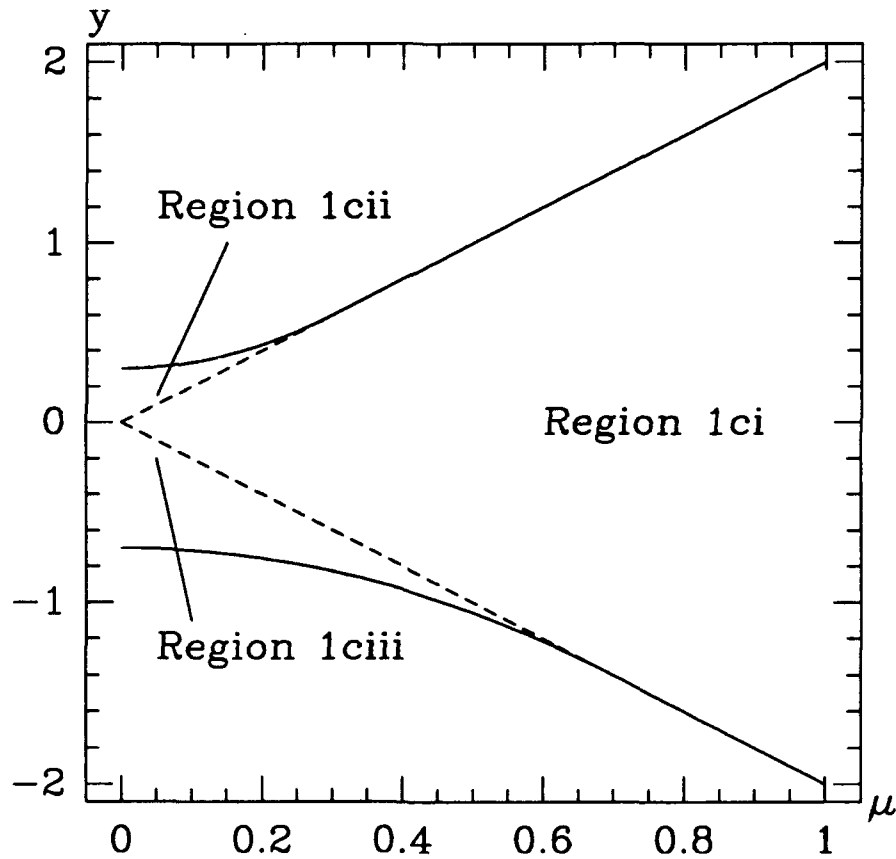
Figure 5.5. Regions in the μy Plane for $(i_2, i_3) = (0.7, -0.3)$. The numbered regions correspond to those in Table 5.4.

Finally, we note that for intermediate gyrostats, there are no trigonometric solutions corresponding to those we found for oblate gyrostats. All of the repeated root cases correspond to fixed points of the unperturbed system. There are of course hyperbolic solutions corresponding to the saddles, and these are easily

Table 5.4. Regions of the μy Plane (Fig. 4.20) for Intermediate Gyrostats $(i_2 > 0 > i_3, i_2 > |i_3|)$

Region	Range of μ	Range of y	a	b	c	d
1ci	$[0, \infty)$	$[-2\mu, 2\mu]$	r_3^+	r_2^-	r_3^-	r_2^+
1cii	$[0, \mu_3)$	$[2\mu, \mu^2/\mu_2 + \mu_2]$	r_3^+	r_2^-	r_2^+	r_3^-
1ciii	$[0, \mu_2)$	$[\mu^2/\mu_3 + \mu_3, -2\mu]$	r_2^-	r_3^+	r_3^-	r_2^+

obtained using the elliptic function solution given here.

5.6 Frequency and Phase

In the next chapter, we apply the method of averaging to the equations of motion, making use of the elliptic function solution given in this chapter. As we have shown, the form of the $\epsilon = 0$ solution depends on where the slow state is in the μy plane. In Chapter 4 we saw that spinup trajectories generally pass through more than one region of the μy plane. Thus evaluating the averaged slow flow entails piecing together different forms of the averaged equations at the transitions from one region to the next. This is discussed in detail in Section 6.3.3. Here we discuss the differences in frequency and phase between the different regions.

5.6.1 Frequency

In Region 1, for both oblate and intermediate gyrostats, the $\epsilon = 0$ solution has the form of Eq. (5.7), which involves $\mathrm{sn}^2(u; k)$. Hence the period in u is $2K$, and since $u = \lambda t + u_0$, the period in t is $2K(k)/\lambda$. In Region 2, on the other hand, the period in u is $4K(k)$, but we have defined u as $u = 2\lambda t + u_0$, so that the period in t is also $2K(k)/\lambda$. Recall that λ is defined differently in the two regions.

Now, we define the *angular* phase by

$$\phi = \begin{cases} \frac{u}{2K} & \text{Region 1} \\ \frac{u}{4K} & \text{Region 2} \end{cases} \tag{5.36}$$

Thus in all cases, the frequency of oscillation is

$$\dot{\phi} = \Omega(y, \mu) \triangleq \frac{\lambda}{2K} \tag{5.37}$$

where $\lambda = \lambda(y, \mu)$ and $K = K(k(y, \mu))$ are evaluated according to the location of the slow state in the μy plane.

5.6.2 Phase Differences

We have shown above that there are two different representations of the solution for Region 1, which we call the *primary* and *alternate* representations. As developed above the only difference between the two forms of the solution is the definitions of the parameters β, α^2, and α_1^2, with the primary definitions given at Eqs. (5.8)–(5.10), and the alternate forms given at Eqs. (5.14)–(5.16). The two solutions are equivalent, of course, differing only by a phase shift, similar to the familiar identity $\sin u = \cos(u - \pi/2)$.

To obtain the phase difference between the two solutions, we let $t = u_0 = 0$ in the primary solution, and let $t = 0$ in the alternate solution, then solve for u_0 in the alternate form, by equating the two solutions. In all subregions of Region 1 (including the intermediate case), this leads to

$$\text{sn}^2(u_0; k) = 1 \tag{5.38}$$

which has the solution $u_0 = K$. Thus the primary and alternate solutions in Region 1 differ in phase by K.

It is easy to show in a similar fashion that the $\text{cn}(u; k)$ solution in Region 2 is in phase with the primary form of the $\text{sn}^2(u; k)$ solution in Region 1aiii at the transition curve between the two regions.

5.6.3 The Phase and Frequency of x_1 Compared to those of x_2 and x_3

We find it convenient to use the x_2x_3 phase plane to illustrate some aspects of the dynamics of spinup. It is important to keep in mind, however, that the frequencies we have obtained above are for the x_1 oscillations, and are not directly applicable to x_2 and x_3. To make this clear, in Fig. 5.6, we show the south pole of the $\varepsilon = 0$ momentum sphere projected onto the x_3x_2 plane. This phase portrait is for the case where the south pole is a saddle point, i.e., $\mu_2 < \mu < \mu_3$.
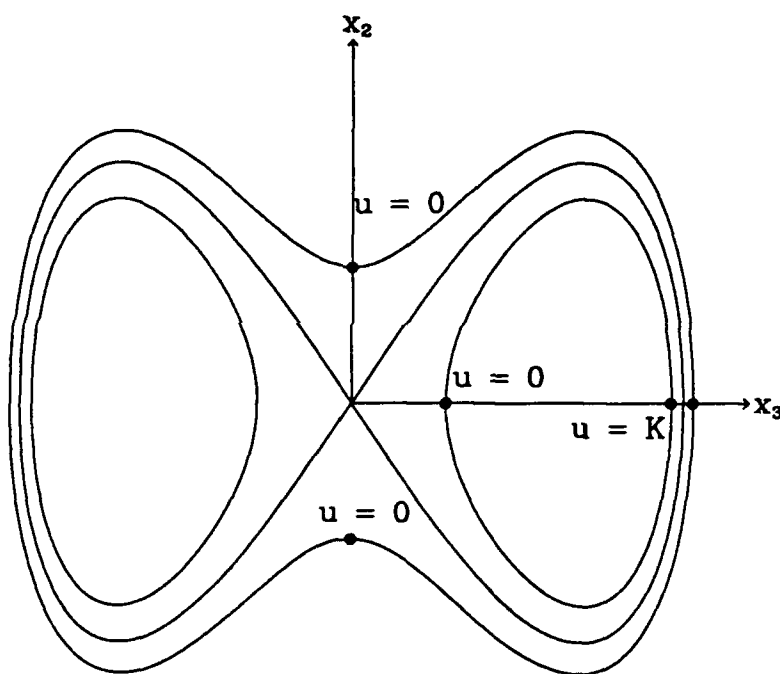
Figure 5.6. Phase of the $\varepsilon = 0$ Solution for $x = x(u; k)$, Shown in the x_3x_2 Plane. The values of u shown correspond to the primary form of the solution. Recall that the angular phase ϕ is related to u by Eq. (5.36). The values for the alternate form are shown below, in Fig. 7.8.

The important thing to note from Fig. 5.6 is that although the trajectories inside the saddle's homoclinic orbit are quite different from those outside the homoclinic orbit, the x_1 oscillations are qualitatively the same.

5.7 Summary

In this chapter we developed the elliptic function solution for for the unperturbed system, by integrating the complete elliptic integral of the first kind developed in Chapter 3. We also identified previously unreported cases with trigonometric solutions. The frequency and phase relationships between the various regions and forms of the solution were discussed in the last section of this chapter. In the following chapter, we apply the method of averaging using the elliptic function solution developed here.

Chapter 6

The Averaged Equations

In this chapter we apply the method of averaging to the reduced differential equations derived in Chapter 3, making use of the $\varepsilon = 0$ solution obtained in Chapter 5. We begin with a brief introduction to the method of averaging, including a standard theorem that both justifies our approach and tells us where to expect problems to arise. In order to use this theorem, we must first transform the reduced equations to a standard form. This is done in Section 6.2. In Section 6.3, we carry out the averaging calculations, obtaining a single first-order non-autonomous differential equation for the flow in the μy plane. The fact that the $\varepsilon = 0$ solution is in terms of elliptic functions means that the averaged equation involves complete elliptic integrals of the first, second, and third kinds. Numerical integration of this equation yields approximate trajectories that are quite accurate in all regions of the μy plane, except when the flow crosses an instantaneous separatrix of the unperturbed system.

As in the developments of the previous chapter, we have found the handbook by Byrd and Friedman [10] indispensable.

6.1 The Method of Averaging

In applying the method of averaging, there are several standard forms which may be used, one of which is the *angular standard form*, developed for example in the texts by Sanders and Verhulst [90] and Murdock [75]. The notation divides the equations into two parts: the *fast* angular variable, and the *slow* state variables:

$$\dot{\phi} = \Omega(\mathbf{r}) + \mathcal{O}(\varepsilon), \qquad \phi \in S^1 \tag{6.1}$$

$$\dot{\mathbf{r}} = \varepsilon \mathbf{f}(\mathbf{r}, \phi) + \mathcal{O}\left(\varepsilon^2\right), \qquad \mathbf{r} \in D \subset \mathbf{R}^n \tag{6.2}$$

where $\mathbf{f}(\mathbf{r}, \phi)$ is periodic in ϕ, and S^1 is a circle of unit length, *i.e.*, $\|S^1\| = 1$. More general forms with $\phi \in T^n$ and $\Omega = \Omega(\mathbf{r}, \phi)$ are also of interest, but here Eqs. (6.1) and (6.2) are sufficient.

A useful form of the theorem we use is found in Theorem 11.4 of Ref. [97], which basically states that solutions to the "averaged" equations

$$\dot{\bar{\phi}} = \Omega(\bar{\mathbf{r}}) \tag{6.3}$$

$$\dot{\bar{\mathbf{r}}} = \varepsilon \bar{\mathbf{f}}(\bar{\mathbf{r}}) \tag{6.4}$$

remain within $\mathcal{O}(\varepsilon)$ of solutions to Eqs. (6.1) and (6.2) for a time of $\mathcal{O}(1/\varepsilon)$. The function $\bar{\mathbf{f}}(\bar{\mathbf{r}})$ is the average of $\mathbf{f}(\mathbf{r}, \phi)$, defined by

$$\bar{\mathbf{f}}(\bar{\mathbf{r}}) = \int_{S^1} \mathbf{f}(\mathbf{r}, \phi) d\phi \tag{6.5}$$

with $\mathbf{r}$ held constant over the integration.

The principal restriction on the applicability of this theorem is that $\Omega(\mathbf{r})$ must be bounded away from zero by a constant independent of ε. The set of points in D where $\Omega(\mathbf{r}) = 0$ is called the *resonance manifold*, for which the usual notation is [90, p. 102]:

$$N = \{\mathbf{r} \in D \subset \mathbf{R}^n | \Omega(\mathbf{r}) = 0\} \tag{6.6}$$

We have more to say regarding the resonance manifold later in this chapter and in Chapter 7.

6.2 Transforming to Standard Form

We now recall the reduced equations developed in Chapter 3:

$$\dot{x} = \pm\sqrt{y_2(x,\mu) - y}\sqrt{y - y_3(x,\mu)} \tag{6.7}$$

$$\dot{y} = -2\varepsilon x \tag{6.8}$$

$$\dot{\mu} = \varepsilon \tag{6.9}$$

In this system, $\mathbf{r} = (y, \mu)$, and since we have shown in the previous chapter that x is a periodic function of t for $\varepsilon = 0$, Eqs. (6.8) and (6.9) are already in the form of Eq. (6.2). It remains to put Eq. (6.7) in the form of Eq. (6.1). Ordinarily, one uses variation of parameters to obtain a differential equation for the phase of the oscillation of x (see, *e.g.*, Ref. [17]). However, the parameters in our $\varepsilon = 0$ solution are very complicated (see Eqs. (5.7)–(5.13)). Therefore, we take a different, but equivalent, approach.

Recall that in Section 5.6.1, we defined the angular phase, ϕ, by

$$\phi \triangleq \begin{cases} \frac{u}{2K} & \text{Region 1} \\[2mm] \frac{u}{4K} & \text{Region 2} \end{cases} \tag{6.10}$$

where $u = \lambda t + u_0$ is the time-like argument of the elliptic functions in the $\varepsilon = 0$ solution, and $K = K(k)$ is the complete elliptic integral of the first kind. For $\varepsilon = 0$, $\dot{\phi}$ is given by Eq. (5.37), which we repeat here:

$$\dot{\phi} = \Omega(y,\mu) = \frac{\lambda}{2K} \tag{6.11}$$

in either of the two regions. Recall that $\lambda = \lambda(y,\mu)$ is defined differently in Regions 1 and 2.

For $\varepsilon \neq 0$, $\dot{\phi}$ is more complicated. We will now argue that, except for the resonance zone,

$$\dot{\phi} = \Omega(y,\mu) + \mathcal{O}(\varepsilon) \tag{6.12}$$

where $\Omega(y,\mu) = \lambda/(2K)$.

We begin by differentiating Eq. (6.10) with respect to time:

$$\dot{\phi} = \frac{d}{dt}\left(\frac{u}{2K}\right) = \frac{d}{dt}\left(\frac{\lambda t + u_0}{2K}\right) \tag{6.13}$$

$$= \frac{\lambda}{2K} + \frac{\dot{\lambda}t + \dot{u}_0}{2K} - \frac{2u\dot{K}}{4K^2} \tag{6.14}$$

$$= \Omega(y,\mu) + \left\{\frac{\dot{\lambda}t + \dot{u}_0}{2K} - \frac{2u\dot{K}}{4K^2}\right\} \tag{6.15}$$

Since the terms whose derivatives appear in the bracket depend only on μ and y, the bracketed term is formally of $\mathcal{O}(\varepsilon)$. However, in a neighborhood of the resonance manifold, we encounter the following special difficulties:

- $\dot{\lambda} \to \infty$ at the two points of pitchfork bifurcation, $\mathbf{P}_{\mu_2}$ and $\mathbf{P}_{\mu_3}$.

- $\dot{K} \to \infty$ faster than $K^2 \to \infty$ at the resonance manifold.

First we show that $\dot{\lambda} = \mathcal{O}(\varepsilon)$, almost everywhere in the μy plane. Recall that, from Eq. (5.13), in Region 1 for oblate gyrostats, $\lambda = \frac{1}{2}\sqrt{i_2 i_3(a-c)(b-d)}$. Thus

$$\dot{\lambda} = \frac{\partial\lambda}{\partial a}\dot{a} + \frac{\partial\lambda}{\partial b}\dot{b} + \frac{\partial\lambda}{\partial c}\dot{c} + \frac{\partial\lambda}{\partial d}\dot{d} \tag{6.16}$$

We start by showing that $\partial\lambda/\partial a$ is bounded almost everywhere, and that $\dot{a} = \mathcal{O}(\varepsilon)$. From the expression for λ above, we have

$$\frac{\partial\lambda}{\partial a} = \frac{i_2 i_3(b-d)}{4\sqrt{i_2 i_3(a-c)(b-d)}} \tag{6.17}$$

whose denominator only vanishes if $a = c$ or $b = d$. The first of these conditions only holds exactly at the bifurcation point $\mathbf{P}_{\mu_3}$, and the second only holds at the bifurcation point $\mathbf{P}_{\mu_2}$. Thus $\partial\lambda/\partial a$ is bounded everywhere except at these two points (see Fig. 4.7).

We now compute $\dot{a}$:

$$\dot{a} = \frac{\partial a}{\partial\mu}\dot{\mu} + \frac{\partial a}{\partial y}\dot{y} \tag{6.18}$$

$$= \varepsilon\left(\frac{\partial a}{\partial\mu} - 2x\frac{\partial a}{\partial y}\right) \tag{6.19}$$

$$= \frac{\varepsilon}{i_3}\left(1 + \frac{i_3 x - \mu}{\sqrt{\mu^2 + i_3(i_3 + y)}}\right) \tag{6.20}$$

where we have used $a = r_2^- = \left(\mu - \sqrt{\mu^2 + i_3(i_3 + y)}\right)/i_3$, which is true everywhere in the μy plane (for $\mu \geq 0$). From Eq. (6.20), $\dot{a} = \mathcal{O}(\varepsilon)$ as long as $\sqrt{\mu^2 + i_3(i_3 + y)} \neq 0$. This term vanishes along the curve $y = -(\mu^2/i_3 + i_3)$ (which is $\mathbf{F}_\mu$ in the μy plane), but this corresponds to $a = \mu/i_3$, which implies $\dot{a} = \dot{\mu}/i_3 = \varepsilon/i_3$. Thus $\dot{a} = \mathcal{O}(\varepsilon)$ everywhere in the μy plane.

The same type of calculations show that the rest of the terms in Eq. (6.16) are also $\mathcal{O}(\varepsilon)$, except at the two bifurcation points $\mathbf{P}_{\mu 2}$ and $\mathbf{P}_{\mu 3}$. Thus we conclude that $\dot{\lambda} = \mathcal{O}(\varepsilon)$ everywhere in Region 1 of the μy plane for oblate gyrostats, except for the two bifurcation points. The proofs for Region 2 and Region 1c for intermediate gyrostats are similar and are omitted.

We now show that

$$\lim_{k^2 \to 1} \frac{\dot{K}}{K^2} = \infty \tag{6.21}$$

To show this, we begin with $\dot{K}$, which by the chain rule, is

$$\dot{K} = \frac{dK}{dk^2} \frac{dk^2}{dt} \tag{6.22}$$

We can show that $dk^2/dt = \mathcal{O}(\varepsilon)$ almost everywhere, using the same procedure as was used for $\dot{\lambda}$ above, with the exceptional points again being $\mathbf{P}_{\mu 2}$ and $\mathbf{P}_{\mu 3}$. Since the calculations are similar, we omit the details, and continue with dK/dk^2, which evaluates to

$$\frac{dK}{dk^2} = \frac{E - k'^2 K}{2k^2 k'^2} \tag{6.23}$$

where we have used Eq. 710.00 of Ref. [10]. The *complimentary modulus*, k' is defined by $k'^2 = 1 - k^2$.

Because $E = E(k)$ is bounded $\forall k$, it is clear that the derivative in Eq. (6.23) is bounded everywhere except *possibly* at the limits $k^2 = 0$ and $k^2 = 1$. For the $k^2 = 0$ limit, we make use of Eq. 112.02 of Ref. [10], and obtain

$$\lim_{k^2 \to 0} \frac{dK}{dk^2} = \frac{\pi}{8} \tag{6.24}$$

Hence

$$\lim_{k^2 \to 0} \frac{dK}{K^2 dk^2} = \frac{1}{2\pi} \qquad (6.25)$$

since $K(0) = \pi/2$.

From Fig. 5.1(d), it is evident that $\lim_{k^2 \to 1} dK/dk^2 = \infty$; however, it is not obvious that dK/dk^2 diverges faster than K^2. So we must show that

$$\lim_{k^2 \to 1} \frac{1}{K^2} \frac{dK}{dk^2} = \infty \qquad (6.26)$$

Using Eq. (6.23), we may write

$$\frac{1}{K^2} \frac{dK}{dk^2} = \frac{E - k'^2 K}{2k^2 k'^2 K^2} \qquad (6.27)$$

$$= \frac{E}{2k^2} \left\{ \frac{1}{k'^2 K^2} \right\} - \frac{1}{2} \left\{ \frac{1}{k^2 K^2} \right\} \qquad (6.28)$$

As $k^2 \to 1$ the second bracket tends to zero, and the multiplying factor outside the first bracket tends to $\frac{1}{2}$. Recalling that $k'^2 = 1 - k^2$, the remaining indeterminate form in the first bracket is

$$\frac{1}{k'^2 K^2} = \frac{(k')^{-2}}{K^2} \to \frac{\infty}{\infty} \quad \text{as} \quad k'^2 \to 0 \qquad (6.29)$$

Making use of the limit

$$\lim_{k^2 \to 1} \left(K(k) - \ln \frac{4}{k'} \right) = 0 \qquad (6.30)$$

which is given at Eq. 112.01 of Ref. [10], two applications of L'Hôpital's rule give

$$\lim_{k'^2 \to 0} \frac{(k')^{-2}}{\left(\ln \frac{4}{k'} \right)^2} = \lim_{k'^2 \to 0} \frac{(k')^{-2}}{\ln \frac{4}{k'}} = \lim_{k'^2 \to 0} \frac{2(k')^{-2}}{1} = \infty \qquad (6.31)$$

Thus, $(dK/dk^2)/K^2$ is unbounded for points in the resonance manifold.

Finally, we note that the phase shift, u_0, is slowly varying. While we have not shown that $\dot{u}_0 = \mathcal{O}(\varepsilon)$, this fact follows from the definition of u_0. For Region 1a, the definition for u_0 is given by Eqs. (C.4) and (C.12) in Appendix C. Since u_0 depends on the roots of $W(x)$, its derivative with respect to time is $\mathcal{O}(\varepsilon)$. From now on, we assume that Eq. (6.12) is valid except in the resonance manifold.

Now, in first-order averaging, we work to $\mathcal{O}(\varepsilon)$ in the slow equations, and to $\mathcal{O}(1)$ in the fast equation, as noted in Section 6.1. To this end, we truncate Eq. (6.12) at $\mathcal{O}(1)$, which is justified by the theorem quoted in Section 6.1. Thus the three governing equations may be written in angular standard form (cf. Eqs. (6.1) and (6.2)) as

$$\dot{\phi} = \Omega(y, \mu) \tag{6.32}$$

$$\dot{y} = -2\varepsilon x \tag{6.33}$$

$$\dot{\mu} = \varepsilon \tag{6.34}$$

where

$$\Omega(y, \mu) = \lambda/(2K) \tag{6.35}$$

and x depends on ϕ, y, and μ according to Eqs. (5.7) and (6.10). Note well that Eqs.(6.32)–(6.34) are approximate due to the truncation in $\dot{\phi}$; *i.e.*, Eq. (6.32) is only valid to $\mathcal{O}(1)$. Also note that the equations are not expected to be valid near the resonance manifold.

We apply the method of averaging to Eqs. (6.32)–(6.34). As noted in Section 6.1, the averaging theorem is not applicable when $\Omega(\mathbf{r}) = 0$. It is now clear, at least mathematically, why the separatrix crossings cause difficulty: the crossings correspond to $K = \infty$, and since λ is bounded, Eq. (6.35) implies $\Omega = 0$ at the separatrices. That is to say, the separatrices correspond to the resonance manifold. Also, from Eq. (6.10), ϕ is undefined at the separatrix crossings. Moreover, the basic notion of averaging, that of replacing the vector field by its average taken over one period of the unperturbed system, is expected to be problematic at the separatrices, where the unperturbed period $\rightarrow \infty$, and hence averaging over one period loses its intuitive appeal. We address these difficulties in more detail below and in Chapter 7.

6.3 The Slow Flow

The principle aim of the method of averaging is to "average out" the fast phase and investigate the dynamics of the slow states. In this section we obtain a single first-order differential equation describing the flow in the μy plane. To do this, we replace the right hand sides of $\dot{y}$ and $\dot{\mu}$ by their averages over one period in ϕ. Thus, the averaged equations are

$$\dot{\phi} = \Omega(\bar{y}, \mu) \tag{6.36}$$

$$\dot{\bar{y}} = -2\varepsilon\bar{x} \tag{6.37}$$

$$\dot{\mu} = \varepsilon \tag{6.38}$$

where $\bar{x}$ is the average value of $x(\phi, y, \mu)$ over one period in ϕ.

Eliminating t from Eqs. (6.37) and (6.38), and using ( )$'$ for $d(\,)/d\mu$, we obtain

$$\bar{y}' = -2\bar{x} \tag{6.39}$$

where the form of $\bar{x} = \bar{x}(y, \mu)$ depends on the region in the μy plane as we show below. This is a single first-order equation for the slow flow. We denote solutions to this equation by $\bar{y} = \bar{y}(\mu; y_0, \mu_0)$, where y_0 and μ_0 are the initial values of y and μ.

Although we have adopted ϕ as the angular variable, we find it convenient to compute $\bar{x}$ by integrating over one period in u, which is of course equivalent to integrating over one period in ϕ. The average of $x(u; k)$ over one period in u is defined by

$$\bar{x} = \frac{1}{4K} \int_0^{4K} x(u; k)\, du \tag{6.40}$$

where $K = K(k)$ is the complete elliptic integral of the first kind, and is the quarter period of both $\mathrm{sn}(u; k)$ and $\mathrm{cn}(u; k)$. While evaluating the integral in Eq. (6.40) we hold both y and μ fixed, since they are constant in the unperturbed system.

6.3.1 Oblate Gyrostats

The form of $\bar{x} = \bar{x}(y, \mu)$ depends on the region in the μy plane, just as the $\epsilon = 0$ solution does. In this section we obtain $\bar{x}$ for oblate gyrostats, where the μy plane is divided into regions as in Fig. 5.4.

Region 1

In Region 1, $x(u; k)$ is given by Eq. (5.7), which involves $\text{sn}^2(u; k)$, so that the period in u is $2K$ instead of $4K$. Furthermore, $\text{sn}^2(u; k)$ is symmetric about $u = K$, so we may use as the average of x the integral

$$\bar{x} = \frac{1}{K} \int_0^K x(u; k)\, du = \frac{\beta}{K} \int_0^K \left\{ \frac{1 - \alpha_1^2 \text{sn}^2(u; k)}{1 - \alpha^2 \text{sn}^2(u; k)} \right\} du \tag{6.41}$$

The integral in Eq. (6.41) is a complete elliptic integral of the third kind. The symbol α^2 which appears in the denominator is known as the *parameter*, and throughout Region 1, one can use Eqs. (5.9) and (5.11) to verify that $0 < k^2 < \alpha^2 < 1$. Referring to Eq. 412.06 of Ref. [10], this integral evaluates to

$$\bar{x} = \frac{\beta}{K} \left\{ K + \frac{\pi(\alpha^2 - \alpha_1^2)[1 - \Lambda_0(\psi, k)]}{2\sqrt{\alpha^2(1 - \alpha^2)(\alpha^2 - k^2)}} \right\} \tag{6.42}$$

where $\psi = \sin^{-1}\sqrt{(1 - \alpha^2)/(1 - k^2)}$. $\Lambda_0(\psi, k)$ is Heuman's Lambda function and involves complete and incomplete elliptic integrals of the first and second kinds (cf. Eq. 150.03 in Ref. [10]):

$$\Lambda_0(\psi, k) = \frac{2}{\pi} \left\{ EF(\psi, k') + KE(\psi, k') - KF(\psi, k') \right\} \tag{6.43}$$

where $K = K(k)$ and $E = E(k)$ are the complete elliptic integrals of the first and second kinds, respectively, $F(\psi, k')$ is the incomplete elliptic integral of the first kind, and $E(\psi, k')$ is the incomplete elliptic integral of the second kind. The *complimentary modulus*, k', is defined by $k'^2 = 1 - k^2$. The other symbols in Eq. (6.42) are defined in Eqs. (5.8)–(5.13).

Remark 8 *The complimentary modulus leads naturally to the complimentary complete elliptic integrals of the first and second kinds:* $K' = K(k')$, *and* $E' = $

$E(k')$. *We will not need these integrals, so throughout this thesis, we will use K for $K(k)$, and E for $E(k)$.*

Region 2

In Region 2, $x(u;k)$ is given by Eq. (5.18) which has period $4K(k)$, so Eq. (6.40) becomes

$$\bar{x} = \frac{\beta}{4K} \int_0^{4K} \left\{ \frac{1 + \alpha_1 \text{cn}(u;k)}{1 + \alpha \text{cn}(u;k)} \right\} du \tag{6.44}$$

This integral may be evaluated using Eq. 361.62 of Ref. [10]:

$$\int \left\{ \frac{1 + \alpha_1 \text{cn}(u;k)}{1 + \alpha \text{cn}(u;k)} \right\} du = \frac{1}{\alpha} \left\{ \alpha_1 u + \frac{\alpha - \alpha_1}{1 - \alpha^2} \left[\Pi(\varphi, \hat{\alpha}^2, k) - \alpha f_1 \right] \right\} \tag{6.45}$$

where $\varphi = \text{am}(u;k)$, $\hat{\alpha}^2 = \alpha^2/(\alpha^2 - 1)$, and f_1 is given at Eq. 361.54 of Ref. [10] and depends on whether $\hat{\alpha}^2$ is less than, greater than, or equal to k^2. Referring to Eq. (5.20), the fact that $A > B > 0$ implies that $\alpha < 1$, hence $\hat{\alpha}^2 < 0 < k^2$. Thus

$$f_1 = \sqrt{\frac{1 - \alpha^2}{k^2 + k'^2\alpha^2}} \tan^{-1} \left[\sqrt{\frac{k^2 + k'^2\alpha^2}{1 - \alpha^2}} \, \text{sd}(u;k) \right] \tag{6.46}$$

where $\text{sd}(u;k) = \text{sn}(u;k)/\text{dn}(u;k)$.

The indefinite integral in Eq. (6.45) must be evaluated at $u = 0$ and $u = 4K$. First we dispense with f_1: $\text{sd}(0;k) = \text{sd}(4K;k) = 0$, and $\tan^{-1}(0) = 0$, hence $f_1|_0^{4K} = 0$. The next detail to address is the value of $\varphi = \text{am}(u;k)$ at the limits of integration: $\text{am}(0;k) = 0$ and $\text{am}(4K;k) = 2\pi$. Furthermore, $\Pi(0, \cdot, \cdot) = 0$, and $\Pi(2\pi, \cdot, \cdot) = 4\Pi(\pi/2, \cdot, \cdot)$.

Thus we arrive at the average value of $x(u;k)$ in Region 2:

$$\bar{x} = \frac{\beta}{\alpha K} \left\{ \alpha_1 K + \frac{\alpha - \alpha_1}{1 - \alpha^2} \Pi(\hat{\alpha}^2, k) \right\} \tag{6.47}$$

where $\Pi(\hat{\alpha}^2, k)$ is the normal complete elliptic integral of the third kind with *parameter* $\hat{\alpha}^2 = \alpha^2/(\alpha^2 - 1) < 0$.

6.3.2 Intermediate Gyrostats

For intermediate gyrostats, the $\varepsilon = 0$ solution is given at Eqs. (5.26)–(5.32), and is of almost the same form as for Region 1 of oblate gyrostats. However, with Eqs. (5.28) and (5.30), one may show that the *parameter*, α^2, has a different range: $0 < \alpha^2 < k^2 < 1$. Thus Eq. 414.06 of Ref. [10] applies, giving

$$\bar{x} = \frac{\beta}{K} \left\{ K + \frac{(\alpha^2 - \alpha_1^2)KZ(\psi, k)}{\sqrt{\alpha^2(1 - \alpha^2)(k^2 - \alpha^2)}} \right\} \tag{6.48}$$

where $Z(\psi, k)$ is Jacobi's Zeta function (cf. Eq. 140.01 in Ref. [10]):

$$KZ(\psi, k) = KE(\psi, k) - EF(\psi, k) \tag{6.49}$$

with argument $\psi = \sin^{-1}(\alpha/k)$. Recall that $K = K(k)$, $E = E(k)$, and that the rest of the parameters are defined at Eqs. (5.27)–(5.32).

This form for $\bar{x}$ holds in all three regions, the difference being the ordering of the roots as given in Table 5.4.

6.3.3 Evaluating the Slow Flow for Spinup Trajectories

The simple form of the averaged equation, Eq. (6.39), is misleading. Recall from Chapter 5 that each of the parameters α^2, α_1^2, β, and k^2 depends on the roots of the gyroscopic function, which in turn depend on both y and μ, as well as the inertia parameters i_2 and i_3. Then $\bar{x}$ depends on these parameters through Eqs. (6.42), (6.47), or (6.48), which involve elliptic integrals of the first, second, and third kinds. Thus $\bar{x}(y, \mu)$, depends in a complicated way on both y and μ, and on the inertia parameters i_2 and i_3.

Given the complexity of $\bar{x}(y, \mu)$, it appears unlikely that an analytic solution to Eq. (6.39) will be found. Furthermore, Eq. (6.39) is nonautonomous, so there are no fixed points in the μy plane. There are, however, special solutions to Eq. (6.39) which may be used in a further perturbation analysis. This possibility is explored in Chapter 8. In this chapter, we discuss only numerical results.

Equation (6.39) may be numerically integrated for given initial values of μ and y, generating a trajectory in the μy plane. The right-hand side of the equation changes form as the trajectory passes through the different regions of the plane. In the following paragraphs we give the details for the different spinup problems, three of which involve *separatrix crossings*. In the next section, we discuss the separatrix crossings.

Oblate Spinup

For oblate spinup, trajectories lie entirely in Region 1ai (see Fig. 4.10). Thus $\bar{x}$ is given by Eq. (6.42), with the various parameters defined under "Region 1a" at Eqs. (5.8)–(5.11), and the roots ordered as given in Table 5.2.

Prolate Spinup

Referring to prolate spinup as represented in Fig. 4.12 (see also the xy planes in Fig. 4.5), we see that trajectories begin in Region 1b, cross the separatrix into Region 2, cross again into Region 1aii, and then finally pass into Region 1ai. This is shown schematically in Fig. 6.1. Recall that trajectories cannot pass out of Region 1ai for the reasons depicted in Fig. 4.8. Thus there are four "legs" to the prolate spinup trajectory.

1. Region 1b: $\bar{x}$ is given by Eq. (6.42), with parameters defined under "Region 1b" at Eqs. (5.8)–(5.11).

2. Region 2: $\bar{x}$ given by Eq. (6.47), with parameters defined at Eqs. (5.19)–(5.22).

3. Region 1aii: $\bar{x}$ is given by Eq. (6.42), with parameters defined under "Region 1a" at Eqs. (5.8)–(5.11).

4. Region 1ai: same as for Region 1aii.

Of course, the ordering of the roots changes between the regions also, as given in Table 5.2.
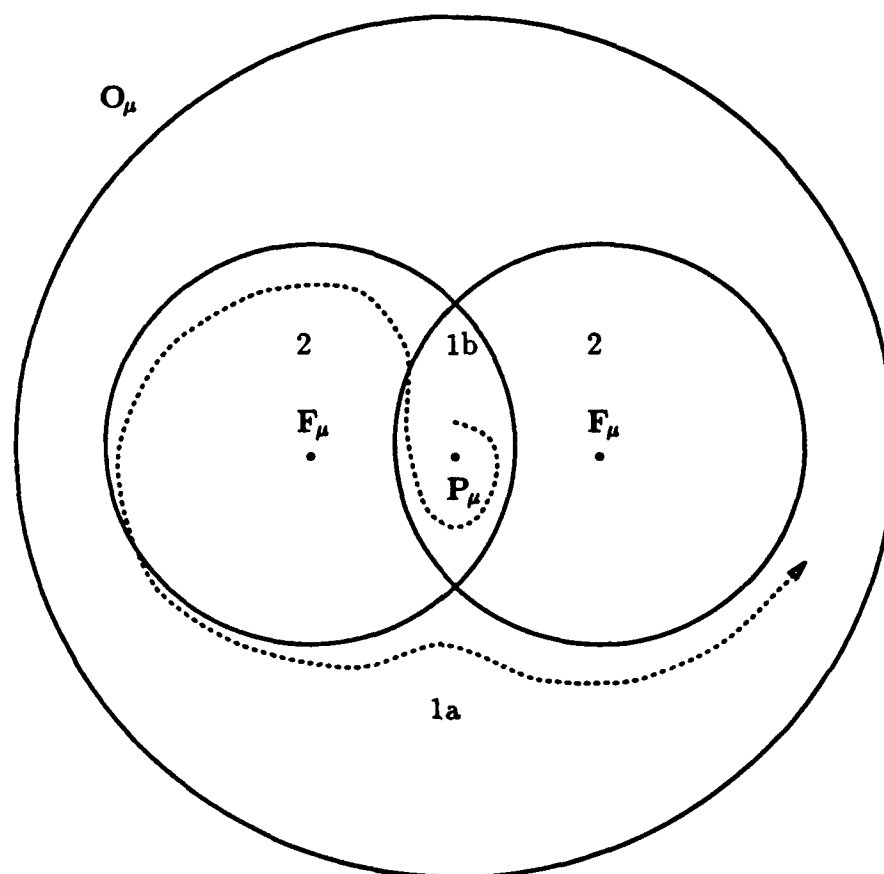
Figure 6.1. Schematic of Prolate Spinup. The trajectory starts near the south pole of the momentum sphere, then crosses an instantaneous separatrix into Region 2, then crosses out of Region 2 into Region 1ai. Compare with Figs. 4.3, 4.5 and 4.12. The numbers correspond to the regions in the μy plane in Fig. 5.4.

We note that all the transitions are smooth in the sense that the two forms for $\bar{x}$ are equal along the curves separating the regions. The transitions from Region 1b to Region 2 and from Region 2 to Region 1aii, however, correspond to separatrix crossings, whereas the transition from Region 1aii to Region 1ai does not. Recall that for $\varepsilon = 0$, the curve separating Region 1aii from Region 1ai corresponds to a trigonometric solution for $x(t)$.

Flat Spin Recovery

A flat spin recovery trajectory passes through Regions 2, 1aiii, and 1ai, in that order (see Fig. 4.13). Thus there are three legs to flat spin recovery:

1. Region 2: $\bar{x}$ is given by Eq. (6.47), with parameters defined at Eqs. (5.19)–(5.22).

2. Region 1aiii: $\bar{x}$ is given by Eq. (6.42), with parameters defined under "Region 1a" at Eqs. (5.8)–(5.11).

3. Region 1ai: same as for Region 1aiii.

The first transition, from Region 1 to Region 1aiii, presents no difficulty, as there is no separatrix crossing involved. However, the second transition, from Region 1aiii to Region 1ai, represents a separatrix crossing.

Intermediate Spinup

Intermediate spinup trajectories are relatively simple compared with those for prolate spinup and flat spin recovery, since there are only two possibilities as shown in Fig. 4.20. Either a trajectory starts in Region 1cii and passes into Region 1ci (with a separatrix crossing), or it starts in Region 1ciii and passes into Region 1ci (also with a separatrix crossing). It is also possible for an initial condition to lie inside Region 1ci, in which case the trajectory remains in Region 1ci.

6.3.4 The Separatrix Crossings

As we have noted in the previous section, three of the four cases involve separatrix crossings, a subject which is of current research interest. Technically, the averaged equation, Eq. (6.39), is not valid in the vicinity of the separatrix, as discussed in Section 6.2. In this chapter, following Copolla and Rand [17], we

use an *instantaneous separatrix crossing*, that is, we assume the flow crosses the instantaneous separatrix instantaneously.

For example, in Region 1aiii for flat spin recovery, we integrate the averaged equation using the correct form of $\bar{x}$ for that region, checking at each time step to see whether the flow has entered Region 1ai. Once the flow enters Region 1ai, we switch to the appropriate form of $\bar{x}$, which in this case is simply a matter of reordering the roots of the gyroscopic function. As we show below, this method results in significant error for some initial conditions.

6.3.5 The Average Cone Angle

Recall that in the dimensionless variables, the cone angle is $\eta = \cos^{-1} x$. For given y and μ, we define the *average* cone angle as

$$\bar{\eta} = \cos^{-1} \bar{x} \tag{6.50}$$

Thus for a specific rotor momentum μ and energy level y, Eq. (6.42), (6.47), or (5.26) may be used with Eq. (6.50) to compute the average cone angle.

In closing this section, we point out that although complicated in appearance, the elliptic integrals involved in $\bar{x}$ are easily computed using a subroutine library such as that given in Ref. [83].

6.4 Comparisons of Exact *vs.* Averaged Trajectories

In this section, we compare trajectories computed as discussed in Section 6.3.3 with "exact" solutions. The exact solutions are obtained by numerically integrating Eqs. (3.25)–(3.28), then computing y by Eq. (3.56). In some cases, the exact and approximate curves are indistinguishable when plotted in the μy plane, so we use the percent relative error, defined as

$$e_r = 100 \left(\frac{y - \bar{y}}{y} \right) \tag{6.51}$$

where y is the "exact" value and $\bar{y}$ is the solution to the averaged equation. In Fig. 6.2, we show e_r *vs.* μ for the various spinup problems. We only give one example for each spinup problem so that the figures are clear; however, these are representative, and we give further evidence of their validity below.

Note that for oblate spinup (Fig. 6.2(a)), the error e_r is much smaller in comparison with the values of ε used than in the other three cases. This is true for a number of reasons. First, oblate spinup does not involve a separatrix crossing. However, this alone is not enough to account for the small error, since the oblate spinup error is smaller than the other cases *before* the separatrix crossings. Also note that in the other spinup problems, the magnitude of the *oscillation* of the relative error decreases once the trajectory passes into Region 1ai (or Region 1ci for the intermediate case). Thus it appears the averaged equation is simply more accurate in Region 1ai(1ci), without considering the separatrix crossing issue. The reason for this interesting result is that $\bar{x}$ is nearly constant in this region, which is in agreement with our observation in Section 4.5 that oblate spinup trajectories are nearly straight lines in the μy plane (since $dy/d\mu = -2x$).

Since $\bar{x}$ plays such an important role, we also plot $\bar{x}$ and x against μ in Fig. 6.3, where $\bar{x}$ is computed as a by-product of integrating the averaged equation, and x is obtained by numerical integration of the dimensionless equations. Note that $\bar{x}$ is nearly constant after the separatrix crossings, and that the oscillations of x decrease in amplitude and increase in frequency. It is easy to verify that as μ increases in Region 1ai, the modulus k^2 tends to zero, while the $\mathcal{O}(1)$ frequency, Ω, tends to ∞, which accounts for the increase in frequency.

As we discussed in Section 4.5.5, the initial phase does affect the dynamics in the unaveraged system, especially for those spinup problems which cross the separatrices of the unperturbed system. In Fig. 6.4, we show this effect for all four spinup problems. The plots were constructed by choosing a specific initial polhode (*i.e.*, specific (μ, y)) and using points on the initial polhode as initial conditions
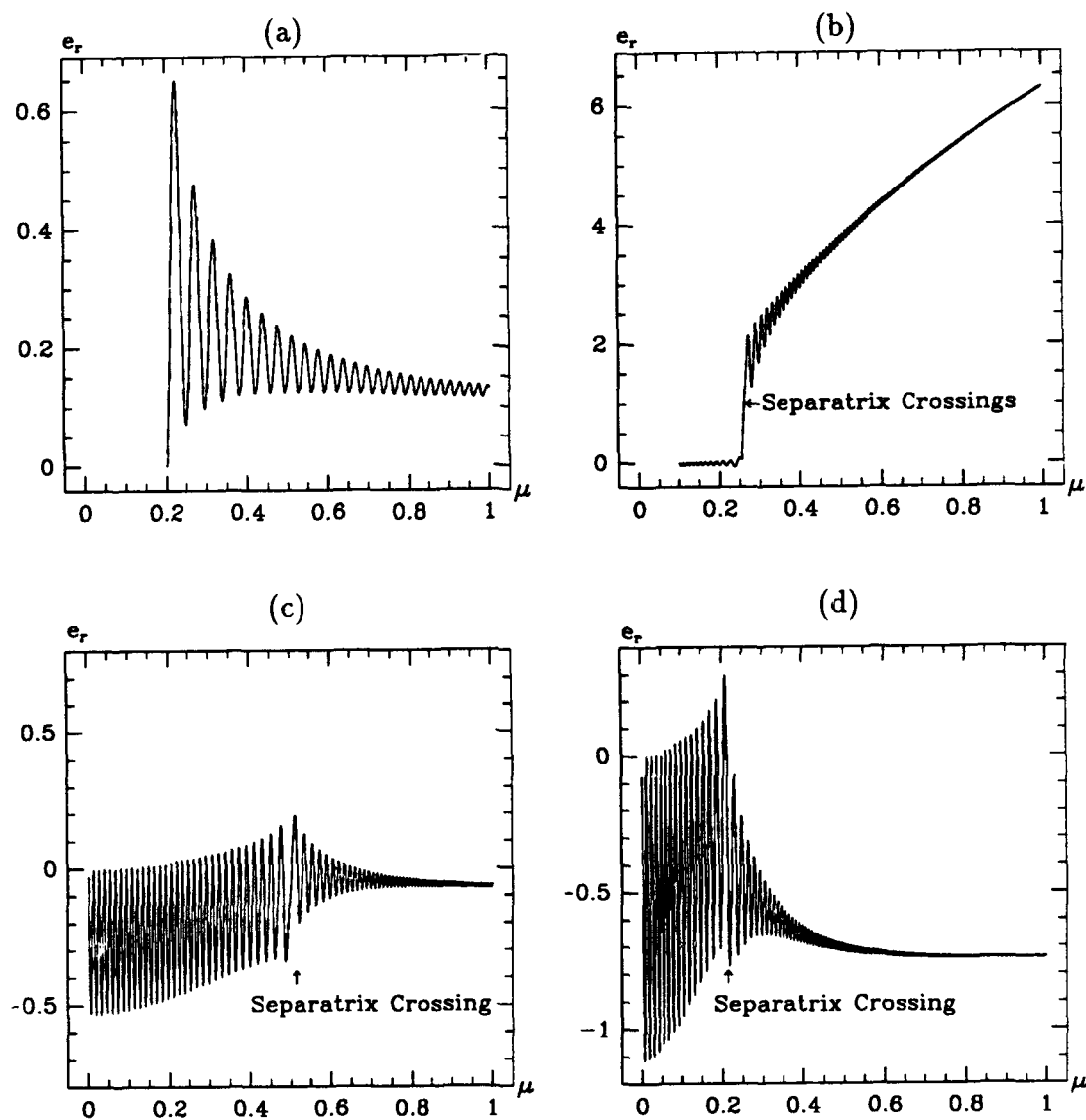
Figure 6.2. Percent Relative Error for the Different Spinup Problems. Different values of ε were used to obtain reasonable errors. For oblate spinup (a), $\varepsilon = 0.01$, while for prolate spinup (b), $\varepsilon = 0.0001$. For both flat spin recovery (c) and intermediate spinup (d), $\varepsilon = 0.001$. The inertia parameters in (a)–(c) are $(i_2, i_3) = (-0.3, -0.7)$. In (d) they are $(i_2, i_3) = (0.7, -0.3)$.
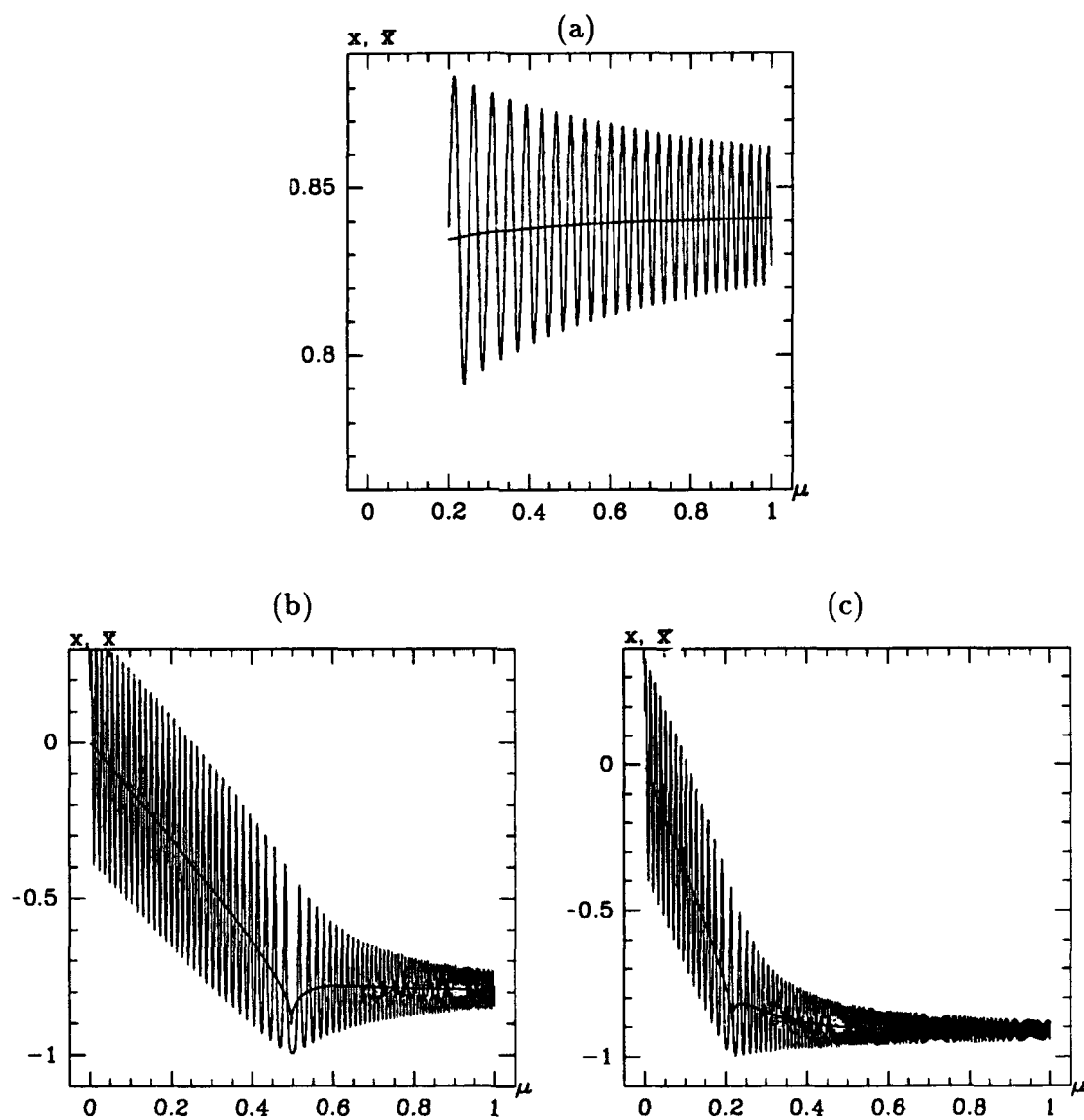
Figure 6.3. x and $\bar{x}$ *vs.* μ for the Different Spinup Problems. (a) Oblate spinup. (b) Flat spin recovery. (c) Intermediate spinup. Prolate spinup is not shown, because for the small value of ε used (0.0001), the frequency of oscillation in the μx plane is too large to obtain a nice plot.

for the full unaveraged equations. The final value of the energy y, denoted as y_f, is defined as the value of y when $\mu = 1$. The final value of $\bar{y}$, denoted $\bar{y}_f$, is defined similarly, and obtained by integrating the averaged equation for the slow flow, up to $\mu = 1$.

In the plots in Fig. 6.4, we have made the "ticks" on the vertical axis proportional to the ε used for each problem. Thus it is clear that for oblate spinup the averaged equation is very close to the exact trajectory, whereas for prolate spinup, the diffusion associated with the two separatrix crossings is significant. For the flat spin recovery and intermediate spinup problems, the accuracy of the averaged equation is fair except for some initial phases which lead to $|y_f - \bar{y}_f| > \mathcal{O}(\varepsilon)$.

6.5 The Phase Equation and Reconstruction of the Angular Momentum

Thus far, we have only compared the averaged energy $\bar{y}$ to the exact energy y. In this section, we also integrate Eq. (6.36) for $\dot{\bar{\phi}}$ and use $\bar{\phi}$, $\bar{y}$, and μ to "reconstruct" $x(t)$. It is important to note that we only need to integrate the averaged equations, Eqs. (6.36)–(6.38), *once* to obtain an approximate solution for *all* initial conditions on a given polhode. After numerically integrating the slow equation, (6.39), $\bar{y}(t)$ and $\mu(t)$ are easily obtained, since $\mu = \mu_0 + \varepsilon t$. We then express $\Omega(\bar{y}, \mu)$ as $\Omega(t)$, and integrate the fast equation for $\bar{\phi}$, Eq. (6.36), *i.e.*,

$$\bar{\phi}(t) = \phi_0 + \int_0^t \Omega(\tau) d\tau \qquad (6.52)$$

where the initial phase ϕ_0 appears only as the constant of integration.

Now, given an averaged flow as $(\bar{\phi}(t), \bar{y}(t), \mu(t))$, reconstructing the flow in terms of $x(t)$ is simply a matter of ᵠ ᵠg the form of $x(t)$ in the unperturbed system, with the parameters allowed to vary as $\bar{y}$ and μ evolve. This is the usual approach when variation of parameters is used. Although we did not formally use
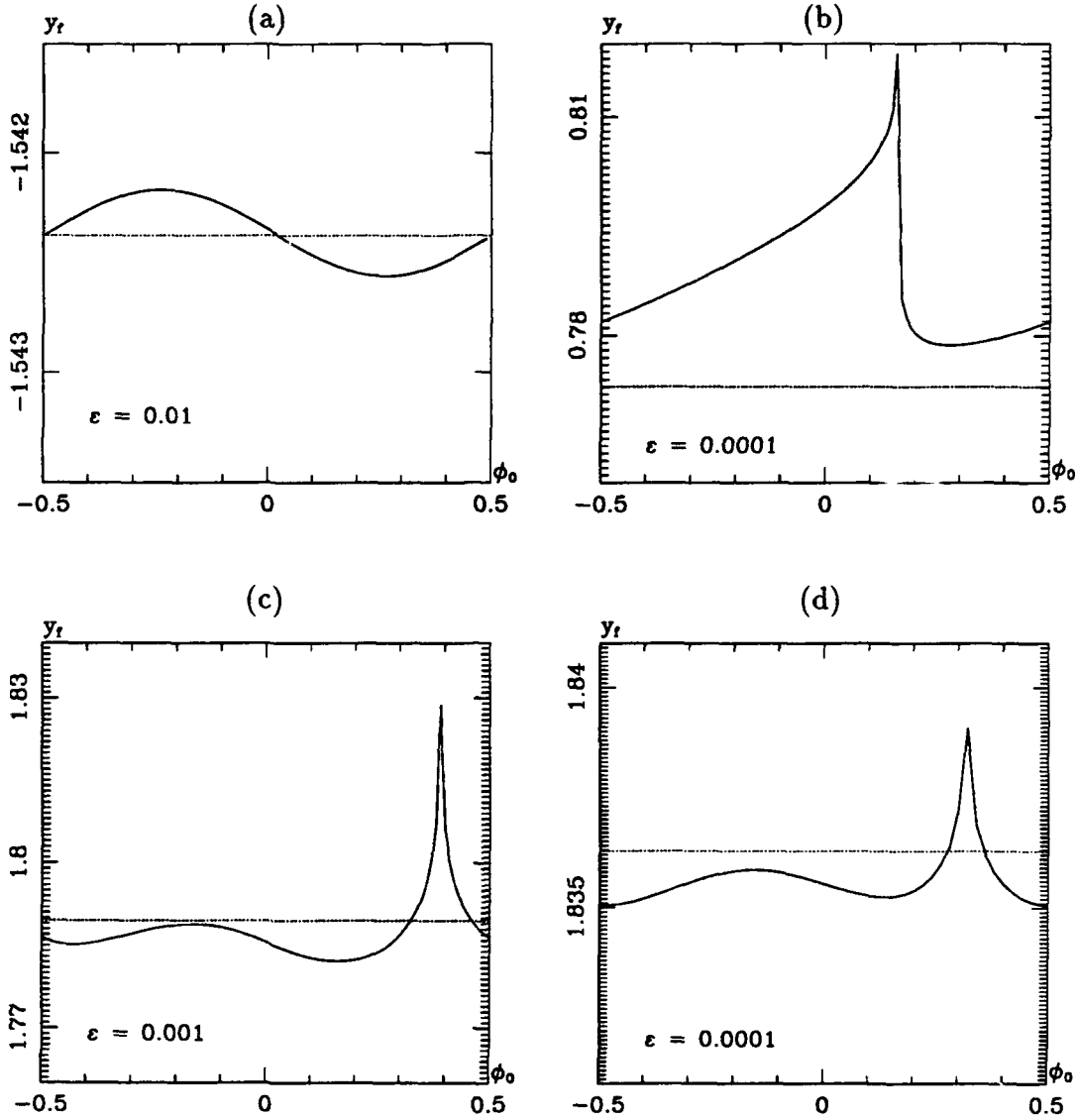
Figure 6.4. Effect of Initial Phase on Accuracy of Averaged Equations. In each plot the final energy y_f is plotted against initial phase ϕ_0. The dotted lines represent the final value of $\bar{y}_f$, the averaged energy. The tick marks are proportional to the value of ε used in the unaveraged equations. (a) Oblate spinup with $\varepsilon = 0.01$. The vertical ticks are spaced by $\varepsilon/10$. Thus the error is $\ll \varepsilon$. (b) Prolate spinup with $\varepsilon = 0.0001$. The vertical ticks are spaced by 100ε. The error is $\gg \varepsilon$ due to the two separatrix crossings. (c) Flat spin recovery with $\varepsilon = 0.001$. The vertical ticks are spaced by ε. The error is $\mathcal{O}(\varepsilon)$ except for the small set of initial conditions which result in the "spike." This spike is bounded above by $y_f = 2$, since $\mu_f = 1$, and $y \leq 2\mu$. (d) Intermediate spinup with $\varepsilon = 0.0001$ and tick spacing of 10ε. Similar comments as for flat spin recovery are applicable.

variation of parameters, our approximate unaveraged system, Eqs. (6.36)–(6.38), is equivalent to what would be obtained with that method.

We denote the reconstructed approximate $x(t)$ as $x_a(t)$, or $x_a(u; k)$. For each point in the averaged flow, $(\bar{\phi}, \bar{y}, \mu) = (\bar{\phi}(\hat{t}), \bar{y}(\hat{t}), \mu(\hat{t}))$, one performs the following steps:

1. Determine which region of the μy plane the point $(\mu, \bar{y})$ is in, using Table 5.2 and Fig. 5.4.

2. Compute the roots of the gyroscopic function according to Table 5.2.

3. If $(\mu, \bar{y})$ is in Region 1, compute the parameters α^2, α_1^2, β, k^2, and λ, according to Eqs. (5.8)–(5.13).

    If $(\mu, \bar{y})$ is in Region 2, compute the parameters α, α_1, β, k^2, and λ, according to Eqs. (5.19)–(5.24).

4. Compute $K = K(k)$ and use it to obtain the argument of the elliptic function: $u = 2K\bar{\phi}$ for Region 1, or $u = 4K\bar{\phi}$ for Region 2.

5. Compute $\text{sn}(u; k)$ for Region 1, or $\text{cn}(u; k)$ for Region 2.

6. Compute $x_a(u; k)$ using Eq. (5.7) for Region 1, or Eq. (5.18) for Region 2.

If the transverse angular momenta are also required, they can be computed using Eqs. (3.58) and (3.59). The correct signs may be chosen by using the sign of $\bar{\phi}$ and the schematic in Fig. 5.6.

Sample plots of $x(t)$ and $x_a(t)$ are given in Fig. 6.5. The exact trajectories in these plots are the same as for the trajectories in Fig. 4.15, which we used to show the dramatic effect of initial phase on the final state. Note that the exact trajectory in Fig. 4.15(a) and (c) is quite different from the averaged trajectory.
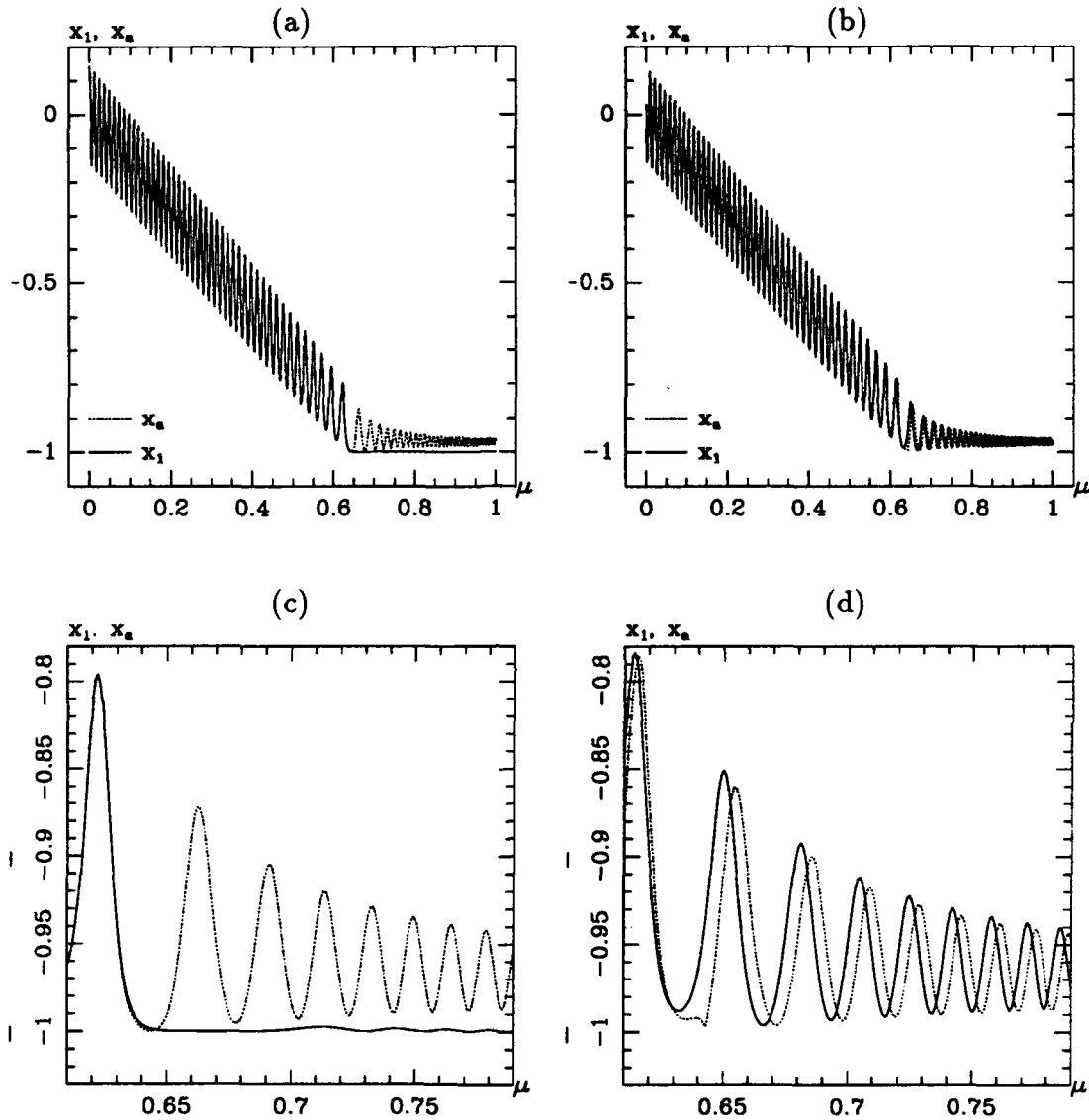
Figure 6.5. Comparison of $x(t)$ and $x_a(t)$ for Two Flat Spin Recovery Trajectories. Plots (a) and (b) show the full trajectory and plots (c) and (d) show close-ups of the effect of the separatrix crossing. These trajectories correspond to the same flow as the trajectories in Fig. 4.15: (a) and (c) are for initial condition (2), and (b) and (c) are for initial condition (1). Note that the averaged trajectory is very accurate before the separatrix crossing, which occurs at $\mu \approx 0.64$.

6.6   Conclusions

The principal result of this chapter is the derivation of a single differential equation for the slow variation of the energy, y, during spinup. Solutions to this equation, obtained by numerical integration, describe a flow in the μy plane, which is the slow state space for the unaveraged system. These trajectories provide an accurate approximation to the exact solutions of the unaveraged system, also obtained by numerical integration, *except* when trajectories cross the instantaneous separatrices of the unperturbed system.

In the next chapter, we continue our investigation of these separatrix crossings.

Chapter 7

Passage through Resonance

In the previous chapter we observed that the averaged equations fail to accurately describe the dynamics near the resonance manifold. This is because trajectories of the unaveraged system exhibit phase-dependent energy change when crossing the instantaneous separatrices of the unperturbed system. Since averaging eliminates the phase from the differential equations for the slow variables, it is not possible to accurately portray separatrix crossing using the averaged equations.

In this chapter we investigate the separatrix crossing for flat spin recovery. The other two spinup problems that experience separatrix crossings, prolate spinup and intermediate spinup, are not discussed here. As we showed in Section 4.5.4, prolate spinup is more effective with a large spinup torque; thus the small torque case to which the averaging theory applies is of less practical interest. Intermediate spinup is quite similar to flat spin recovery, and the treatment we give here may easily be extended to the intermediate case.

We begin the chapter with a discussion of separatrix crossing in general. The separatrix crossing problem is sometimes treated as a boundary layer problem, in which one attempts to *connect* the averaged equations, which are valid on either side of the separatrix, with a boundary layer approximation, or separatrix crossing model. Included in our discussion is a brief introduction to the literature

on this subject.

Recall that the separatrix corresponds to a *resonance manifold* in the slow state space, defined as the set of points where the $\mathcal{O}(1)$ frequency $\Omega(y, \mu)$ vanishes (see Eq. (6.6)). For flat spin recovery, the resonance manifold of interest is the segment of $\mathbf{P}_\mu$ between $\mathbf{P}_{\mu_2}$ and $\mathbf{P}_{\mu_3}$ (see Fig. 4.7). In Section 7.2, we introduce a local coordinate which is transverse to the resonance manifold, and we examine flat spin recovery trajectories as they cross the separatrix. The sensitivity to small changes in initial conditions is illustrated with an example, and we reach the striking conclusion that *no separatrix crossing model, however accurate, can accurately connect the averaged equations across the separatrix for all initial conditions*. This is true because of the combined effects of two phenomena: (1) the method of averaging introduces a small $(\mathcal{O}(\varepsilon))$ error in amplitude and phase, and (2) the small $(\mathcal{O}(\sqrt{\varepsilon}))$ set of trajectories that get delayed near the saddle point during the separatrix crossing is extremely sensitive to changes in initial phase.

However, it is possible to connect *most* trajectories across the separatrix, and we develop an approximate equation for the change in energy across the separatrix. This equation accurately describes the change in energy for a given change in phase, and we use it to derive an accurate formula for the "thickness" of the last cycle before separatrix crossing. A missing piece of information, however, is the length of *time* that a trajectory spends near the separatrix, and we find that the approximate solution must be applied iteratively through the boundary layer in order to obtain good agreement with exact solutions.

7.1 Discussion

The problem of separatrix crossing occurs in many physical applications and has been the subject of active research over the past two decades. After discussing the problem, we describe some of these investigations. In particular, we show why one standard approach is not directly applicable to the present problem (cf. Eq. (7.1)).

In the method of averaging, the dynamics of the unperturbed system are used to study the dynamics of the perturbed system. Thus any special solutions of the unperturbed equations will have a significant role in the dynamics of the averaged system. When the unperturbed system has a saddle type equilibrium point, the stable and unstable manifolds of the saddle form separatrices, separating qualitatively different types of motion [97, p. 36]. Under time-dependent perturbation, the separatrices no longer function to separate distinct kinds of motions, since solutions of the perturbed system can cross the separatrices of the unperturbed system. Nevertheless, it is useful for us to think about separatrices of the slowly evolving perturbed system which leads to the concept of separatrix crossing.

Two distinct possibilities exist for separatrix crossing: a trajectory originating outside of a separatrix can get *captured* and land inside the separatrix, or a trajectory initially inside a separatrix can *escape*. The underlying physics of separatrix crossing also presents two possibilities (which may occur together): the crossing may occur due to a change in the separatrix (growing, shrinking, and even disappearing separatrices are possible), or the crossing may be effected by energy addition or dissipation. Our problem falls into the *escape due to shrinking/disappearing separatrix* category; however, the capture problem discussed in Section 4.6 is an example of *capture due to a growing separatrix.*

Resonance capture by way of crossing a separatrix has been investigated by several authors. Neishtadt [76] studied resonance capture in a model celestial mechanics problem. Calculating the change in an energy-like quantity near the separatrix, he was able to compute the probability of capture into a region enclosed by the separatrices of a saddle point. His method of connecting trajectories across the separatrix consisted of using the averaged equations up to the separatrix, then calculating the probability of capture. Then the averaged equations appropriate for the region of highest probability are used. In later papers, Neishtadt obtained approximate expressions for the change in the adiabatic invariant at

separatrix crossing for one degree of freedom [77] and two degree of freedom [78] systems. Neishtadt's work is also summarized in the monographs by Arnold, Kozlov, and Neishtadt [4], and Lochak and Meunier [63].

Henrard [31] applied adiabatic invariant theory to the study of one degree of freedom Hamiltonian systems with slowly varying parameter. Like Neishtadt, he investigated the change in an energy-like quantity upon crossing the separatrix, and derived an estimate on the probability of capture. Cary et al [11] also studied the change in adiabatic invariant at a separatrix, showing that the change has phase-dependent terms of $\mathcal{O}(\varepsilon)$ and $\mathcal{O}(\varepsilon \ln \varepsilon)$, resulting in a dispersion of trajectories crossing the separatrix.

Using elliptic functions and the method of averaging, Coppola and Rand [17] studied a system with a periodically disappearing separatrix. The disappearing separatrix in their problem is qualitatively equivalent to the south pole of the momentum sphere (near the bifurcation point $\mathbf{P}_{\mu_2}$) in the present work. Their first approach was to assume the flow crosses the separatrix instantaneously. As this method failed to accurately describe the dynamics, they developed a separatrix crossing model by expanding the unaveraged equations in a Taylor series about the separatrix. While their model improved the qualitative agreement between the averaged and unaveraged equations, some error remained, attributable to the uncertainty of the boundary layer thickness.

Rand et al [84] investigated a model spinup problem with imbalance, also using elliptic functions and averaging. This system has an expanding separatrix, and trajectories may be captured as they pass around the separatrix. They obtained an approximate representation of the set of initial conditions leading to capture.

In a series of papers, Bourland and Haberman [6,8,7], treat separatrix crossing for second-order nonlinear oscillators with time-varying potential, with and without energy dissipation. In the first two papers [6,8], they used the method

of multiple scales, while in the more recent paper [7], they applied the method of averaging after putting the equations into angular standard form. They obtained an interesting result that appears to offer a means of improving separatrix crossing models: Although usually the difference between the exact energy and the first order averaged energy is $\mathcal{O}(\varepsilon)$, they showed that, near the separatrix, when the trajectory is *farthest from the saddle point*, the difference is $o(\varepsilon)$ [6,8].

In most of these references, the notion of "excluded initial conditions" is introduced. For example, Henrard [31] excluded a neighborhood of the stable manifold of the saddle point, conceding that his approach is not applicable for this small set of trajectories. A more rigorous approach is taken by Lochak and Meunier [63, pp. 78–101]. First they define two types of *resonant zones* which enclose the resonance manifold: a narrow resonant zone which trajectories may pass through but not revisit, and a larger zone which covers the narrow zone. Then they exclude all initial conditions such that their exact trajectories are either trapped in the resonant zone or are delayed there for a time greater than $\mathcal{O}(\sqrt{\varepsilon}\ln(1/\varepsilon))$. Similarly, we find below that some initial conditions have exact trajectories which cannot be obtained using averaging coupled with a separatrix crossing model, regardless of the accuracy of the separatrix crossing model.

It is also possible to view separatrix crossing as a resonance problem, for which a substantial theory exists. The monographs by Arnold, Kozlov and Neishtadt [4], Sanders and Verhulst [90], and Lochak and Meunier [63], all treat resonance problems arising when $\Omega = 0$, of which the present problem is an example. However, the standard method proposed in these books is apparently not directly applicable to problems of the type considered here. Their approach is to expand local coordinates in a Taylor series about the resonance, which results in a second-order differential equation for the approximate phase, ϕ_a:

$$\ddot{\phi}_a - \varepsilon \frac{\partial \Omega}{\partial \mathbf{r}}\left(\mathbf{r}_r\right)\mathbf{f}\left(\phi_a, \mathbf{r}_r\right) = 0 \tag{7.1}$$

where $\mathbf{r}_r$ is a point in the resonance manifold, *i.e.*, $\Omega\left(\mathbf{r}_r\right) = 0$, and $\mathbf{f}$ is the
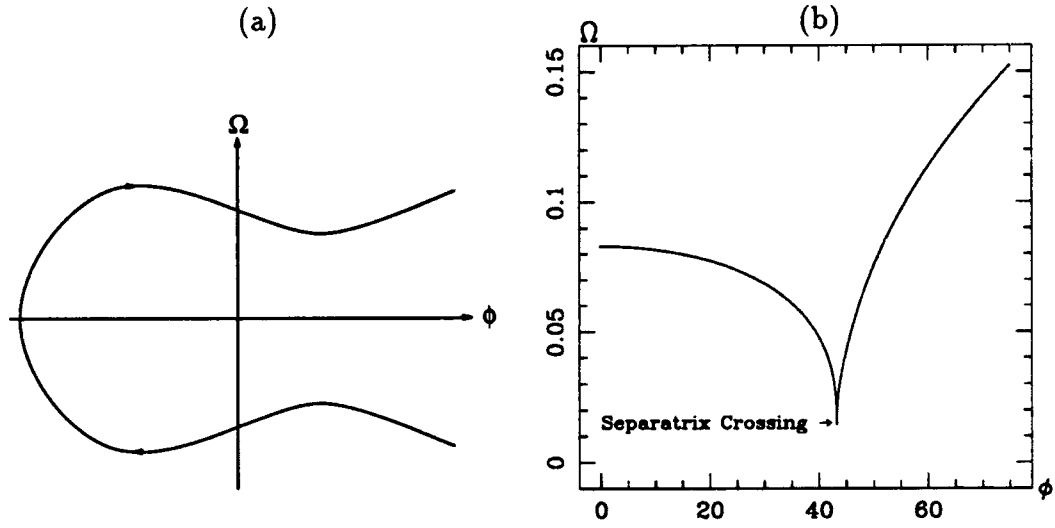
Figure 7.1. Two Different Frequency-Phase Relationships. In (a) we show a typical plot for the types of problems considered in the resonance literature. In (b) we show a sample plot for a flat spin recovery. In both cases, the frequency passes through zero; however, it happens in different ways.

unaveraged slow vector field in Eq. (6.2).

The difficulty with applying this approach to our problem is that the gradient $\partial\Omega/\partial r$ is is not uniformly bounded as r approaches the resonance manifold. (Recall that for the present system, $r = (y, \mu)$.) We prove this by calculating $\partial\Omega/\partial\mu$:

$$\frac{\partial\Omega}{\partial\mu} = \frac{-\lambda}{2K^2}\frac{\partial K}{\partial\mu} + \frac{1}{2K}\frac{\partial\lambda}{\partial\mu} \tag{7.2}$$

$$= \frac{-\lambda}{2}\left\{\frac{1}{K^2}\frac{dK}{dk^2}\right\}\frac{\partial k^2}{\partial\mu} + \frac{1}{2K}\frac{\partial\lambda}{\partial\mu} \tag{7.3}$$

The term in brackets is unbounded for points on the separatrix, as we showed in Section 6.2. Neither λ nor $\partial k^2/\partial\mu$ are identically zero in the resonance manifold, so we conclude that $\partial\Omega/\partial\mu$ is unbounded on the separatrix, and that Eq. (7.1) is not well-defined. The difference between the case represented by Eq. (7.1) and the separatrix crossing problem considered here is the manner in which Ω passes through zero, as illustrated in Fig. 7.1.

Since these calculations are fairly general, it appears that the approach mentioned above is not applicable to separatrix crossing problems formulated as in Eqs. (6.32)–(6.34). However, it should be possible to reformulate the problem in such a way as to make it possible to use Eq. (7.1). Since we are interested in the dynamics near the south pole of the momentum sphere, we can project the phase portrait of the sphere onto the x_3x_2 plane, and obtain a second-order equation for $\ddot{x}_3$, which will be similar to the Duffing equation [18].

In the next section we take a closer look at the resonance manifold for flat spin recovery.

7.2 The Resonance Manifold

For flat spin recovery, the resonance manifold of interest is the dashed line $\mathbf{P}_\mu$ in the μy plane, defined by $y = 2\mu$, $\mu_2 < \mu < \mu_3$. Unfortunately, it is difficult to differentiate between nearby trajectories when plotted in the μy plane. In Chapter 6 we used the relative error e_r to alleviate this difficulty. In this chapter we introduce a new coordinate ρ, by

$$\rho = 2\mu - y \tag{7.4}$$

which is perpendicular to the resonance manifold, and has the property that $\rho = 0$ on the resonance manifold, with $\rho < 0$ before the separatrix crossing and $\rho > 0$ after the crossing. The plots in Fig. 7.2 illustrate the definition of ρ as well as showing the branches of unperturbed equilibria in the $\mu\rho$ plane. For comparison, we also show a single trajectory of the unaveraged system projected onto the μy and $\mu\rho$ planes. This trajectory corresponds to initial condition (1) in Fig. 4.15.

With the use of Eqs. (6.8) and (6.9), we find that

$$\dot{\rho} = 2\varepsilon(1 + x) \tag{7.5}$$

where no approximation has been made. From Eq. (7.5) it is clear that $\dot{\rho}$ is strictly positive unless the trajectory is exactly the saddle point. This follows
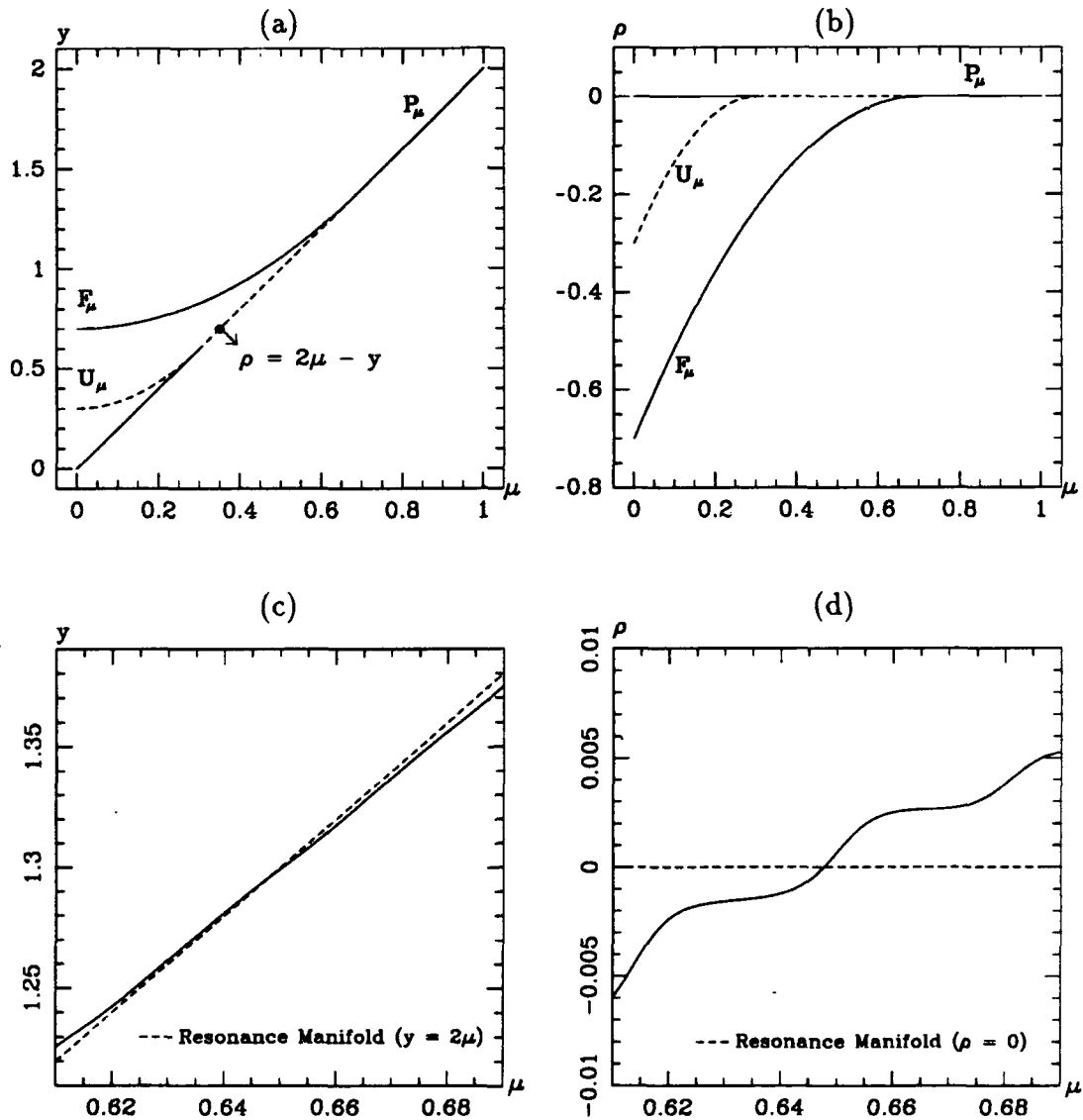
Figure 7.2. Definition of the Transverse Coordinate ρ. Also shown are the $\mu\rho$ plane (b), and a closeup of a separatrix crossing, projected onto the μy plane (c), and onto the $\mu\rho$ plane (d). The trajectory in (c) and (d) corresponds to the flat spin recovery trajectory in Fig. 4.15 for initial condition (1).

from the fact that $x = -1$ at the saddle, and $|x| \leq 1$ everywhere, since the angular momenta are restricted to the unit momentum sphere by Eq. (3.29).

We will return to Eq. (7.5) in the next section. But first, let us look closely at flat spin recovery and try to understand what happens near the separatrix. Recall that in Section 4.5.5, we gave an example with two initial conditions on the same polhode with different initial phase (Fig. 4.15). That is, the two initial conditions share the same $y(0) = y_0$ and $\mu(0) = \mu_0$, but are out of phase by $\Delta\phi \approx 1/4$. The point of the example was to show how the initial phase is important for trajectories that cross a separatrix. We use those same initial conditions here to discuss the separatrix crossing problem.

In Figs. 7.3 and 7.4, we show the separatrix crossing trajectories of Fig. 4.15, this time projected onto the $x_3 x_2$ plane. We also show the instantaneous separatrices as they appear *at the time of crossing*, which is *different* for the two trajectories.

Figures 7.3 and 7.4 are misleading since the separatrices which are shown are only valid for the exact values of μ at which the crossings occur. For example, the initial points p are actually *inside* their associated instantaneous separatrices, whereas the final points r are *outside*. Only the points q are shown in their actual relationships with the instantaneous separatrices. Another way to picture these trajectories is to show a "three-dimensional" plot of the $x_3 x_2$ plane as it varies with μ. This is done in Figs. 7.5, 7.6, and 7.7.

Now, trajectories can cross the instantaneous separatrix far from the saddle point, or very close to the saddle. Crossings far from the saddle are well-approximated by the instantaneous crossing model we used in Chapter 6. As crossings occur closer to the saddle, however, the trajectories spend an *almost* arbitrarily long time near the saddle point (*almost*, because the saddle becomes a center in finite time). Trajectories that are near the saddle when the saddle changes to a center will remain near the center.
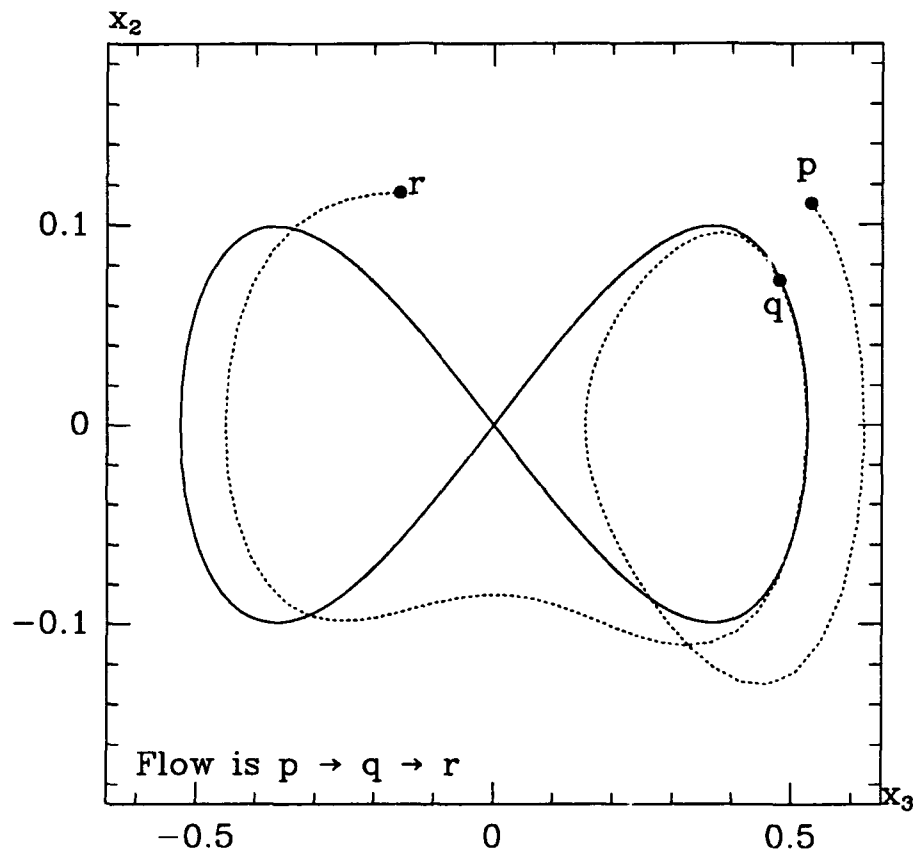
Figure 7.3. Flow in the $x_3 x_2$ Plane Near a Separatrix. This flow corresponds to initial condition (1) in Fig. 4.15. The separatrix crossing occurs at point q, and we show the instantaneous separatrix at the time of crossing. Note that the trajectory does not pass very close to the saddle point.
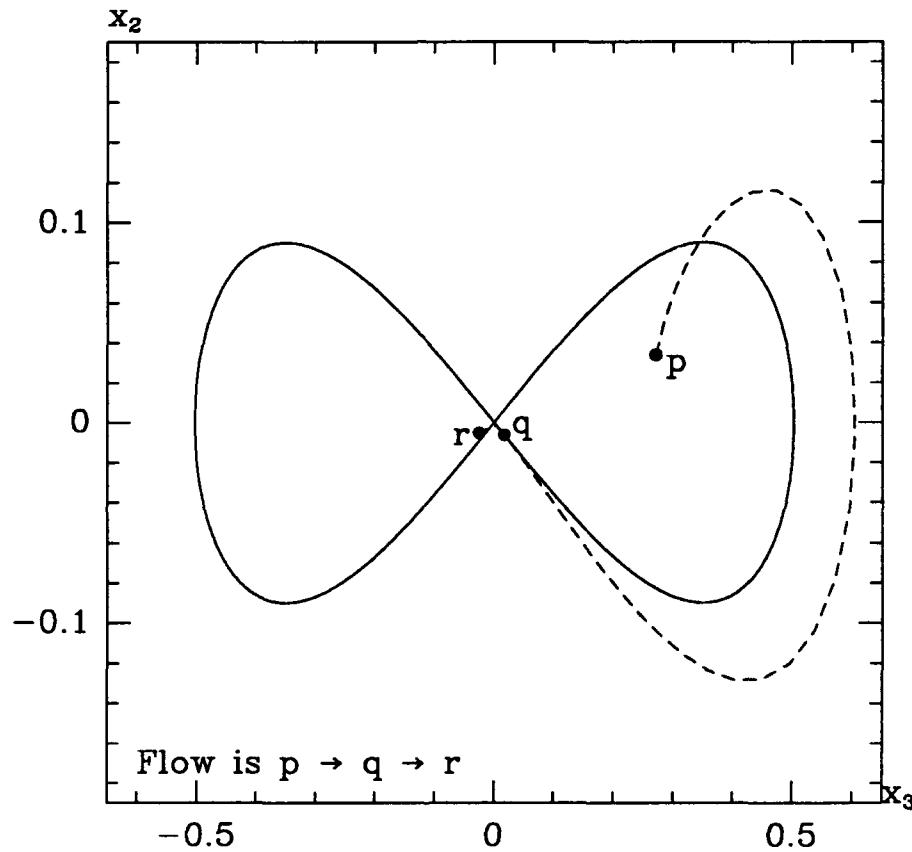
Figure 7.4. Flow in the x_3x_2 Plane Near a Separatrix with Delay Near the Saddle. This flow corresponds to initial condition (2) in Fig. 4.15. The separatrix crossing occurs at point q, very close to the saddle point. We show the instantaneous separatrix at the time of crossing. The points q and r *are* connected by a curve which is very close to the separatrices.
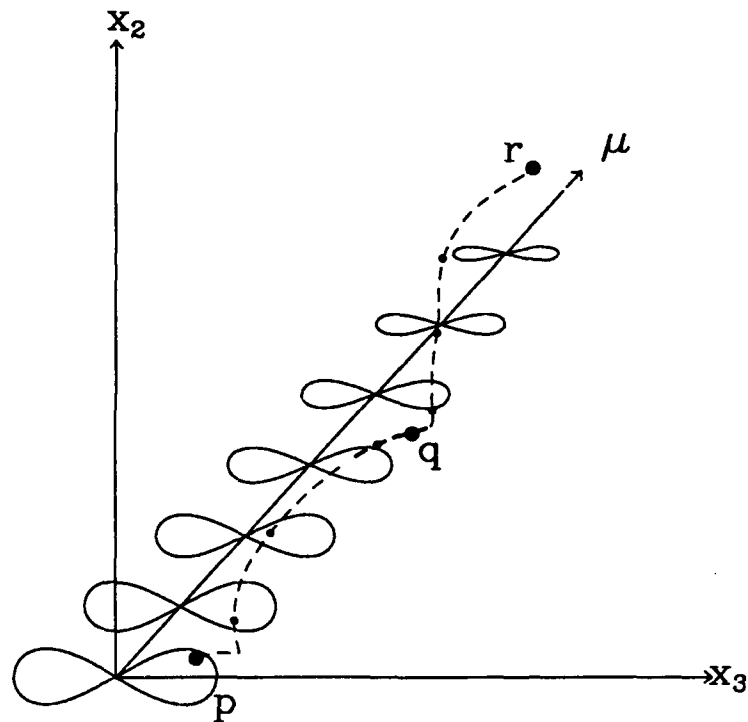
Figure 7.5. Three-Dimensional Flow in the $x_3 \mu x_2$ Space Near a Separatrix. This flow corresponds to initial condition (1) in Fig. 4.15, and to the trajectory in Fig. 7.3. We superimpose the instantaneous separatrices for several values of μ onto the trajectory. The dots on the trajectory indicate where the trajectory passes through the planes of the instantaneous separatrices. The points p, q, and r correspond to the points in Fig. 7.3. As the separatrix "shrinks," the trajectory escapes and begins to oscillate outside the instantaneous separatrix. The point q marks the point of separatrix crossing.
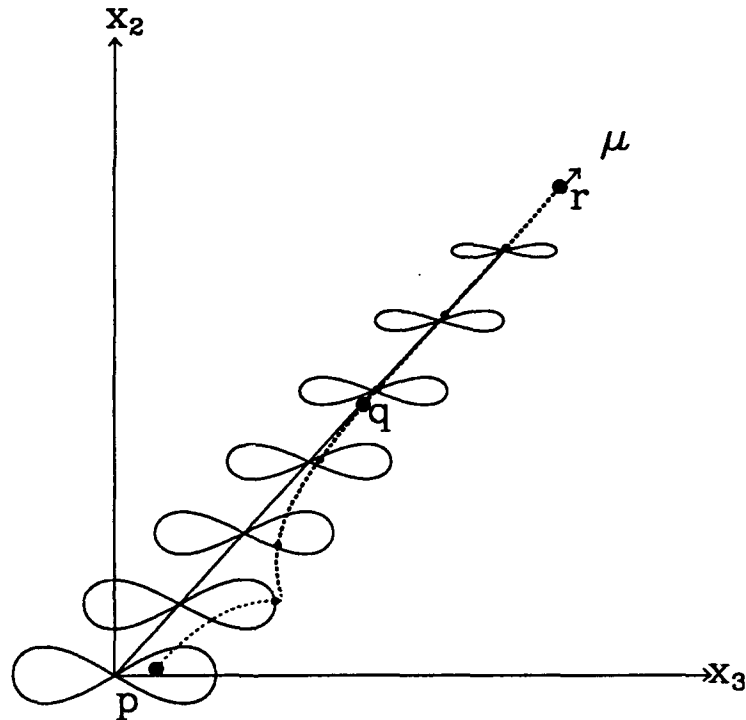
Figure 7.6. Three-Dimensional Flow in the $x_3 \mu x_2$ Space Near a Separatrix with Delay Near the Saddle. This flow corresponds to initial condition (2) in Fig. 4.15, and to the trajectory in Fig. 7.4. We superimpose the instantaneous separatrices for several values of μ onto the trajectory. The dots on the trajectory indicate where the trajectory passes through the planes of the instantaneous separatrices. The points p, q, and r correspond to the points in Fig. 7.4. As the separatrix "shrinks," the trajectory gets delayed near the saddle point, and the delay continues after the trajectory passes outside the instantaneous separatrix. The point q marks the point of separatrix crossing. Once the saddle has changed to a center, the trajectory oscillates about the center with a smaller amplitude than the trajectory of Fig. 7.5.
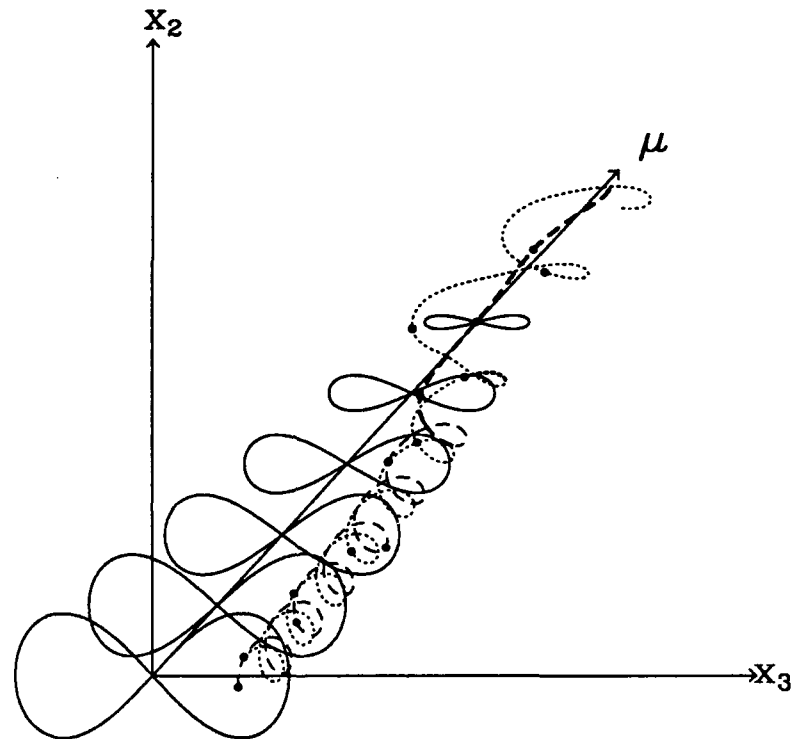
Figure 7.7. Three-Dimensional Flow in the $x_3\mu x_2$ Space Near a Separatrix Comparing Two Trajectories. This figure shows both of the trajectories of Figs. 7.3–7.6 and for a longer interval along the μ axis. The two trajectories started on the same initial polhode (see Fig. 4.15), but experience the separatrix crossing in dramatically different ways. The dots on the trajectories indicate where the trajectories pass through the planes of the instantaneous separatrices.

Those trajectories that cross near the saddle can cross before or after the saddle point. Typically those that cross *after* the saddle spend a long time near the equilibrium *before* the crossing, while those that cross *before*, are delayed near the equilibrium *after* the crossing. The net effect in either case is that the size of the separatrix decreases during the time spent near the saddle, so that when the trajectory at last begins to oscillate around the separatrix, the amplitude of oscillation is *smaller* than for an instantaneous crossing. Thus the "bad" initial conditions actually lead to a smaller residual cone angle (see Figs. 4.15). The trajectories that cross near the saddle account for the sharp "spikes" in the y_f vs. ϕ_0 plots of Fig. 6.4.

Remark 9 *The fact that trajectories near the "pseudo-stable manifold" of the saddle point are desirable from a practical point of view (smaller cone angle), suggests the possibility of trying to control the system in order to attain such a trajectory. Recall, however, that the gyrostat is a greatly simplified model of a real dual-spin spacecraft. The delicate balance required to accomplish this sort of control would be easily destroyed by the countless perturbations present in a real system.*

7.3   An Approximate Solution

In order to develop an approximate equation for the separatrix crossing, we require the $\varepsilon = 0$ solution in a neighborhood of the separatrix. This entails using the solution developed in Chapter 5, with the modulus, k^2, close to unity. As shown in Appendix C, the primary solution is not applicable here, since it reduces to the saddle point in the $k^2 = 1$ limit. Hence we use the alternate form of the solution, which describes the separatrix for $k^2 = 1$. This form of the solution is defined by Eq. (5.7) which is repeated here for convenience:

$$x(u; k) = \beta \left\{ \frac{1 - \alpha_1^2 \text{sn}^2(u; k)}{1 - \alpha^2 \text{sn}^2(u; k)} \right\} \tag{7.6}$$
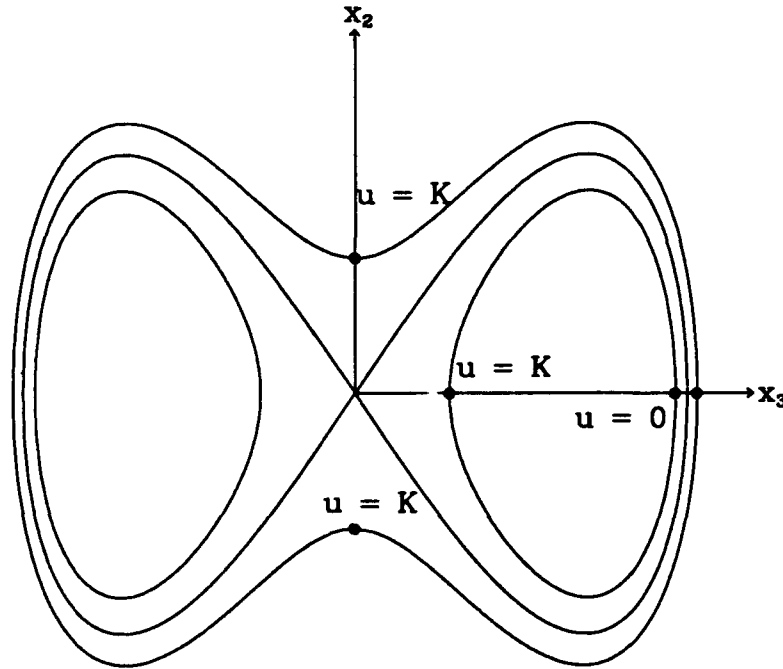
Figure 7.8. Phase of the Alternate $\epsilon = 0$ Solution for x in the x_3x_2 Plane. Compare with Fig. 5.6, and note the $\Delta u = K$ phase shift.

The parameters are defined by Eqs. (5.11)–(5.16). Recall that for this form of the solution, $\alpha^2 < 0$. Furthermore, near the resonance manifold, $|\alpha^2| < 1$, since the roots a and b are closer in value than the roots b and d. Also, recall that the two forms of the solution differ in phase by $\Delta u = K$, a fact we must use when we patch the averaged equations to the approximation we develop in this section. The phases associated with the alternate solution are shown in Fig. 7.8.

Recall that at the separatrix, the modulus is $k^2 = 1$. In order to obtain an equation valid *near* the separatrix, we expand $\mathrm{sn}^2(u; k)$ in a series for k^2 near one. From Eq. 127.02 in Ref. [10], we have

$$\mathrm{sn}(u; k) = \tanh u + \frac{k'^2}{4}\mathrm{sech}^2 u \left(\sinh u \cosh u - u\right) + \mathcal{O}\left(k'^4\right) \tag{7.7}$$

where $k'^2 = 1 - k^2$ is the complimentary modulus. Squaring this expression for $\mathrm{sn}(u; k)$, we obtain

$$\mathrm{sn}^2(u; k) = \tanh^2 u + \frac{k'^2}{2}\left(\tanh^2 u - u \tanh u\, \mathrm{sech}^2 u\right) + \mathcal{O}\left(k'^4\right) \tag{7.8}$$

Upon substituting Eq. (7.8) into Eq. (7.6) and expanding the resulting expression in a Taylor series about $k'^2 = 0$, we obtain an approximate expression for $x(u; k)$ near the resonance manifold:

$$x(u; k) = \beta \left\{ \frac{1 - \alpha_1^2 \tanh^2 u}{1 - \alpha^2 \tanh^2 u} + \right. \tag{7.9}$$

$$\left. k'^2 \frac{\left(\alpha_1^2 - \alpha^2\right)\left(\tanh^2 u - u \tanh u \operatorname{sech}^2 u\right)}{2\left(1 - \alpha^2 \tanh^2 u\right)^2} \right\}$$

which is valid to $\mathcal{O}(k'^2)$.

The basis of our treatment of the separatrix crossing is to assume that Eq. (7.9) holds for the flow in a neighborhood of the separatrix, with the parameters α^2, α_1^2, β, and λ held constant, i.e., only the phase u is allowed to vary. Recall that these parameters all depend on y and μ through the roots of the gyroscopic function.

Now we return to Eq. (7.5):

$$\dot{\rho} = 2\varepsilon \left(1 + x(u; k)\right) \tag{7.10}$$

where we will use $x(u; k)$ from Eq. (7.9). In order to obtain an approximate solution to this equation, we recall that $u = \lambda t + u_0$, so that

$$dt = \frac{du}{\lambda + \dot{\lambda}t + \dot{u}_0} \tag{7.11}$$

We have shown earlier that $\dot{\lambda}$ and $\dot{u}_0$ are $\mathcal{O}(\varepsilon)$, and may be ignored as long as the flow is not near the bifurcation points P_{μ_2} and P_{μ_3} (see Chapter 6). Thus, letting $\lambda dt = du$, and using Eq. (7.9), Eq. (7.10) may be written as

$$\int_{\rho^-}^{\rho^+} d\rho = \frac{2\varepsilon}{\lambda} \int_{u^-}^{u^+} \left(1 + x(u; k)\right) du \tag{7.12}$$

where $x(u; k)$ is given by Eq. (7.9), and the superscripts $-$ and $+$ on the limits of integration denote the values of ρ and u at the entrance to and exit from the resonance boundary layer.

Making use of the change of variables $v = \tanh u$, Eq. (7.12) can be solved in closed form, yielding

$$\frac{\lambda(\rho^+ - \rho^-)}{2\varepsilon} = \left\{ \left(u^+ - u^- \right) + f(u^+) - f(u^-) \right\} \tag{7.13}$$

where

$$f(u) = \frac{a(\alpha^2 - \alpha_1^2)}{\alpha^2 - 1} \left\{ \frac{\tan^{-1}[\sqrt{-\alpha^2}\tanh u]}{\sqrt{-\alpha^2}} + \frac{(\alpha_1^2 - 1)}{\alpha^2 - \alpha_1^2}u - \right. \tag{7.14}$$

$$\frac{k'^2}{4}\left[\frac{2u}{\alpha^2 - 1} - \frac{u(1 - \tanh^2 u) - \tanh u}{1 - \alpha^2 \tanh^2 u} - \right.$$

$$\left.\left.\frac{2\tan^{-1}[\sqrt{-\alpha^2}\tanh u]}{(\alpha^2 - 1)\sqrt{-\alpha^2}} \right] \right\}$$

Equation (7.13) is an approximate solution for the change in "energy" associated with a change in phase near the separatrix. It is approximate in the sense that in the integration of Eq. (7.12), we held the slowly varying parameters constant. However, when a trajectory spends a very long time near the saddle point, the change in μ is not small, hence the parameters which depend on μ may experience significant change. Nonetheless, Eq. (7.13) agrees with the actual change in ρ for a given phase for most trajectories, as we show in the next section.

Remark 10 *Since the $\varepsilon = 0$ solution for intermediate gyrostats, Eq. (5.26), is of the same form as the $\varepsilon = 0$ solution for oblate gyrostats in Region 1, Eq. (5.7), the result obtained here is directly applicable to intermediate gyrostats.*

7.4   The Boundary Layer Thickness

The approximate "inner" solution, Eq. (7.13), obtained in the previous section will be used to *patch* or *connect* the "outer" averaged equations through the resonance manifold where averaging is not valid. The central difficulty here is deciding when to stop using the averaged equations and start applying the inner solution, and when to return to the averaged equations. In this section, we use some heuristics to define a suitable condition for switching between the outer and

inner equations, and we obtain an accurate estimate of the change in ρ during one cycle near the separatrix. However, when we use Eq. (7.13) to patch through the boundary layer, we find that the approximation significantly underestimates the exit value of μ. After discussion of the reason for this, we use an Euler integration technique to obtain approximate solutions through the boundary layer.

To justify our approach, we need to examine the periodic nature of the evolution of ρ. In Fig. 7.9, we show a plot of ρ *vs.* ϕ for a flat spin recovery trajectory as it passes through the resonance manifold, $\rho = 0$. Note that ρ *vs.* ϕ is a cylindrical phase space, $(\rho, \phi) \in \mathbf{R} \times S^1$, and the trajectories "wrap around" at the left and right edges of the figure.

Note that for a polhode inside the separatrix loop (see Fig. 7.8), the point closest to the saddle has phase $\phi = 1/2$, whereas in the primary form of the solution, this point has phase $\phi = 0$. In order to keep the saddle point "centered" in Fig. 7.9, we let the phase go from 0 to 1, with the understanding that $\phi > 1/2$ corresponds to $u \in (-K, 0)$; *i.e.*,

$$\phi \stackrel{\triangle}{=} \begin{cases} \frac{u}{2K} & u \in [0, K] \\ \frac{u}{2K} + 1 & u \in (-K, 0] \end{cases} \tag{7.15}$$

The periodicity which is evident in Fig. 7.9 is a generic feature for small ε, which we have observed for a wide range of initial conditions and values of the parameters i_2 and i_3. Additional trajectories plotted on this curve would "fill" the gaps between the curve shown. We denote by ρ^* the change in ρ during one period in ϕ. The value of knowing ρ^* is in knowing that within one cycle the trajectory will cross the instantaneous separatrix, *i.e.*, the trajectory will pass through $\rho = 0$. Thus ρ^* can be viewed as the thickness of a *boundary layer* or *resonant zone* which includes the resonance manifold. We can calculate ρ^* "exactly" by integrating the full equations backwards from the point $(\phi, \rho) = (1, 0)$ until ϕ passes through $\phi = 0$ (see Fig. 7.11). Then ρ^* is the absolute value of the final value of ρ. Clearly this is not a very useful approach, except in verifying the results obtained by
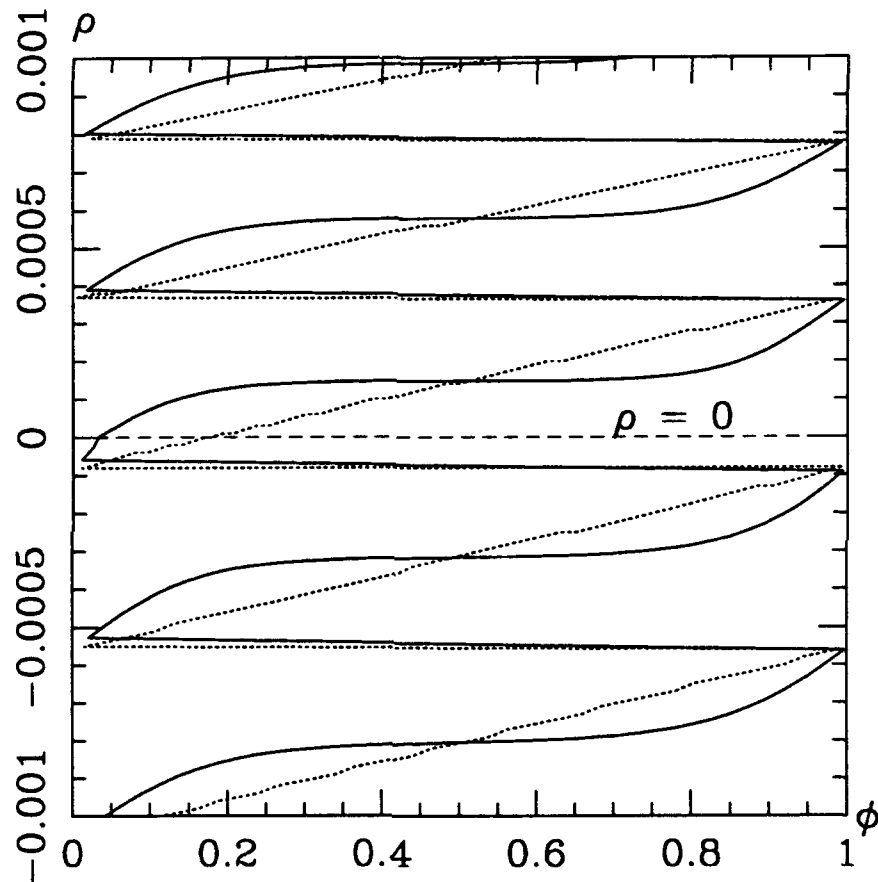
Figure 7.9. ρ vs. ϕ in a Neighborhood of a Separatrix Crossing ($\varepsilon = 0.0001$). The solid curve is the "exact" trajectory, while the dashed curve was obtained from the averaged equations, with "instantaneous" separatrix crossing. Note that the exact trajectory is well approximated by the averaged trajectory, both before and after the crossing ($\rho = 0$). This is typical for trajectories that do not pass too near the saddle.
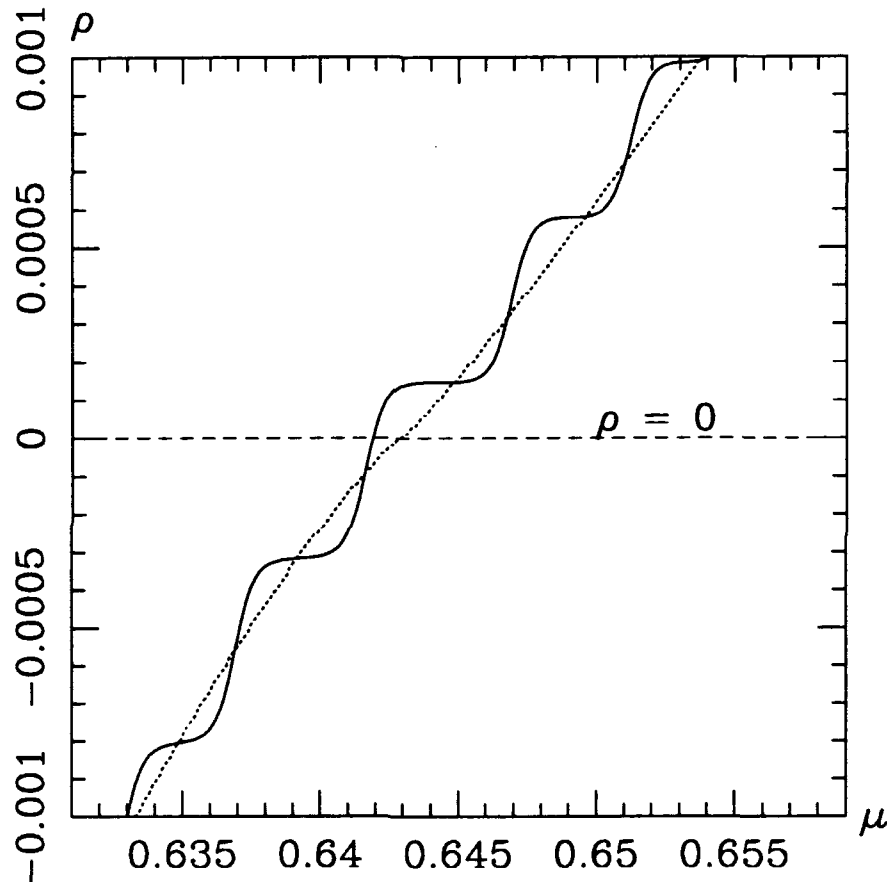
Figure 7.10. ρ vs. μ in a Neighborhood of a Separatrix Crossing ($\epsilon = 0.0001$). This is another view of the trajectory shown in Fig. 7.9. Note that the trajectory passes through the resonance manifold, $\rho = 0$, transversally, and that the averaged trajectory agrees with the exact trajectory. Compare this with the trajectory shown in Fig. 7.16, which is *not* transverse to the resonance manifold.
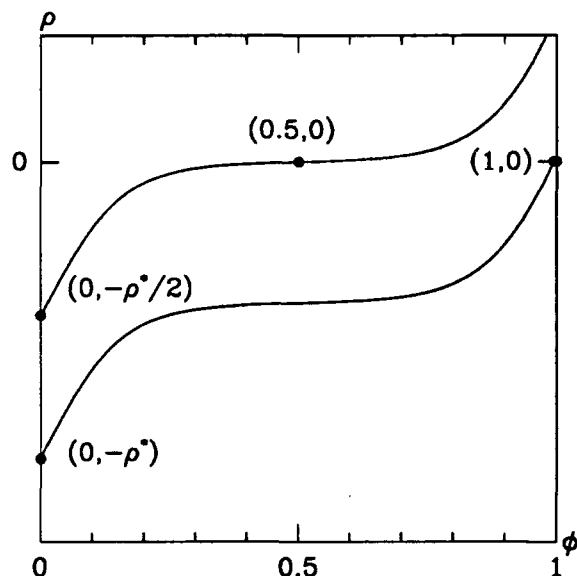
Figure 7.11. Schematic Showing Calculation of ρ^*. The "exact" value of ρ^* is obtained by numerically integrating the full equations backwards from $(\phi, \rho) = (1, 0)$ to $(0, -\rho^*)$. The approximate value is obtained by evaluating Eq. (7.13) with endpoints $(\phi^-, \rho^-) = (0, -\rho^*/2)$, $(\phi^+, \rho^+) = (0.5, 0)$.

approximate methods. In Fig. 7.12, we show the exact value of ρ^* calculated in this way, along with two approximations which we obtain below. Note that the approximate curves agree very well with the exact curve.

We obtain the estimates of ρ^* using the approximate solution developed in the previous section (Eq. (7.13)). Note that in Fig. 7.9, $\rho^* \approx 5\varepsilon$. The fact that $\rho^* = \mathcal{O}(\varepsilon)$ is another generic feature which we have observed for small ε, and we exploit this observation in obtaining an approximation for ρ^*. First, we *assume* $\rho^* = \varepsilon$, and for a given value of μ, we can calculate the parameters in Eq. (7.13), since $y = 2\mu - \rho$, and the parameters depend only on y and μ. Thus, since we have chosen $\rho^* = \varepsilon$, the parameters depend only on μ and ε. Then, referring to Fig. 7.11, we take $\rho^+ = 0$, $u^+ = K$, $u^- = 0$, and $\rho^- = -\rho^*/2$, and Eq. (7.13) gives:

$$\rho^* = \frac{4\varepsilon}{\lambda} \left(K + f(K) \right) \tag{7.16}$$

where f is given at Eq. (7.14), and we have used $f(0) = 0$. Recall that u and ϕ
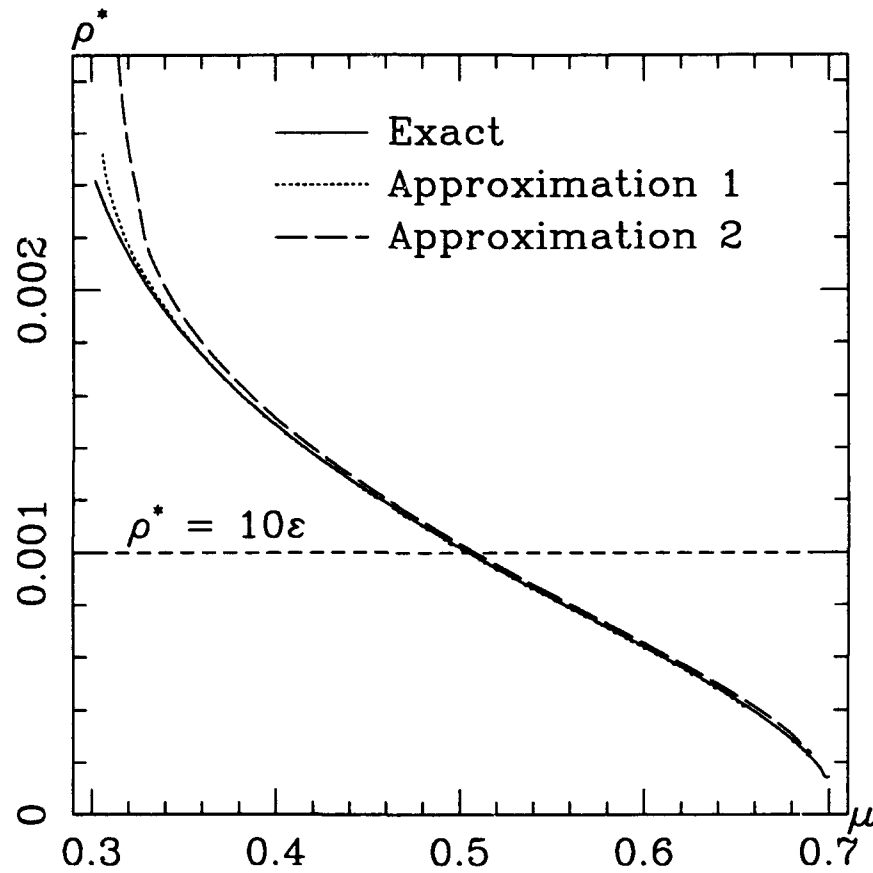
Figure 7.12.   Boundary Layer Thickness: ρ^* vs. μ for ϵ = 0.0001 and $(i_2, i_3) = (-0.3, -0.7)$. The exact curve was obtained by numerical integration of the full equations, whereas the approximations were obtained using Eq. (7.16): Approximation 1 was obtained from one application of Eq. (7.16), and Approximation 2 was obtained iteratively. Note that the iterative solution is not as accurate as the "one-step" solution. The line $\rho^* = 10\epsilon$ is shown for comparison.

are related by Eq. (7.15).

Equation (7.16) defines an approximate value of ρ^* as a function of μ and ε. In the plots in Fig. 7.12 the value of ρ^* obtained by the calculation of Eq. (7.16) is labeled "Approximation 1."

A reasonable refinement would seem to be to iterate Eq. (7.16), using the newly calculated value of ρ^* to recompute the parameters and obtain a "better" estimate of ρ^*. However, although this iterative procedure converges, it does not provide a better estimate of ρ^*. In fact, the estimate appears to be worse, as shown in Fig. 7.12. This can be explained by recalling that our approximation is based on Eq. (7.13), which is itself an approximate solution to the integral equation, Eq. (7.12). One expects the solution to be exactly correct for some value of ρ between the limits of integration, ρ^- and ρ^+, which is what we have observed here, since $\rho^* \geq |\rho^-| > \varepsilon > \rho^+ = 0$.

Now, recall the result of Bourland and Haberman [6,8] which we mentioned in Section 7.1: the difference between the exact energy and the averaged energy is $o(\varepsilon)$ when the trajectory is near the separatrix and farthest from the saddle. Although we have not proven this result for the present system, it can be seen in Fig. 7.9 that the average value of ρ is closest to the exact value of ρ when $\phi = 0, 1/2$, or 1. The point farthest from the saddle corresponds to $\phi = 0$ (or 1, which is equivalent). In order to use this observation for our boundary layer "entry" condition, we need to start "looking" for $\bar{\phi} = 0$ when $\rho = -\rho^*$. Since $\phi = 1/2$ also corresponds to a small difference between the exact and averaged trajectory, we also use $\bar{\phi} = 1/2$ as an entry condition.

This leads us to a tentative algorithm for obtaining trajectories using Eq. (7.13) to cross the separatrix:

1. Given an initial polhode, that is initial values of y and μ, (y_0, μ_0), arbitrarily select the initial phase $\phi_0 = 0$. (Recall that the initial phase enters solutions to the averaged equations only as a constant of integration, Eq. (6.52).)

2. Integrate the averaged equations, Eqs. (6.36)–(6.38), until $\rho = 2\mu - \bar{y} \approx \rho^*$, where ρ^* is computed using Eq. (7.16). Denote the "final" values of $(\bar{y}, \mu, \bar{\phi})$ by (Y, M, Φ).

3. Recalling Eq. (6.52), choose a set of points in the interval $(-0.5, 0.5)$ to use as ϕ_0.

4. Continue integrating the averaged equations, using $(y, \mu, \phi) = (Y, M, \Phi + \phi_0)$ as initial conditions, while checking for the stopping condition on $\bar{\phi}$: $\bar{\phi} = 0$ or $1/2$.

5. When $\bar{\phi}$ satisfies either of the criteria in step 4, apply the approximate solution through one "period" using the current state to compute ρ^- and the parameters in Eq. (7.13):

$$\rho^+ = \rho^- + \rho^* \tag{7.17}$$

6. Compute the exit state. Since $\Delta u = 2K$, and $u = \lambda t + u_0$, with λ and u_0 held constant, $\Delta t = 2K/\lambda$, so

$$\mu^+ = \mu^- + \varepsilon(2K/\lambda) \tag{7.18}$$

(We will see below that this update is not accurate.)

The exit energy $\bar{y}^+$ is then given by

$$\bar{y}^+ = 2\mu^+ - \rho^+ \tag{7.19}$$

Since we have assumed K constant through the boundary layer, with $\Delta u = 2K$, the exit phase is the same as the entry phase:

$$\bar{\phi}^+ = \bar{\phi}^- \tag{7.20}$$

7. Continue integrating the averaged equations using the boundary layer exit values of $(\bar{y}, \mu, \bar{\phi})$ as initial conditions. This is continued until $\mu = 1$.
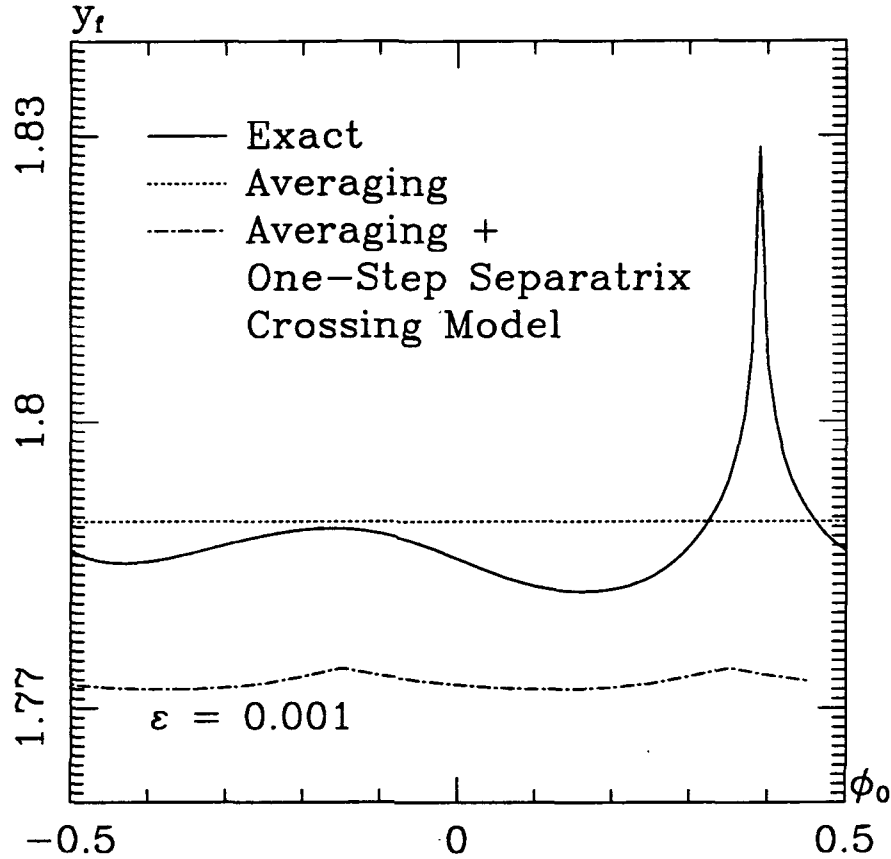
Figure 7.13. Comparison of One-Step Separatrix Crossing Model with Exact Solution and Averaging Solution for $\varepsilon = 0.001$, $(i_2, i_3) = (-0.3, -0.7)$. The final energy $y_f(\mu = 1)$ is plotted against the initial phase ϕ_0. Cf. Figs. 7.17 and 6.4.

8. Steps 4–7 are repeated using the values of ϕ_0 chosen in step 3. In this way we obtain a map of $\bar{y}_f$ vs. ϕ_0 for all the initial conditions on a single polhode.

In Fig. 7.13, we compare the final energy, $y_f = y(\mu = 1)$, as a function of initial phase, when computed exactly, and with the approximation developed here. It is evident that this procedure does not work well.

The reason is that, in Eq. (7.18), we computed Δt using the values of K and λ at the *entry* to the boundary layer, since we do not know the values of these parameters for later times. Recall that $\Omega(y, \mu) = \lambda/(2K)$ and note that in
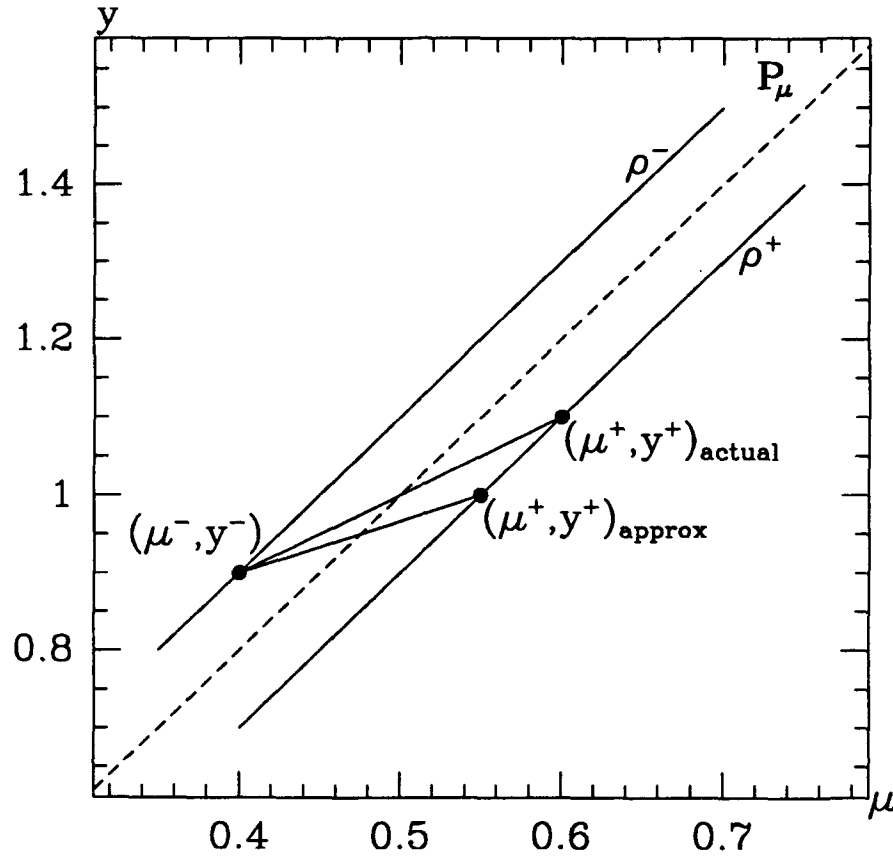
Figure 7.14. Error in Calculating μ^+ with Eq. (7.18). Since the "average" value of K over the time interval associated with the separatrix crossing is typically *larger* than the value at the entry point, Eq. (7.18) will usually underestimate the actual change in μ for a given change in ρ. The two lines shown are not trajectories, but schematic representations of the map from (μ^-, y^-) to (μ^+, y^+).

Fig. 7.1, $\Omega \rightarrow 0$ at the separatrix crossing. This implies that $2K/\lambda \rightarrow \infty$ at the separatrix crossing, hence our value of Δt cannot be correct. Since $2K/\lambda \rightarrow \infty$ in the interval of interest, the "average" value of $2K/\lambda$ will usually be larger than the value calculated at the entry to the boundary layer. (The possible exception is if the exit value of $2K/\lambda$ is *much* less than the value at entry. We have not found an example where this occurs.) Thus the value of μ^+ we calculate in Eq. (7.18) is *smaller* than the actual value of μ^+. This means that the calculated point (μ^+, y^+) will differ from the actual point as shown in Fig. 7.14.

The result is that the final energy $\bar{y}_f$ will be smaller than the actual final energy, which explains the error seen in Fig. 7.13.

7.5 Euler Integration through the Boundary Layer

As we have seen, the principal difficulty with our inner solution is the fact that $\Delta t \neq \Delta u / \Omega(y^-, \mu^-)$, since $\Omega(y, \mu)$ is not well represented in the boundary layer by its value at the entrance to the boundary layer. In addition, our decision to use $\bar{\phi}^- = 0$ or $1/2$ required us to take a relatively "thick" boundary layer, thereby perhaps extending the solution farther beyond its range of validity. Recall, however, that we introduced the criterion for ϕ^- in order to benefit from the (apparently) $o(\varepsilon)$ accurate averaged energy. In this section we use Euler's integration technique to obtain more accurate trajectories through the boundary layer.

Now, there are several more or less "exact" methods of obtaining the flow through the boundary layer. For example, one could integrate the averaged equations up to the entrance to the boundary layer, then switch to the full system of equations for the separatrix crossing, finally returning to the averaged equations at the exit from the boundary layer. This might be called the "best" separatrix crossing model, since presumably a better estimate would be unlikely. However, as we have noted above, this method will not accurately follow trajectories corresponding to particular initial conditions, because of the error incurred by averaging and the extreme sensitivity to changes in initial phase.

Here we take a simpler approach, making use of the approximate expression for $x(u)$ in the vicinity of the separatrix, Eq. (7.9). What we need is a relationship between $\Delta \rho$ and Δu that is applicable for small intervals of time, so that the $\Delta \mu$ update used above will be reasonably accurate. First, note that Eqs. (7.10)

and (7.11) imply that

$$\frac{du}{d\rho} = \frac{\dot{u}}{\dot{\rho}} \approx \frac{\lambda}{2\varepsilon\left(1 + x(u;k)\right)} \tag{7.21}$$

where $x(u;k)$ is defined approximately by Eq. (7.9). Thus for small $\Delta\rho = \rho^+ - \rho^-$, we obtain

$$u^+ = u^- + \frac{\lambda\Delta\rho}{2\varepsilon}\frac{1}{1 + x(u^-;k)} \tag{7.22}$$

where it is understood that this is an approximation. Starting at the entrance to the boundary layer, we apply Eq. (7.22) iteratively, at each step updating the slow states as follows. Since the steps are "small," the change in time, Δt, is approximately $\Delta u/\lambda$. Thus the updates for μ and y, are similar to those given earlier, Eqs. (7.18) and (7.19):

$$\mu^+ = \mu^- + \frac{\varepsilon}{\lambda}(u^+ - u^-) \tag{7.23}$$

$$y^+ = 2\mu^+ - \rho^+ \tag{7.24}$$

We can now make the following modification to the algorithm developed in the previous section. Step 5 is changed to read:

5. When $\bar{\phi}$ satisfies the above condition, begin iteratively applying Eq. (7.22), updating the slow states at each iteration.

Also, the updates in Step 6 are performed using Eqs. (7.23) and (7.24), instead of the equations given previously.

Since this iterative scheme is essentially a numerical integration through the boundary layer, we expect it to give a good approximation of trajectories as they cross the separatrix. In Fig. 7.15, we show a trajectory that gets delayed near the saddle point. The iterative separatrix crossing model describes the actual trajectory better than the instantaneous crossing model. To demonstrate the improvement over the instantaneous separatrix crossing, in Fig. 7.16 we show the same trajectory in the $\mu\rho$ plane, contrasted with results from both the instantaneous crossing and the iterative crossing model.
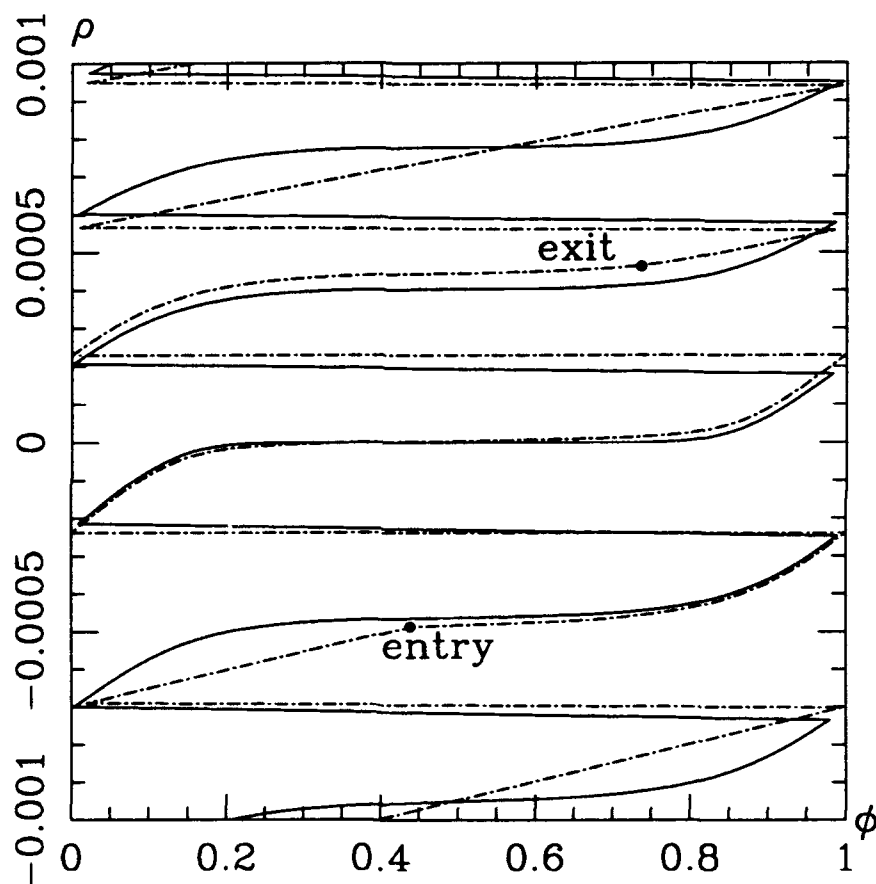
Figure 7.15. ρ *vs.* ϕ in a Neighborhood of a Separatrix Crossing ($\varepsilon = 0.0001$). The solid curve is the "exact" trajectory, and the dashed curve was obtained from the averaged equations, using the iterative separatrix crossing model.

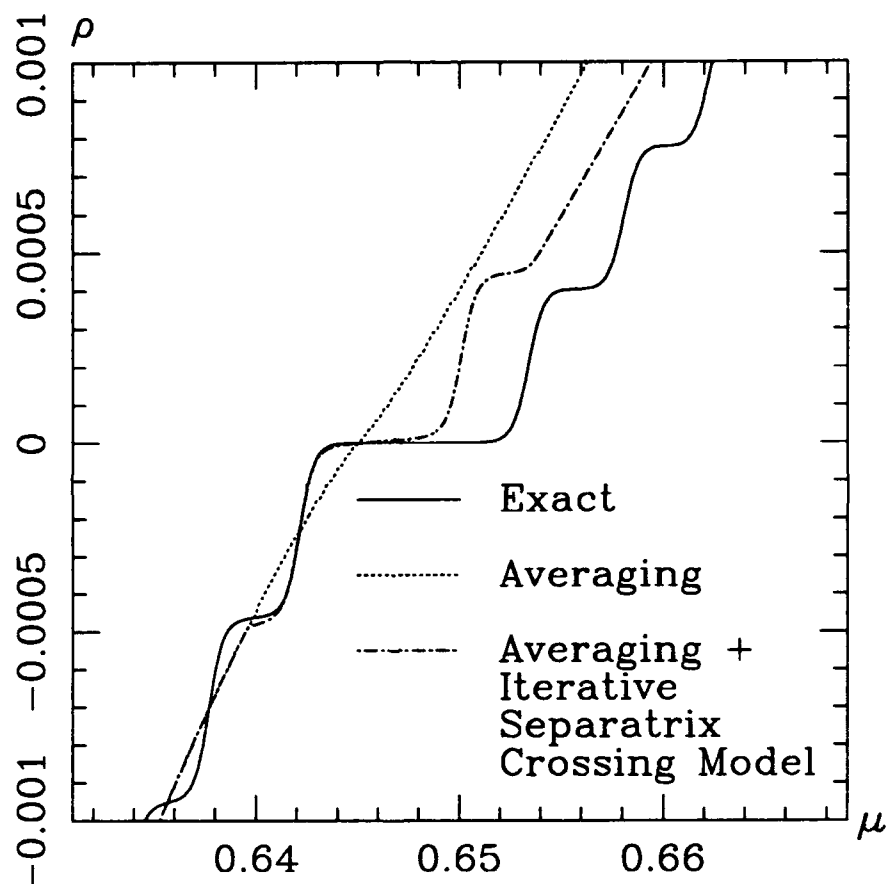Figure 7.16. ρ *vs.* μ in a Neighborhood of a Separatrix Crossing ($\epsilon = 0.0001$). This is another view of the trajectory shown in Fig. 7.15. Also shown is the trajectory obtained from averaging with instantaneous separatrix crossing.

In Fig. 7.17 we compare the final value of the energy, y_f, as a function of the initial phase, ϕ_0, as computed by three different methods: numerical integration of the full equations, numerical integration of the averaged equations with instantaneous crossing of the separatrix, and numerical integration of the averaged equations with the iterative separatrix crossing model.

Remark 11 *Strictly speaking, it is not the* initial *phase that affects the separatrix crossing, but rather the* entry *phase, i.e., the phase at which the trajectory encounters the instantaneous separatrix. Thus, instead of plotting y_f vs. ϕ_0, perhaps we should plot y_f vs. ϕ^-. However, recall that Eq. (6.52) states that the initial phase appears as an additive constant to the solution of the fast equation. Thus, $\phi_0 - \phi^- = \text{CONST}$ for a given initial polhode. Also, from Fig. 7.11 and the discussion of ρ^*, we know that the trajectories that pass closest to the saddle are those that pass near the entry point $(\phi, \rho) = (0, -\rho^*/2)$. Thus, there is no additional information to be gained by plotting y_f against ϕ^- instead of ϕ_0.*

7.6   Conclusions

The crossing of the frozen separatrices of the unperturbed system by trajectories of the perturbed system corresponds to a resonance condition in the unaveraged equations, Eqs. (6.32)–(6.34). In this chapter, we investigated this resonance for the flat spin recovery problem. We obtained a very accurate approximate solution for the thickness of the boundary layer, or resonant zone, using an expansion of the $\varepsilon = 0$ solution near the separatrix. We also obtained a reasonably accurate approximation for the flow through the resonance, by patching the numerical solutions to the averaged equations through the resonant zone using Euler integration. A "one-step" separatrix crossing model was developed as well; however, it fails because we cannot predict the length of time the trajectory spends near the separatrix. It may be that this approach can be improved by developing an accurate estimate of the time spent near the separatrix.
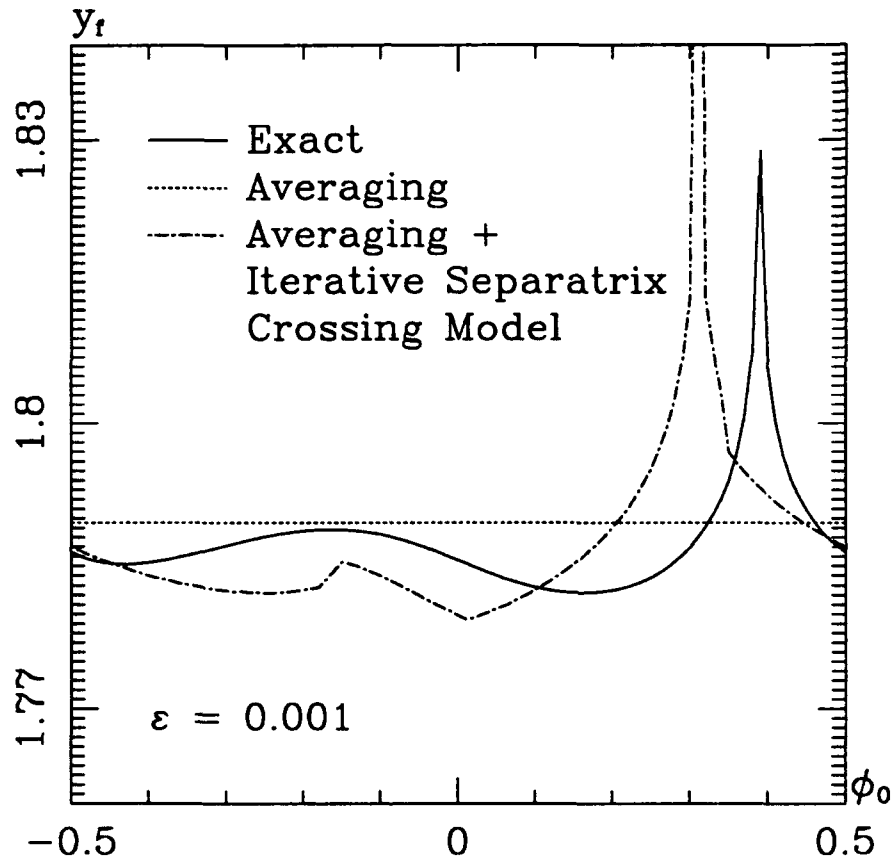
Figure 7.17. Comparison of Separatrix Crossing Model with Exact Solution and Averaging Solution for $\varepsilon = 0.001$, $(i_2, i_3) = (-0.3, -0.7)$. The final energy $y_f(\mu = 1)$ is plotted against the initial phase ϕ_0. Note that the iterative separatrix crossing model captures the qualitative features of the actual system. However, due to the error incurred in averaging, and the sensitivity to small changes in initial conditions, we cannot accurately approximate trajectories that cross the separatrix. Cf. Figs. 7.13 and 6.4.

Chapter 8

Exact and Approximate Solutions to the Averaged Equation

In Chapter 6 we saw that numerical solutions to the averaged equation

$$\bar{y}' = -2\bar{x} \tag{8.1}$$

accurately describe the dynamics of the slow variables as long as the resonance zones are avoided, and are reasonably accurate even in some of the passage through resonance cases. For this reason, it is worthwhile to seek approximate analytical solutions to the averaged equation. In this chapter, we develop an approximate solution for oblate spinup, and solutions for two of the legs of flat spin recovery. These approximations compare quite well with exact solutions of the original equations, as shown in representative plots.

We begin by enumerating all of the exact solutions to the averaged equation for oblate gyrostats. (We do not discuss intermediate gyrostats in this chapter.) Then these solutions are used as a base for a further perturbation analysis to obtain approximate solutions. The basic idea is to first show that the solid curves in the μy plane (see Fig. 4.6) are exact solutions to Eq. (8.1). Then we define a local coordinate, ζ, representing the perpendicular distance from an exact solution in the μy plane. Expansion of Eq. (8.1) in a Taylor series in ζ then yields

an equation which may be solved using an ordinary perturbation approach.

8.1 Exact Solutions

In this section we show that the solid curves, $\mathbf{O}_\mu$, $\mathbf{P}_\mu$, and $\mathbf{F}_\mu$, are exact solutions to the averaged equation. We begin with the simplest case, $\mathbf{O}_\mu$, or $y = -2\mu$.

As we noted in Table 5.3, the repeated root of the gyroscopic function along $\mathbf{O}_\mu$ is $a = b = 1$, with the result that $x = 1$ for $\epsilon = 0$. Since $\mathbf{O}_\mu$ is an equilibrium point for the perturbed system as well as for the unperturbed system, we expect that $\bar{x} = 1$ at $\mathbf{O}_\mu$ as well, and this is in fact the case. This follows easily from $a = b = 1$, since this implies $\alpha^2 = \alpha_1^2 = k^2 = 0$, which, when substituted into Eq. (6.42), gives $\bar{x} = 1$. This in turn implies $\bar{y}' = -2$, or $\bar{y} = -2(\mu - \mu_0) + y_0$. Since any initial condition (y_0, μ_0) satisfying $y_0 = -2\mu_0$ gives $\bar{y} = -2\mu$, $\mathbf{O}_\mu$ is an integral curve of the averaged equation.

The argument that $\mathbf{P}_\mu$ is an exact solution to Eq. (8.1) is identical to the argument for $\mathbf{O}_\mu$. However, we must keep in mind that when $\mathbf{P}_\mu$ is a saddle point, it represents (in the μy plane) both the equilibrium point and the separatrices of the unperturbed system, since they share the same value of the energy y.

For the flat spin equilibria, $\mathbf{F}_\mu$, the exact solution is $\bar{y} = -(\mu^2/i_3 + i_3)$, with repeated root $a = b = \mu/i_3$. (Recall that this branch of unperturbed equilibria is not a solution to the perturbed system.) This trajectory passes through two regions: Region 2 and Region 1aiii. In Region 2, the repeated root leads to $\beta = \mu/i_3$, $\alpha = \alpha_1 = k^2 = 0$. Substituting these values into Eq. (6.47) gives $\bar{x} = \mu/i_3$. (This calculation must be done carefully, as $\alpha = 0$ appears in the denominator of Eq. (6.47).) Using this value of $\bar{x}$ in Eq. (8.1), we obtain $\bar{y} = -(\mu^2/i_3 + i_3)$ for any initial condition starting on $\mathbf{F}_\mu$.

Remark 12 *The fact that $\mathbf{F}_\mu$ is an exact solution to the first-order averaged system has an important implication regarding the use of our approach to obtain an estimate for the residual cone angle at the conclusion of spinup (see Section 4.5).*

In the unaveraged system, Eqs. (3.25)–(3.28), solutions starting exactly at the all-spun flat spin equilibrium point move away from F_μ by an amount depending on ε. Because F_μ is an exact solution of the first-order averaged equations, first-order averaging cannot be used to determine how this effect depends on ε. Thus, to derive a relationship between ε and η for recovery from exact flat spin (see Appendix A), the averaging process would need to be extended to $\mathcal{O}(\varepsilon^2)$. This would increase the complexity by introducing incomplete elliptic integrals of the third kind.

Since $k^2 = 0$ for the exact solutions corresponding to centers on the momentum sphere, we will also use a small modulus assumption in our perturbation approach. This assumption, however, is not uniformly valid, due to the singular points P_{μ_2} and P_{μ_3}. In Fig. 8.1, we show curves of constant modulus for two different values of $k^2 = \text{CONST}$. It is evident that the small k^2 assumption is more appropriate near O_μ and near F_μ in Region 2. However, in Region 1aiii, the modulus increases "faster" as one moves away from F_μ. Similar comments are applicable to P_μ in Region 1aii, and to P_μ for $\mu > \mu_3$.

8.2 Oblate Spinup

The oblate spinup problem is discussed in detail in Section 4.5, and trajectories are shown in Fig. 4.10. As shown in the previous section, the line O_μ (or $y = -2\mu$), is an exact solution to Eq. (8.1). We will also use the fact that the modulus satisfies $k^2 = 0$ along O_μ, and is "small" near O_μ. Oblate spinup trajectories lie entirely inside Region 1ai, and, as shown in Fig. 4.10, are approximately straight lines. In Region 1ai, $\bar{x}$ is given by Eq. (6.42), which we repeat here for convenience:

$$\bar{x} = \frac{\beta}{K} \left\{ K + \frac{\pi(\alpha^2 - \alpha_1^2)[1 - \Lambda_0(\psi, k)]}{2\sqrt{\alpha^2(1 - \alpha^2)(\alpha^2 - k^2)}} \right\} \tag{8.2}$$

where

$$\psi = \sin^{-1}\sqrt{(1 - \alpha^2)/(1 - k^2)} \tag{8.3}$$
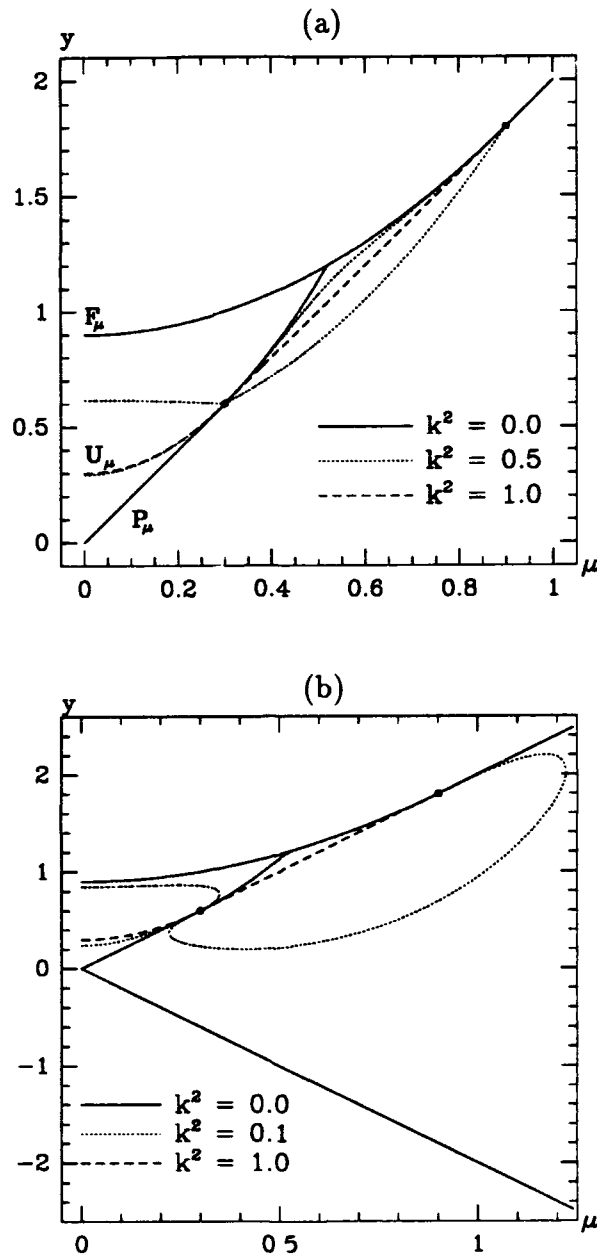
Figure 8.1. Constant Modulus in the μy Plane for $(i_2, i_3) = (-0.3, -0.9)$. In (a) we show curves of $k^2 = 0.5$ in the upper half of the plane, and in (b) we show $k^2 = 0.1$. Points between the dotted curves and the solid curves correspond to "small" k^2, and points between the dotted curves and the dashed curves correspond to "large" k^2. Note that in almost all of Region 1aiii $k^2 > 0.1$, whereas in Regions 1ai, 1aii, and 2, the domain of $k^2 < 0.1$ is reasonably large. Note the different scale for μ in (b).

$$\beta = b \tag{8.4}$$

$$\alpha^2 = \frac{a-b}{a-c} \tag{8.5}$$

$$\alpha_1^2 = \frac{c}{b}\alpha^2 \tag{8.6}$$

$$k^2 = \frac{(a-b)(c-d)}{(a-c)(b-d)} \tag{8.7}$$

and $a = r_2^-$, $b = r_3^-$, $c = r_2^+$, and $d = r_3^+$ are the roots of the gyroscopic function, given by

$$r_2^\pm = \frac{\mu \pm \sqrt{\mu^2 + i_3(i_3 + y)}}{i_3} \tag{8.8}$$

$$r_3^\pm = \frac{\mu \pm \sqrt{\mu^2 + i_2(i_2 + y)}}{i_2} \tag{8.9}$$

All of these quantities are taken from Chapters 5 and 6, and it is evident that each parameter depends only on y, μ, and the inertia parameters i_2 and i_3.

Note also that α^2 and α_1^2 are both $\mathcal{O}(k^2)$, and we can write them as

$$\alpha^2 = \sigma^2 k^2 \tag{8.10}$$

$$\alpha_1^2 = \frac{c}{b}\sigma^2 k^2 \tag{8.11}$$

where

$$\sigma^2 = \frac{b-d}{c-d} > 1 \tag{8.12}$$

since $b > c > d$.

Before we do the required calculations, we outline the procedure to be followed. First, noting that $k^2 = 0$ when $\xi = 0$, we expand the elliptic integrals in $\bar{x}$ as power series in k^2, making use of the series developments given in Appendix D. Next, referring to Fig. 8.2, we define the local variable ξ by

$$\xi = y + 2\mu \tag{8.13}$$

Thus ξ is perpendicular to $\mathbf{O}_\mu$, and $\xi = 0$ corresponds to the exact solution $y = -2\mu$. Then we expand $\bar{x}$ as a power series in ξ, to say $\mathcal{O}(\xi)$, *i.e.*,
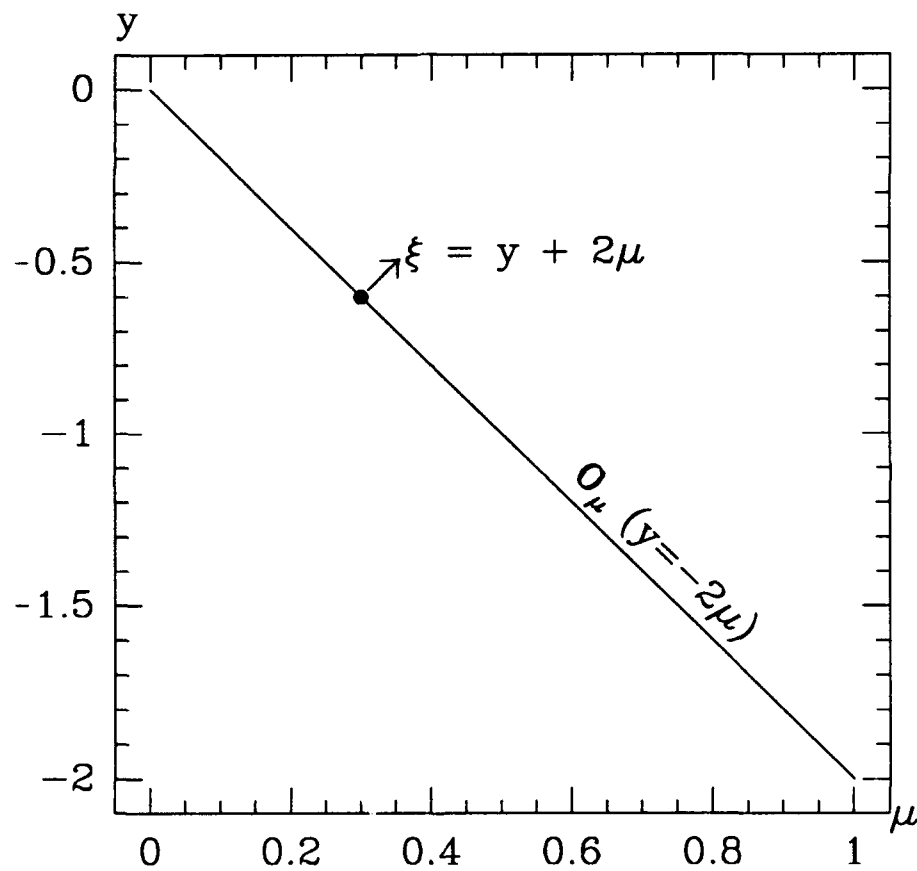
$$\bar{x} = 1 - f(\mu)\xi + \mathcal{O}(\xi^2) \tag{8.14}$$

Figure 8.2. Local Perturbation Coordinate ξ for Oblate Spinup. ξ is perpendicular to O_μ, where the modulus satisfies $k^2 = 0$, and k^2 is small for small ξ. Cf. 8.1.

where we have used the fact that $\bar{x} = 1$ when $\xi = 0$. Differentiating Eq. (8.13) with respect to μ, and applying Eqs. (8.1) and (8.14), we obtain

$$\frac{d\xi}{d\mu} = 2f(\mu)\xi \tag{8.15}$$

where we have truncated the $\mathcal{O}(\xi^2)$ terms. This equation is separable and leads to

$$\xi = \xi_0 \exp\left\{2\int_{\mu_0}^{\mu} f(\hat{\mu})d\hat{\mu}\right\} \tag{8.16}$$

where $\xi_0 = \xi(0) = y_0 + 2\mu_0$. Rewriting ξ and ξ_0 in terms of $\bar{y}$, μ, y_0, and μ_0, we obtain

$$\bar{y}_a(\mu) = -2\mu + (y_0 + 2\mu_0)\exp\left\{2\int_{\mu_0}^{\mu} f(\hat{\mu})d\hat{\mu}\right\} \tag{8.17}$$

where the subscript a denotes that this is an approximate solution. This concludes the outline of the procedure. As a final note, we point out that the evaluation of $f(\mu)$ is quite complex. Most of the calculations were done using the symbolic programming languages MACSYMA [85] and Mathematica [105], with some "manual" assistance to circumvent the problem areas we discuss in Section 8.4. We now carry out the calculations necessary to obtain $f(\mu)$, and ultimately $\bar{y}_a(\mu)$.

In order to expand Eq. (8.2) as a power series in k^2, we need the series representations of $K(k)$ and $\Lambda_0(\psi, k)$, as developed in Appendix D. Keeping only terms of $\mathcal{O}(k^2)$, we repeat the series here for convenience:

$$K(k) = \frac{\pi}{2}\left(1 - \frac{1}{4}k^2\right) \tag{8.18}$$

$$\Lambda_0(\psi, k) = \sin\psi\left(1 - \frac{1}{4}k^2\right) \tag{8.19}$$

where it is understood that the series are valid to $\mathcal{O}(k^2)$.

Since ψ and k are functions of y and μ, then so is Λ_0. Making use of Eqs. (8.3) and (8.10), we can write Λ_0 as

$$\Lambda_0(y, \mu) = \sqrt{\frac{1 - \sigma^2 k^2}{1 - k^2}}\left(1 - \frac{1}{4}k^2\right) \tag{8.20}$$

Using this version of Λ_0, we can write $\bar{x}$ as a function of k^2, b, c, and σ^2, all of which are functions of the four roots of the gyroscopic function:

$$\bar{x} = \beta \left\{ 1 + \frac{\sigma^2(1 - c/b)\left[1 - \sqrt{\frac{1-\sigma^2 k^2}{1-k^2}}(1 - k^2/4)\right]}{(1 - k^2/4)\sqrt{\sigma^2(1 - \sigma^2 k^2)(\sigma^2 - 1)}} \right\} \tag{8.21}$$

The next step is to use the definition of ζ, Eq. (8.13) to put $y = \zeta - 2\mu$ in a, b, c, and d, wherever they appear in $\bar{x}$, using Eqs. (8.4)–(8.7). This is a lengthy calculation, and was performed using Mathematica. Once this step is completed, we have an explicit expression for $\bar{x}$ in terms of the variables μ and ζ only. We then expand $\bar{x}$ in a Taylor series in ζ, keeping only terms of $\mathcal{O}(\zeta)$, which gives

$$\bar{x} = 1 - \left\{ \frac{1}{2(\mu - i_2)} - \frac{(i_2 - i_3)(2i_2 i_3 - (i_2 + i_3)\mu)}{8(\mu - i_2)\sqrt{i_3(\mu - i_2)(i_2\mu - i_2 i_3)}} \right\} \zeta \tag{8.22}$$

This approximate expression for $\bar{x}$ explicitly defines $f(\mu)$ in Eq. (8.14): $f(\mu)$ is the coefficient of ζ.

Now, knowing $f(\mu)$, we can evaluate the integral in Eq. (8.16), and substitute the result into Eq. (8.17) to obtain:

$$\begin{aligned}
\bar{y}_a(\mu) &= -2\mu + (y_0 + 2\mu_0)\left(\frac{\mu - i_2}{\mu_0 - i_2}\right) \times \\
&\quad \exp\left\{ \frac{i_2 - i_3}{2\sqrt{i_2 i_3}}\left[\frac{\mu_0}{\sqrt{(\mu_0 - i_2)(\mu_0 - i_3)}} - \frac{\mu}{\sqrt{(\mu - i_2)(\mu - i_3)}} \right] \right\}
\end{aligned} \tag{8.23}$$

For initial conditions starting near O_μ, Eq. (8.23) gives an accurate trajectory in the μy plane. It is also evident that if $y_0 = -2\mu_0$, the exact solution $y = -2\mu$ is obtained. Some comparisons are shown in Fig. 8.3, showing that the error increases with increasing distance from the line O_μ, as expected.

8.3 Flat Spin Recovery

For flat spin recovery, the trajectories pass through three regions of the μy plane, Regions 2, 1aiii, and 1ai, as explained in Section 4.5 and shown in Fig. 4.13. In this section we obtain approximate solutions for $\bar{y}(\mu)$ in two of these regions:

Figure 8.3. Comparison of Approximate and Exact Solutions to the Averaged Slow Flow in Region 1ai for Oblate Spinup for $(i_2, i_3) = (-0.3, -0.7)$. The approximate and exact solutions are shown for three different initial conditions. Referring to Fig. 8.2, we note that the approximation is increasingly accurate as $\xi \to 0$.

Region 2 and Region 1ai. The reason for not treating Region 1aiii is discussed in Section 8.4.

8.3.1   Region 2

For Region 2, the procedure is similar to that for Region 1ai for oblate spinup; however, since $\mathbf{F}_\mu$ is quadratic in μ, the details are different. The local coordinate ξ in this case is defined by

$$\xi = -y - \left(\frac{\mu^2}{i_3} + i_3\right) \tag{8.24}$$

which is perpendicular to the curve $\mathbf{F}_\mu$ in the μy plane, as shown in Fig. 8.4.
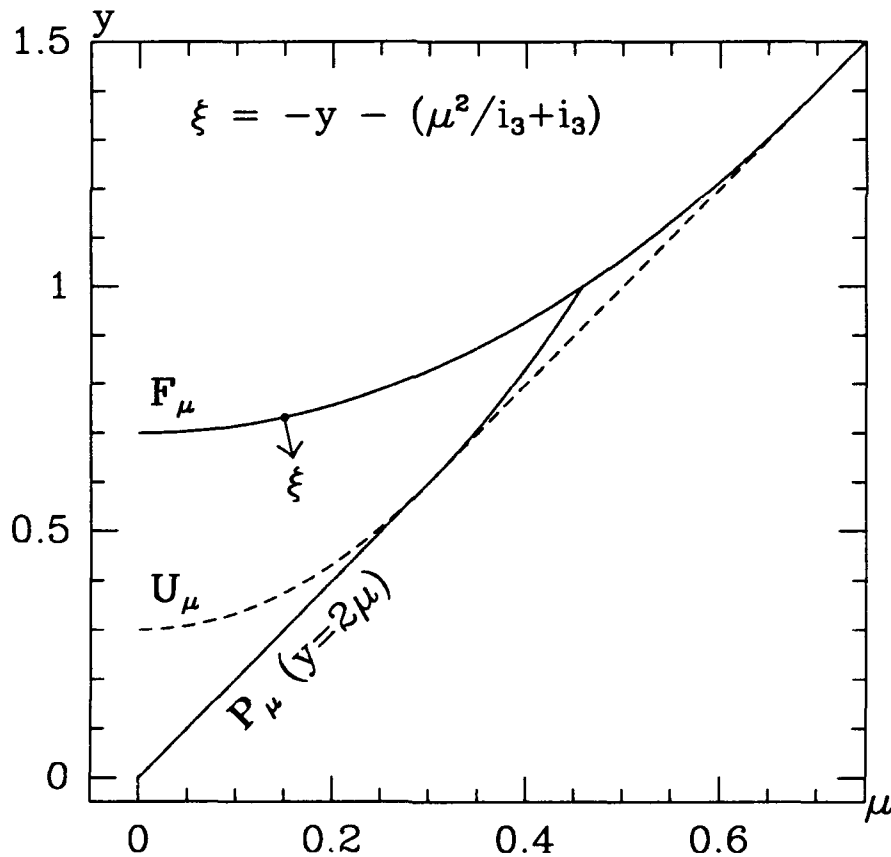
Figure 8.4. Local Perturbation Coordinate ξ for Flat Spin Recovery in Region 2. ξ is perpendicular to $\mathbf{F}_\mu$, where the modulus satisfies $k^2 = 0$, and k^2 is small for small ξ.

When $\xi = 0$, $x = \mu/i_3$, so we expect to find

$$\bar{x} = \frac{\mu}{i_3} + f(\mu)\xi + \mathcal{O}(\xi^2) \tag{8.25}$$

In Region 2, $\bar{x}$ is given by Eq. (6.47), and the parameters are defined at Eqs. (5.19)–(5.24). Making use of the series representation of $\Pi(\hat{\alpha}^2, k)$ derived in Appendix D, and performing similar calculations to those done in the previous section, we we obtain the $\mathcal{O}(\xi)$ approximation

$$\bar{x} = \frac{\mu}{i_3} + \frac{\mu}{2(\mu^2 - i_3^2)}\xi \tag{8.26}$$

As before, differentiating Eq. (8.24) and substituting Eq. (8.26) into the result gives

$$\frac{d\xi}{d\mu} = \frac{\mu}{\mu^2 - i_3^2}\xi \tag{8.27}$$

to $\mathcal{O}(\xi)$. This equation is easily solved to obtain $\xi(\mu)$, after which Eq. (8.24) leads to the approximate solution:

$$\bar{y}_a(\mu) = -\left(\frac{\mu^2}{i_3} + i_3\right) + \left[y_0 + \frac{\mu_0^2}{i_3} + i_3\right]\sqrt{\frac{i_3^2 - \mu^2}{i_3^2 - \mu_0^2}} \tag{8.28}$$

Some sample comparisons are shown in Fig. 8.5. Again, the agreement is quite good for trajectories reasonably close to the exact solution $\mathbf{F}_\mu$, and as expected, the exact solution is obtained for initial conditions starting on the curve $\mathbf{F}_\mu$.

8.3.2 Region 1ai

In Region 1ai for flat spin recovery, the procedure is exactly the same as for oblate spinup. The only difference is that the perturbation is from $\mathbf{P}_\mu$ ($\mu > -i_3$) instead of $\mathbf{O}_\mu$. Thus the local coordinate is

$$\xi = 2\mu - y \tag{8.29}$$

Omitting discussion of the lengthy calculations, the resulting approximate solution is

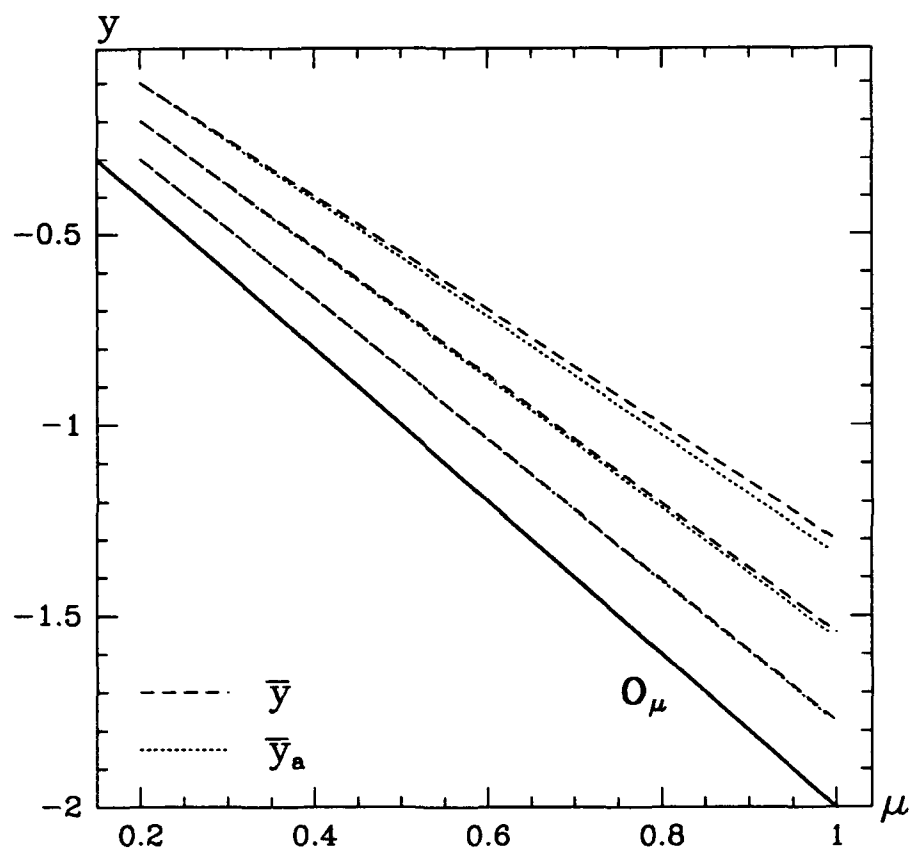$$\bar{y}_a(\mu) = 2\mu - (2\mu_0 - y_0)\frac{\mu + i_2}{\mu_0 + i_2}\exp\{F(\mu) - F(\mu_0)\} \tag{8.30}$$

Figure 8.5. Comparison of Approximate and Exact Solutions to the Averaged Slow Flow in Region 2 for Flat Spin Recovery for $(i_2, i_3) = (-0.3, -0.7)$. The approximate and exact solutions are shown for three different initial conditions (marked by dots). Referring to Fig. 8.4, we note that the approximation is increasingly accurate as $\xi \to 0$.

where

$$F(\mu) = \frac{(i_2 - i_3)\mu}{2\sqrt{i_2 i_3 (\mu + i_2)(\mu + i_3)}} \qquad (8.31)$$

Note that this solution has a singularity at $\mu = -i_3$, which is the value of μ at which the bifurcation $\mathbf{P}_{\mu_3}$ occurs. This may be understood by recalling that $k^2 = 1$ along $\mathbf{P}_\mu$ when $\mathbf{P}_\mu$ is a saddle point, whereas our development explicitly uses a small modulus assumption. Comparisons between exact and approximate solutions are shown in Fig. 8.6.

8.4 Difficulties in Region 1aiii

We were unable to obtain an approximate solution in Region 1aiii due to difficulties encountered with the symbolic programming languages MACSYMA and Mathematica and differentiation of functions involving square roots of the independent variable. Note that $\bar{x}$ involves many square roots through its dependence on the roots of the gyroscopic function, which depend on y and μ, Eqs. (8.8) and (8.9). Thus, when the substitution $y = -\xi - (\mu^2/i_3 + i_3)$ is made, ξ appears exclusively as the argument of square roots. Because of this aspect of $\bar{x}$'s dependence on ξ, obtaining a Taylor series about $\xi = 0$ must be done carefully.

Consider the following example: Suppose one has the function

$$g(x) = \sqrt{(a - b)^2 + x} \qquad (8.32)$$

for which the correct Taylor series, about $x = 0$, is

$$g(x) = |a - b| + \mathcal{O}(x) \qquad (8.33)$$

Using MACSYMA's TAYLOR function to compute the Taylor series gives

$$g(x) = b - a + \mathcal{O}(x) \qquad (8.34)$$

which is only correct if $b > a$. Furthermore, putting $a = c$ in $g(x)$ causes MACSYMA to answer

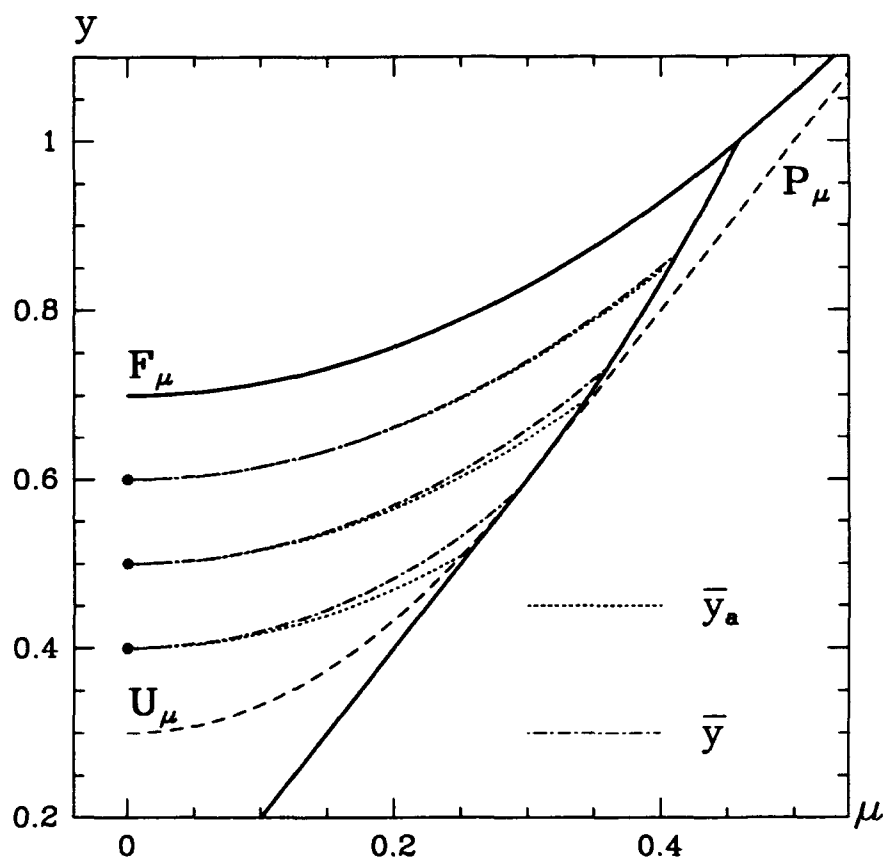$$g(x) = c - b + \mathcal{O}(x) \qquad (8.35)$$
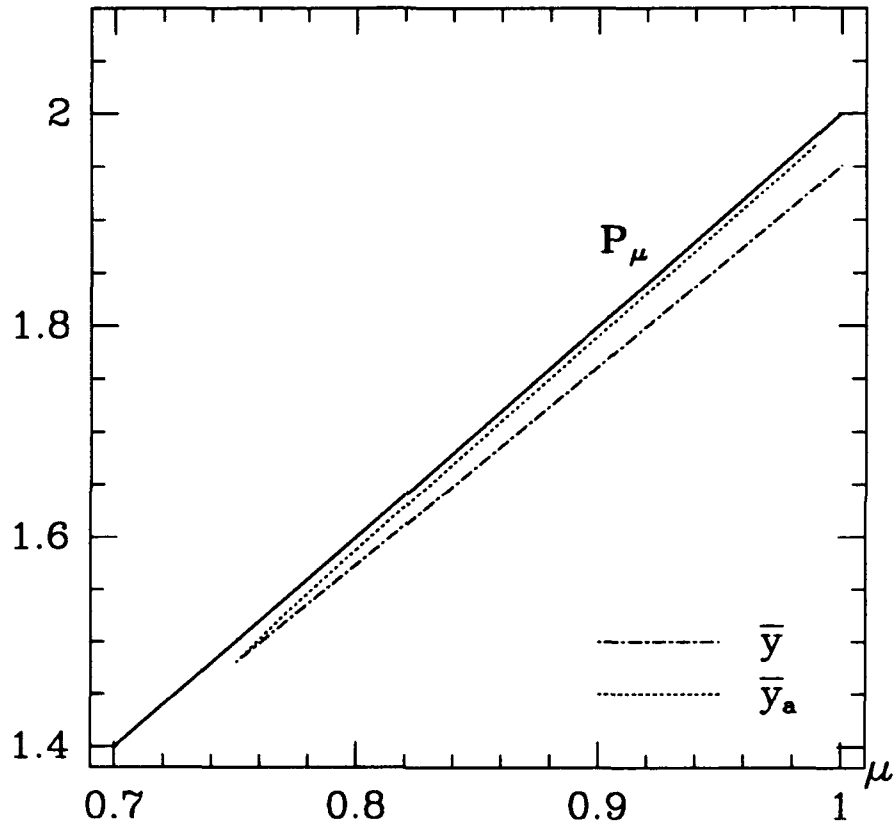
Figure 8.6. Comparison of Approximate and Exact Solutions to the Averaged Slow Flow in Region 1ai for Flat Spin Recovery for $(i_2, i_3) = (-0.3, -0.7)$. The divergence of the two solutions is due to the fact that the small k^2 assumption is not as applicable in this region (cf. Fig 8.1), and to the singularity in Eq. (8.31) at $\mu = -i_3$. As $\xi_0 \to 0$ and μ_0 becomes "sufficiently" greater than $-i_3$, the accuracy of the approximation increases.

which is only correct if $c > b$, or, since $c = a$, $a > b$, which disagrees with the previous response. Incredibly, *the answer depends on the alphabetical order of the variables.*

While Mathematica does not commit this error, it does have a tendency to rearrange expressions according to some internal rules. One rearrangement that causes problems with the kind of calculations we have been performing is the following: whenever Mathematica encounters an expression like $\sqrt{-a}$, it replaces it with $i\sqrt{a}$.

We were able to overcome these difficulties for the problems we did solve, by manually performing difficult parts of the calculations. However, for Region 1aiii, the intermediate expressions were large and we were unable to simplify them sufficiently to obtain a solution.

Note also that the small k^2 assumption is not as applicable in Region 1aiii as in Region 2. Thus an approximate solution using $\mathcal{O}(k^2)$ approximations would not be as accurate as the Region 2 solution.

8.5   Conclusions

Perturbing off of exact solutions to the averaged equation leads to approximate solutions for the slow evolution of the energy, y, during spinup. These approximate solutions are very accurate for initial conditions near the appropriate exact solutions. The techniques used here should be applicable to other problems leading to averaged equations involving elliptic integrals.

The difficulties we encountered with differentiating square roots could probably be resolved by developing routines to manipulate such functions, especially to calculate the Taylor series.

Chapter 9

Summary and Conclusions

In this chapter we give a brief summary of the results obtained in the thesis, followed by further discussion of some of the problems which remain to be solved.

9.1 Summary

We have studied the dynamics of rigid axial gyrostats when the angular momentum of the rotor about its symmetry axis is increased by the application of a small constant internal torque, ε. We have shown that this four-dimensional problem can be reduced to a one-dimensional problem by exploiting conservation of angular momentum and applying the method of averaging. This reduction results in a single first-order non-autonomous ordinary differential equation for the slow evolution of kinetic energy during spinup. This *slow flow* equation involves complete elliptic integrals of the first, second, and third kinds. While it cannot be solved analytically, one advantage of the averaged equation for the slow flow is that the required step size for numerical integration is independent of ε, whereas for the full system of equations, the required step size decreases as ε decreases. Hence for small ε, where the averaged equations are most applicable, numerical integration of the slow flow equation is more efficient than for the full system.

Previous studies of spinup dynamics have used the full four-dimensional flow,

and have subsequently been restricted either to particular classes of gyrostats, or to particular regions of phase space. In this work, however, we have given a unified treatment for *all* axial gyrostats. Our ability to do this was enhanced by our discovery of a previously unknown symmetry relating oblate and prolate gyrostats, thereby reducing the number of cases which must be considered.

While averaging works well almost everywhere, the phase space of the system contains resonant zones where the frequency of the unperturbed system vanishes, and hence the averaged equations are not valid in these regions. These resonant zones correspond to regions of phase space where the trajectories of the perturbed system cross the *frozen* or *instantaneous* separatrices of the unperturbed system, and are easily identified in terms of our one-dimensional representation of spinup dynamics. For most trajectories, the averaged equation provides an acceptable approximation of the exact flow, even if an instantaneous separatrix is crossed. However, for some trajectories that pass very close to the saddle point, the error is significant. An important observation is that the $\mathcal{O}(\varepsilon)$ error incurred in averaging implies that *no separatrix crossing model can accurately predict how* all *trajectories will cross the separatrix.*

In our investigation of the separatrix crossing problem, we obtained an approximate solution for the change in energy associated with a change in phase for the flow near these instantaneous separatrices, and used this solution to obtain an accurate formula for the thickness of the resonant zone, or boundary layer. An Euler integration technique, using the $\varepsilon = 0$ solution in a neighborhood of the separatrix, was used to connect the averaged solutions across the separatrix. This technique gives results that agree qualitatively with the exact solutions.

Since the averaged equations provide an accurate approximation for the flow outside of the resonant zones, but are not explicitly integrable themselves we obtained approximate analytical solutions to the averaged slow flow equation. These solutions are reasonably simple and quite accurate for trajectories which

remain near the equilibrium points of the unperturbed system. The calculations involved, however, are not simple, and we were unable to obtain approximate solutions in some cases.

9.2 Approximate Solutions of the Averaged Equations

As noted in Section 8.4, we were unable to obtain an approximate solution to the averaged slow flow equation for flat spin recovery in Region 1aiii, due to difficulties with the computer algebra systems we used. If these difficulties could be resolved, and solutions were obtained for Region 1aiii, then it would be possible, in principle, to patch the solutions in Regions 2, 1aii and 1ai (near P_μ) together to obtain a complete analytic approximation for flat spin recovery. The central problem with connecting these solutions will be dealing with the singularity at the bifurcation value $\mu = \mu_3$ (cf. Eqs. (8.30) and (8.31)).

Similar solutions could be obtained for intermediate spinup. However, for prolate spinup, this procedure is not likely to work. Recall that for prolate spinup, small torque means large cone angle after the separatrix crossings (cf. Fig. 4.12). This means that for small ε, the post-separatrix crossing prolate spinup trajectories are not near any of the unperturbed equilibrium points. Therefore perturbing from the unperturbed equilibria is not applicable. In the case of large torque, the trajectories do remain near the equilibrium point P_μ; however, the averaged equations are not expected to be valid for large ε. Hence we do not expect the method to yield valid results for prolate spinup.

9.3 Separatrix Crossing

As we discussed in Section 7.1, the separatrix crossing problem has generated much interest over the past two decades. A useful result obtained here is the accurate formula for the "thickness" of the last cycle before the separatrix crossing. This formula was based on an approximate solution for the energy for a given

change of phase near the separatrix. While this solution describes how the energy changes, it gives no clue as to how much *time* is spent near the separatrix. What is needed to complement our inner solution is a relationship between the change in phase, Δu, and the change in time, Δt. Assuming such a relationship can be developed, one would be able to accurately connect the averaged solutions across the separatrix.

9.4   More General Gyrostatic Problems

We have focused on *axial* gyrostats, which possess a unique symmetry due to the alignment of the rotor axis with a principal axis of the platform. This symmetry is evident in the topology of the polhodes on the $\varepsilon = 0$ momentum spheres (cf. Fig. 4.3). In the μy plane, this symmetry means the curves $\mathbf{F}_\mu$ and $\mathbf{U}_\mu$ each correspond to two equivalent branches of equilibria on the sphere.

What happens when we break this symmetry? That is, what if the rotor's axis of symmetry is not aligned with a platform principal axis? In this case, it is easy to verify that the moment of inertia tensor is still constant, and that the $\varepsilon = 0$ integrals corresponding to conservation of angular momentum, conservation of kinetic energy, and conservation of axial angular momentum of the rotor are all constants of the motion. Thus the $\varepsilon = 0$ motion corresponds to constant energy polhodes on the momentum sphere, just as in the axial case. On the momentum sphere, the effect of breaking the symmetry is to change the pitchfork bifurcations we discussed in Chapter 4 to saddle-node bifurcations (see Ref. [26, pp. 146–149]). In fact, Wittenburg [103] has shown how to reduce the equations of motion to an elliptic integral in this case; however, the integral is more complicated than for axial gyrostats, and he did not invert the integral to obtain solutions for the angular momentum variables as functions of time. If these solutions can be explicitly obtained, the techniques developed here can readily be extended to this more general case.

Appendix A

Gebman and Mingori's Work

The flat spin recovery problem has received some attention in the literature. The work that is most similar to this thesis is the paper by Gebman and Mingori [23], published in 1976, which is based on Gebman's Ph.D. thesis [24]. Since their work is relevant to our treatment of flat spin recovery, we devote this appendix to a discussion of their approach and results.

First, we point out the fundamental difference between the problem they investigated and the problem considered here. In their treatment, the initial flat spin condition is *exactly* at flat spin, that is to say,

$$(x_1, x_2, x_3, \mu) = (0, \pm 1, 0, 0) \tag{A.1}$$

which corresponds to the point $(\mu, y) = (0, -i_3)$ in the μy plane in Fig. 4.13. Conversely, in our treatment the initial conditions are essentially arbitrary. To apply the asymptotic approximations obtained in Chapter 8, the initial condition should be "close" to flat spin, but not necessarily on the equilibrium point. Also we provide a unified approach to dealing with all spinup problems, not just the flat spin recovery problem.

In the analysis of [23]–[24], the authors dealt directly with the angular momentum variables, in a dimensionless form somewhat different from that used here. The relationships between their variables and parameters and those used

172

Table A.1. Original Parameters

Parameter	Gebman	Hall
Moments of Inertia		
Maximum	$I_1 + K_1$	I_2
Intermediate	$I_2 + K_1$	I_3
Minimum	$I_3 + K_3$	I_1
Platform (Axial)	I_3	I_p
Rotor (Axial)	K_3	I_s
Angular Momentum	$(I_1 + K_1)\Omega$	h
Axial Torque	L	g_a
Time	T	$\tilde{t}$

Note that Gebman's rotor is aligned with the 3-axis whereas ours is aligned with the 1-axis.

in this thesis are given in Tables A.1–A.4. They used a two-scale expansion to obtain approximate analytic solutions for the angular momenta in the domains corresponding to Regions 2, 1aiii, and 1ai (see Figs. 5.4 and 4.13). To get across the separatrix, they stretched time and obtained a parameter-free second-order differential equation with time-varying coefficients for the motion through the resonance (see Remark below). They then numerically integrated this equation and matched the result to the two "outer" solutions.

They ran several comparisons for different values of the parameters, with varying degrees of success. For example, in his thesis, Gebman noted that "the errors do not seem to follow any particular pattern," giving as an example a case where the "percentage error in the asymptotic estimate ... 'jumps' from -11.8 percent to -1.7 percent for only a 3 percent increase in ϵ." [24, p. 151].

He also devoted a section of his thesis to "The Phase Difference Problem,"

Table A.2. Dimensionless Parameters

Parameter	Gebman	Hall
Inertia	$\lambda = \sqrt{\frac{(I_1-I_2)I_3}{(I+2+K_1)(I_1+K_1-I_3)}}$	$i_2 = 1 - I_p/I_2$
		$i_3 = 1 - I_p/I_3$
Torque	$\varepsilon_G = \frac{L(I_2+K_1)}{(I_1+K_1-I_3)(I_1-I_2)\Omega^2}$	$\varepsilon = g_a I_p/h^2$
Time	$t = \alpha T$	$t = h\tilde{t}/I_p$
	$\alpha = \sqrt{\left(\frac{I_1+K_1}{I_3} - 1\right)\left(\frac{I_1+K_1}{I_2+K_1} - 1\right)}\Omega$	
	$\bar{\alpha} = \alpha/\Omega$	

discussing the fact that the phase of the asymptotic approximation differed significantly from the exact solution as represented by numerical integration of the full equations. He hypothesized that for smaller ε this discrepancy would disappear.

However, as we have seen in Chapter 7, the passage through resonance can be quite sensitive to small changes in either the initial conditions or ε.

Remark 13 *The "parameter-free" differential equation obtained by Gebman and Mingori is*

$$\frac{d^2y}{d\tau^2} + \frac{1}{2}y^3 + \tau y = 0 \tag{A.2}$$

in which τ is a time-like variable obtained by scaling the "original" time. Patching numerical solutions of this equation to the analytical approximations obtained for the "outer" regions involved patching the asymptotic initial conditions as $\tau \rightarrow -\infty$ and the "post-resonance" conditions as $\tau \rightarrow +\infty$.

In an unrelated paper by Haberman [29], a similar equation is identified as the "second Painlevé transcendent" (cf. Ince [40, pp. 345–355]), and he uses matched asymptotic expansions to obtain the asymptotic behavior of this equation. A possible extension of Gebman and Mingori's work would be to apply Haberman's findings to Eq. (A.2).

Table A.3. Relation Between the Dimensionless Parameters

Gebman	Hall
$\lambda = \sqrt{\dfrac{i_2 - i_3}{i_2}}$	$i_2 = \dfrac{\bar{\alpha}}{\bar{\alpha} + \lambda}$
$\bar{\alpha} = \dfrac{\sqrt{i_2(i_2 - i_3)}}{1 - i_2}$	$i_3 = \dfrac{\bar{\alpha}(1 - \lambda^2)}{\bar{\alpha} + \lambda}$
$\varepsilon_G = \dfrac{\varepsilon}{i_2(i_2 - i_3)}$	$\varepsilon = \dfrac{\bar{\alpha}^2 \lambda^2 \varepsilon_G}{(\bar{\alpha} + \lambda)^2}$

Table A.4. Gebman's Auxiliary Parameters

$G = 0.880 \dfrac{\sqrt{1 + \frac{1}{2}\left(\frac{I_1 - I_2}{I_2 + K_1}\right)}}{\left(1 - \frac{I_3}{I_1 + K_1}\right)\left(\frac{I_1 - I_2}{I_2 + K_1}\right)}$	$G = 0.880(1 - i_2)\dfrac{\sqrt{1 + \frac{1}{2}\left(\frac{i_2 - i_3}{1 - i_2}\right)}}{i_2(i_2 - i_3)}$
$\text{BAIR} = \dfrac{I_3}{I_1 + K_1}$	$\text{BAIR} = 1 - i_2$
$\text{IDR} = \dfrac{I_1 - I_2}{I_2 + K_1}$	$\text{IDR} = \dfrac{i_2 - i_3}{1 - i_2}$

BAIR = Bearing Axis Inertia Ratio

IDR = Inertia Distribution Ratio

Appendix B

The Inertia Parameter Space

In Chapter 3 we stated without proof that the triangle inequalities for moments of inertia lead to restrictions on the dimensionless inertia parameters i_2 and i_3 as illustrated in Fig. 3.2. In this appendix we carry out the calculations that lead to Fig. 3.2 and the equations for the boundary curves, Eq. (3.43).

The triangle inequalities for a rigid body's moments of inertia are

$$I_1 + I_2 > I_3 \tag{B.1}$$

$$I_2 + I_3 > I_1 \tag{B.2}$$

$$I_3 + I_1 > I_2 \tag{B.3}$$

where the $I_j (j = 1, 2, 3)$ are the principal moments of inertia. These follow directly from the definitions of the principal moments of inertia as follows. The principal moments of inertia may be defined as integrals over the body, *e.g.*,

$$I_1 = \int_{\mathcal{B}} (r_2^2 + r_3^2) dm \tag{B.4}$$

where r_2 and r_3 are the projections onto the principal axes $\mathbf{e}_1$ and $\mathbf{e}_2$ of a position vector $\mathbf{r}$ which points to the element of mass dm. The moments of inertia I_2 and I_3 are similarly defined. Then

$$I_1 + I_2 = \int_{\mathcal{B}} (r_1^2 + r_2^2 + 2r_3^2) dm \tag{B.5}$$

or

$$I_1 + I_2 = I_3 + \int_B 2r_3^2 \, dm \tag{B.6}$$

Since all the quantities involved are real, Eq. (B.1) is proved. The other two inequalities follow by permuting the indices.

Now, our dimensionless inertia parameters are defined by

$$i_j = 1 - I_p/I_j, \qquad j = 1, 2, 3 \tag{B.7}$$

from which we can write

$$I_j = I_p/(1 - i_j), \qquad j = 1, 2, 3 \tag{B.8}$$

Note that since $I_j > 0$ and $I_p > 0$, it follows from Eq. (B.8) that $1 - i_j > 0$, or $i_j < 1$. Substituting Eq. (B.8) into Eq. (B.1), then simplifying and rearranging, we obtain

$$i_3 < \frac{1 - i_1 i_2}{2 - i_1 - i_2} \tag{B.9}$$

This inequality defines the bounding curve (III) in Fig. 3.2, reproduced here in Fig. B.1(a). Note that since $i_1 < 1$ and $i_2 < 1$, this curve has no singularities in the domain of interest. Also, a simple L'Hôpital calculation shows that the asymptote as $i_2 \to -\infty$ is $i_3 \to i_1$.

A similar calculation using Eq. (B.3) leads to the curve (II). However, this can also be obtained by Symmetry 1, obtaining

$$i_2 < \frac{1 - i_1 i_3}{2 - i_1 - i_3} \tag{B.10}$$

Solving this inequality for i_3 gives

$$i_3 > \frac{2i_2 - i_1 i_2 - 1}{i_2 - i_1} \tag{B.11}$$

which defines bounding curve (II), shown in Fig. B.1(b).

Finally, substituting Eq. (B.8) into Eq. (B.2), we obtain

$$i_3 > \frac{1 + i_1 i_2 - 2i_1}{i_2 - i_1} \quad \text{if} \quad i_1 > i_2 \tag{B.12}$$

$$i_3 < \frac{1 + i_1 i_1 - 2i_1}{i_2 - i_1} \quad \text{if} \quad i_1 < i_2 \tag{B.13}$$

Figure B.1. Bounding Curves (III) and (II) in the $i_2 i_3$ Plane. (a) Curve (III), defined by Eq. (B.9), for $i_1 = 0.3$. (b) Curve (III) and Curve (II), defined by Eq. (B.11), for $i_1 = 0.3$.

There is a singularity evident at $i_1 = i_2$. However, the second branch is inapplicable, since Eq. (B.9) gives a stronger upper bound for i_3, as shown in Fig. B.2(a).

Thus the bounding curves in Fig. 3.2 (and the figures that follow) are defined by Eqs. (B.13), (B.11), and (B.9). It is evident in these expressions that the extent of the admissible region depends on the value of i_1. As we noted in Section 3.4, $i_1 = I_s/I_1$, hence $0 < i_1 < 1$, with the limits $i_1 = 0$ and $i_1 = 1$ corresponding to gyrostats with rod-shaped rotor ($I_s = 0$) and rod-shaped platform ($I_p = 0$), respectively. Thus the $i_1 i_2 i_3$ parameter space is a three-dimensional space bounded above and below by the planes $i_1 = 0$ and $i_1 = 1$. Between these planes the space is bounded by the curves defined by Eqs. (B.13), (B.11), and (B.9).

In Fig. B.3, we show the $i_2 i_3$ plane for several values of i_1. Qualitatively, there are two possibilities:

1. In case $i_1 < 1/2$, all four quadrants of the plane intersect the admissible region. Hence all three types of gyrostats are possible.
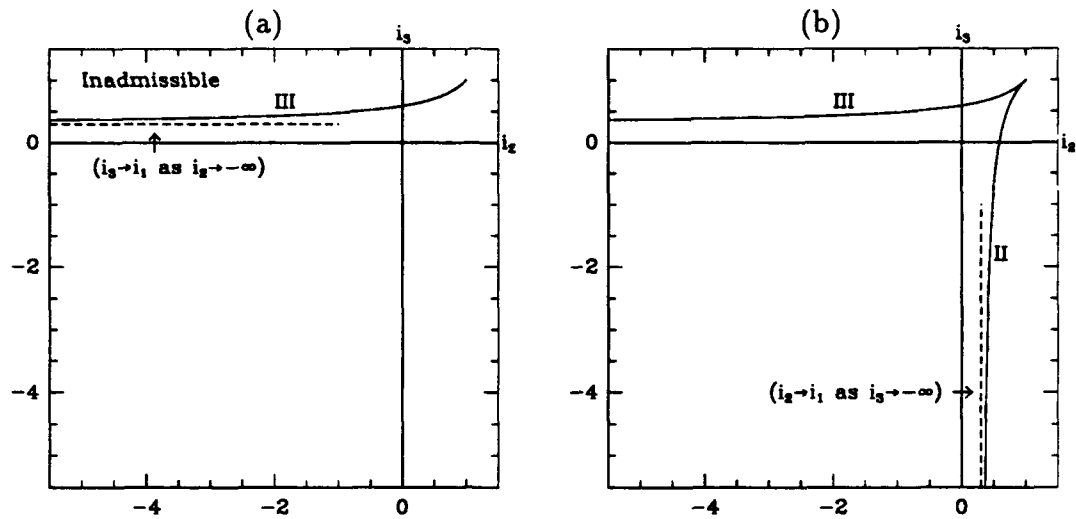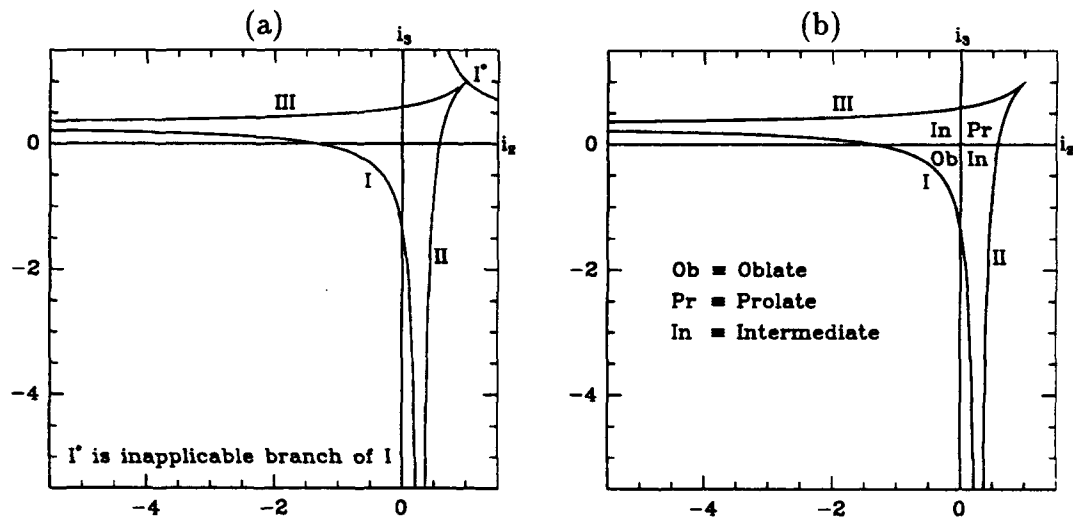
Figure B.2. Bounding Curves (III) and (II) in the $i_2 i_3$ Plane. (a) Curve (III), defined by Eq. (B.9), for $i_1 = 0.3$. (b) Curve (III) and Curve (II), defined by Eq. (B.11), for $i_1 = 0.3$.

2. For $i_1 = 1/2$, curve (I) passes through the origin of the $i_2 i_3$ plane. Therefore, oblate gyrostats are not possible for $i_1 \geq 1/2$.

In the limit $i_1 \to 1$, the bounding curves approach the straight lines $i_3 = 1$, $i_2 = 1$, as shown in Fig. B.3(d).
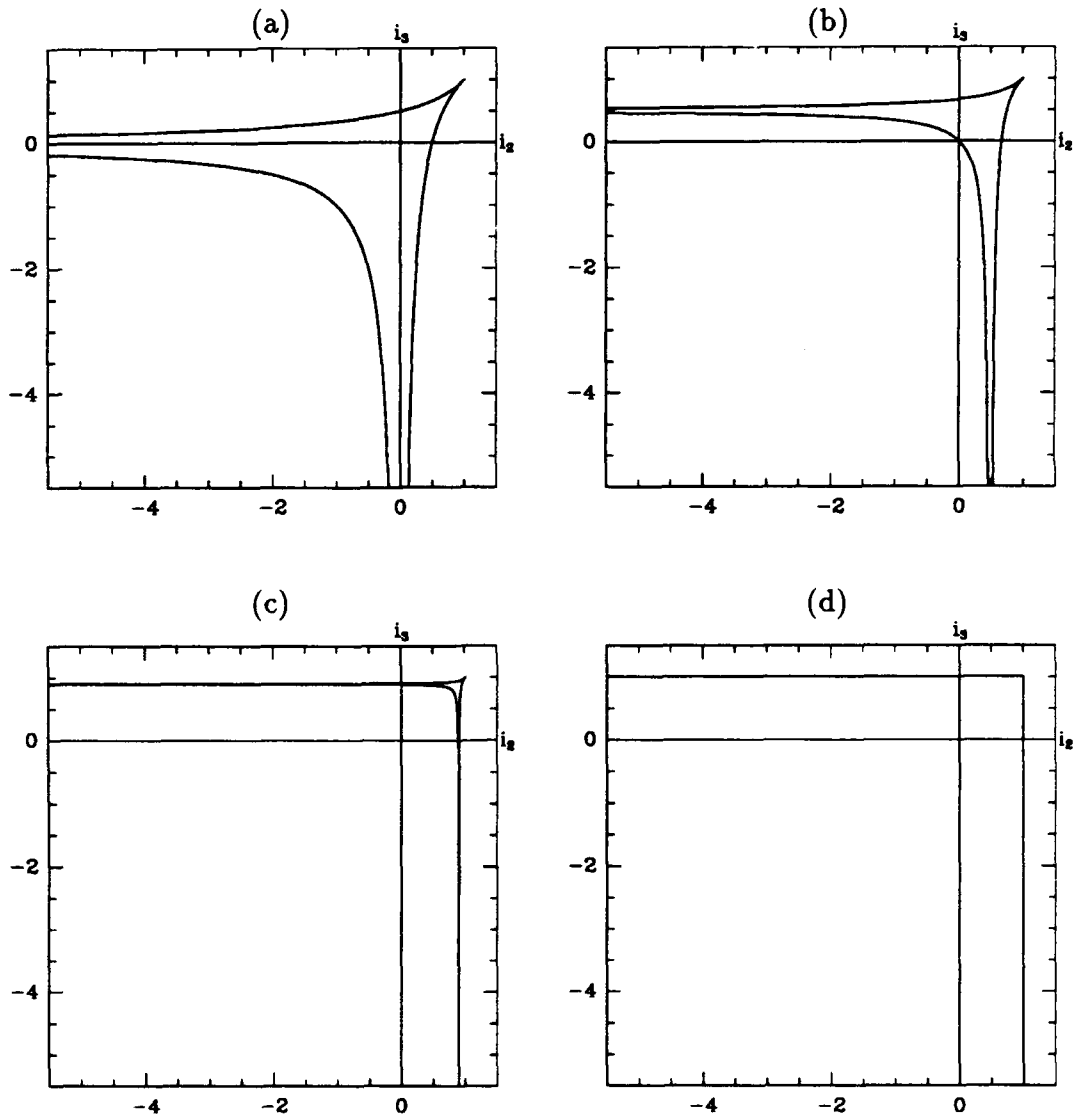
Figure B.3. The i_2i_3 Plane for Several Values of i_1. In (a), $i_1 = 0$, which corresponds to a single rigid body, or equivalently a gyrostat with a rod-shaped rotor. In (b), $i_1 = 0.5$, which is the critical value above which oblate gyrostats (as defined in Chapter 3) are not possible. In (c), $i_1 = 0.9$, and in (d), $i_1 = 1.0$. This is the limiting case of a rod-shaped platform, and also corresponds to a single rigid body.

Appendix C

Inversion of Elliptic Integrals of the First Kind

The $\varepsilon = 0$ solution given in Chapter 5 is found by evaluating the elliptic integral of the first kind given at Eq. (3.64), and inverting the result to obtain an expression for the angular momentum x as a function of time in terms of Jacobi's elliptic functions. In this appendix, we give the details of the calculations involved and discuss one possible pitfall.

To begin, we choose the general case of Region 1a as defined in Chapter 5, Table 5.2, and Fig. 5.4. For this case, the four roots are real with $a \geq x \geq b > c > d$. Referring to Byrd and Friedman [10], either of Eq. 256.00 or Eq. 257.00 is applicable. The difference between the two formulas is that for Eq. 256.00, $a \geq x > b$, while for Eq. 257.00, $a > x \geq b$. Of course, x generally takes on all values on the closed interval $[b, a]$, so the distinction does not at first appear important. The two solutions are different, however, in the limiting case where $k^2 = 1$, i.e., motion on the saddle and its separatrix. The separatrix condition for this case is characterized by $\mu \in (\mu_2, \mu_3)$ with energy level $y = 2\mu$. From Table 5.2, one may see that this corresponds to $b = c = -1$. At this energy level, there are three distinct trajectories: the two homoclinic orbits (which are

equivalent by symmetry), and the saddle point itself. As will be shown below, Eq. 256.00[10] reduces to the saddle point in the limiting case, while Eq. 257.00[10] gives the separatrix. For $k^2 \neq 1$, the two solutions are equivalent.

First we repeat Eq. 256.00[10], using our notation:

$$\int_b^x \frac{d\xi}{\sqrt{(a - \xi)(\xi - b)(\xi - c)(\xi - d)}} = g\,\mathrm{sn}^{-1}(\sin\psi, k) \tag{C.1}$$

$$= g\,F(\psi, k) \tag{C.2}$$

where

$$g = \frac{2}{\sqrt{(a - c)(b - d)}} \tag{C.3}$$

$$\psi = \sin^{-1}\sqrt{\frac{(a - c)(x - b)}{(a - b)(x - c)}} \tag{C.4}$$

$$k^2 = \frac{(a - b)(c - d)}{(a - c)(b - d)} \tag{C.5}$$

and $F(\psi, k)$ is an incomplete elliptic integral of the first kind. We wish to use this formula to evaluate Eq. (3.64), repeated here for clarity:

$$t = \int_{x(0)}^{x(t)} \frac{d\xi}{\sqrt{i_2 i_3 (a - \xi)(\xi - b)(\xi - c)(\xi - d)}} \tag{C.6}$$

Remark 14 *Note that the quartic under the radical in the integrand of Eq. (C.6) is not a monic polynomial, i.e., the coefficient of the highest order term is not 1. In the treatment given by Leimanis [56] this fact was overlooked. In going from Eq. 16.31[56] to Eq. 16.37[56], the coefficient equivalent to $i_2 i_3$ was dropped.*

At any rate, Eq. (C.6) becomes

$$\sqrt{i_2 i_3}\, t = \int_{x(0)}^{x(t)} \frac{d\xi}{\sqrt{(a - \xi)(\xi - b)(\xi - c)(\xi - d)}} \tag{C.7}$$

where now the right-hand side is almost in the form of Eq. (C.1). Since the lower limit of Eq. (C.1) is fixed at $x = b$, the integral in Eq. (C.7) must be separated into the sum of two integrals, viz.

$$\sqrt{i_2 i_3}\, t = -\int_b^{x(0)} \frac{d\xi}{\sqrt{W(\xi)}} + \int_b^{x(t)} \frac{d\xi}{\sqrt{W(\xi)}} \tag{C.8}$$

where $W(\xi)$ is the quartic in Eq. (C.7), which we have called the *gyroscopic function*, following Leimanis [56].

Applying Eq. (C.1) gives

$$\sqrt{i_2 i_3}\, t = g[-\mathrm{sn}^{-1}(\sin\psi_0, k) + \mathrm{sn}^{-1}(\sin\psi, k)] \tag{C.9}$$

where ψ_0 and ψ are given by Eq. (C.4) with $x = x(0)$ and $x = x(t)$, respectively. Rearranging gives

$$u = \mathrm{sn}^{-1}(\sin\psi, k) \tag{C.10}$$

where

$$u \;=\; \lambda t + u_0 \tag{C.11}$$

$$u_0 \;=\; \mathrm{sn}^{-1}(\sin\psi_0, k) \tag{C.12}$$

$$\lambda \;=\; \frac{\sqrt{i_2 i_3}}{g} = \frac{1}{2}\sqrt{i_2 i_3 (a-c)(b-d)} \tag{C.13}$$

Solving for $x(t) = x(u; k)$ gives

$$x(u; k) = \frac{-b(b-c) + c(a-b)\mathrm{sn}^2(u; k)}{-(a-c) + (a-b)\mathrm{sn}^2(u; k)} \tag{C.14}$$

The method of averaging (Chap. 6) requires that we integrate this expression over the period of $x(u; k)$ in u, which results in a complete elliptic integral of the third kind. Thus, it is convenient to write $x(u; k)$ in the form used in Ref. [10] (*e.g.*, Eq. 410.06[10]):

$$x(u; k) = b\left\{\frac{1 - \alpha_1^2 \mathrm{sn}^2(u; k)}{1 - \alpha^2 \mathrm{sn}^2(u; k)}\right\} \tag{C.15}$$

with $\alpha^2 = (a-b)/(a-c)$ and $\alpha_1^2 = c\alpha^2/b$.

At the saddle and along the separatrix for Case 1a, the two roots b and c are equal: $b = c = -1$, from which $\alpha_1^2 = \alpha^2$, and $x(u; 1) = -1$. That is, the solution obtained from Eq. 256.00[10] gives the saddle point in this limiting case.

Another way to see this is to note from Eqs. (C.1) and Eq (C.10) that $F(\psi, k) = u$, and from Eq. (C.4) that $b = c \Rightarrow \psi = \pi/2$. Furthermore, $F(\pi/2, 1) = K(1) = \infty$. So, at the separatrix energy level, $u = \infty$, and since λ

is bounded and non-zero, this implies $t = \infty$. Thus, since the separatrix is the stable (and unstable) manifold of the saddle, $t = \pm\infty$ corresponds to the time at which the separatrix reaches the saddle point.

Applying Eq. 257.00[10] in the same manner, one obtains

$$x(u; k) = a \left\{ \frac{1 - \alpha_1^2 \text{sn}^2(u; k)}{1 - \alpha^2 \text{sn}^2(u; k)} \right\} \tag{C.16}$$

with $\alpha^2 = -(a-b)/(b-d)$ and $\alpha_1^2 = d\alpha^2/a$. The separatrix condition $b = c = -1$ does not give $\alpha_1^2 = \alpha^2$ in this case, thus $x(u; 1)$ varies with u, following the separatrix.

Finally, we note that the *parameter*, α^2, has a different range for the two solutions: Eq. 256.00[10] gives $0 < k^2 < \alpha^2 < 1$, while Eq. 257.00[10] gives $\alpha^2 < 0$. These in turn lead to two different forms for the complete elliptic integral of the third kind (compare Eq. 410.06 and Eq. 412.06[10]).

Appendix D

Expansion of Complete Elliptic Integrals

In developing the approximate solutions to the slow flow equation in Chapter 8, it was necessary to expand the various elliptic integrals in Taylor series for small modulus, k^2, and, for the integrals of the third kind, for small parameter, α^2. In this appendix, we develop the required series for the complete integrals of the first and second kinds, and for two versions of complete elliptic integrals of the third kind.

The basic idea here is to expand the integrand of each integral in an appropriate Taylor series, and then integrate the series. The expansions for the integrals of the first and second kinds are available in Ref. [10], and we simply repeat them here for convenience. However, the expansions for the integrals of the third kind were not available in a convenient form, and we give the details of their derivation here.

In all cases, we carry the series to $\mathcal{O}\left(k^4\right)$, or to $\mathcal{O}\left(k^2\alpha^2\right)$.

D.1 Complete Elliptic Integral of the First Kind

The complete elliptic integral of the first kind is defined by Eq. 110.06 of Ref. [10]:

$$K(k) = \int_0^{\pi/2} \frac{d\vartheta}{\sqrt{1 - k^2 \sin^2 \vartheta}} \tag{D.1}$$

which may be written as a series in k^2:

$$K(k) = \frac{\pi}{2} \left[1 + \frac{1}{4}k^2 + \frac{9}{64}k^4 + \mathcal{O}\left(k^6\right) \right] \tag{D.2}$$

as given at Eq. 900.00 of Ref. [10] where the remaining terms in the series are given as a convenient recurrence formula.

D.2 Complete Elliptic Integral of the Second Kind

The complete elliptic integral of the second kind is defined by Eq. 110.07 of Ref. [10]:

$$E(k) = \int_0^{\pi/2} \sqrt{1 - k^2 \sin^2 \vartheta} \, d\vartheta \tag{D.3}$$

which may be written as a series in k^2 as given at Eq. 900.07 of Ref. [10]:

$$E(k) = \frac{\pi}{2} \left[1 - \frac{1}{4}k^2 - \frac{3}{64}k^4 + \mathcal{O}\left(k^6\right) \right] \tag{D.4}$$

D.3 Normal Complete Elliptic Integral of the Third Kind

The normal complete elliptic integral of the third kind is defined by Eq. 110.08 of Ref. [10]:

$$\Pi(\alpha^2, k) = \int_0^{\frac{\pi}{2}} \frac{d\varphi}{(1 - \alpha^2 \sin^2 \varphi)\sqrt{1 - k^2 \sin^2 \varphi}} \tag{D.5}$$

We begin by expanding the integrand of Eq. (D.5) ($d\Pi/d\varphi = d\Pi(\varphi, \alpha^2, k)/d\varphi$) in a Taylor series about $k^2 = 0$ and $\alpha^2 = 0$:

$$\frac{d\Pi}{d\varphi} = 1 + (\alpha^2 + \frac{k^2}{2}) \sin^2 \varphi + \mathcal{O}(k^4, \alpha^4) \tag{D.6}$$

Carrying out the integration defined in Eq. (D.5) gives the following approximation for $\Pi(\alpha^2, k)$ for small modulus and parameter:

$$\Pi(\alpha^2, k) = \frac{\pi}{2}\left\{1 + \frac{\alpha^2}{2} + \left(\frac{1}{4} + \frac{3\alpha^2}{16}\right)k^2\right\} + \mathcal{O}(k^4, \alpha^4) \tag{D.7}$$

D.4 Heuman's Lambda Function

As with the expansion of $\Pi(\alpha^2, k)$, we obtain an approximate expression for $\Lambda_0(\psi, k)$ for small k^2 by first expanding the integrand in a power series in k^2, then evaluating the resulting integral. Thus, using Eq. 730.04 of Ref. [10], we have

$$\frac{d\Lambda_0(\varphi, k)}{d\varphi} = \frac{2(E - k'^2 K \sin^2\varphi)}{\pi\sqrt{1 - k'^2 \sin^2\varphi}} \tag{D.8}$$

Replacing the complimentary modulus k'^2 via $k'^2 = 1 - k^2$, this becomes

$$\frac{d\Lambda_0(\varphi, k)}{d\varphi} = \frac{2[E - (1 - k^2)K \sin^2\varphi]}{\pi\sqrt{\cos^2\varphi + k^2 \sin^2\varphi}} \tag{D.9}$$

Making use of the fact that $\varphi \in [0, \pi/2]$, another rewrite gives

$$\frac{d\Lambda_0(\varphi, k)}{d\varphi} = \frac{2[E - (1 - k^2)K \sin^2\varphi]}{\pi\cos\varphi\sqrt{1 + k^2 \tan^2\varphi}} \tag{D.10}$$

which may readily be expanded in a power series in small k^2:

$$\begin{aligned}
\frac{d\Lambda_0(\varphi, k)}{d\varphi} &= \frac{2}{\pi}\left\{(E - K)\frac{1}{\cos\varphi} + K\cos\varphi\right. \tag{D.11}\\
&\quad -\frac{1}{2}\left[(E - K)\frac{1}{\cos^3\varphi} - \frac{E}{\cos\varphi} + K\cos\varphi\right]k^2\\
&\quad +\frac{1}{2}\left[\frac{3}{4}(E - K)\frac{1}{\cos^5\varphi} - \left(\frac{3E}{2} - \frac{5K}{4}\right)\frac{1}{\cos^3\varphi}\right.\\
&\quad \left.+\left(\frac{3E}{4} - \frac{K}{4}\right)\frac{1}{\cos\varphi} - \frac{1}{4}K\cos\varphi\right]k^4\\
&\quad \left.+\mathcal{O}\left(k^6\right)\right\}
\end{aligned}$$

Integrating over the interval $\varphi \in [0, \psi]$, we obtain

$$
\begin{aligned}
\Lambda_0(\psi, k) = \frac{2}{\pi} \Bigg\{ & (E - K)L + K \sin\psi \\
& + \left[\frac{1}{4}(E + K)L \right. \\
& \left. - \frac{1}{4}(E - K)\frac{\sin\psi}{\cos^2\psi} - \frac{1}{2}K\sin\psi \right] k^2 \\
& + \left[\frac{3}{64}(3E + K)L - \frac{1}{64}(15E - 11K)\frac{\sin\psi}{\cos^2\psi} \right. \\
& \left. + \frac{3}{32}(E - K)\frac{\sin\psi}{\cos^4\psi} - \frac{K}{8}\sin\psi \right] k^4 \\
& + \mathcal{O}\left(k^6\right) \Bigg\}
\end{aligned}
\tag{D.12}
$$

where

$$
L = \ln\left(\frac{1 + \sin\psi}{\cos\psi} \right)
\tag{D.13}
$$

The next step in expanding Λ_0 is to substitute the series for $K(k)$ and $E(k)$ into Eq. (D.12). Carrying out this substitution gives

$$
\Lambda_0(\psi, k) = \sin\psi \left[1 - \frac{1}{4}k^2 + \left(\frac{1}{16\cos^2\psi} - \frac{7}{64} \right) k^4 \right] + \mathcal{O}\left(k^6\right)
\tag{D.14}
$$

Appendix E

A Simple Second-Order Example

In Chapter 3, we reduced the four Euler equations for the axial gyrostat,

$$\dot{x}_1 = (i_2 - i_3)x_2x_3 \tag{E.1}$$

$$\dot{x}_2 = (i_3x_1 - \mu)\,x_3 \tag{E.2}$$

$$\dot{x}_3 = -(i_2x_1 - \mu)\,x_2 \tag{E.3}$$

$$\dot{\mu} = \varepsilon \tag{E.4}$$

to three equations where the slow-fast separation is evident:

$$\dot{x} = \pm\sqrt{y_2(x,\mu) - y}\sqrt{y - y_3(x,\mu)} \tag{E.5}$$

$$\dot{y} = -2\varepsilon x \tag{E.6}$$

$$\dot{\mu} = \varepsilon \tag{E.7}$$

where $x = x_1$, and $y_2(x,\mu)$ and $y_3(x,\mu)$ are the bounding parabolas defined at Eqs. (3.60) and (3.61), and shown in Fig. 4.5. Then, in Chapter 6, we used the method of averaging to obtain a single first-order equation for the slow flow:

$$\bar{y}' = -2\bar{x}(y,\mu) \tag{E.8}$$

where $\bar{x}(y,\mu)$ is the average of x over one period of the unperturbed motion, and $()' = d()/d\mu$.

In this appendix, we present the equivalent analysis for a general class of non-linear second-order oscillators with a slowly-varying parameter. After developing the general results, we treat in some detail a specific example.

E.1   The General System

The system of equations we are interested in here is:

$$\ddot{x} + \frac{\partial V}{\partial x}(x, \mu) = 0 \tag{E.9}$$

$$\dot{\mu} = \varepsilon \tag{E.10}$$

where $V(x, \mu)$ is a potential function. When $\varepsilon = 0$, $\mu = \text{CONST}$, and Eq. (E.9) admits the energy integral

$$y = \frac{1}{2}\dot{x}^2 + V(x; \mu) = \text{CONST} \tag{E.11}$$

from which

$$\dot{x} = \pm\sqrt{2\left(y - V(x; \mu)\right)} \tag{E.12}$$

which may be separated to obtain

$$\pm \int_{x(0)}^{x(t)} \frac{d\xi}{\sqrt{y - V(\xi; \mu)}} = \int_0^t dt = t \tag{E.13}$$

The reader should note the similarity of Eq. (E.13) to Eq. (3.64). In particular, $V(x, \mu)$ is analogous to either of $y_2(x, \mu)$ or $y_3(x, \mu)$. In order for $\dot{x}$ to be a real-valued function, we require $y \geq V(x; \mu)$.

For a general potential, $V(x; \mu)$, Eq. (E.13) will be difficult, if not impossible, to integrate; however, if $V(x; \mu)$ is a polynomial of small degree in x, then the equation may be solved explicitly. More precisely, if the degree is n, then the cases listed in Table E.1 are possible. Note that $n = 1$ implies $\ddot{x} = \text{CONST}$ (for $\varepsilon = 0$), and leads to a polynomial solution for $x(t)$. Hyperelliptic integrals are discussed in Ref. [10, pp. 252–271]; in particular, it is shown that several classes of hyperelliptic integrals can be reduced to sums of elliptic integrals. We do not discuss hyperelliptic integrals further.

Table E.1. Classification of the $\varepsilon = 0$ Integral

n	Type of Integral in Eq. (E.13)
1,2	elementary
3,4	elliptic
≥ 5	hyperelliptic

Now, as with spinup of gyrostats, we are primarily interested in the $\varepsilon \neq 0$ case, in which y and μ are not constant. In this case, one may easily show that

$$\dot{y} = \varepsilon V_\mu(x, \mu) \tag{E.14}$$

where the subscript μ denotes partial differentiation with respect to μ. Equation (E.14) is valid for any ε. Thus, Eqs. (E.9) and (E.10) may be rewritten as

$$\dot{x} = \pm\sqrt{2\left(y - V(x, \mu)\right)} \tag{E.15}$$

$$\dot{y} = \varepsilon V_\mu(x, \mu) \tag{E.16}$$

$$\dot{\mu} = \varepsilon \tag{E.17}$$

which are quite similar to Eqs. (E.5)–(E.7).

Finally, if a periodic $\varepsilon = 0$ solution for $x(t)$ can be explicitly determined by evaluating the integral in Eq. (E.13), and if $V_\mu(x; \mu)$ is sufficiently simple, we may apply the method of averaging to this system, obtaining a single slow flow equation:

$$\bar{y}' = \overline{V_\mu}(y, \mu) \tag{E.18}$$

where

$$\overline{V_\mu} = \frac{1}{T} \int_0^T V_\mu(x, \mu)dt \tag{E.19}$$

and T is the period of the $\varepsilon = 0$ solution for $x(t)$.

E.2 An Example with Cubic $V(x, \mu)$

In this section, we apply the results obtained in the previous section to the particular case where $V(x, \mu)$ is a cubic polynomial in x, which implies that Eq. (E.9) has a quadratic nonlinearity. Specifically, we use

$$\ddot{x} + \mu x + x^2 = 0 \tag{E.20}$$

$$\dot{\mu} = \varepsilon \tag{E.21}$$

To emphasize the relationship between this system and the gyrostat, we use $y_1(x, \mu)$ to represent the potential function $V(x, \mu)$; that is,

$$y_1(x, \mu) = \frac{1}{2}\mu x^2 + \frac{1}{3}x^3 \tag{E.22}$$

When $\varepsilon = 0$, the energy integral is

$$y = \frac{1}{2}\dot{x}^2 + y_1(x; \mu) \tag{E.23}$$

When $\varepsilon \neq 0$, Eqs. (E.15)–(E.17) become (cf. Eqs. (E.5)–(E.7)):

$$\dot{x} = \pm\sqrt{2\left(y - y_1(x, \mu)\right)} \tag{E.24}$$

$$\dot{y} = \frac{1}{2}\varepsilon x^2 \tag{E.25}$$

$$\dot{\mu} = \varepsilon \tag{E.26}$$

Note that for $\dot{x}$ to be real, we need $y \geq y_1(x, \mu)$.

In Fig. E.1, we show the xy plane for this system for a fixed value of μ, as well as the frozen phase portrait for the same value of μ. Note that the local maximum of $y_1(x, \mu)$, $y_1^*(\mu) = y_1(-\mu, \mu) = \mu^3/6$, corresponds to the saddle point in the phase plane.

Now, the $\varepsilon = 0$ solution for $x(t)$ for this system results from evaluating the elliptic integral, Eq. (E.13), with the particular potential function $y_1(x; \mu)$. Writing Eq. (E.24) as $\dot{x} = \pm\sqrt{P(x)}$, the $\varepsilon = 0$ solution depends on the roots of the cubic polynomial

$$P(x) = 2\left(y - \frac{1}{2}\mu x^2 - \frac{1}{3}x^3\right) \tag{E.27}$$
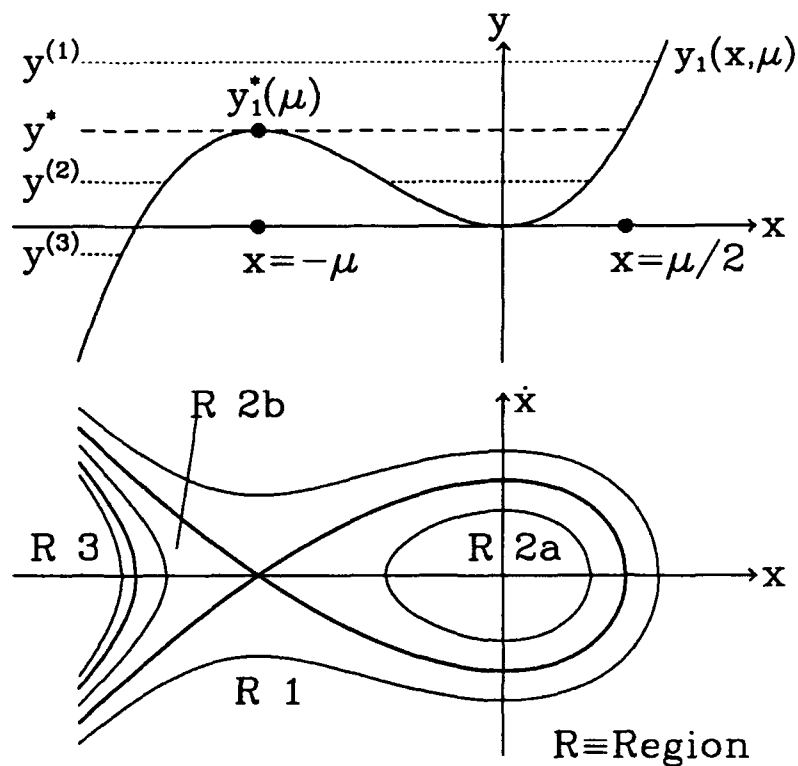
Figure E.1. The xy Plane and Phase Plane for Quadratic Nonlinearity ($\mu = 1.5$). The dotted lines of constant energy in the xy plane correspond to the level curves of the frozen phase portrait in the $x\dot{x}$ plane. The thick level curves in the $x\dot{x}$ plane represent the three critical trajectories separating the regions in which the form of the unperturbed solution is distinct.

194

It is apparent from Fig. E.1 that for positive μ, there are four different cases: 1) $y \geq y_1^*$; 2a) $0 \leq y \leq y_1^*$, $x \geq -\mu$; 2b) $0 \leq y \leq y_1^*$, $x \leq -\mu$; and 3) $y \leq 0$. Cases 1 and 3 correspond to one real and two complex roots of the cubic, while Cases 2a and 2b correspond to three real roots. In each case the form of the solution is distinct.

We only develop the solution for Case 2a, since it is clearly oscillatory. We denote the three real roots to $P(x) = 0$ by a, b, and c, with $a \geq x \geq b > c$. Thus Eq. 236.00 of Ref. [10] applies, and the $\varepsilon = 0$ solution is

$$x(u; k) = a - (a - b)\text{sn}^2(u; k) \tag{E.28}$$

where

$$k^2 = \frac{a - b}{a - c} \tag{E.29}$$

$$u = \lambda t + u_0 \tag{E.30}$$

$$\lambda = \frac{1}{2}\sqrt{\frac{2}{3}(a - c)} \tag{E.31}$$

To average the slow equations, (E.25) and (E.26), we need to evaluate the average of $x^2(u; k)$ over one period of this periodic solution; that is,

$$\overline{x^2}(y, \mu) = \frac{1}{4K} \int_0^{4K} x^2(u; k)\, du \tag{E.32}$$

Making use of Eqs. 310.02 and 310.04 of Ref. [10], we obtain after simplification

$$\overline{x^2}(y, \mu) = a^2 - \frac{2a(a - c)}{K}(K - E) + \tag{E.33}$$

$$\frac{(a - c)^2}{3K}\left\{(2 + k^2)K - 2(1 + k^2)E\right\} \tag{E.34}$$

Note that $k^2 = 0$ implies $K = E$, from which $\overline{x^2} = 0$, as expected, since this corresponds to the center at $(x, \dot{x}) = (0, 0)$.

Now, analogous to our development in Chapter 6, we have reduced the study of Eqs. (E.20) and (E.21) to the study of the averaged slow flow described by

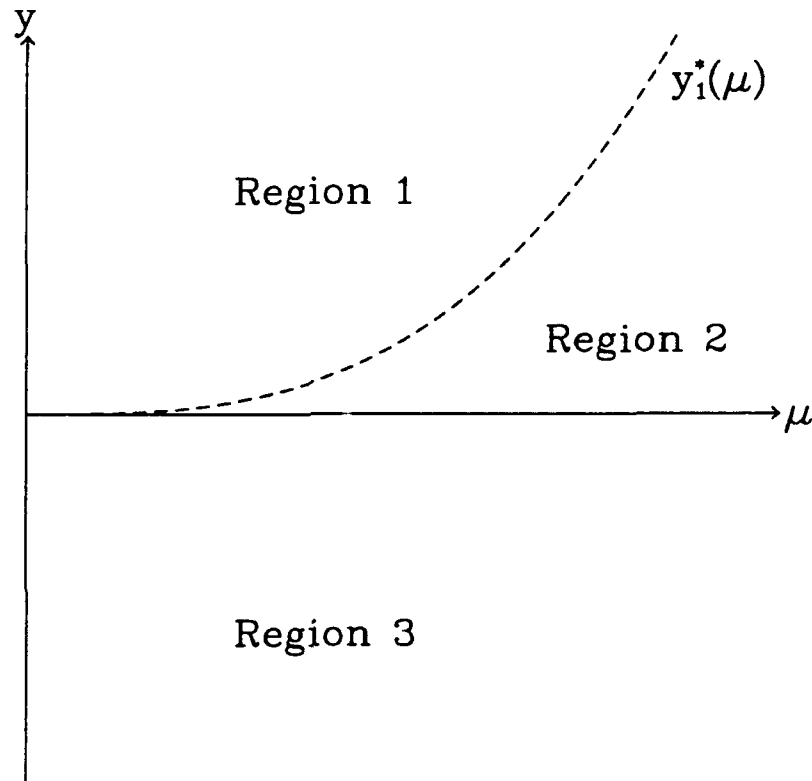$$\overline{y}' = \overline{x^2}(y, \mu) \tag{E.35}$$

Figure E.2. The μy Plane for Quadratic Nonlinearity. The Region numbers correspond to the four different cases discussed in the text, each solution having a distinct form, and to the superscripts on y in Fig. E.1. The μ axis corresponds to the center at $(x, \dot{x}) = (0, 0)$, as well as to an open orbit to the left of the saddle point. More generally, in Region 2, two $\varepsilon = 0$ orbits exist, the closed orbits inside the homoclinic orbit, and the open orbits to the left of the saddle point (cf. Fig. E.1). The dashed curve, $y_1^*(\mu)$ represents the saddle point, as well as the separatrices. The crossing of this curve by trajectories of the perturbed system is a *separatrix crossing* as discussed in Chapters 6 and 7.

where $\overline{x^2}$ is given at Eq. (E.33), and $()' = d()/d\mu$. That is, we can now study the flow in the μy plane shown in Fig. E.2.

We do not continue this example, as it is only intended to illustrate the techniques used in this thesis by applying them to a simpler problem. However, we can easily prove an assertion about *escape from resonance* for this problem using the tools developed here. Consider a situation where $\mu(0) > 0$, and $x(0)$ lies in the potential well inside the homoclinic orbit of the saddle in Fig. E.1. A non-trivial question is: *For $\varepsilon > 0$ is it possible for the trajectory to escape and move to one of the regions of unbounded trajectories?* The answer is *no*, and has been shown for a similar system in Rand *et al* [84], using a different argument.

We show that no motion which starts *inside* the separatrix can later be *outside* the separatrix as follows. Recall that $y = y_1^*(\mu)$ is the energy level of the separatrix. We show that if at some time $y < y_1^*(\mu)$ (*i.e.*, motion lies inside the separatrix), then $y < y_1^*(\mu)$ for all future times (*i.e.*, motion stays inside the separatrix). The method is to show that $Y = y - y_1^*$ is a monotonically decreasing function of time, *i.e.*, $\dot{Y} < 0$. We have $\dot{y} = \varepsilon x^2/2$, and it is easy to show that $\dot{y}_1^* = \varepsilon \mu^2/2$, so $\dot{Y} = \varepsilon(x^2 - \mu^2)/2$. For motion inside the separatrix, $-\mu < x < \mu/2$ (cf. Fig. E.1). Therefore $x^2 < \mu^2$ for any motion inside the separatrix, giving $\dot{Y} < 0$. We emphasize that the strict inequality holds here. that is, the energy of the system cannot "catch up" with the energy of the saddle point. Hence, we have proved that escape from inside the homoclinic orbit cannot occur.

Bibliography

[1] G. J. Adams. Dual-spin spacecraft dynamics during platform spinup. *Journal of Guidance and Control*, 3(1):29–36, Jan–Feb 1980.

[2] B. N. Agrawal. Effects of asymmetries in the rotor and flexible joint of a dual-spin spacecraft. *Journal of Spacecraft and Rockets*, 11(9):611–612, Sep 1974. Synoptic.

[3] Brij N. Agrawal. *Design of Geosynchronous Spacecraft.* Prentice-Hall, Englewood Cliffs, NJ, 1986.

[4] V. I. Arnol'd, V. V. Kozlov, and A. I. Neishtadt. *Dynamical Systems III*, volume 3 of *Encyclopaedia of Mathematicr' ⌐ ⌐ences.* Springer-Verlag, New York, 1988.

[5] P. M. Bainum, P. G. Fuechsel, and J. V. Fedor. Stability of a dual-spin spacecraft with a flexible momentum wheel. *Journal of Spacecraft and Rockets*, 9(9):640–646, Sep 1972.

[6] F. Jay Bourland and Richard Haberman. Separatrix crossing: Time-invariant potentials with dissipation. *SIAM Journal on Applied Math*, 50(6):1716–1744, December 1990.

[7] F. Jay Bourland and Richard Haberman. Connection across a separatrix with dissipation. 1991. Submitted.

[8] F. Jay Bourland, Richard Haberman, and William L. Kath. Averaging methods for the phase shift of arbitrarily perturbed strongly nonlinear oscillators with an application to capture. *SIAM Journal on Applied Math*, 51(3):1150–1167, June 1991.

[9] Richard L. Burden, J. Douglas Faires, and Albert C. Reynolds. *Numerical Analysis.* Prindle, Weber & Schmidt, Boston, second edition, 1981.

[10] Paul F. Byrd and Morris D. Friedman. *Handbook of Elliptic Integrals for Engineers and Physicists.* Springer-Verlag, Berlin, second edition, 1971.

197

[11] John R. Cary, D. F. Escande, and J. L. Tennyson. Adiabatic-invariant change due to separatrix crossing. *Physical Review A*, 34(5):4526–4275, November 1986.

[12] J. Chen and Thomas R. Kane. Reorientation of a gyrostat. *Journal of the Astronautical Sciences*, XXVII(1):85–90, Jan–Mar 1979.

[13] J. E. Cochran. Nonlinear resonances in the attitude motion of dual-spin spacecraft. *Journal of Spacecraft and Rockets*, 14(9):562–572, Sep 1977.

[14] J. E. Cochran and J. R. Beaty. Near-resonant and transition motion of a class of dual-spin spacecraft. *Journal of the Astronautical Sciences*, XXVI(1):19–45, Jan–Mar 1978.

[15] J. E. Cochran and P. H. Shu. Effects of energy addition and dissipation on dual-spin spacecraft attitude motion. *Journal of Guidance, Control and Dynamics*, 6(5):368–373, Sep–Oct 1983.

[16] John E. Cochran, Ping-Huei Shu, and Stephen D. Rew. Attitude motion of asymmetric dual-spin spacecraft. *Journal of Guidance, Control and Dynamics*, 5(1):37–42, Jan–Feb 1982.

[17] Vincent T. Coppola and Richard H Rand. Chaos in a system with a periodically disappearing separatrix. *Nonlinear Dynamics*, 1:401–420, 1990.

[18] Vincent Timothy Coppola. *Averaging of Strongly Nonlinear Oscillators Using Elliptic Functions*. PhD thesis, Cornell University, Ithaca, New York, 1989.

[19] M. R. M. Crespo da Silva. Nonlinear resonant attitude motions in gravity-stabilized gyrostat satellites. *International Journal of Nonlinear Mechanics*, 7(6):621–641, Dec 1972.

[20] M. R. M. Crespo da Silva. On the dynamical equivalence between two types of vehicles with rotors. *Journal of the British Interplanetary Society*, 25(3):177–181, Mar 1972.

[21] C. K. Cretcher and D. Lewis Mingori. Nutation damping and vibration isolation in a flexibly coupled dual-spin spacecraft. *Journal of Spacecraft and Rockets*, 8(8):817–823, Aug 1971.

[22] R. H. Cronin and T. R. Kane. Gravitational stabilization of a two-body satellite. *Journal of Spacecraft and Rockets*, 10(5):291–294, May 1973.

[23] J. R. Gebman and D. Lewis Mingori. Perturbation solution for the flat spin recovery of a dual spin spacecraft. *AIAA Journal*, 14(7):859–867, Jul 1976.

[24] Jean Rene Gebman. *Perturbation Analysis of the Flat Spin Recovery of a Dual-Spin Spacecraft.* PhD thesis, University of California, Los Angeles, 1974.

[25] R. Grossman, P. S. Krishnaprasad, and J. E. Marsden. The dynamics of two coupled rigid bodies. In Fathi M. A. Salam and Mark L. Levi, editors, *Dynamical Systems Approaches to Nonlinear Problems in Systems in Circuits*, pages 373–378, Philadelphia, 1988. SIAM. (Also available as NTIS AD-A187 592/1/HDM, and as AFOSR-TR-87-1432).

[26] J. Guckenheimer and P. J. Holmes. *Nonlinear Oscillations, Dynamical Systems, and Bifurcations of Vector Fields*, volume 42 of *Applied Mathematical Sciences*. Springer-Verlag, New York, 1983.

[27] M. Guelman. Gyrostat trajectories and core energy. *Journal of Guidance, Control and Dynamics*, 11(6):577–583, Nov–Dec 1988.

[28] M. Guelman. On gyrostat dynamics and recovery. *Journal of the Astronautical Sciences*, XXXVII(2):109–119, Apr–Jun 1989.

[29] Richard Haberman. Nonlinear transition layers — The second Painlevé transcendent. *Studies in Applied Mathematics*, 57:247–270, 1977.

[30] Christopher D. Hall. Equivalence of two classes of dual-spin spacecraft spinup problems. *Journal of Guidance, Control and Dynamics*, 1991. (To appear).

[31] J. Henrard. Capture into resonance: An extension of the use of adiabatic invariants. *Celestial Mechanics*, 27:3–22, 1982.

[32] M. G. Hollars. Minimum energy trap states of dual-spin spacecraft. *Journal of Guidance, Control and Dynamics*, 5(3):286–290, May–Jun 1982.

[33] P. J. Holmes and J. E. Marsden. Horseshoes and Arnold diffusion for Hamiltonian systems on Lie groups. *Indiana University Mathematics Journal*, 32(2):273–309, Mar–Apr 1983.

[34] C. H. Hubert. Dynamics of the generalized dual-spin turn. *RCA Review*, 41(3):449–471, Sep 1980.

[35] C. H. Hubert. The use of energy methods in the study of dual-spin spacecraft. In *Proceedings of AIAA Guidance & Control Conference*, Aug 1980. AIAA Paper 80-1781.

[36] C. H. Hubert. Spacecraft attitude acquisition from an arbitrary spinning or tumbled state. *Journal of Guidance and Control*, 4(2):164–170, Mar–Apr 1981.

[37] Carl Henry Hubert. *An Attitude Acquisition Technique for Dual-Spin Spacecraft.* PhD thesis, Cornell University, Ithaca, NY, 1980.

[38] Peter C. Hughes. *Spacecraft Attitude Dynamics.* John Wiley & Sons, New York, 1986.

[39] R. L. Huston. Gyroscopic stabilization of space vehicles. *AIAA Journal,* 1(7):1694–1696, Jul 1963.

[40] E. L. Ince. *Ordinary Differential Equations.* Dover, New York, 1956.

[41] A. J. Iorillo. Nutation damping dynamics of axisymmetric rotor stabilized satellites. In *ASME Annual Winter Meeting,* Chicago, 1965.

[42] A. J. Iorillo. Hughes gyrostat system. In *Proceedings of the Symposium on Attitude Stabilization and Control of Dual-Spin Spacecraft,* pages 257–266, El Segundo, CA, 1967. Air Force Systems Command and Aerospace Corporation. Air Force Report No. SAMSO-TR-68-191, Aerospace Report No. TR-0158(3307-01)-16. (Also available as NTIS ADA 670 154.).

[43] Thomas R. Kane. Solution of the equations of rotational motion for a class of torque-free gyrostats. *AIAA Journal,* 8(6):1141–1143, Jun 1970.

[44] Thomas R. Kane. Torque-free motion of a simple gyrostat initially at rest. *Journal of the Astronautical Sciences,* XXV(4):365–370, Oct–Dec 1977.

[45] Thomas R. Kane and R. C. Fowler. Equivalence of two gyrostatic stability problems. *Journal of Applied Mechanics,* 37(4):1146–1147, Dec 1970.

[46] Thomas R. Kane and David A. Levinson. Energy-sink analysis of systems containing driven rotors. *Journal of Guidance and Control,* 3(2):234–238, May–Jun 1980.

[47] Thomas R. Kane, Peter W. Likins, and David A. Levinson. *Spacecraft Dynamics.* McGraw-Hill, New York, 1983.

[48] Thomas R. Kane and D. Lewis Mingori. Effect of a rotor on the attitude stability of a satellite in a circular orbit. *AIAA Journal,* 3(5):936–940, May 1965.

[49] Marshall H. Kaplan. *Modern Spacecraft Dynamics & Control.* John Wiley & Sons, New York, 1976.

[50] R. J. Kinsey, D. L. Mingori, and R. H. Rand. Spinup through resonance of rotating unbalanced systems with limited torque. In *Proceedings of the 1990 AIAA/AAS Astrodynamics Conference, Part 2,* pages 805–813, Aug 1990. AIAA Paper 90-2966.

[51] Jair Koiller. A mechanical system with a "wild" horseshoe. *Journal of Mathematical Physics*, 25(5):1599–1604, May 1984.

[52] P. S. Krishnaprasad. Lie-Poisson structure, dual-spin spacecraft and asymptotic stability. *Nonlinear Analysis, Theory, Methods & Applications*, 9(10):1011–1035, 1985.

[53] P. S. Krishnaprasad and C. A. Berenstein. On the equilibria of rigid spacecraft with rotors. *Systems and Control Letters*, 4:157–163, May 1984.

[54] V. D. Landon and B. Stewart. Nutational stability of an axisymmetric body containing a rotor. *Journal of Spacecraft and Rockets*, 1(6):682–684, Nov–Dec 1964.

[55] Derek F. Lawden. *Elliptic Functions and Applications*, volume 80 of *Applied Mathematical Sciences*. Springer-Verlag, New York, 1989.

[56] Eugene Leimanis. *The General Problem of the Motion of Coupled Rigid Bodies about a Fixed Point*. Springer-Verlag, New York, 1965.

[57] H. Leipholz. Ein beitrag zu dem problem des kreisels mit drehzahlabhängiger selbsterregung. *Ingenieur-Archiv*, 32(4):255–285, 1963.

[58] Mark Levi. Morse theory for a model space structure. In Marsden et al. [69], pages 209–216. Proceedings of the AMS-IMS-SIAM Joint Summer Research Conference, July 30–August 5, 1988, Brunswick, Maine.

[59] Tieshou Li and Robert W. Longman. Stability relationships between gyrostats with free, constant-speed, and speed-controlled rotors. *Journal of Guidance, Control and Dynamics*, 5(6):545–552, Nov–Dec 1982.

[60] Peter Likins. Spacecraft attitude dynamics and control — A personal perspective on early developments. *Journal of Guidance, Control and Dynamics*, 9(2):129–134, Mar–Apr 1986.

[61] Peter W. Likins. Attitude stability criteria for dual spin spacecraft. *Journal of Spacecraft and Rockets*, 4(12):1638–1643, Dec 1967.

[62] Peter W. Likins, Gan-Tai Tseng, and D. Lewis Mingori. Stable limit cycles due to nonlinear damping in dual-spin spacecraft. *Journal of Spacecraft and Rockets*, 8(6):568–574, Jun 1971.

[63] Pierre Lochak and Claude Meunier. *Multiphase Averaging for Classical Systems: With Applications to Adiabatic Theorems*, volume 72 of *Applied Mathematical Sciences*. Springer-Verlag, New York, 1988.

[64] R. W. Longman. Stability analysis of all possible equilibria for gyrostat satellites under gravitational torques. *AIAA Journal*, 10(6):800–806, Jun 1972.

[65] R. W. Longman. Stable tumbling motions of a dual-spin satellite subject to gravitational torques. *AIAA Journal*, 11(7):916–921, Jul 1973.

[66] R. W. Longman, P. Hagedorn, and A. Beck. Stabilization due to gyroscopic coupling in dual-spin satellites subject to gravitational torques. *Celestial Mechanics*, 25(4):353–373, Dec 1981.

[67] R. W. Longman and R. E. Roberson. General solution for the equilibria of orbiting gyrostats subject to gravitational torques. *Journal of the Astronautical Sciences*, 16(2):49–58, Apr–Jun 1969.

[68] Michael S. Lukich and D. Lewis Mingori. Attitude stability of dual-spin spacecraft with unsymmetrical bodies. *Journal of Guidance, Control and Dynamics*, 8(1):110–117, Jan–Feb 1985.

[69] J. E. Marsden, P. S. Krishnaprasad, and J. C. Simo, editors. *Dynamics and Control of Multibody Systems*, volume 97 of *Contemporary Mathematics*, Providence, 1989. American Mathematical Society. Proceedings of the AMS-IMS-SIAM Joint Summer Research Conference, July 30–August 5, 1988, Brunswick, Maine.

[70] Č. Masaitis. On the motion of two linked bodies. *Archive for Rational Mechanics and Analysis*, 8(1):23–35, Jul 1961.

[71] A G. Mavraganis. The integral invariants of n gyrostats. *Mechanics Research Communications*, 17(2):75–80, Mar–Apr 199C.

[72] J. E. McIntyre and M. J. Gianelli. Bearing axis wobble for a dual spin vehicle. *Journal of Spacecraft and Rockets*, 8(9):945–951, Sep 1971.

[73] D. Lewis Mingori. Effects of energy dissipation on the attitude stability of dual-spin satellites. *AIAA Journal*, 7(1):20–27, Jan 1969.

[74] D. Lewis Mingori, Gan-Tai Tseng, and Peter W. Likins. Constant and variable amplitude limit cycles in dual-spin spacecraft. *Journal of Spacecraft and Rockets*, 9(11):825–830, Nov 1972.

[75] James A. Murdock. *Perturbations: Theory and Methods*. John Wiley & Sons, New York, 1991.

[76] A. I. Neishtadt. Passage through a separatrix in a resonance problem with a slowly-varying parameter. *Journal of Applied Mathematics and Mechanics*, 39(4):594–605, 1975.

[77] A. I. Neishtadt. Change in adiabatic invariant at a separatrix. *Soviet Journal of Plasma Physics*, 12(8):568–573, 1986.

[78] A. I. Neishtadt. On the change in the adiabatic invariant on crossing a separatrix in systems with two degrees of freedom. *Journal of Applied Mathematics and Mechanics*, 51(5):586–592, 1987.

[79] Peter J. Olver. *Applications of Lie Groups to Differential Equations*, volume 107 of *Graduate Texts in Mathematics*. Springer-Verlag, New York, 1986.

[80] Michael P. Paquette. Detumbling of two inter-connected rigid bodies using Liapunov methods for feedback control. Master's thesis, Air Force Institute of Technology, Wright-Patterson AFB, OH, 1986. (Also available as NTIS AD-A179 207/6/HDM).

[81] Madeleine Pascal. Problème restreint des trois corps appliqué à un gyrostat. *Celestial Mechanics*, 11(3):319–336, May 1975.

[82] George W. Patrick. The dynamics of two coupled rigid bodies in three space. In Marsden et al. [69], pages 315–355. Proceedings of the AMS-IMS-SIAM Joint Summer Research Conference, July 30–August 5, 1988, Brunswick, Maine.

[83] William H. Press, Brian P. Flannery, Saul A. Teukolsky, and William T. Vetterling. *Numerical Recipes in C: The Art of Scientific Computing*. Cambridge University Press, Cambridge, 1990. (Also available in FORTRAN and Pascal versions).

[84] R. H. Rand, R. J. Kinsey, and D. L. Mingori. Dynamics of spinup through resonance. *International Journal of Nonlinear Mechanics*, 1992. To appear.

[85] Richard H. Rand. *Computer Algebra in Applied Mathematics: An Introduction to MACSYMA*, volume 94 of *Research Notes in Mathematics*. Pitman Publishing, Boston, 1984.

[86] F. P. J. Rimrott. *Introductory Attitude Dynamics*. Springer-Verlag, New York, 1989.

[87] R. E. Roberson. Euler's problem on permanent axes, extended to the spinning gyrostat. *Journal of Applied Mechanics*, 37(4):1154–1156, Dec 1970.

[88] R. E. Roberson. Stability of orbiting gyrostats in the elementary cases. *Ingenieur-Archiv*, 39(5):317–329, Oct 1970.

[89] R. E. Roberson. The equivalence of two classical problems of free spinning gyrostats. *Journal of Applied Mechanics*, 38(3):707–708, Sep 1971.

[90] Jan A. Sanders and Ferdinand Verhulst. *Averaging Methods in Nonlinear Dynamical Systems*, volume 59 of *Applied Mathematical Sciences*. Springer-Verlag, New York, 1985.

[91] M. P. Scher. Effects of flexibility in the bearing assemblies of dual-spin spacecraft. *AIAA Journal*, 9(5):900–905, May 1971.

[92] M. P. Scher and R. L. Farrenkopf. Dynamic trap states of dual-spin spacecraft. *AIAA Journal*, 12(12):1721–1724, Dec 1974.

[93] S. Sen and P. M. Bainum. The motion and stability of a dual-spin satellite during the momentum wheel spin-up maneuver. *Journal of Spacecraft and Rockets*, 10(12):760–766, Dec 1973.

[94] J.-J. E. Slotine and M. D. Di Benedetto. Hamiltonian adaptive control of spacecraft. *IEEE Transactions on Automatic Control*, 35(7):848–852, Jul 1990.

[95] T. M. Spencer. Energy-sink analysis for asymmetric dual-spin spacecraft. *Journal of Spacecraft and Rockets*, 11(7):463–468, Jul 1974.

[96] Kazuo Tsuchiya. Attitude behavior of a dual-spin spacecraft composed of asymmetric bodies. *Journal of Guidance and Control*, 2(4):328–333, Jul–Aug 1979.

[97] Ferdinand Verhulst. *Nonlinear Differential Equations and Dynamical Systems*. Universitext. Springer-Verlag, Berlin, 1990.

[98] Vito Volterra. Sur la théorie des variations des latitudes. *Acta Mathematica*, 22(3–4):201–357, Dec 1898–Jun 1899.

[99] J. Weissberg and K. Ninomiya. Improved method for the initial recovery maneuver. *Journal of Guidance, Control and Dynamics*, 10(3):316–319, May–Jun 1987.

[100] R. A. Wenglarz. Dynamically unbalanced dual-spin space stations with rigid or low-coupling interconnections. *Journal of Spacecraft and Rockets*, 8(10):1032–1037, Oct 1971.

[101] J. R. Wertz, editor. *Spacecraft Attitude Determination and Control*. D. Reidel, Dordrecht, Holland, 1978.

[102] William E. Wiesel. *Spaceflight Dynamics*. McGraw-Hill, New York, 1989.

[103] Jens Wittenburg. Beiträge zur dynamik von gyrostaten. In *Convegno Internazaionale sul Tema: Metodi Valutativi Nella Fisica-Matematica, Roma, 15–19 dicembre 1972*, Problemi Attuali di Scienza e di Cultura, Quaderno N. 217, pages 217–354. Accademia Nazionale dei Lincei, 1975.

[104] Jens Wittenburg. *Dynamics of Systems of Rigid Bodies.* B. G. Teubner, Stuttgart, 1977.

[105] Stephen Wolfram. *Mathematica: A System for doing Mathematics by Computer.* Addison-Wesley, Reading, MA, second edition, 1991.

[106] Hai Xing Yang. Method for stability analysis of an asymmetric dual-spin spacecraft. *Journal of Guidance, Control and Dynamics*, 12(1):123–125, Jan–Feb 1989.